Directing Interfacial Events Using Biomimetic Polymer Brushes

by

Ramya Kumar

A dissertation submitted in partial fulfillment
of the requirements for the degree of
Doctor of Philosophy
(Chemical Engineering)
in The University of Michigan
2018

Doctoral Committee:

Professor Joerg Lahann, Chair
Professor Jinsang Kim
Professor Paul H. Krebsbach
Assistant Professor Timothy F. Scott

“They enter into blinding darkness who worship ignorance; into still greater darkness, as it were, do they enter who delight in knowledge.”

”He who knows both knowledge and ignorance together, crosses death through ignorance and attains immortality through knowledge.”

-The Isha Upanishad

Ramya Kumar

rmykmr@umich.edu

ORCID: 0000-0002-8725-0023

Dedicated to the memory of my deceased grandparents,

Balambal and Krishnamoorthy Iyer.

ACKNOWLEDGEMENTS

My time in Ann Arbor as a PhD student has been memorable and enriching thanks to a multitude of people who've made a difference to my life. This list is by no means exhaustive.

My advisor

My doctoral advisor, Prof. Joerg Lahann, has been a maverick in many ways, including his approach to recruiting. Right from the first time we met, it was clear to me that he didn't care as much about past accomplishments or pedigree as the student's motivation, attitude and willingness to work hard. He took a significant risk by accepting me into his lab, despite my lack of a stellar CV and the fact that I was a non-traditional student returning to the academy after a three-year stint in industry. I will always remain grateful to him for believing in my potential even at times when I didn't. He let me be myself, find my own identity and was always very open-minded and receptive to my ideas. Whenever I was down and dejected in my early years, it seemed like Prof. Lahann had near-infinite stores of patience, trust and optimism. At the same time, whenever I slipped into a rut or a comfort zone, he has always been resolute in shaking me out of it and nudging me to take risks and broaden my intellectual horizons. He has always "agreed to disagree" with his students and relished having his ideas questioned and sometimes challenged. There were times when he was gentle with criticism and times when he

was unsparing, but he has mostly been right.

Both of us believe in the value of failure as an educational stimulus. Failing frequently and failing willingly at lab has made me a better person and a better scientist and for the opportunity to make friends with failure, I'm very grateful. In the face of failures, even a 5-minute discussion with him would be very inspiring. Talking to him would instantly make me feel more optimistic about stalled projects. It has been my privilege to work with someone, who is not only of the best minds in biomaterials and polymer chemistry, but also a generous and principled human being.

Committee members

All my committee members had my best interests at heart and have provided valuable scientific insights. I'm very grateful to Prof. Krebsbach and Prof. Kim for their feedback and for taking the time to improve the quality of this dissertation. I would like to thank Prof. Nagrath for her practical inputs and suggestions while serving on my committee during my prelim and data meeting. I would like to thank Prof. Tim Scott for his generosity in stepping in to serve on my committee during the final stretch. I'm sure his perspectives as a macromolecular scientist will prove to be very illuminating.

Lab mates and collaborators

Being a part of Lahann Lab has been one of the most fulfilling experiences in my life. Not everyone is lucky enough to to work at a beautiful facility like NCRC, surrounded by talented, motivated and helpful peers. My lab mates have been an extraordinary source of inspiration for me at every phase in my degree. As a new student, I looked up to the illustrious examples provided by Sahar, Aftin, Xiaopei,

Jaewon, Asish and Tom. They didn't just display exemplary hard work, humility and work ethic, but they also went out of their way to help me start my own journey. Students from my own generation- Jake, Kenneth, Stacy and Nathan have been a source of comradeship, solace and healthy competition. What makes the Lahann Lab unique is we have the knack of egging each other on and keeping each other on our toes while still being collaborative and helpful. I'm particularly grateful to Stacy for her friendship and for making my time at Ann Arbor memorable and filled with laughter, love and sunshine. Whether it was defusing my personal crises or holding my hand in the hospital emergency room or celebrating my progress, Stacy has been with me very step of the way. Meeting her is one of the best things that could have happened to me at this lab. Kenneth has been a huge source of support, time and time again, in many projects. Selfless, brilliant and hardworking, I couldn't have asked for a better friend and colleague. I'm also fortunate to have met some highly talented and ambitious younger students, Ayse, Danny, Dylan, Nahal, Jonathan and Jason, who I'm sure will leave the lab a better place than they found it. Funnily, I learned as much from the newer students as I did from the senior students since the research focus and skill sets have been continually evolving. Hakan, Luis, Kathleen, Brad and Steph were some amazing post-docs who were also a lot of fun to hang out with. I would be remiss if I didn't thank my lab mates and collaborators from Karlsuhe Institute of Technology for their constant support. Domenic, Artak, Christoph and Fabian tirelessly kept synthesizing PCP-EB for me, without which this dissertation would not have happened. Domenic, in particular, has played a huge role in my PhD. The three months we spent together on the carbohydrate monomer synthesis transformed the trajectory of my PhD. I learned a lot about the finer aspects of organic synthesis from Domenic. He was an inexhaustible and resourceful chemist and possessed a boundless enthusiasm for research, which was very inspiring. Alexander Welle

has been a huge source of support and insight in his role as a ToF-SIMS expert. Meike Koenig has been a great co-author and has helped me with the finer details of surface characterization all these years. I'm also thankful to Gowthamy, Anke, Fabrice for their friendship.

My precocious undergrads, Tristan, Grant, Aymen, Jay, Irina, Julia and Salwan, have been a joy to work with. Tristan was instrumental in troubleshooting many problems in the UVO-initiated PMEDSAH process. Irina, Julia and Salwan have contributed to this thesis and have been acknowledged in the respective chapters. Aymen has been a reliable contributor to many industry collaborations. I'm grateful to have had the opportunity to mentor these budding engineers and I'm sure they will have fantastic research careers ahead.

Finally, I would like to thank my collaborators who worked with me on several projects- Prof. Luis Villa-Diaz, Tugba Topal, Dr. Xu Qian, Prof. Krebsbach, Prof. Henry Hess, Dr. James Sugai, Dr. Pienta, Amber de Groot, Dr. Jelani Zarif. Their expertise and skills made everything possible in the face of my unfamiliarity with several aspects of biological research.

I would also like to thank Haiping Sun, Kai Sun of MC2 for helping me gain expertise in XPS and AFM analysis. Linda Barthel of MIL is acknowledged for training me on fluorescence microscopy. I would also like to thank Vinod Radhakrishnan (Anton Paar) and Antonio (Accurion Gmbh) for helping me fix broken instruments from time to time.

I express heartfelt gratitude to the chemical engineering graduate program, primarily Susan Hamlin, Phil Savage, Lola and Bob Ziff for making me feel welcome and included in the department. My experience would not have been the same without their kindness. I'm thankful to Susan Montgomery and Lola for their hard hitting common sense advice provided on many occasions. I would like to thank Tim Scott for showing me the ropes of handling a large undergrad class and for

being a fantastic example to learn from. I would also like to thank my co-GSIs Jeff and Tiffany for making that semester fun!

Mary Beth Westin deserves special praise for competence and efficiency in handling all my unreasonable and impatient requests and managing the impossible on a daily basis. Lisa Moran has been a huge source of support and has always gone out of her way to make life easier for all of us.

Finally I would like to thank my colleagues from CRLT-Engineering for providing an avenue of learning outside my research. As a teaching consultant for two years, I learned so much about pedagogy and about myself, thanks to Bill, Tershia and Audra. I would also like to thank my fellow ETCs- Liam, Jeff, Molly, Maggie, Maia, Sahithya, Kathleen, Emily, Steve, Jon, and so many others for the sense of community and for all the candid conversations.

Family and friends

Words cannot describe how instrumental my mother, Chitra, has been to my personal and professional growth. Without her unconditional support and love, I would have probably quit graduate school. Right from pushing me to pursue higher education, to letting me cry on her shoulder when things were going badly, to giving me harsh but practical advice, she has always been there for me. From so many thousands of miles away, she has always been able to make me laugh even on days all my experiments failed, days I trudged through the snow, back and forth between lab and home, days when life seemed pointless. She always pushed me to keep going, keep fighting, again and again, to the very end. Thanks to my mother, I've been able to stand up for myself as a feminist and to speak my truth without fear. I have learned so much from her example all my life and continue to do so every day. My father, Kumar, has been a silent and steady source of support and has always believed that I would do well. Both my parents have made

numerous personal sacrifices so that I could pursue a PhD in the US and I cannot thank them enough for this. My sister, Aishu, has not just been a cheerleader and has always brought me back to my senses whenever I whined too much. I would also like to thank my extended family, my uncles, aunts and cousins for their encouragement. The memory of my late maternal grand parents has always been a source of inspiration for me during the low points of my PhD. My grandmother passed away unexpectedly the year I applied for grad school. I wish she had lived to see me finish my degree. My spouse, Krishna has been an unselfish sounding board at the end of every day, both good and bad ones, for giving me thoughtful advice about dealing with rejection and also celebrating my successes. I first met him in 2013, when I was in a particularly bad phase in my grad school career. It is no exaggeration to say that our relationship has made me a more productive and happier researcher. He has been a calming influence and I have been able to enjoy the process instead of focusing on the results. He is also a non-pareil LaTeX troubleshooter. Apart from encouraging me to learn LaTeX (on which this thesis is formatted), he has rescued many a conference talk from my blunders. I would like to thank all my friends and colleagues from my previous employer (Integrated Product Development, Dr. Reddy's Labs) for helping me get started on my research career. There are simply too many people to thank from DRL. Everything I learned in the lab and the production units as a young and inexperienced chemical engineer has made my PhD journey easier, in ways, intangible and concrete. Many of my DRL colleagues, particularly my former boss Srividya, were outstanding scientists who had received their doctoral training at some fine schools in the US. I am grateful to Srividya for playing a significant role in motivating me to apply for graduate school here. I would also like to thank my professors at my alma mater, BITS Pilani, particularly BV Babu, HK Mohanta and RP Vaid, for making me fall in love with the chemical engineering profession and ensuring that I turned out

at least half-decent at it. I'm also thankful to chemistry teachers from high school, Ms. Sundari and Ms. Susan, who influenced my choice of major. Finally, I would like to thank all my non-Lahannian friends for keeping me sane and reminding me that life that exists outside lab and that the outer life too, is beautiful. Shweta Ramdas and I spent 12 years in the same school in our hometown, only to speak to each other for the first time in Ann Arbor. I count her among the few people who know me as I truly am and I'm grateful for every conversation. Mahesh has been a good friend throughout the time he was here and helped me settle down in Ann Arbor. Vasudha and I were room mates for three years and I couldn't have had a more caring room mate and friend. Raghu, Naina, Anshula, Shilpa, Rukmani, Mohit, Surojit, Janani and everyone else... thanks for being there.

Medical professionals

I cannot stress enough, the importance of a healthy body and mind while pursuing a PhD. I've had minor health scares and accidents along the way. These could have easily prevented me from meeting the physical and intellectual demands of my research, but for the dedication and professionalism of people associated with Michigan Medicine and UHS. I would like to thank my therapist Dr. James Jobe, my doctors, Dr. Dina Kakish, Dr. Eran Vieregge, Dr. Jasmine Parvaz, Dori-Ann Danbury (PA-C) and most of all, my physical therapist Debbie Klinger, who made sure I got back on my feet and helped me walk and then run long distances again.

Funding

On a practical note, I deeply appreciate that our lab has almost always been well-funded and that we've always had the financial freedom to explore new ideas. I am grateful to the Department of Chemical Engineering (first semester fellowship

and GSI support), DTRA (HDTRA1-12-1-0039), NIH (R01DE016530) and Rackham Graduate School (Rackham Predoctoral Fellowship) for generous financial support provided during various phases of my degree.

Running

My journeys as a researcher and a runner have followed parallel paths, with blood, pain, tears, sweat and frequent falls being constant companions. Yet, I've had my share of glorious sunrises and moments of exhilaration in six years of grad school and as many half-marathons. I began both these journeys somewhat later in life than most people, and have found myself in the middle of the pack rather than up in front. In both arenas, my performance has been characterized by doggedness rather than natural talent, plodding rather than sprinting, and grit rather than brilliance. Running has forced me to bring both my heart and gut to my studies, not just my head. Though running and research tend to be intensely solitary activities that attract shy and private personality types, nobody can do it alone. I've been very fortunate in the people who cheered me on from the sidelines, the people who ran with me, and the people who encouraged me to sign up in the first place. I owe my finisher's medal to so many people who cared.

As any runner will attest, finishing a race is a bittersweet feeling, and the sight of the finish line is in equal parts, heartbreaking and uplifting. I wonder if I left it all out there on the road, whether I could have paced myself more wisely and whether I could have somehow exceeded my limits. Though I'll never know the answers to those questions, I walk away from the race, more courageous and stoic than before. As I finish one race, I know that many more roads and finish lines lie in wait. The race ends, the running goes on...

TABLE OF CONTENTS

LIST OF FIGURES

Figure

LIST OF TABLES

Table

Abstract

Polymer brushes are versatile surface modification tools, wherein composition, architecture and biological functionality can be controlled precisely and independently. By growing biomimetic polymer chains from substrate-bound initiator sites through atom transfer radical polymerization (ATRP), engineered biointerfaces were developed for four application areas.

Spatioselective deactivation of ATRP initiator coatings made via chemical vapor deposition polymerization was demonstrated to synthesize micropatterned polymer brushes in a substrate-independent, modular and facile manner. Exposure of 2-bromoisobutyryl groups to UV light resulted in the loss of the bromine atom and effectively inhibited polymer brush growth. Microstructured brushes were selectively grown from those areas on the initiator that were protected from UV exposure, as confirmed by atomic force microscopy (AFM), Time-of-Flight Secondary Ion Mass Spectrometry (ToF-SIMS) and imaging ellipsometry. Protein patterns based on specific as well as non-specific adsorption can be created on technologically relevant substrates such as polystyrene, PDMS, polyvinyl chloride and steel.

Model surfaces can aid in examining different hypotheses relevant to viral adsorption and formulating design rules for virus-resistant coatings. Thermodynamic models predicted that the extent of viral adsorption is shaped by the interplay between electrostatic attraction offered by binding sites and steric and hydration re-

pulsions arising from surrounding polymer brushes. To verify these predictions, electrostatically heterogeneous carbohydrate-functional brushes were developed. Experimental results confirmed model predictions and offered guidelines for designing virus-resistant surfaces in realistic scenarios where electrostatically attractive defects are prevalent. By allowing the carbohydrate brushes to attain brush thicknesses between 3-5 nm, low levels of protein and viral adsorption could be achieved, even when the defect density was as high as 25-30%.

The development of polymeric materials that facilitate the culture of large numbers of human pluripotent stem cells in fully defined conditions, poses a critical engineering challenge. Prior work had indicated that modifying the extent of zwitterionic self-association of PMEDSAH coatings could enhance the propagation rate of human embryonic stem cells (hESCs). Moderately self-associated PMEDSAH coatings were reported to be capable of expanding an initial population of 20,000 hESCS to 4.7 billion pluripotent cells at the end of five weeks, which is 2-fold and 12-fold higher than the estimated propagation rates for unassociated and highly associated coatings respectively. It was hypothesized that a property-prediction tool based on statistical design of experiments could identify reaction parameters that would yield targeted gel architectures. Model predictions were used to decrease the critical thickness at which the wettability transition occurs by merely increasing the catalyst quantity from 1 mol% to 3 mol%.

Pro-regenerative M2 macrophages (M2 Mps) have the potential to remediate chronic inflammation in a spectrum of disorders pertaining to macrophage polarization, such as diabetic wounds. By targeting the CD206 receptor on these cells using α-mannose molecules presented in multivalent architectures, we could engineer coatings that preferentially adhered to M2 cells over pro-inflammatory M1 cells. While a selectivity ratio (for M2 over M1) between 6 to 7 was observed on mannosylated surfaces, the control glucosylated surfaces did not discriminate be-

tween M1 and M2 phenotypes, exhibiting a selectivity ratio between 0.4 to 0.7.

By applying insights from polymer chemistry, surface science, and thermodynamics, an intimate understanding of biomedically relevant interfacial phenomena was acquired. This enabled the development of a platform based on multifunctional polymer brushes to address diverse problems at the interface of polymers and biology.

CHAPTER I

Introduction

1.1 The need for engineered biointerfaces

Biointerfaces, ubiquitous and pivotal in physiological processes, are considered a key organizing principle in living systems.[2] Ranging from the assembly of proteins at intracellular interfaces, to the interchange of biomolecules and signals at intercellular junctions, or the transport processes occurring between various organ systems, examples can be found at various length scales and for almost every biological function performed within living organisms. From a chemical engineering perspective, the biological processes comprising life can be modeled simply as molecular transformations and transport processes involving three components: 1) cells, 2) water and 3) biomacromolecules such as proteins, peptides, nucleic acids, carbohydrates.[3] The interfaces between these three components are not merely static staging grounds for biological events, but are intelligent and responsive structures orchestrating life processes, playing the roles of gates, valves, amplifiers, reactors, controllers or catalysts.[4,5]

Considering the enormous influence of interfaces in physiology, it is perhaps unsurprising that when biomaterials fail, the failure most often originates from the interface and not from the bulk of the material.[6] Blood clotting, microbial infiltration, non-specific protein and cellular adhesion, foreign body reaction, are some

of the commonly observed modes of failure for biomedical implants. These typically occur at the surfaces of orthopedic implants, stents, heart valves, implanted sensors, dialysis machines or drug delivery vehicles. Importantly, these biointerfacial events carry life-and-death consequences as they can hinder the biomaterial from fulfilling its healing and sometimes life-saving functions.

The grand challenge in biomaterials research is to engineer the elusive attribute of “biocompatibility". Biocompatibility is an often misapplied term, whose definition has been the subject of vigorous debate within the community.[7] Since biomaterials research is inherently interdisciplinary, spanning engineering, medicine and polymer chemistry, the term “biocompatibility" has been assigned varying definitions by practitioners trained in different disciplines.[8] In the view of a surface scientist, a material is said to be biocompatible if the interface between the biomaterial and its physiological environment is designed such that resulting interactions with cells, biomolecules or pathogens promote the intended physiological outcome.[9]

Within this definition of biocompatibility, engineering biointerfaces requires a three-pronged approach: 1) Constructing models that quantitatively predict interfacial outcomes, given an input function of surface design parameters. 2) Developing a toolbox of surface characterization tools to understand the interactions between relevant biological entities and biomaterial surfaces. 3) Employing modeling-derived insights as well the molecular picture of adsorption processes from characterization tools to engineer surfaces that possess the optimal composition, architecture and interfacial properties. Recognizing the significance of tailoring interfacial properties for different biomedical contexts, the development of platform technologies for surface characterization as well as model-guided surface modification has emerged as a key research focus.[10]

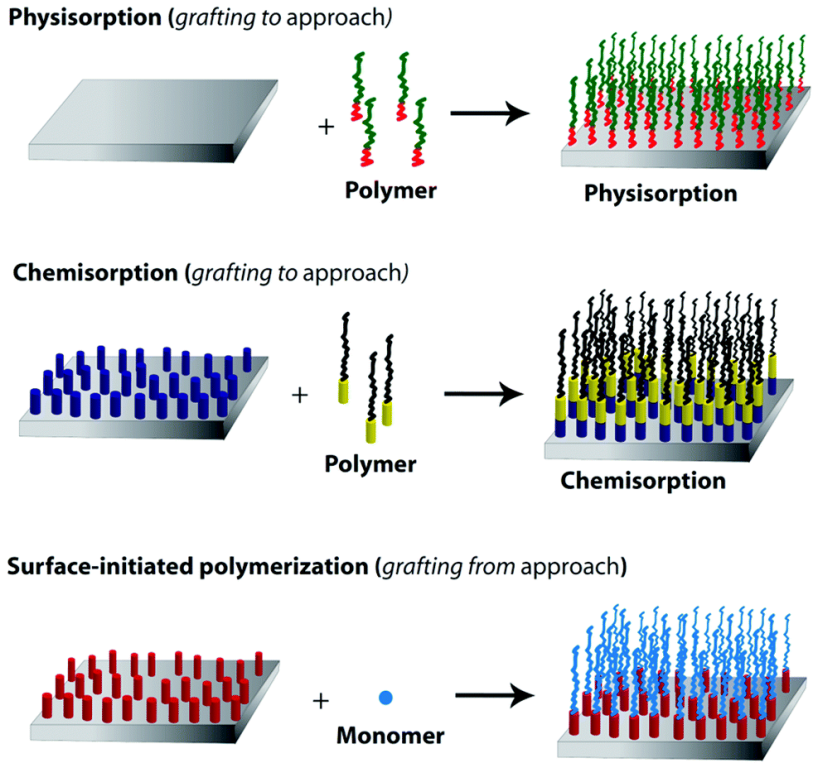

Figure 1.1: Schematic illustration of the preparation of polymer brushes using grafting to and grafting from methods. Cartoon adapted from Kocak et al.[1]

1.2 Engineering functional interfaces using polymer brushes

Surface modification techniques leave the bulk properties and composition of the biomaterial unchanged, while dramatically transforming its interactions with cells, biomolecules and pathogens. Due to the flexibility, multifunctionality and versatility afforded by polymers, they are ideal surface modification tools to impart properties such as hydrophilicity, bio-compatibility, protein resistance, lubrication, stimuli-responsiveness, surface charge and chemical reactivity to the substrate.[11] There are two synthetic strategies for introducing a polymeric nanofilm on a surface: grafting to and grafting from (Figure 1.1).[1]

In one version of the grafting to approach, thin polymer films can be produced using a variety of physical approaches such as spin coating, spray coating, dip coating from a polymer in solution or by self-assembly of block copolymers con-

taining adhesive segments that rely on electrostatic or hydrophobic interactions to physically adsorb to the surface.[12] In the absence of covalent bonds between the polymers and the substrate, the coating is unlikely to be chemically and mechanically robust and is therefor vulnerable to delamination upon exposure to solvent or heat or by competitive displacement.[13] These coatings don't possess long-term stability against delamination in physiological buffers, or changes in pH and temperature. An additional consequence of their instability is that these physisorbed polymers cannot be further modified by chemical reactions thereby limiting their utility.[13] To control the ordering and orientation of the coated polymer at a molecular level, covalent anchoring strategies are required.

Another version of the grafting to strategy involves the covalent ligation of pre-synthesized polymer chains with reactive end groups to substrates functionalized with complementary reactive entities.[14] Examples of covalent bonds include those between carboxylic acids and amine groups, epoxies and thiols, silane chemistry, alkynes and azides. While this approach helps graft monodisperse and well-characterized polymer chains to the substrate, high grafting densities and controllable thicknesses are difficult to achieve due to steric repulsions between long polymer chains.[14,15] Further, the kinetics of grafting-to processes are limited by diffusion of long polymer chains and are frequently slow and inefficient, mostly failing to yield true polymer brushes, where the distance between tethering points is smaller than the radius of gyration.[15]

In contrast, the "grafting from" approach is capable of producing dense, tunable and multifunctional polymer brushes which meet the above definition. This proceeds via the functionalization of the substrate with polymerization-enabling initiators and subsequent growth of polymer brushes from the initiation sites created on the surface through a bottom-up polymerization process wherein polymer chains are grown directly from the substrate.[14] The convergence of controlled radi-

cal polymerization (CRP) methods such as ATRP, reversible addition-fragmentation chain transfer (RAFT), nitroxide mediated polymerization (NMP), photoiniferter mediated polymerization (PIMP) and ring-opening metathesis polymerization (ROMP) with grafting-from strategies has enabled the synthesis of polymer brushes of diverse architectures and functionalities.[16] It is now possible to create polymer brushes with precisely and independently controlled grafting densities, molecular weight distributions and chemical and biological functionalities. The development of SI-CRP[17] techniques such as SI-ATRP, SI-NMP, SI-RAFT and SI-PIMP has transformed the synthetic possibilities of polymer brushes, enabling the formation of structures hitherto unrealizable.

Similar to other CRP techniques, SI-ATRP allows for exquisite control over the kinetics of brush growth, thereby achieving the target brush thickness and molecular weight distribution. However, SI-ATRP offers additional advantages of tolerating the presence of both impurities and a multitude functional groups within the monomer.[18] Moreover, for biofunctional monomers, it is sometimes essential to conduct the reaction at room temperature and aqueous media, conditions that are more easily realizable in ATRP compared to other techniques.[19,20]

SI-ATRP proceeds in two steps: 1) functionalization of the substrate with bromoisobutyryl initiators followed by 2) growth of polymer brushes from these surface-bound initiation sites. Due to its compatibility with initiator immobilization strategies such as click chemistry, thiol-based initiators for gold substrates, silane-based initiators for silica substrates and chemical vapour deposition polymerization initiators, it is possible to grow polymer brushes from diverse substrates. The versatility of SI-ATRP initiation has been successfully exploited to grafting polymer brushes from nanoparticles[21], 3D printed constructs[22], electrospun fibers[23–25], and even cysteine residues in living cells and proteins.[26]

SI-ATRP offers a rich and multidimensional design space, spanning numerous

physicochemical, biological and architectural design variables. Being amenable to several polymerizable backbones such as acrylates, methacrylates, methacrylamides, acrylamides, stryenes or vinyl benzenes. ATRP enables us to calibrate the polymerization kinetics by tuning the reactivity of the monomer. By choosing an appropriate pendant chain, such as zwitterionic groups, carbohydrate residues, oligoethylene glycol (OEG), or reactive moieties such as alkynes, azides, maleimides or activated esters, we can incorporate functionality into polymer brushes. In several instances, post-polymerization modification processes focusing on either the halogenated chain end or the functional side chains can be employed to further enhance the chemical and biological activity of the brushes.[27] In addition to homopolymer brushes, mixed brushes, block copolymer brushes, statistical copolymer brushes, gradient, hyperbranched, crosslinked brushes and other complex architectures such as Y-shaped, loop-type and bimodal brushes can be realized.[27] Finally, polymer brushes can be readily combined with other classes of nanomaterials such as quantum dots[28], liquid crystals[29,30], MOFs,[31] organic electronics,[32] etc. to create novel multifunctional materials.

1.3 Motivation for this dissertation

As a theoretical construct, the history of polymer brushes dates back to the seminal work of Alexander[33] and De Gennes,[34] who employed the Flory argument to develop a structural and mathematical definition of polymer brushes. A simple scaling relationship between polymer brush height h_0, degree of polymerization N and segment diameter a was proposed by assuming that monodisperse polymer chains are grafted from a non-interacting substrate with a density σ. The spherical blobs or segments are assumed to be uniformly distributed across the depth of the polymer brush in a stepwise fashion The equilibrium height of the polymer brushes is calculated by minimizing the free energy and is determined

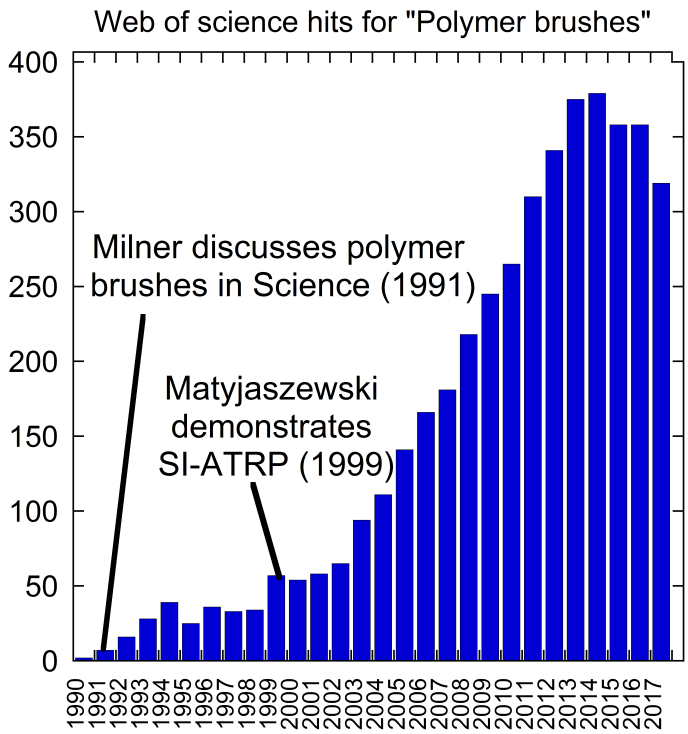

Figure 1.2: Number of hits for the search term, "polymer brushes" plotted against year. Sourced from Web of Science.

by the balance between the excluded volume interactions between adjacent polymer chains and the entropic loss caused by chain stretching. The Flory argument approximates the loss in configurational entropy caused by chain stretching by assuming a random walk from the substrate surface to the outer edge of the polymer brush. Ultimately, the following expressions are obtained:

$h_0 \approx Na^{5/3}\sigma^{1/3}$ in a good solvent (1.1)

$h_0 \approx Na^{2}\sigma^{1/2}$ in a bad or θ solvent (1.2)

Though these simple scaling expressions are useful in several contexts, Alexander and DeGennes' description of segment distribution as a step function proved to

be inaccurate. In 1991, Milner used self-consistent field theory (SCFT) to derive a more detailed relationship between brush parameters and also succeeded in predicting the parabolic segment distribution profiles accurately, which describes experimental results better than the AdG theory does, especially for large molecular weights and high grafting densities.[35] Subsequently, theoretical researchers have investigated the physical and thermodynamic behavior of end-tethered polymer chains using self-consistent field theory, density functional theory, Monte Carlo and molecular dynamics simulations.[36–38] These models were particularly valuable in pointing out contrasts in the physical behavior of dilute, end-tethered "mushroom-like" polymer coils formed via grafting to methods and fully extended, densely ordered polymer brushes.[39–41] Theoretical models have been instrumental in motivating the development of well-controlled SI-CRP methods that can produce monodisperse and densely grafted polymer brushes. It was only in 1999, when Matjaszewski and others demonstrated SI-ATRP without the use of sacrificial initiators to form well-defined polymer brushes, that this theoretical ideal of "true polymer brushes" could be realized experimentally.[42,43] From 2000 onwards, research activity in this area has grown exponentially as seen in Figure 1.2. Progress in polymer brush research has been driven largely by the synthetic ingenuity of chemists, leading to a steadily expanding library of functional monomers, reaction systems and polymer architectures. The creativity and versatility afforded by polymer brush synthetic techniques makes them ideal tools for engineering biomaterial surfaces possessing the requisite interfacial properties. Currently, polymer brushes are being widely utilized in several areas of biomedical research: in cell sheet harvesting, protein purification, as platforms for biosensing and cell culture, stealth coatings for drug delivery, non-fouling coatings and anti-microbial surfaces.[19] However several engineering challenges prevent the widespread adoption of polymer brushes in biomedical research, preventing them from reaching

their fullest potential. They are:

- **Biofunctionality**: In contrast to bionert non-fouling brushes, which have been embraced in several research areas, very little attention has been paid to developing biofunctional polymer brushes that can bind to biomolecules via specific interactions. Such biofunctional brushes can be used to provide spatiotemporal guidance for cell behavior.

- **Trial & Error Approaches**: Polymer chemists frequently employ iterative "one-factor-at-a-time" experimentation to navigate the vast design space involved in polymer brush synthesis. The optimization of SI-ATRP reaction parameters and identification of the relevant brush properties (surface charge, thickness, wettability etc.) is often time-consuming and tedious.

- **Substrate-specificity**: In order to prepare stable polymer brushes, initiator immobilization methods often rely on the presence of specific functional groups on the substrates, limiting the choice of substrates to a handful of model surfaces like silicon and gold. For many biomedically relevant substrates, polymer brushes are synthetically inaccessible.

To address these challenges and to potentiate polymer brushes in biomedical research, a multi-pronged strategy (Figure 1.3) has been applied:

1. Bioimetic motifs: Carbohydrates and zwitterions are not only reminiscent of chemical structures found in abundance within organisms, but can elicit a well-defined predictable response from cells and other biomolecules. By incorporating these bioinspired motifs within polymer brushes, we can recapitulate biological interactions occurring within the body. If the biomaterial presents ligands that are recognized by our cells, this will allow us to direct the behavior of cells, biomolecules and other entities. Instead of restricting

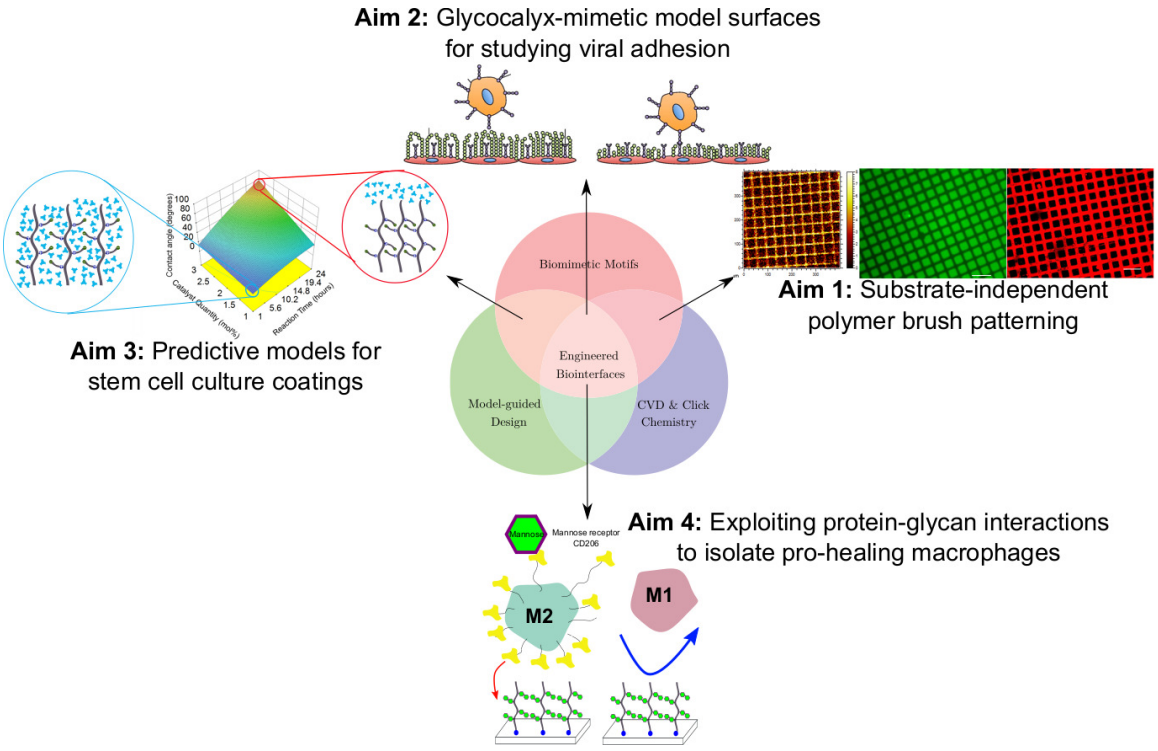

Figure 1.3: Dissertation outline and summary of aims.

polymer brushes to non-fouling or "stealth" applications, it would be more beneficial to design brushes that can actively communicate with cells by presenting and amplifying biological signals in the form of bioactive ligands immobilized to polymer brushes. Polymer brushes are particularly attractive scaffolds for ligand presentation due to their inherent multivalency and chain flexibility.

2. Model-guided design: Although polymer brushes have a rich multidimensional design space and a vast synthetic capacity for generating new information and insights, developing first-principles based models that quantitatively relate surface design decisions to interfacial properties and ultimate performance is a difficult undertaking. Additionally, knowledge-driven models do not account for uncontrollable experimental errors, multidimensional surface design space and may generate unreliable predictions that do not

guarantee the desired end-use properties for our materials. In this dissertation, unbiased data-driven models constructed from decision-oriented design of experiments and simplified thermodynamic models have been used in concert to guide the design of polymer brushes for various applications. Model-guided design is expected to save time, experimental effort and lead to a deeper understanding of the relationships between polymer brush properties and performance.

3. Reactive coatings: Chemical vapor deposition (CVD) polymerization is a surface modification platform for preparing reactive coatings in substrate independent manner from functional paracyclophane precursors. We can functionalize the substrate with a library of chemical moieties, including the ATRP initiator, irrespective of substrate chemistry and properties. SI-ATRP from a CVD polymerized initiator coating represents a universal approach to growing polymer brushes from any material. In addition, CVD copolymerization of one or more functional paracylophanes bearing alkyne, amine or alcohol functionalities, with the ATRP initiating unit enables us to further enhance the functionality of our brush coatings.

1.4 Dissertation aims

This dissertation aims to bridge the gap between the enormous progress made in polymer brush synthesis and unmet needs in biomedical research by engineering a multifunctional plaftorm based on biomimetic polymer brushes. In order to obtain the desired biointerfacial outcomes, a model-guided approach to polymer brush design and synthesis will be employed, in concert with the use of biomimetic motifs and reactive coatings created via CVD copolymerization.

Four areas of application have been addressed in this dissertation:

- To engineer a facile and scalable approach for the spatioselective adhesion of cells and biomolecules, in a substrate-independent manner.
- To design a model surface that provides an experimental framework for understanding and preventing viral adsorption to surfaces.
- To develop and validate a property prediction tool that can guide the synthesis of coatings for rapid proliferation of human embryonic stem cells (hESCs).
- To demonstrate the capabilities of carbohydrate brushes to capture pro-regenerative macrophages, paving the way for cell-based therapeutics that can be deployed in conditions such as diabetic wounds, that result from dysregulated macrophage polarization.

Chapter II reports the synthesis of micropatterned polymer brushes through photolytic deactivation of chemically vapor deposited SI-ATRP initiators. Two modes of spatially selective protein immobilization will be discussed.

In Chapter III, the development and validation of an electrokinetic approach for studying adsorption kinetics will be described. Real time ζ-potential measurements were employed to visualize the adsorption of virus-like nanoparticles on electrostatically heterogeneous model surfaces.

Chapter IV details the design and synthesis of carbohydrate-based model surfaces that were used to probe viral adsorption and derive design rules for virus-resistant coatings.

In Chapter V, statistical design of experiments was applied to develop a model that could predict the relationship between SI-ATRP reaction parameters and the interfacial attributes of poly(zwitterionic) brushes employed for hESC culture.

Chapter VI investigates the utility of mannose-functionalized surfaces for the selective capture of M2-polarized macrophages. Specifically, the role of glycan stere-

ochemistry and architecture was examined in promoting specific interactions between mannose and the CD206 receptors on the macrophages.

Chapter VII will conclude this dissertation and provide directions for future studies.

CHAPTER II

Substrate-Independent Micropatterning of Polymer Brushes based on Photolytic Deactivation of Chemical Vapor Deposition-based SI-ATRP Initiator Films

The material in this chapter has been adapted with minor modifications from the following manuscript in preparation
Ramya Kumar, Alexander Welle, Fabian Becker, Irina Kopyeva, Joerg Lahann, "Substrate-Independent Micropatterning of Polymer Brushes based on Photolytic Deactivation of Chemical Vapor Deposition-based SI-ATRP Initiator Films"

2.1 Abstract

Precise microscale arrangement of biomolecules and cells is essential for tissue engineering, microarray development, diagnostic sensors and fundamental research in the biosciences. Biofunctional polymer brushes have attracted broad interest in these applications. However, patterning approaches to create microstructured biointerfaces based on polymer brushes often involve tedious, expensive and complicated procedures that are specifically designed for model substrates. We report a substrate-independent, facile and scalable technique to prepare micropatterned and biofunctional polymer brushes. Employing chemical vapor de-

position (CVD) polymerization, a functionalized polymer coating decorated with 2-bromoisobutyryl groups that act as atom transfer radical polymerization (ATRP) initiators, was prepared and subsequently modified using UV light. Exposure of 2-bromoisobutyryl groups to UV light with wavelengths between 187-254 nm resulted in the loss of bromine and effectively prevented polymer brush growth. Microstructured brushes were selectively grown from those areas on the initiator that were not exposed to UV treatment, as confirmed by atomic force microscopy (AFM), Time-of-Flight Secondary Ion Mass Spectrometry (ToF-SIMS) and imaging ellipsometry. Furthermore, spatial control over protein adhesion was achieved in two ways: 1) Patterned non-fouling brushes resulted in non-specific protein adsorption to areas not covered with polymer brushes. 2) Patterned brushes decorated with specific binding sides (biotin molecules) gave rise to specific protein immobilization on areas covered with polymer brushes. This novel technique is independent of the substrate's physicochemical properties and can be extended to technologically relevant substrates such as polystyrene, PDMS, polyvinyl chloride and steel. With further work, photolytic deactivation of CVD-based initiator films promises to advance the utility of patterned biofunctional polymer brushes across a spectrum of biomedical applications.

2.2 Introduction

Several research areas in biomedical science require spatial control over the presentation of cells and biomolecules such as polysaccharides, growth factors or extracellular matrix (ECM) proteins[44]. Examples of such research objectives include spatio-temporal control of interactions between cells and ECM proteins to elucidate signaling pathways[45,46], high-throughput platforms for screening protein-protein and protein-glycan interactions for pharmacology and proteomic studies[47], bioMEMS devices for diagnostics and sensing[48], engineering neuronal net-

works on synthetic materials[49] and well-defined protein arrays that direct stem cell fate using geometric and chemical cues[50]. Engineered biointerfaces are essential tools to accomplish these goals and it is particularly desirable that platforms for obtaining custom biomolecular patterns are simple, substrate-independent and scalable.

A rich toolbox of bottom-up and top-down surface engineering techniques has been developed to meet these challenges. Direct protein-writing approaches such as dip-pen nanolithography,[51] inkjet printing,[52] laser ablation, nanoimprint lithography[53] (NIL), polymer pen lithography[54] (PPL), colloidal lithography[55] (CL) and e-beam lithography[56] are geometrically versatile and allow for the orthogonal creation of multiplexed protein patterns. Unfortunately, these methods are often limited by low throughput and the requirement of multiple serial processing steps, each of which needs delicate handling, sometimes in cleanrooms[57]. Micro-contact printing (μCP) and its variations have been widely used in creating protein arrays[58] and patterns thanks to its inexpensive nature and flexibility of use in lab-on-chip and microfluidic applications.[59] However, μCP can suffer from technical difficulties owing to PDMS stamp collapse with decreasing feature sizes, and pattern reproducibility issues due to stamp inking and drying.[60]

Alternatively, indirect approaches rely on patterned polymer brushes to direct biomolecular and cellular adhesion.[19] Polymer brushes have been used to impart the desired interfacial properties and create surfaces with tailored architectures, or chemical and biological functionalities[61]. Depending on the brush composition, researchers have either engineered resistance to non-specific protein adsorption[62] or precisely controlled the composition and orientation of proteins that can recognize and bind to bioactive polymer brushes through specific interactions.[63,64]

Polymer brush synthesis has dramatically benefited from the development of surface-initiated polymerization techniques such as surface-initiated atom transfer

radical polymerization (SI-ATRP),[43] surface-initiated radical addition-fragmentation transfer (SI-RAFT)[17] and surface-initiated nitroxide mediated polymerization (SI-NMP)[65], of which SI-ATRP is most widely used. Polymer brushes are typically synthesized in two steps: i) immobilization of an SI-ATRP initiator (usually the bromoisobutyryl group) followed by ii) SI-ATRP of the desired monomer from the initiation sites to form densely tethered polymer chains. By exerting spatial control over either of these two steps, it is possible to create micro and nano-scale patterns of polymer brushes.[27] The advent of oxygen-tolerant SI-RAFT[66] and SI-ATRP[67] has eliminated the necessity of specialized equipment (such as schlenk lines and glove boxes) and formal training in air-free chemistry techniques, making polymer brushes more accessible to non-experts[68]. Previously developed polymer brush patterning strategies can be classified into three categories: 1) Selective activation of a photosensitive iridium catalyst by irradiating the reaction system through a mask[69]; or selective initiator functionalization via photolysis of nitrophenyl-protected molecules[70]. 2) Creating patterns of the SI-ATRP initiator using DPN[71–73], PPL[54] or CL[74,75] techniques, μCP[76], or the application of DOPA-based macro-initiators.[77–79] 3) Post-polymerization top-down approaches involving selective degradation of the polymer brushes using e-beam treatment[80,81] or the use of photodegradable polymer brushes.[82] 4) Spatially selective deactivation of the bromoisobutyryl initiator using near-UV photolithography,[83,84] and direct e-beam treatment for bond scission[85].

There are some shortcomings associated with current techniques for patterning polymer brushes. Photolabile monomers and photosensitive catalyst systems can be challenging to synthesize. Besides requiring clean room conditions, e-beam lithography is time-consuming, when large substrate areas and high numbers of substrates have to be patterned.[86] Common to all these patterning platforms is that they are restricted to a handful of substrate choices, making it difficult to

adapt them to petri dishes, well plates, microfluidic devices or other substrates typically employed in biomedical research. Photolytic deactivation of silane-based initiator systems confine their application to Si/SiO_2 substrates, whereas μCP and DPN-based approaches rely on patterning gold substrates with thiol-based initiators. Specialized initiators have been developed for graphene[87], graphene oxide[88], ITO[89] and titanium[84] substrates, but they typically require extensive multi-step synthesis. Overall, there is a need for a rapid, facile and substrate-independent patterning strategy that resolves these technological issues while achieving a high degree of pattern fidelity and reproducibility.

Chemical vapor deposition (CVD) polymerization is a substrate-independent surface-modification tool that yields reactive coatings in a solvent-free, pinhole-free and conformal manner.[90] Capable of coating almost any substrate material[51], CVD presents a versatile route to chemically reactive surfaces[91]. In the past, soft elastomeric stamps such as PDMS were used to transfer chemical patterns onto reactive CVD-based coatings via click reactions.[92,93] Subsequently, these patterns could be amplified into cellular and biomolecular patterns. CVD-mediated microstructuring was not limited to flat substrates; three-dimensional objects were also patterned by employing photolithography on benzophenone based CVD polymers.[94] Significantly, Jiang et al.[95] developed a CVD-based ATRP initiator immobilization strategy that decoupled SI-ATRP from the underlying surface chemistry. In addition to developing a bromoisobutyryl based CVD precursor that could be vapor-deposited on any substrate, they employed Vapor-Assisted Micropatterning in Replica Structures (VAMPIR)[96] to create patterned initiator surfaces. Due to its reliability, scalability, flexibility and substrate-independence, the union of CVD with traditional patterning approaches has been highly beneficial. However, VAMPIR is typically limited to discontinuous patterns and intimate contact must be ensured between the PDMS construct and the substrate for VAMPIR to be effective.[97]

Here, we report a patterning strategy for polymer brushes using CVD-based initiator surfaces that is substrate-independent and can create polymer brushes along arbitrary micropatterns. By exposing the CVD-polymerized bromoisobutyryl coatings to UV light through a photomask, we were able to deactivate the initiator on the exposed regions, while preserving the ATRP-initiating abilities of the coating on the masked regions. This UV-treated surface was then employed as a substrate for SI-ATRP, resulting in well-defined patterns of polymer brushes. Our platform confers the ability to simultaneously process multiple patterns in parallel and can be applied to a large library of substrates, as long as they are compatible with the CVD process, regardless of chemical composition, optical and mechanical properties. Moreover, the development of bioinert and bioactive polymer brushes makes it possible to orchestrate contrasting biointerfacial outcomes on these patterned brushes. While Iwata et al. [83] employed UV to completely strip off the ATRP initiator layer that was deposited in the form of a SAM, our technique merely debrominates the surface while leaving the polymer backbone intact.

2.3 Experimental

2.3.1 Chemical vapor deposition

Around 30 mg of the precursor, [2.2]paracyclophane-4-methyl 2-bromoisobutyrate (PCP-EB) was sublimed at 115-125 °C under reduced pressure (0.3 mbar) and then pyrolysed at 550 °C. Substrates were placed on a cooled stage (14 °C) where radical species got adsorbed. Subsequently, they underwent polymerization to form coatings composed of poly[(*p*-xylylene-4-methyl-2-bromoisobutyrate)-*co*-(*p*-xylylene)] (PPX-EB).

2.3.2 Initiator patterning

First, substrates were coated with PPX-EB using the procedure described above. Then, copper TEM grids (Structure Probe, Inc., PA) were placed on the substrates and treated in the 144AX chamber (Jet light, CA) for 10-30 minutes. Thereafter the grids were removed and the patterned substrates were used for SI-ATRP.

2.3.3 Surface-initiated atom transfer radical polymerization

After UV treatment, the patterned PPX-EB substrates were subjected to SI-ATRP using typical schlenk techniques. For the SI-ATRP of poly(2-methacryloyl-oxyethyl phosphorylcholine) or poly(MPC) brushes, the following procedure was employed. Copper (I) bromide, copper (II) bromide and 2,2, bipyridyl were purchased from Sigma Aldrich and used without further purification. Substrates were placed in a glove bag and degassed using 3 cycles of vacuum-argon purge and left at room temperature under argon. 10 mL of methanol and 2 mL of water were mixed together in the monomer flask and then degassed by three cycles of freeze-pump-thaw. In parallel, 10 mg $CuBr_2$, 34.5 mg CuBr and 140 mg 2,2 bipyridyl were placed in a separate catalyst flask and degassed using 3 cycles of vacuum-argon purge. After the completion of the final thaw operation, 3 mL of the solvent mixture was transferred to the catalyst flask from the monomer flask under argon using a degassed needle and syringe. Then, 5 g of 2-methacryloyloxyethyl phosphorylcholine (Sigma Aldrich) was added to the monomer flask under argon. Upon dissolution, the brown-colored catalyst mixture was added to the degassed monomer solution and mixed thoroughly at ambient temperature (22 °C) under argon. This mixture was transferred to the glove bag and distributed such that each substrate was submerged completely in the reaction solution. The SI-ATRP reaction was allowed to proceed for 24 hours under argon atmosphere. Finally, substrates were rinsed repeatedly with 0.05 M EDTA solution and deionized wa-

ter and dried.

For the synthesis of Poly(propargyl methacrylate-co-{[2-(methacryloyloxy) ethyl] dimethyl-(3-sulfopropyl) ammonium hydroxide} brushes, a similar procedure was employed. Propargyl methacrylate (PMA) was purchased from Dajac Labs (Trevose, PA). Substrates were placed in a glove bag along with a 20 mL vial and degassed using 3 cycles of vacuum-argon purge and maintained in an inflated state under argon.To a schlenk flask, 25 mL methanol was added. To a second schlenk flask, 3.5 ml propargyl methacrylate (PMA), 3.5mL dimethylformamide and 70 μL Me_6TreN were added. Both flasks were subjected to thee cycles of freeze pump thaw. After the third freeze, 28.5 mg of CuBr, 4.8 mg of $CuBr_2$ added under argon to the PMA flask. Then, pump and thaw operations proceeded as usual to yield a blue solution. For the methanol flask, 5 g MEDSAH added under argon upon completion of the third freeze operation. Thereafter, pump and thaw were completed as usual and clear solution obtained. Both flask were taken into the glove bag and the bag was degassed twice. Then 5 mL of the MEDSAH solution was combined with 1.2 mL of the PMA solution in a 20 mL vial placed in the glove bag to achieve a 1:1 mole ratio of the two monomers. The vial was shaken well and poured over the substrates. The glove bag was kept inflated with argon for four hours, after which, substrates were rinsed repeatedly with 0.05 M EDTA solution and deionized water and dried.

2.3.4 Atomic force microscopy

AFM of patterned areas was performed using a Dimension Icon (Bruker, WI). Measurements were taken in tapping mode at room temperature in air using PNP-TRS probes (Nano World, CA) with resonant frequency and spring constants of 0.32 N/m and 67 kHz. Measurements were taken at a scan rate of 0.1 Hz over a 55×55 μm^2 area.

2.3.5 Imaging ellipsometry

Height differences on patterned brushes were visualized using the Accurion EP3 imaging ellipsometer (Accurion GmbH, Germany) fitted with a 10× objective.The Δ maps were recorded at a wavelength of 531.9 nm and thickness values were fitted using interpolation and a refractive index of 1.58.

2.3.6 Protein patterning & fluorescence microscopy

For the non-specific protein adhesion studies, glass cover slips patterned with poly(MPC) brushes were incubated with 50 μg/ml solution of bovine serum albumin conjugated to Alexa Fluor 594 (catalog # A13101, Thermo Fisher Scientific) in 10 mM PBS. Subsequently, the cover slips were washed copiously with 10 mM PBS and then deionzied water, and then dried and imaged.

For specific protein adhesion, glass cover slips bearing patterned brushes composed of poly(propargyl methacrylate-co-{[2-(methacryloyloxy) ethyl] dimethyl-(3-sulfopropyl) ammonium hydroxide} were employed. First, they were biotinylated using the Husigen copper catalyzed 1,3 alkyne azide cycloaddition. In brief, a solution consisitng of 10 mg/ml solution of biotin-PEG-azide (PG2-BNAZ-5k, Nanocs, NY) was prepared in 10 mM PBS. Substrates were incubated in this solution and shaken at 70 RPM over 24 hours. Then the substrates were washed thoroughly and passivated with a 1 mg/ml solution of BSA in 10 mM PBS with 0.01% v/v Tween-20. Thereafter, a solution of 50 μg/ml Cy3-conjugated streptavidin (catalog # S6402, Sigma Aldrich) was prepared by dissolution in PBS containing 0.01 % (v/v) Tween 20. Biotinylated brushes were incubated with this solution for 10 minutes. The substrates were repeatedly washed with PBS and finally rinsed with deionized water. Substrates were dried and fluorescence micrographs recorded. All fluorescence imaging was performed using Nikon E-800 microscope. Exposure times were substrate-dependent, with steel requiring 1-2 s whereas glass required

only 500 ms. For all other substrates, exposure times of 500 ms to 1 s were used.

2.3.7 X-ray photoelectron spectroscopy

XPS was performed on a Kratos AXIS Ultra DLD spectrometer equipped with a monochromated Al Kα source. Samples were pumped down till the pressure in the analysis chamber was around 10^{-10} Pa. The analysis region was around 710 μm^2. Survey spectra were initially collected to ascertain peak ranges of interest (C,O,Br) over a binding energy range of 0-600 eV, pass energy of 160 eV, step size of 0.5 eV, and dwell time of 0.1 s. Thereafter elemental composition was determined by performing high resolution scans of the C 1s, O 1s and Br 3d regions collected using a pass energy of 20 eV, step size of 0.1 eV, and sweep time of 60 s. Peak fitting and data analysis were performed using the CasaXPS software.

2.3.8 ToF-SIMS

ToF-SIMS (Time-of-Flight Secondary Ion Mass Spectrometry) was performed on a TOF.SIMS5 instrument (ION-TOF GmbH, M*ü*nster, Germany). This instrument is equipped with a Bi cluster primary ion source and a reflectron type time-of-flight analyzer. UHV base pressure was $< 5\times10^{-8}$ mbar. For high mass resolution analyses, the Bi source was operated in the "high current bunched" mode providing short Bi_3^+ primary ion pulses at 25 keV energy, a lateral resolution of approximately 4 μm, an a target current of 0.1 pA at a repetition rate of 5 kHz. The short pulse length of 0.8 ns allowed for high mass resolution. The primary ion beam was usually rastered across a 300×300 μm^2 field of view on the sample, and 128×128 data points were recorded. Spectra were calibrated on the omnipresent C^-, C_2^-, C_3^-, or on the C^+, CH^+, CH_2^+, and CH_3^+ peaks. Based on these datasets the chemical assignments for characteristic fragments were determined. For high lateral resolution imaging, "burst alignment" mode, providing only nominal mass

resolution, was applied. Here, 100×100 μm^2 fields of view on the sample were analyzed, and 128×128 data points were recorded.

For depth profiling a dual beam analysis was performed in non-interlaced mode. For patterned initiator samples, prior to MPC grafting, Figure 2, the primary ion source was operated in "high current bunched" mode with a scanned area of 300×300 μm^2 (3 frames), ; or in "burst alignment" mode with a scanned area of 100×100 μm^2 (5 frames) , and a sputter gun operated with $Ar_{500}{}^+$ cluster ions, 5 keV, (scanned over a concentric field of 600×600 μm^2, target current 0.8 nA; or 450×450 μm^2, , target current 0.5 nA, respectively) was applied to erode the sample for 3 s followed by a 0.3 s pause.

For samples carrying poly(MPC) brushes, the primary ion source was operated in "high current bunched" mode with a scanned area of 300×300 μm^2 (3 frames), or in "burst alignment" mode with a scanned area of 100×100 μm^2 (5 frames) , and a sputter gun operated with $Ar_{1700}{}^+$ cluster ions, 10 keV, (scanned over a concentric field of 500×500 μm^2, or 350×350 μm^2, respectively, target current 1.0 nA) was applied to erode the sample for 3 s followed by a 0.3 s pause.

2.3.9 Patterning experiments with non-model substrates

PDMS samples were prepared by uniformly mixed PDMS prepolymer and curing agent (Sylgard 184, Dow Corning, USA) at a ratio of 10:1 and were cured at 70 for 1 hr. Glass coverslips (Fisher Scientific, USA), Thermanox polystyrene coverslips (Ted Pella Inc), polyvinyl chloride sheets (Ted Pella, Inc., USA), and steel (Goodfellow, USA) were used as received. Substrates were coated with PPX-EB through CVD and then poly(MPC) using SI-ATRP as described in previous sections.

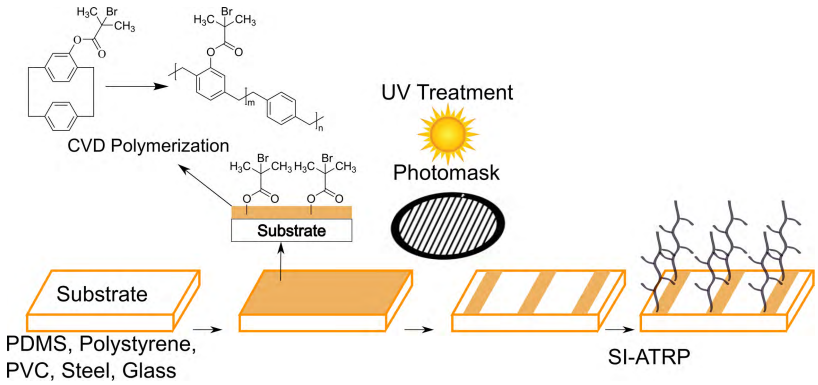

Figure 2.1: Spatioselective deactivation of SI-ATRP initiator using UV-ozone treatment through a photomask. Polymer brush growth only occurs from masked regions whereas in treated regions, the initiator activity is suppressed.

2.4 Results and discussion

Figure 2.1 outlines the first step of the research strategy involving coating of substrates with the SI-ATRP initiator, poly[(*p*-xylylene-4-methyl-2-bromoisobutyrate)-*co*-(*p*-xylylene)] (PPX-EB) through CVD polymerization of the precursor [2.2]paracyclophane-4-methyl 2-bromoisobutyrate (PCP-EB). The thickness of these PPX-EB coatings was determined using ellipsometry and confirms the formation of the coating. Additionally, XPS and FTIR were performed in order to ascertain that the ATRP-initiating ester bromide functional groups were present.

Next, PPX-EB coated substrates were exposed through photomasks with hexagonal patterns to UV light for treatment times ranging from 10-20 minutes in order to understand the impact on the spatial distribution of residual bromine on the initiator layer. To measure bromine content as a function of spatial location (lateral and depth profiling), we employed Time-of-Flight Secondary Ion Mass Spectrometry (ToF-SIMS). Static ToF-SIMS has excellent surface sensitivity (<2 nm) and a lateral resolution down to 150 nm and was hence employed to capture chemical contrasts across these patterns. To probe deeper layers and buried interfaces, dynamic SIMS based on erosion of the sample with an argon cluster ion beam was employed to capture chemical contrasts across these patterns. In Figure 2.2,

the bromine distribution of the hexagonally patterned initiator coatings changes as a function of UV treatment time. We noticed that the highest intensity signals from the $^{79}Br^-$ and $^{81}Br^-$ fragments were emitted from the areas lying between the hexagons (yellowish in colour), with the interiors of the hexagons displaying very low Br^- intensity (darker regions in the heatscale). An unexpected, albeit interesting observation was the progressive deterioration of pattern quality upon increasing UV treatment time. High-resolution images of the bromine chemical maps (Figures 2.2(d), 2.2(e) and 2.2(f)) revealed that the bromine in the hexagonal borders became progressively thinner with increased treatment times. Also, characteristic halos could be discerned in the UV-treated regions inside the hexagons in the 15 minute and 20 minute samples, signifying an increase in ablated area. During UV treatment, deep UV light (between 185 and 257 nm) can generate ozone from oxygen.[98] The simultaneous action of UV light and ozone results in surface oxidation of carbon-based materials and is frequently employed for polymer surface modification and in stripping surfactant layers from end-capped Pt and Pd nanoparticles to improve their catalytic activity.[99] For SI-ATRP reactions to be initiated, the halogen atom (usually bromine) needs to be transferred from the initiator species to the coordination complex formed between the ligand and the Cu(I) bromide. If the bromine atom is absent on the initiator surface, SI-ATRP will not occur. Further, ozone-triggered bromine depletion can explain why treatment time plays such a critical role. Once the optimum treatment time is exceeded, UV-generated ozone diffuses under the mask and begins to ablate masked areas. With longer treatment time, the ozone diffuses across larger areas beneath the mask, explaining why we obtained differences in feature sizes despite using identical photomasks. These findings agree well with a recent report by Sheridan et al.[100], who reported that UV treatment could deactivate the ATRP-initiating bromoisobutyryl groups.

In order to further our mechanistic understanding of the UV-induced bromine

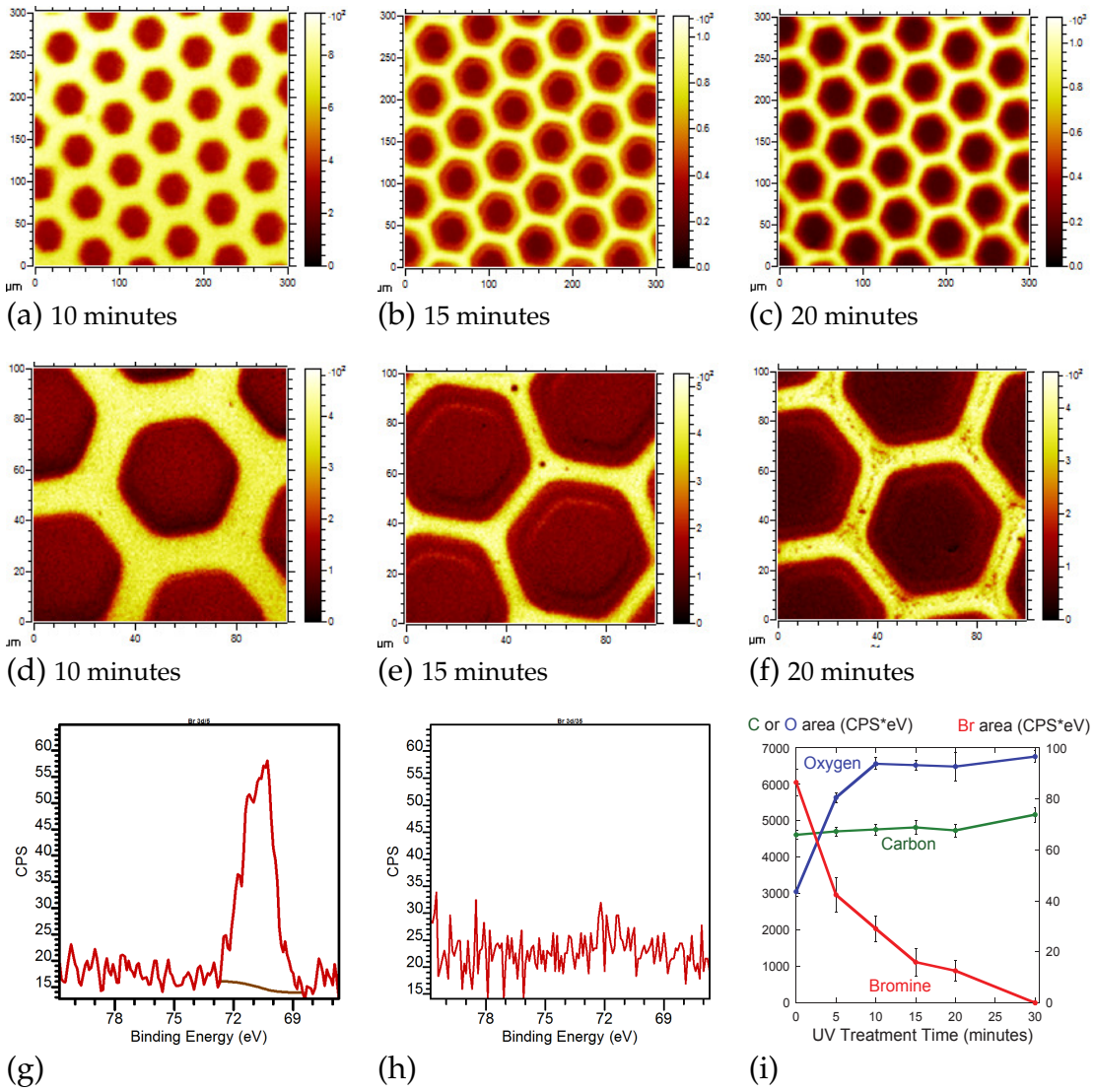

Figure 2.2: Evolution of vapor-deposited initiator (PPX-EB) surface composition with UV treatment. (a)-(f) Depth integrated lateral distribution of Br from ToF-SIMS (sum of both isotopes.) (a) & (d) Distribution of Br^- on PPX-EB surfaces treated for 10 minutes through a hexagonal photomask. (b) & (e) When treatment time was increased to 15 minutes, we could discern shrinkage in the areas previously emitting Br^-. This is apparent in the formation of a halo around the hexagonal borders and the reduced thickness of hexagon borders. (c) & (f) At the 20 minute time point, we could observe a starker contrast between the interior of the hexagons and the borders. This was also accompanied by reduction of bromine content within the masked border regions, apparent in the red streaks formed in the yellow hexagonal bands. (g)-(i) XPS data of unpatterned samples: (g) High resolution scan of Br 3d on PPX-EB prior to UV treatment. (h) High resolution scan of Br 3d after 30 minutes of UV exposure. (i) Even 5 minutes of treatment causes a steep decrease in area under Br 3d peaks (red). This decrease continued with progressively higher UV treatment times until the peak disappeared. While the C 1s (green) area remained more or less constant with UV treatment, oxygen (blue) content increased significantly.

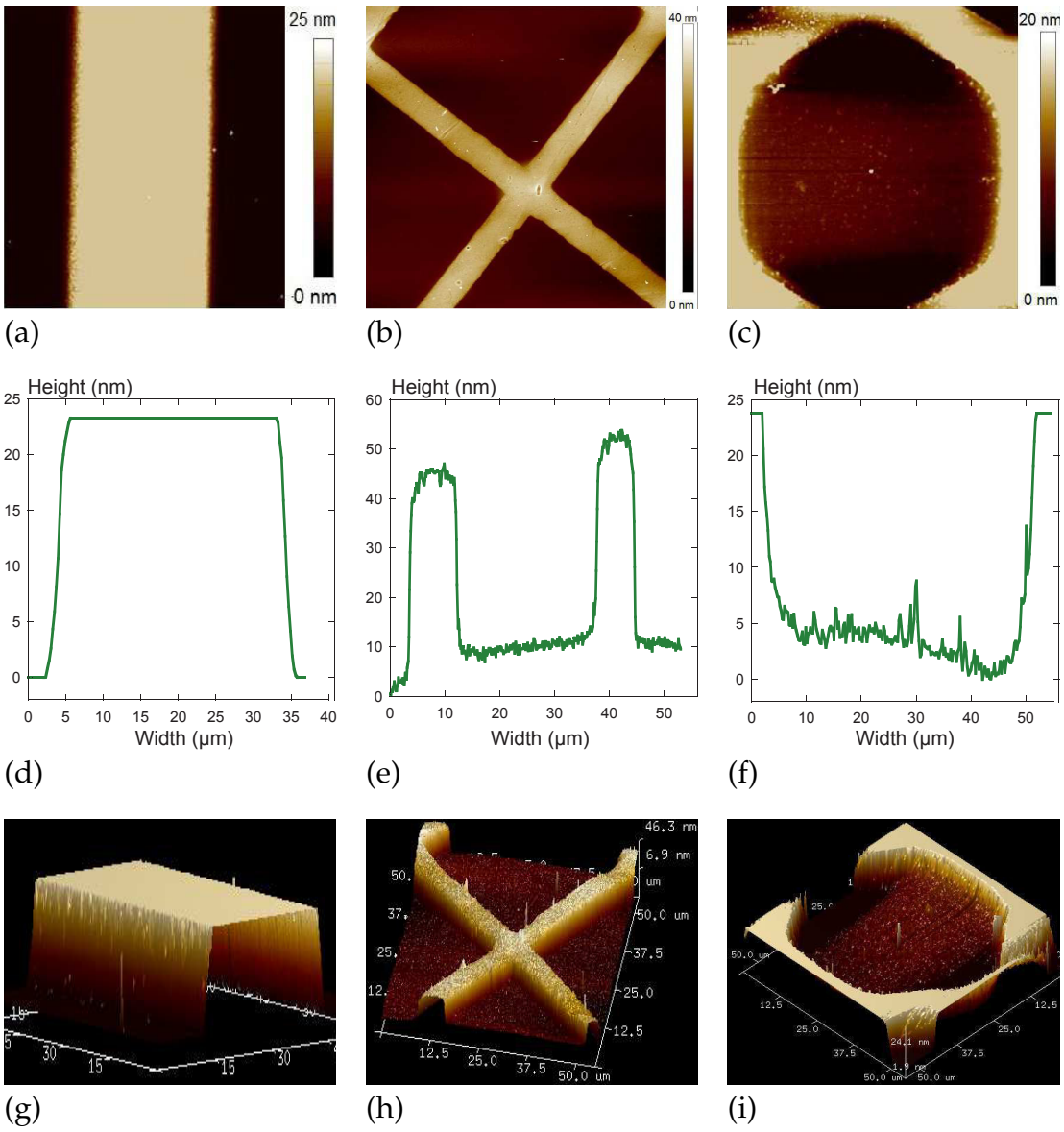

Figure 2.3: Atomic Force Microscopy (AFM) was used to visualize the topographic contrasts of patterned poly(MPC) brushes. (a), (b), (c) Two-dimensional topographical maps of the patterned poly(MPC) brushes obtained from AFM imaging of dry substrates. Topographic contrasts were congruent with the geometry of the photomask employed. (d), (e), (f) Height profiles from AFM measurements. Brush heights of 20-40 nm were observed, which agreed with the imaging ellipsometry results. (g), (h), (i) Three-dimensional projections of the patterned surfaces.

depletion process, we conducted XPS measurements of homogeneously treated PPX-EB surfaces (without photomasks) to understand how its elemental composition changes with UV treatment time. As seen in Figure 2.2(g), the Br 3d signal at 70.3 eV can be clearly discerned from the untreated PPX-EB surface, whose theoretical bromine content is around 4.8%. However, after 30 minutes of UV treatment (Figure 2.2(h)), the peak intensity falls drastically and can no longer be discriminated from the background. Upon quantifying the area under the Br 3d peak obtained from high-resolution scans (Figure 2.2(i)), we observed that the bromine content was significantly reduced even within 5 minutes of UV exposure and continued to decrease steadily with increasing treatment time before being reduced to near-zero levels at 30 minutes. The quantification of high-resolution XPS spectra (Table S3 in SI) agreed well with our conclusions from the chemical maps generated by ToF-SIMS, where there were strong contrasts in bromine content between treated and masked areas. Further, we were able to glean additional insights from XPS, specifically the role of ozone in the initiator deactivation process. In contrast to Br 3d, the O 1s signal rises continually with UV exposure. The oxygen content was observed to increase from 18.3 % for the untreated PPX-EB surfaces to 31.8 % after 30 minutes of UV exposure. This indicates that the removal of bromine from the PPX-EB surface is accompanied by the transformation of C-H and C-Br bonds into aldehydes, alcohols and acids by ozone. This conclusion is supported by the changes in the high resolution C 1s spectra (Figure S4 in SI), which show a gradual increase in C=O and C−O signals with higher UV treatment times. Together, the XPS and ToF-SIMS results led us to conclude that the ability of PPX-EB to initiate polymer brush growth is hindered by its exposure to ozone.

Next, we proceeded to verify that the initiator patterns could be used to prepare microstructured polymer brushes. We grafted poly(2-methacryloyloxyethyl phosphorylcholine) (poly(MPC)) brushes from these patterned PPX-EB substrates

and acquired ToF-SIMS images, focusing on the PO_2^- and PO_3^- fragments emitted by the phosphorylcholine brushes. We observed a strong contrast in PO_2^- and PO_3^- signals owing to the high thickness and density of the poly(MPC) brushes in the masked areas compared to the dilute and short polymer chains present in the UV-treated regions. Regions from which PO_2^- and PO_3^- signals (characterizing the poly(MPC) brushes) were observed, overlapped with the areas from which the Br^- signals (associated with the initiator coatings) were recorded. The PO_x and bromide signals were co-localized in the masked areas which were shielded from UV exposure, confirming that patterned polymer brushes arise from the patterned initiator coatings.

To demonstrate the geometric versatility and ease of controlling feature shapes, we prepared poly(MPC) brushes using initiator coatings patterned using photomasks with hexagonal, square and striped patterns. We characterized these patterned poly(MPC) brushes using atomic force microscopy (AFM) as shown in Figure 2.3, where the height profiles, two-dimensional topographic maps and three-dimensional projections, all reveal thickness differences existing between the regions from which the brushes were successfully grafted. We observed that the geometrical shapes of the brushes were identical to that of that of the patterned photomask employed. Using AFM, we also confirmed that the dry brush thickness was between 25-40 nm.

To complement the AFM study, brush thickness was studied as a function of spatial location using imaging ellipsometry. From Figures 2.4(b), 2.4(e) and 2.4(h), we discerned the variation in brush thickness between areas where the polymer brush growth was allowed to proceed and the areas where brush growth was inhibited. Thickness differences between the brush patterns and the surrounding brush-free substrate were between 20-40 nm, which is consistent with the differences in dry thickness reported by the AFM study.

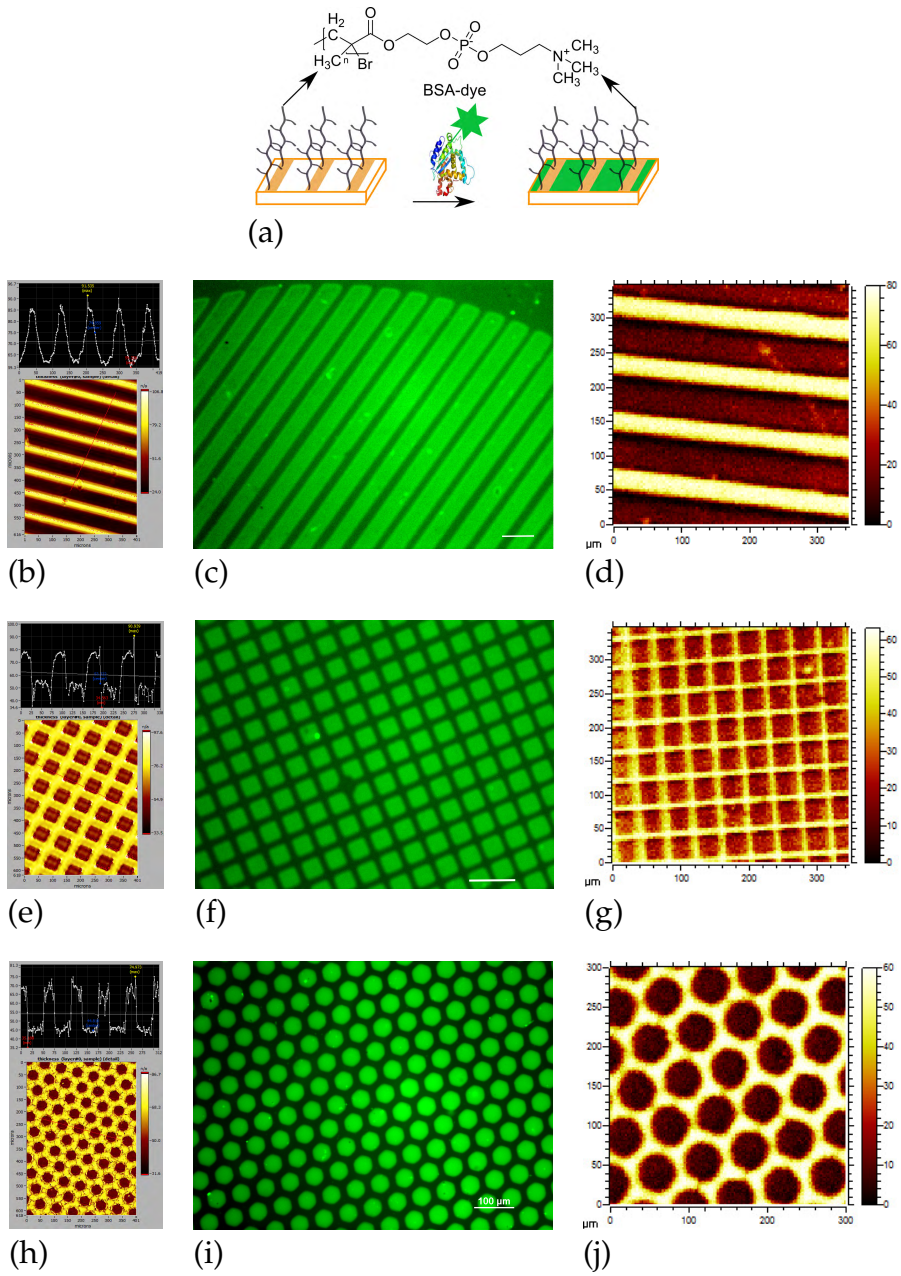

Figure 2.4: (a) Controlled deposition of fluorescent BSA occurs in areas where zwitterionic poly(2-methacryloyloxyethyl phosphorylcholine) or poly(MPC) brushes are absent. No protein adhesion occurs in domains where the poly(MPC) brushes are grafted. Geometric versatility of our approach. (b), (e), (h) Imaging ellipsometry profiles indicate thickness differences between UV-treated and untreated regions. Thick poly(MPC) brushes were formed only on untreated areas whereas only a dilute thin layer resulted in the UV-treated areas. (c), (f), (i) Fluorescence-labeled bovine serum albumin only adheres to regions where poly(MPC) is absent. Scale bar is 100 μm. (d), (g), j ToF-SIMS snapshot of PO_2^- and PO_3^- fragments reveal high phosphonate intensity in untreated areas but very weak signals from treated areas. The imaging ellipsometry, fluorescent protein patterns and ToF-SIMS together suggest that our patterning strategy was successful.

We further hypothesized that the exceptional resistance of poly(MPC) brushes to non-specific protein adsorption[101] should lead to the selective deposition of proteins such as bovine serum albumin on domains where the initiator was deactivated and where poly(MPC) brush growth was prevented. We thus challenged these surfaces with a solution of BSA labeled with a fluorescent molecule and imaged the substrate thereafter. In Figures 2.4(c), 2.4(f) and 2.4(i), it is evident that BSA adhesion only happened in areas where the brushes were absent and that no protein adsorption occurred in areas where the brushes were grafted. To substantiate this conclusion, these substrates were characterized in parallel using ToF-SIMS (Figures 2.4(d), 2.4(g) and 2.4(j)). We observed that the PO_2^- and PO_3^- signals associated with the poly(MPC) brushes emanated from the same regions where protein adhesion was circumvented. This unambiguously establishes that a high level of geometric control over non-specific protein deposition was achieved by controlling the spatial distribution of non-fouling brushes. If we consider the results gathered from complementary studies involving AFM, imaging ellipsometry, ToF-SIMS and BSA adsorption (Figure 2.4), we can conclude that our approach to polymer brush patterning represents a viable and robust path to creating protein patterns.

Next, we designed biointerfaces with specific interactions between biomolecules and polymer brushes. We engineered patterned polymer brushes presenting reactive alkyne side chains that can be further functionalized with biomolecules via click chemistry. To this end, we prepared copolymer brushes composed of propargyl methacrylate[102] and zwitterionic monomer, [2-(methacryloyloxy)ethyl]dimethyl-(3-sulfopropyl)ammonium hydroxide (MEDSAH) from patterned initiator surfaces (Figure 2.5(a)). These copolymer brushes are designed such that the hydrophilic MEDSAH ensures that that non-specific protein adhesion is prevented,[103] while the propargyl methacrylate offers reactive groups to which biomolecules such as biotin can be tethered via Husigen's copper catalyzed 1,3 alkyne azide cycloaddition (CuAAC)[92]. Using FTIR spectroscopy (Figure 2.5), we verified that the pendant alkyne groups (at 3300 and 2125 cm^{-1}) as well as the sulfobetaine side chains were present in the copolymer brushes. Next, biotin-PEG-azide was clicked to the alkyne side chains in the patterned copolymer brushes using CuAAC. Subsequently, we exploited the strong and specific affinity existing between streptavidin and biotin to immobilize streptavidin-cy3 onto the biotinylated brushes. Ultimately, we obtained streptavidin-cy3 patterns in the form of fluorescent hexagons (Figure 2.5), which conformed to the geometry of the photomask. Moreover, the ratio between the propargyl methacrylate repeat units and MEDSAH can be tuned by controlliong the cmposition of the monomer feed as seen in Figure 2.5(c). By engineering specific interactions between patterned polymer brushes and proteins, we were able to develop and validate a simple protein patterning approach that can be employed generically for patterning any streptavidin-conjugated biomolecule.

Finally, in order to demonstrate the substrate independence of our technique, we created protein patterns based on non-specific BSA adhesion around microstructured poly(MPC) brushes grafted from diverse substrates. Apart from the model substrates glass and quartz, we also studied patterned brush formation on poly(vinyl

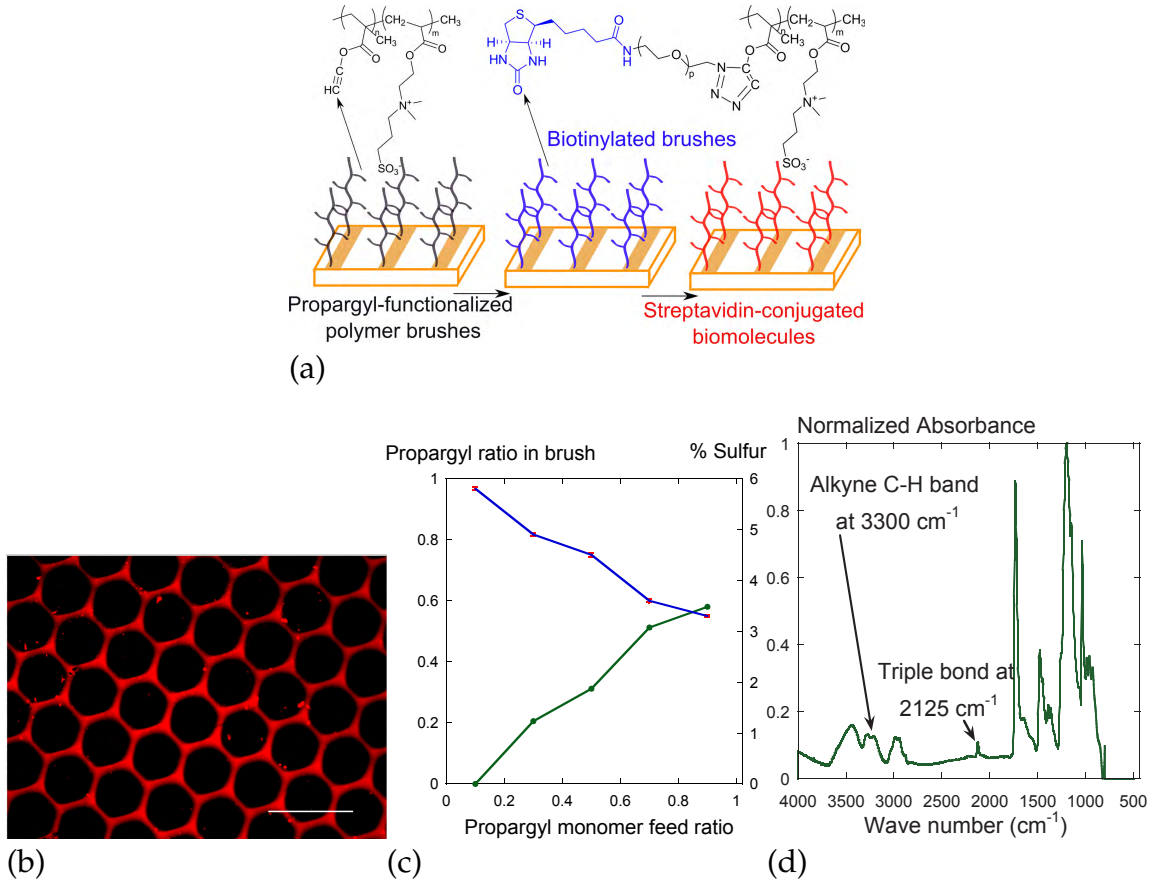

Figure 2.5: A generic strategy for engineering specific interactions between proteins and microstructured polymer brushes. (a) In the first step, copolymer brushes, poly(propargyl methacrylate-co-{[2-(methacryloyloxy) ethyl] dimethyl-(3-sulfopropyl) ammonium hydroxide}), consisting of zwitterionic repeat units and clickable alkyne-containing repeat units were grafted from the patterned initiator layer. Then, biotin-PEG-azide was clicked to the reactive alkyne side chains in the brushes. Finally streptavidin-conjugated molecules were immobilized to the patterned polymer brushes by taking advantage of the strong and specific interaction between streptavidin and biotin. (b) Biotinylated brushes bound to streptavidin bearing a fluorescent tag. Scale bars is 100 μm. This approach can be generalized to precisely pattern any streptavidin-conjugated biomolecule. (c) XPS measurements of sulfur content indicate that the ratio of propargyl repeat units and thereby teh degree of biotinylation can be tuned by varying the monomer feed composition. (d) FTIR confirms the presence of alkyne groups in the copolymer brushes, which were then conjugated to biotin-PEG-azide molecules.

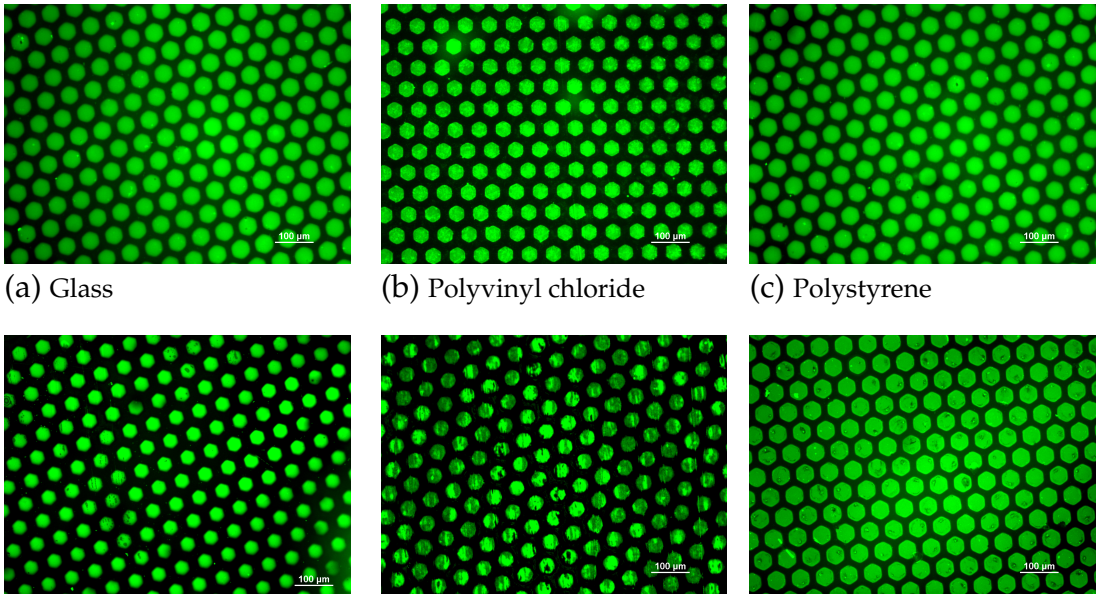

(a) Glass (b) Polyvinyl chloride (c) Polystyrene

(d) Quartz (e) Steel (f) PDMS

Figure 2.6: Our patterning approach can be applied to virtually any substrate independent of surface chemistry. Fluorescence micrographs of BSA bound to patterned poly(MPC) brushes grown from initiator (PPX-EB) coatings that were vapor deposited on (a) glass, (b) polyvinyl chloride, (c) polystyrene, (d) quartz, (e) steel, and (f) polydimethylsiloxane (PDMS). These images demonstrate that patterning quality can be obtained not just on a model substrates, but also on conventional polymers and metals.

chloride) (PVC), polystyrene (PS), polydimethylsiloxane (PDMS) and steel (Figure 2.6). Although these substrates vary widely in their mechanical, optical and interfacial properties (roughness, refractive index, hardness, surface charge, hydrophobicity), comparable pattern quality was obtained on all substrates, including the steel substrates, which possessed micron-scale surface roughness. Our technique can therefore be applied not only for model surfaces such as gold, silicon and glass, but also technologically more relevant "non-model" materials possessing less than ideal surface characteristics.

2.5 Conclusions

In summary, we have developed and validated a facile and substrate-independent approach to patterning proteins through both specific and non-specific means using microstructured polymer brushes. Our patterning strategy relies on spatially selective deactivation of a vapor-deposited SI-ATRP initiator surface by combining a patterned photomask with UV treatment. Mechanistically, we demonstrate that the ozone formed under these conditions plays a critical role in the deactivation of the ATRP initiator groups. Post SI-ATRP, AFM and imaging ellipsometry revealed thickness and topographical contrasts between the polymer brush domains and the inactivated regions. Chemical characterization of the patterned brushes was completed using ToF-SIMS, which substantiated the conclusions from AFM and ellipsometry. Finally, we demonstrated patterned non-fouling brushes that spatially regulate non-specific protein adsorption as well as biotinylated brushes that promote specific protein recognition events on the desired locations. Given the prominent utility of polymer brushes in biotechnology,[19] this surface-modification approach will likely find broad applicability in cell patterning, high-throughput screening, bioMEMS devices and enzymatic assays.

CHAPTER III

Examining Nanoparticle Adsorption on Electrostatically "Patchy" Glycopolymer Brushes using Real-time ζ-potential Measurements

The material in this chapter has been adapted with minor modifications from the following published article

Ramya Kumar, Irina Kopyeva, Kenneth Cheng, Kai Liu, and Joerg Lahann, "Examining Nanoparticle Adsorption on Electrostatically "Patchy" Glycopolymer Brushes Using Real-Time ζ-Potential Measurements", *Langmuir*, 2017, 33, (25), 6322-6332

3.1 Abstract

Biomaterial surfaces can possess chemical, topographical or electrostatic heterogeneity, which can exert profound influences on their performance. By developing experimental models that reliably simulate this nanoscale heterogeneity, we can predict how these "patchy" surfaces are transformed by their interactions with the dynamic physiological environment. In this work, we present a model surface where well-defined glycopolymer brushes are interspersed with positively

charged binding sites, giving rise to an interface presenting a mixture of repulsive and adhesive cues to an approaching virus particle. We show that the density of the affinity sites can be tuned precisely by modifying the chemical vapor deposition (CVD) copolymerization conditions. Using ζ-potential measurements, we quantified the surface charge of these coatings and established that their isoelectric point (IEP) can be controlled by varying the surface composition. Further, we examined the effects of binding site density and glycopolymer brush architecture on the adsorption kinetics of virus-like nanoparticles using a new approach based on time-resolved ζ-potential measurements. Most materials have charge-bearing, dynamic surfaces that are sensitive to electrostatic effects. Hence adsorption-triggered changes in ζ-potential measurements can be captured in real time to monitor interfacial events. To validate this electrokinetic method, we examined the effect of neutravidin concentration on its rate of binding to biotinylated surfaces using ζ-potential and compared our results with QCM studies. Real-time ζ-potential measurements present an interesting platform to probe the structure and function of chemically and electrostatically heterogeneous polymer interfaces. Tunable glycopolymer coatings have enormous utility as model systems to examine the roles of polymer brush architecture and surface charge on virus-biomaterial interactions.

3.2 Introduction

Reliable experimental models can identify design specifications for optimal biomaterial performance but developing a suitable model system is challenging. This is largely due to the complexity of biological responses triggered by the biomaterial within the host organism[104]. Interactions between biomaterials and the physiological environment, such as the formation and remodeling of the protein corona, the receptor-mediated binding of viruses and cells[105], begin within nanoseconds but

its effects can last for years[106]. In addition to dealing with the complex physiological environment, we have to take into account the additional layer of complexity inherent within heterogeneous biomaterial surfaces. Nanoscale heterogeneity can exist in several forms- the surface can contain randomly distributed domains of neutral, positive and negative surfaces charge; or the surface could be amphiphilic with both hydrophobic and hydrophilic characteristics, leading to interesting interfacial behavior[107]. Consider the example of non-fouling polymer brushes that prevent non-specific adsorption. Despite advances in surface-initiated polymerization techniques, it is possible for nanoscale defects to form in the brush due to trace impurities, low grafting density, or processing limitations[108]. As a result, the non-fouling performance of the brushes in a biomedical setting will be compromised[109], leading to undesirable outcomes such as hospital-acquired infections and thrombosis[110]. Since the defects can interact with proteins and pathogen species through hydrogen bonding, Van der Waals interactions, electrostatic attraction, or hydrophobic interactions, the surface simultaneously offers both adhesive and repulsive cues to the adsorbate species. A suitable experimental model will help us understand the adsorption characteristics of these chemically and topographically heterogeneous interfaces. The use of such model surfaces will ensure that interfacial interactions promote intended functional outcomes, ranging from the prevention of non-specific adsorption to the modulation of bioactive molecules.

Santore and co-workers showed that electrostatically heterogeneous model surfaces possessing systematically engineered "defects" are useful in several contexts-:the prevention of non-specific adsorption, selective protein and bacterial capture, protein separation, and importantly, fundamental understanding of the underlying mechanisms of adhesion[111]. By carefully introducing charged binding sites at the base of protein-resistant brushes, the competing effects of steric repulsion and electrostatic attraction could be controlled precisely, achieving the desired

bioadhesion outcome[112]. Nanotextured surfaces composed of positively charged patches such as poly-l-lysine hydrobromide (PLL), and polyethylene glycol (PEG) brushes have been used extensively as model systems to probe the effects of defect density, brush architecture, ionic strength, flow conditions and protein and particle characteristics on the adsorption kinetics[113–115]. Though several useful insights have been gleaned from these surfaces, they have a few drawbacks. First, the creation of cationic patches and PEG brushes is based on physisorption rather than covalent attachment, imperiling their use in biological environments for long durations[15]. Secondly, even though PEG is the most commonly employed non-fouling polymer brush due to ease of synthesis, its use is fraught with the risk of auto-oxidative[116] degradation *in vivo*. Investigators seeking to identify alternatives possessing comparable non-fouling properties have concluded that zwitterionic polymer brushes and carbohydrate-based polymer brushes are the most promising options[51]. In a comparison of mannitol-terminated and PEG-terminated SAMs, it was discovered that PEG-terminated SAMs lost the fidelity of their cell patterns[117]. In contrast the mannitol patterns were able to retain their non-fouling properties over a long term and the cell pattern fidelity was preserved. From the perspective of technological relevance and clinical translation, it would be advantageous to replace PEG-based model systems with biomimetic carbohydrate-based model surfaces while investigating the role of binding site density on the adsorption of proteins, bacteria or viruses.

Carbohydrate-based polymer films are inspired by the sugary sheath surrounding the endothelial cells, the glycocalyx[118]. On account of its hydration and steric resistance, the endothelial glycocalyx can achieve near zero-levels of non-specific protein adsorption[119]. Theoretical and experimental studies indicate that glycocalyx-inspired surfaces composed of sorbitol and mannitol interact strongly with hydrating water molecules. These studies concluded that the enthalpic cost of disrupting

this hydration layer generates repulsive forces, and ultimately renders adsorption thermodynamically unfavorable[120,121].

Through surface-initiated atom transfer radical polymerization (SI-ATRP) and chemical vapor deposition (CVD) copolymerization, we have a developed a robust and substrate-independent glycopolymer brush platform. The versatility and control afforded by SI-ATRP enables us to create of a high spatial density of sorbitol molecules with any desired brush architecture. In addition, we have rendered the glycopolymer coating electrostatically heterogeneous by embedding positively charged binding sites or defects in the form of aminomethyl functional groups, which can be co-presented with the sorbitol brushes in any desired ratio. In this paper, we describe the design and synthesis of a tunable electrostatically patchy glycopolymer brush interface that can build on the progress made by preceding model systems in understanding adhesion events. Additionally, we have demonstrated tunable binding of virus-like nanoparticles to our model surface by varying the relative densities of binding sites and glycopolymer brushes. We used carboxylate-functionalized polystyrene nanoparticles as "model viruses" for two reasons-: 1) Its size is comparable to those of many viruses. 2) Most viruses have isoelectric points below 6, implying that they possess negative charge at physiological pH[122].

To study adsorption kinetics at the nanometer scale, a variety of techniques have been used -: attenuated total reflectance infrared spectroscopy[123,124] (ATR-IR), ellipsometry[125], optical waveguide light mode spectroscopy[126,127] (OWLS), total internal reflection fluorescence[128,129] (TIRF), atomic force microscopy[130] (AFM), and quartz crystal microbalance-dissipation[131,132] (QCM-D). In recent years, surface plasmon resonance spectroscopy[133,134] (SPR) has emerged as the gold standard for studying biointerfacial phenomena. The use of optical methods to track the binding of viruses and their nanoparticle surrogates is difficult owing to their small size and limited ability to scatter light[135]. Fluorescence based schemes for vi-

ral detection are hindered by photobleaching and low emission rates. Hence, measuring the adsorption kinetics of virus-like particles to our surface would require alternative approaches. Since we are interested in visualizing binding events occurring on electrostatically heterogeneous surfaces, we decided to depart from the traditionally used toolbox listed above and instead, explore an electrokinetic approach for the detection and time-resolved measurement of nanoparticle binding. In this work, we apply real-time ζ-potential measurements to study the adhesion of virus-like nanoparticles to our glycopolymer coatings.

Typically, biomaterials perform their function in an aqueous environment, where functional groups on its surface can be ionized, preferential adsorb ions, and eventually acquire an electrical double layer. Consequently, the ζ-potential is a sensitive indicator of interfacial charge development in physiological fluids such as blood[136]. Prior work has linked changes in the ζ-potential to biofilm formation[22], viral adhesion[137], changes in the performance of an implanted neuronal electrode[138], progression of osteogenesis[139] or the inflammatory response to a biomaterial[140]. Although electrostatic effects exert a profound influence over the rate at which biomolecules, pathogens and cells adsorb to the material surface, there have been very few studies employing ζ-potential measurements to elucidate adsorption events in a time-resolved manner. In pioneering work, Norde et al.[141] reported that measuring temporal changes in ζ-potential was an effective way to record the adsorption kinetics of a charged protein, such as lysosyme, on a complementarily charged surface, such as glass or silica[142]. Here, the change of the ζ-potential from its baseline value was linearly dependent on the amount of adsorbed protein. Etheve and Dejardin[143] were able to build on this earlier work by simultaneously acquiring the values of both ζ-potential and the deposited mass of protein. The outcome was a defined relationship between the change in ζ-potential and the total amount of adsorbed protein. So far, in situ ζ-potential measurements have

been predominantly used to characterize equilibrium states of surfaces exposed to proteins[144,145], viruses[146,147] or nanoparticles[148,149]. In comparison, time-resolved ζ-potential measurements are still in their infancy[150] in spite of their prominent potential for understanding interfacial events at a biomaterials interface in a label-free and inexpensive manner.

In this report, we examine the effect of the surface composition of electrostatically heterogeneous glycopolymer on the binding kinetics of virus-like nanoparticles using real-time ζ-potential measurements. Before we embarked on these measurements, we validated our electrokinetic approach by comparing its adsorption response with that of QCM and verifying whether similar trends were observed. For this validation study, we chose to measure the adsorption kinetics of a well-characterized binding pair–neutravidin and biotin. This contribution employs electrokinetic measurements to study two interfacial processes: (i) the specific binding of neutravidin to biotin with the objective of comparing adsorption trends with those from QCM and validating the technique (ii) the non-specific charge-promoted binding of virus-like nanoparticles to glycopolymer brush interfaces interspersed with positively charged binding sites.

3.3 Experimental

The first and second sections describe chemical vapor deposition (CVD) polymerization and surface-initiated ATRP procedures. In the third, fourth and fifth sections, characterization procedures for these coatings using ζ-potential, FTIR and fluorescence are described. The sixth and seventh section explains the collection of real-time ζ-potential measurements using our electrokinetic analyzer and QCM measurements respectively. Finally, the modeling procedure is summarized in the eighth section.

3.3.1 Chemical vapor deposition

As described in Nandivada et al.[92], the precursor, ethynyl[2,2]paracyclophane was sublimed at 100 °C and then subjected to thermal pyrolysis at 660 °C under low pressure (0.3 bar). The radical species that were generated thus, adsorbed to the cooled substrate (15 °C) in the deposition chamber and underwent polymerization. Coatings composed of poly(4-ethynyl-*p*-xylylene-*co*-*p*-xylylene) (PPX-alkyne) were obtained. Poly(p-xylylene) (PPX-N) was prepared using the same procedure from [2,2]paracyclophane. 4-Aminomethyl[2,2]paracyclophane (PCP-AM) was obtained from Uniglobe Kisco and coatings of poly(*p*-xylylene-4-aminomethyl)-*co*-(*p*-xylylene)] (PPX-AM) were prepared using the same operating parameters. To prepare poly[(*p*-xylylene-4-methyl-2-bromoisobutyrate)-*co*-(*p*-xylylene)] (PPX-EB), we employed the CVD conditions described in Jiang et al.[95] In brief, 32 mg of [2.2]paracyclophane-4-methyl 2-bromoisobutyrate (PCP-EB) was sublimed at 115-125 °C under reduced pressure (0.3 mbar) and then pyrolysed at 540 °C. Deposition of the polymer onto the substrate occurred on a sample holder maintained at 14 °C. To prepare a copolymer of [2.2]paracyclophane-4-methyl 2-bromoisobutyrate (PCP-EB) and 4-aminomethyl[2,2]paracyclophane (PCP-AM), a two-source CVD system was employed as described by Elkasabi et al.[151] An amount of 25 mg of PCP-AM was loaded into one source and 32 mg of PCP-EB was loaded into the second source. The two source furnaces were heated independently to pyrolysis temperatures of 660 °C and 540 °C respectively. The ratio of the two functional groups deposited on the target surface of the coating was controlled by changing the separation distance to the respective source. For the PCP-EB precursor, the separation was held constant at 0.8 cm while for the PCP-AM, distances ranging from 2.8-3.2 cm were employed. Each precursor was sublimed between 80 °C and 110 °C at a pressure of 0.125 torr. The sample holder was cooled to 14 °C and rotated continuously to ensure compositional homogeneity. At each source, a flow rate of 10

standard cubic centimeters per minute was maintained using Argon carrier gas in order to carry the sublimated dimers into the pyrolysis zone, from where they entered the deposition chamber to form coatings of poly[(*p*-xylylene-4-methyl-2-bromoisobutyrate)-*co*-(*p*-xylylene-4-aminomethyl)-*co*-(*p*-xylylene)] on the substrates. Once the PCP-EB precursor was sublimed completely, deposition was stopped immediately.

3.3.2 Glycopolymer brush synthesis

Sorbitol methacrylate monomer (SMA) was purchased from Monomer Polymer Dajac Labs, Trevose, PA, and polymerized from the PPX-EB initiator surfaces using SI-ATRP to yield glycopolymer brushes. Substrates bearing bromoisobutyryl groups (EB), either the homopolymer PPX-EB or the copolymer with PCP-AM, were prepared according to the CVD process described in previous sections. Prior to SI-ATRP, substrates were coated with either the copolymer or with PPX-EB. The initial and final values of the coating thickness were ascertained using nulling ellipsometry before and after SI-ATRP. Upon subtracting the initial thickness from the final thickness, the extent of brush growth could be measured. Results from ellipsometry studies are furnished in the supplementary information section. In a typical SI-ATRP run, copper (I) chloride, copper (II) chloride and 2,2, bipyridyl were purchased from Sigma Aldrich and used without further purification. Substrates were placed in a glove bag and degassed using 3 cycles of vacuum-argon purge and left at room temperature under argon. 8 mL of solution of 1 g/ml SMA in methanol, 2 mL of methanol and 6 mL of water were mixed together in the monomer flask and then degassed by three cycles of freeze-pump-thaw. In parallel, a mixture of 3 mL methanol and 1 mL water was degassed using freeze-pump-thaw cycles in a separate catalyst flask. The catalyst was pre-complexed with the ligand and dissolved separately from the monomer as the Cu^{I} and Cu^{II} tend to

form a strong complex with the sorbitol monomer. After completion of the third freeze operation, 207.4 mg bipyridyl, 35.5 mg CuCl and 7.9 mg $CuCl_2$ were added to the catalyst flask under argon. Pump and thaw operations were continued subsequent to catalyst addition. Upon dissolution, the brown-colored catalyst mixture was added to the degassed monomer solution and mixed thoroughly at room temperature. This mixture was transferred to the glove bag and distributed such that each substrate was submerged completely in the reaction solution. The SI-ATRP reaction was allowed to proceed for 24 hours under argon atmosphere. Finally, substrates were rinsed repeatedly with 0.05 M EDTA solution and deionized water and dried.

3.3.3 FTIR spectroscopy

To verify whether the desired functional groups were present on the surface of the polymer coatings, Fourier-transformed infrared (FTIR) spectroscopy was performed using Nicolet 6700 spectrophotometer in the grazing angle configuration against a gold background. Polymers were deposited on gold wafers and 128 scans were collected with a resolution of 4 cm^{-1}.

3.3.4 Isoelectric point determination

For measuring the ζ-potential as a function of pH and to determine the isoelectric point (IEP), streaming current measurements were collected for multiple values of pH. Polymer coatings were prepared using the CVD processes described in previous sections. The clamping cell of the electrokinetic analyzer SurPASS (Anton Paar GmBH) was used in asymmetric mode[152] to acquire streaming current readings from the samples across a pH range of 3 to 6. Polypropylene foil was used as the reference. For each sample, titration was performed from the neutral to the acidic range using 0.1 M hydrochloric acid as the titrant and 0.001

M potassium chloride solution as the electrolyte. The pH value was controlled using an automated titration unit, which effected pH changes in increments of 0.3, while the electrolyte solution was stirred continuously. The electrolyte solution was purged continuously with nitrogen to prevent carbon dioxide dissolution and unintended changes in the pH value. Streaming current was measured using Ag/AgCl electrodes and the Helmholtz-Smoluchwski equation[153–155] was applied to compute the ζ-potentials. Flow rates of 50-70 ml/min were observed at a pressure of 400 mbar and a gap of 100-120 μm was maintained between the sample and the polypropylene reference standard. Samples were rinsed for 3 minutes before each measurement to equilibrate the surface against the electrolyte solution.

3.3.5 Fluorescence measurements for streptavidin and nanoparticle adsorption

Initially, samples were incubated in a solution of 0.1 % (w/v) bovine serum albumin (Sigma Aldrich) in phosphate buffered saline (PBS) for 30 minutes and then thoroughly rinsed with PBS. Subsequently, they were incubated in streptavidin-Cy3 (50 μg/ml) in PBS containing 0.02 % (v/v) Tween 20 for 10 minutes. The substrate was then repeatedly washed with PBS and finally rinsed with deionized water. Substrates were dried and fluorescence micrographs recorded using a fluorescence scanner (Fluorochem M, Protein Simple Inc) with an exposure time of 200 ms. The fluorescence intensity was extracted using ImageJ and an average of readings obtained from three substrates for each sample group (PPX-N, PPX-alkyne clicked with PEG, PPX-alkyne clicked with biotin-PEG-azide[92]) was computed. The PS-COOH nanoparticles (Molecular Probes, carboxylated latex, 0.02 μm, 4% w/v) were purchased from Life Technologies and diluted down to a concentration of $8*10^{-7}$g/mL in 0.1 mM phosphate buffer solution. The pH of the solution was adjusted to 5.90 by mixing NaH_2PO_4 and Na_2HPO_4 in the desired ratio. Glass coverslips coated with the polymers of interest were incubated with this nanoparticle

suspension for 60 minutes and then imaged using a Nikon fluorescence microscope. ImageJ was used to quantify the density of adsorbed nanoparticles. Three substrates were used per sample group.

3.3.6 Adsorption kinetics through ζ-potential measurements

This adsorption accessory (Attract, Anton-Paar GmbH) enabled the acquisition of ζ-potential values at a temporal resolution of 1 second. Since our samples were rigid and did not exhibit swelling, streaming current measurements accompanied by the Helmholtz Smoluchowski correlation were used to compute ζ-potential. Measurements were performed in symmetric mode wherein both the top and bottom surfaces of the rectangular slit flow chamber were comprised of the polymer coating of interest. Consistent with the procedure for IEP determination, a solution of 1 mM potassium chloride in Milli-Q water was continually purged with nitrogen gas to prevent the dissolution of carbon dioxide and subsequent changes in pH. Streaming current measurements were collected every second at a pressure of 200 mbar and a separation of 100-120 μm between the two parallel surfaces forming the flow chamber. Before the adsorbate species could be added, baseline measurements were acquired for a duration of ten minutes to ascertain that a stable baseline was observed. After the baseline phase of the experiment was completed, the desired quantity of adsorbate was added and ζ-potential recorded every second for the duration of the adsorption phase. The adsorption response was quantified by subtracting the average of ζ-potential values collected in the baseline phase from the ζ-potential observed at any instant of time. The magnitude of ζ-potential change was employed to determine the time and concentration dependence of adsorption. For adsorption kinetics experiments, carboxylated polystyrene nanoparticles (PS-COOH), nanoparticles were obtained from Thermo Fisher (Molecular Probes, carboxylated latex, 0.02 μm, 4% w/v). We employed a

nanoparticle concentration of $8*10^{-7}$g/mL. The pH value was maintained constant at 6.00 for the experiments investigating the effect of copolymer composition on nanoparticle adsorption.

For the neutravidin-biotin binding experiments, a 1 mM solution of phosphate buffer was employed. The buffer solution consisted of NaH_2PO_4 and Na_2HPO_4 mixed in a ratio of 81:19 v:v to achieve a pH of 7.4. The upper and lower faces of the rectangular slit chamber were coated with PPX-alkyne according to the procedure outlined in the second section. Substrates were subsequently biotinylated using biotin-PEG-azide (PG2-BNAZ-5k, Nanocs, NY) as described previously[92]. As a control, one pair of the PPX-alkyne coated surfaces was coated with 8-arm star PEG (MW 10K, PSB-881, Creative PEG works, NC) using 1 mg/ml of the functional PEG reagent, 1 mM $CuSO_4$ (Sigma Aldrich) and 8 mM sodium ascorbate (Sigma Aldrich). Neutravidin (catalog # 31050) was purchased from Life technologies. To understand the effect of neutravidin concentration on binding kinetics, three concentration values were studied-: 10, 100 and 1000 nM.

3.3.7 QCM measurements to measure the binding kinetics of neutravidin to biotin

The QCM-200 instrument (Stanford Research Systems, CA) was used for these studies. AT-cut quartz crystals coated with chrome/gold (O100RX1, Stanford Research Systems, CA) were functionalized with PPX-alkyne according to the procedure outlined in the second section. Quartz crystals were biotinylated using biotin-PEG-azide (PG2-BNAZ-5k, Nanocs, NY) as described previously[92]. As a control, one of the PPX-alkyne coated crystals was coated with 8-arm star PEG (MW 10K, PSB-881, Creative PEG works, NC) using 1mg/ml of the PEG compound, 1mM $CuSO_4$ (Sigma Aldrich) and 8 mM sodium ascorbate (Sigma Aldrich). Prior to measurement, the biotinylated crystal surfaces were allowed to equilibrate overnight

in a 1 mM solution of phosphate buffer. The buffer solution consisted of NaH_2PO_4 and Na_2HPO_4 mixed in a ratio of 81:19 v:v to achieve a pH of 7.4. Then, they were mounted on a flow cell and the phosphate buffer was pumped through the flow cell at a flow rate of 0.1 ml/hour using a syringe pump. Once a stable baseline was observed, neutravidin was injected and the adsorption response recorded. The adsorbed neutravidin mass was computed from the frequency decrease through the Sauerbrey equation[156].

3.3.8 Extraction of apparent rate constants using kinetic modeling

Neutravidin-biotin adsorption experiments performed with the electrokinetic analyzer and the QCM yielded plots of adsorption response y as a function of time t. Assuming that the adsorption behavior conforms to a first-order kinetic model, these values were fitted according to the following monoexponential equation where A denotes plateau value of adsorption (units of mV for streaming potential and ng/cm^2 for QCM) and k is the apparent rate constant of adsorption with units of sec^{-1}.

$$y = A(1 - e^{-kt})$$

The quality of the fit was assessed using the following model diagnostics-:

- RMSE which estimates total deviation of the response values from the fitted values.
- R-squared, which signifies how well the fit describes experimental behavior.
- Degree of freedom adjusted R-squared which detects "over fitting".

3.4 Results and discussion

3.4.1 Binding kinetics of neutravidin to biotinylated surfaces assessed via QCM and real-time ζ-potential measurements

Before conducting electrokinetic measurements to examine the adsorption of nanoparticles to electrostatically heterogeneous glycopolymer surfaces, we needed to establish the validity of this technique. We employed QCM studies in parallel with real-time ζ-potential measurements to investigate a well-established binding process and then compared results obtained from both methods. We wished to verify whether similar trends in neutravidin-biotin association are observed from both methods while monitoring the binding events in real time.

The non-covalent interaction between biotin and avidin analogues has been widely exploited in developing biosensors, drug delivery systems, biomolecular imaging probes, immunoassays and other applications where high affinity and specificity are desired[157]. This is a well-established model for affinity interactions and is considered to be a reliable binding pair. Since biotin-avidin association happens extremely rapidly, the acquisition of kinetic data and determination of the binding constant for this interaction are quite challenging[158]. Nevertheless, the binding kinetics of streptavidin with biotin[159] has been thoroughly characterized by a variety of techniques, including fluorescence resonance energy transfer[158] (FRET), QCM-D[160] and SPR[161]. Compared to streptavidin (pI of 5-6[162]) and avidin (pI of 10.5[162]), neutravidin (pI of 6.3[162]) has an isoelectric point closest to neutral pH and is expected to exhibit the least non-specific binding among the three. Hence neutravidin has been used in our study. We evaluate the adsorption kinetics of neutravidin on biotinylated surfaces using two methods in parallel- real-time ζ-potential measurements and QCM measurements.

The surfaces of the QCM crystals and the measurement surfaces of the elec-

trokinetic analyzer were coated with poly(4-ethynyl-p-xylylene-co-p-xylylene) (PPX-alkyne), which displays highly reactive alkyne functional groups. The Huisgen 1,3-dipolar cycloaddition between azides and terminal alkynes was used to conjugate biotin-PEG-azide to the substrates using a procedure described in the methods section and in previous reports[92]. To confirm that biotinylation was successful, fluorescence measurements were performed with both biotinylated cover slips and non-biotinylated PEG-coated cover slips (negative control) using a fluorescently labeled streptavidin molecule. Fluorescence results are discussed in the supporting information section.

After verifying that biotinylation was successful, we proceeded to detect and quantify the binding of neutravidin molecules to these surfaces (Figure 3.1(a)) using real-time ζ-potential measurements and QCM. In a typical measurement, the buffer was pumped through the measurement chamber, which was a flow cell in the form of a rectangular slit. Flow conditions in our measurement chamber are in the laminar regime and the velocity profile can be described by the Hagen-Poiseuille equation. Since, rapid transport of neutravidin is not possible in this flow setup, the rate constants observed from these studies are only transport-limited “apparent rate constants" and not the true rate constants.

ζ-potential values were recorded continuously at a frequency of one measurement per second. After a stable baseline was established, neutravidin was injected into the flow circuit and changes in ζ-potential could be observed in real time. Three concentrations of neutravidin were studied-:10 nM, 100 nM and 1000 nM. In addition, a control experiment was performed at 1000 nM on a PEGylated surface devoid of biotin molecules. The adsorption response (Figure 3.1(b)) could be obtained by subtracting the average of the ζ-potential values collected during the baseline phase from the ζ-potential values obtained after the introduction of neutravidin. The average ζ-potential values collected during the baseline phase were

quite similar across all experimental runs-: -44 mV for 10 nM experiment, -42.4 mV for 100 nM and -41.93 mV for the 1000 nM experiment. In all three experiments, upon addition of neutravidin, the ζ-potential became less negative, resulting in its net increase. However the magnitude of increase in the ζ-potential was highest for the 1000 nM concentration at 29.9 mV, followed by the 100 nM run which had a 23.4 mV change (Figure 3.2(c)). Among the three experiments, the least change in ζ-potential (19.1 mV) was observed in the 10 nM condition (Figure 3.2(c)). This change in ζ-potential can be attributed to the adsorption of neutravidin to the surface caused by its specific association with biotin molecules. It appears that the rate of increase of ζ-potential values as well as the magnitude of its increase is a function of neutravidin concentration, with higher concentrations promoting more rapid changes. When we consider the control experiment, the average baseline ζ--potential was -40.6 mV, which was only slightly higher than the values obtained with the biotinylated surfaces. However when we added neutravidin to achieve a 1000 nM concentration, we did not observe any departure of the ζ-potential trends from baseline levels, indicating that neutravidin did not adsorb to the surface in the absence of biotin. (Figure 3.1(b)).

Now, we will describe the reasons for the oscillations and scatter obtained in our adsorption data, A target pressure of 150 mbar was employed to pump the fluid through the measurement chamber and this pressure difference is achieved by the motorized movement of plungers placed within two 100 ml glass syringes. The oscillatory nature of the adsorption traces can be attributed to the periodic emptying and refilling of the syringe. Every time 100 ml of the electrolyte solution flows through the measurement chamber, this periodic refilling is performed to re-establish the target pressure. This cyclical pressure variation occurs every 90 seconds or so and is a typical feature of this technique. Further, overshoots in the target pressure can result in the spikes in the data. This scatter in the adsorption

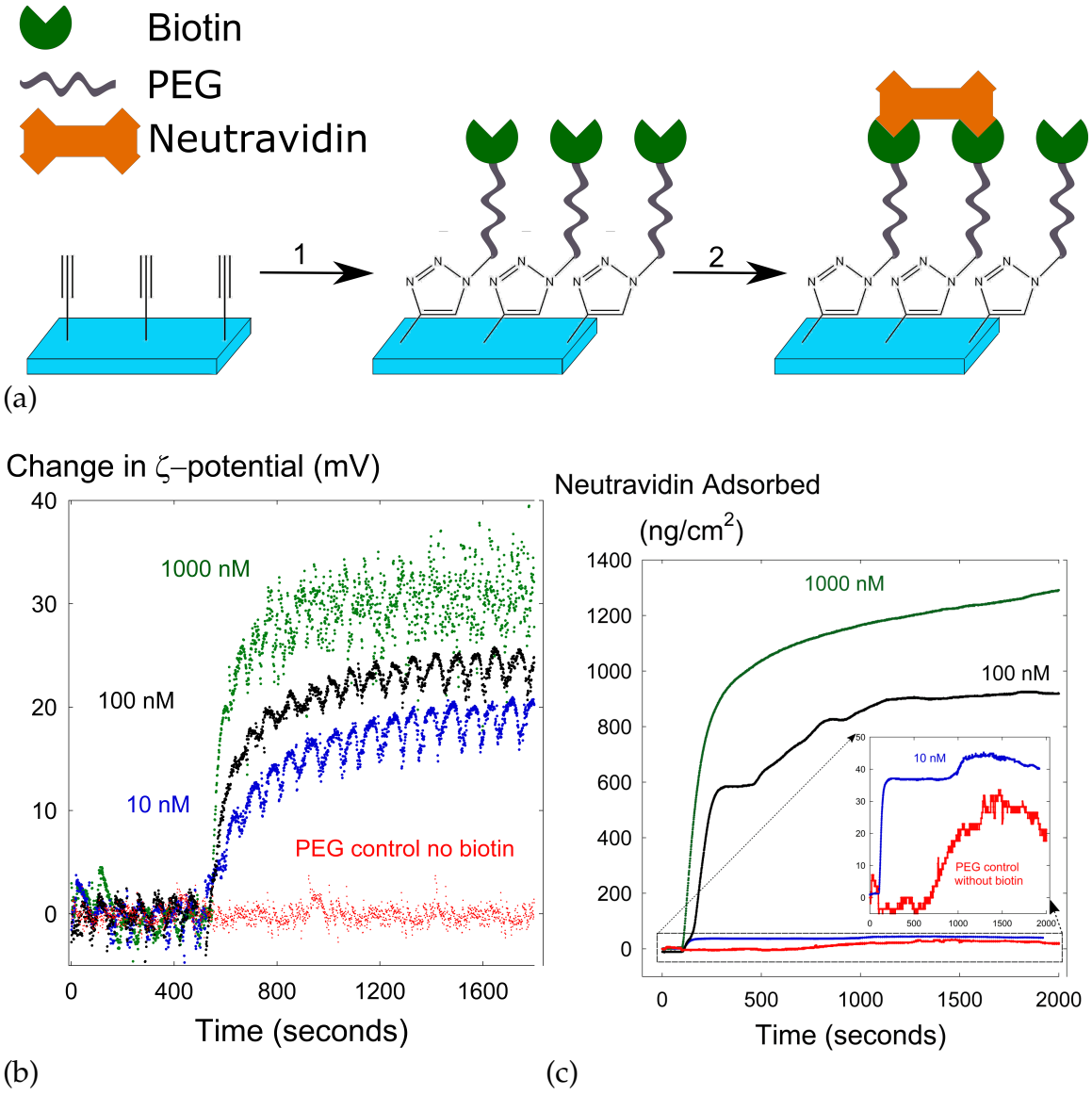

Figure 3.1: (a) In step 1, biotin-PEG-azide is conjugated to reactive alkyne groups on the PPX-alkyne substrate using Huisgen 1,3-dipolar cycloaddition. In step 2, neutravidin binds to the biotinylated surfaces. Binding kinetics were studied as a function of neutravidin concentration using (b) Real-time ζ-potential measurements and (c) Quartz crystal microbalance (QCM) measurements. Three concentrations of neutravidin were employed (10 nM in blue, 100 nM in black and 1000 nM in green). For the control experiment, a PEGylated surface without any biotin was studied using a neutravidin concentration of 1000 nM (red). In both QCM and real-time ζ-potential measurements, the rate and extent of neutravidin adsorption was controlled by its solution concentration. Also, no adsorption could be detected in the control experiment even when the highest neutravidin concentration was employed.

response has been observed in prior reports on time-resolved ζ-potential measurements[143,150]. When we constructed monoexponential adsorption models from the ζ-potential data (described in the next section), we concluded that this scatter does not affect the ability of the technique to clearly discriminate between adsorption trends from different neutravidin concentrations.

Next, we repeated this study using QCM instead of ζ-potential (Figure 3.1(c)). In all three experiments performed with biotinylated surfaces (10 nM, 100 nM and 1000 nM), we observed a decrease in frequency upon neutravidin addition. The frequency decrease was transformed into an estimate of adsorbed mass using the Sauerberey equation[156]. Neutravidin adsorption was highest when the concentration of neutravidin was 1000 nM, and an adsorption plateau of 1214 ng/cm^2 was reached. This plateau value was lowered dramatically when concentrations of 100 nM (931 ng/cm^2) and 10 nM (40.3 ng/cm^2) were used, indicating that the extent of neutravidin coverage on the surface is controlled by its concentration. This result mirrors what we observed in the ζ-potential studies performed using the same coatings and identical concentration values.

Interestingly, for the control experiment where the adsorption of 1000 nM neutravidin was measured on a PEGylated surface, a plateau value of 20-30 ng/cm^2 was obtained, which is only slightly less than the value (40.3 ng/cm^2) for the 10 nM experiment performed with a biotinylated surface (Figure 3.1(c)). Though a near-zero adsorption signal was obtained from this control surface using ζ-potential measurements in the 1000 nM neutravidin run, the adsorption signal from the parallel QCM control experiment is somewhat high. This suggests that the uptake of water and sodium phosphate salts by the QCM crystal also contributes to the adsorption signal. In the absence of measurements of the energy dissipation factor ΔD, it is difficult to subtract these non-neutravidin contributions from the buffer solution itself and obtain more accurate adsorption profiles. Results from

our quantitative analysis are discussed in the next section.

3.4.2 Kinetic modeling of adsorption data

Consistent with previous studies that employ Langmuirian adsorption kinetics, we assumed that neutravidin binding follows a first order process and that our ζ-potential and QCM data can be described by a monoexponential fit. The model equation and fitting procedures are described in the methods section. Two model parameters-: 1) A, the plateau value of adsorption (units of mV for streaming potential and ng/cm^2 for QCM) and 2) k, the apparent rate constant of adsorption (units of sec^{-1}) were computed within a 95 % confidence interval. As an example, Figure 3.2(a) shows how closely the model (A= 23.4 mV and k= 7.96 * 10^{-3} sec^{-1}) fits the experimental values for the ζ-potential experiment describing the kinetics of neutravidin adsorption at 100 nM. Despite the scatter in the data, we can see that most values fall within the prediction boundaries within a 95 % confidence interval, indicating that the monoexponential model describes experimental behavior accurately. We concluded that the monoexponential model matches our experimental trends for both measurement approaches. From a closer look at the QCM adsorption traces, it appears that the biexponential model may have been more suitable than the monoexponential model. If we consider the QCM experiments performed at 10 nM and 100 nM, we can discern two phases of adsorption, an extremely rapid first phase and a slower second phase. After the initial exponential increase in adsorbed neutravidin is completed and a stable plateau value is attained, a second slower phase of adsorption begins. In contrast to the other two experiments, we don't detect two plateaus in the 1000 nM QCM run. Yet, we can see that the steep exponential climb is followed by a gradual linear growth in the mass of adsorbed neutravidin. This biphasic adsorption behavior can be explained by the heterogeneity of binding sites on the neutravidin molecule, with each site

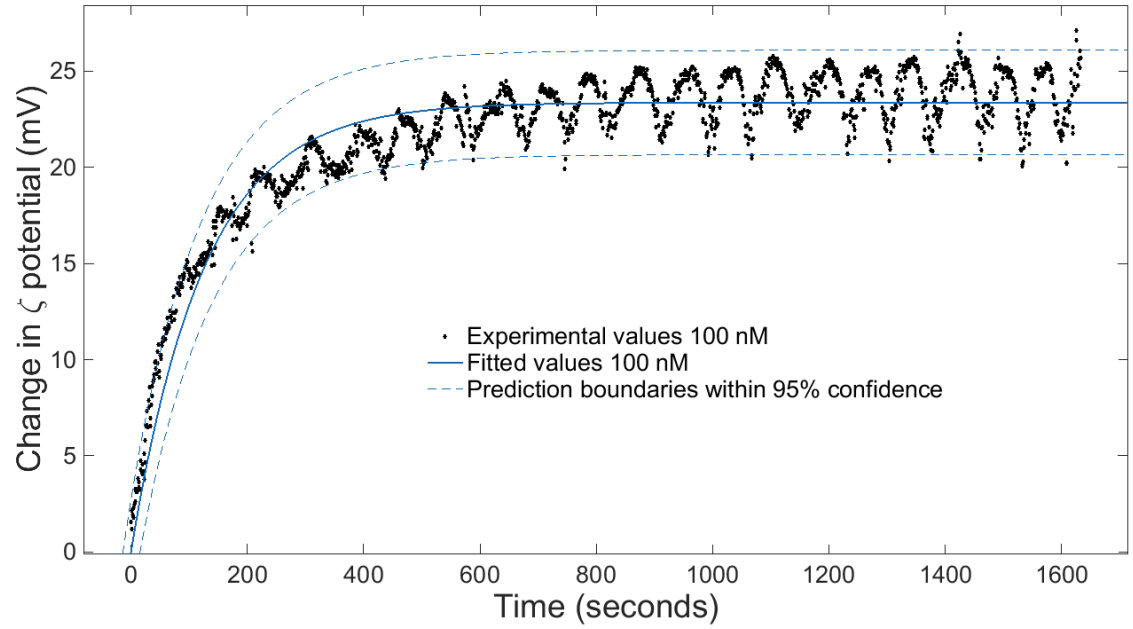

(a)

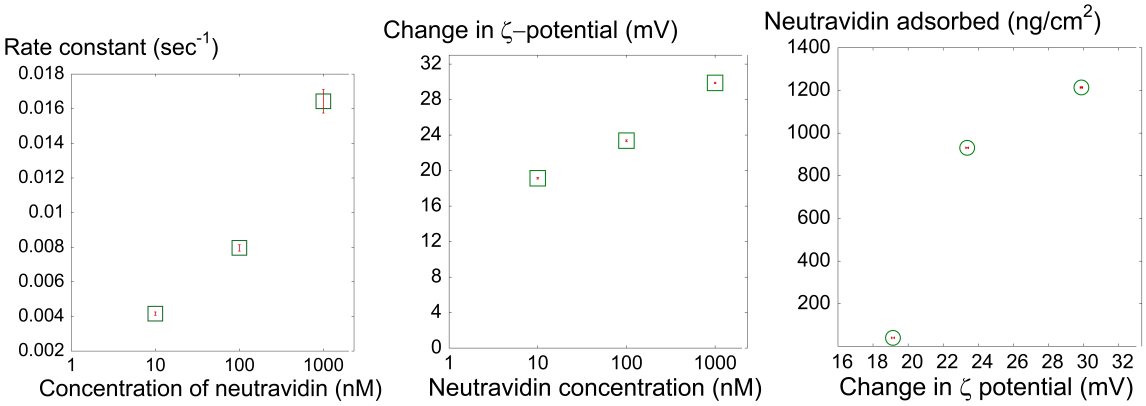

(b) (c) (d)

Figure 3.2: (a) Experimental values from the real-time ζ-potential measurements of the adsorption of 100 nM neutravidin to biotinylated surfaces were fitted to the monoexponential model with model parameters A= 23.4 mV and k= 7.96 * 10^{-3} sec^{-1}. The model values (solid blue line) compares well with experimental values (black dots) within the prediction boundaries (95 % confidence interval). The monoexponential model successfully captures the experimental adsorption trends despite the oscillations and scatter inherent to the technique. (b) Apparent rate constants are plotted against the logarithm of neutravidin concentration. The rate of neutravidin adsorption increases exponentially with concentration. (c) The magnitude of ζ-potential increase is plotted as a function of neutravidin concentration. (d) Calibration curve for ζ-potential change against the mass of bound neutravidin measured using QCM. Vertical and horizontal error bars are in red.

possessing different affinities[158]. Though the binding of the first biotin molecule is sterically unhindered and quite rapid, the binding of the second biotin molecule is hindered by the presence of adjacent biotin molecules that have already associated with neutravidin[163]. This two-step adsorption behavior was not evident in the ζ-potential experiments because electrokinetic methods, unlike QCM, lack the ability to detect changes in molecular orientation. Since this biphasic adsorption was did not appear in the ζ-potential runs, we have used the monophasic monoexponential model for both the QCM and ζ-potential adsorption data for the sake of consistency and ease of modeling. From the model diagnostic tests, we concluded that the accuracy with which the monoexponential model predicts the QCM adsorption response is adequate.

In Figure 3.2(b), we can see that the apparent rate constant of binding increases linearly with the logarithm of neutravidin concentration, a result which is in good agreement with previous studies. The apparent binding constant extracted from the slope of this plot is in the order of 10^4 $M^{-1}sec^{-1}$, which is far lower than values of $3.0*10^6$–$4.5*10^7$ $M^{-1}sec^{-1}$ reported using droplet microfluidics techniques[158,164], where the transport limitation is greatly minimized by rapid mixing. In comparison, ζ-potential measurement is quite limited in its ability to characterize rapid binding processes, resulting in an apparent neutravidin-bioitin binding constant that is two to three orders of magnitude lower.

We can define a binding constant in terms of the adsorption response by evaluating the slope of Figure 3.2(c), (9.4mV/μmole of neutravidin), which allows us to estimate neutravidin concentration from the change in ζ-potential. In addition, we have mapped the adsorption signal from real-time ζ-potential measurements to the values of adsorbed neutravidin mass from QCM (Figure 3.2(d)), providing a means to evaluate the quantity of bound neutravidin from the ζ-potential signal.

We conducted a parallel study of neutravidin-biotin adsorption in order to

compare results from from QCM and real-time ζ-potential measurements. We concluded that time-resolved electrokinetic measurements can yield kinetic trends that closely mirror those obtained from QCM. Upon completion of the investigation of biotinylated surfaces, we proceeded to interrogate electrostatically heterogeneous glycopolymer surfaces using this validated technique.

3.4.3 Tuning the surface density of binding sites on brush surfaces.

Next, we applied real-time ζ-potential measurements to evaluate the adsorption kinetics of nanoparticulate models of viruses[135] on electrostatically heterogeneous polymer brush surfaces. Our surface design seeks to recapitulate aspects of the nanostructured organization of brush-like interfaces found in the body, most particularly the endothelial glycocalyx[165]. Our composite surface consists of two components (Figure 3.3(a)). The first element is a copolymer formed by chemical vapor deposition (CVD) copolymerization of two paracyclophane-based monomers. One co-monomer contains an initiator (ester bromide or EB) for surface-initiated atom transfer radical polymerization (SI-ATRP) and the other co-monomer an ionizable amine moiety (aminomethyl or AM). The protonated amine functions as a positively charged binding site to which negatively charged species of interest such as viruses[122] can adsorb. The second element is composed of glycopolymer brushes bearing sorbitol side chains, which are grafted from the EB initiation sites on the copolymer using SI-ATRP. The density of the binding sites relative to that of the SI-ATRP initiation sites on the copolymer coating can be tuned by modifying the CVD co-polymerization conditions. The model system can provide answers to the following questions: How does the density of aminomethyl groups affect the rate of adsorption of the virus-like nanoparticles? How does the introduction of a glycopolymer brush influence the adsorption behavior?

First, the surface composition of the copolymer was tuned by varying the CVD

process parameters as described in the methods section. To engineer varying ratios of AM and EB functional groups, copolymers were prepared using different CVD parameters. As seen in Figure 3.3(b), the FTIR spectra show an increasing intensity of the carbonyl peak of the EB component from top to bottom, indicating that the surface concentration of the AM group in the copolymer was reduced successively. We concluded that surface composition is tunable and that the ratios of ester bromide and aminomethyl functional groups present on the surface could be controlled merely by varying the CVD parameters appropriately.

To further validate this result, we employed ζ-potential measurements to compare the interfacial charge of these copolymers of varying surface compositions. It was hypothesized that if a greater number of aminomethyl groups were present on the surface, then the resulting copolymer would carry a higher positive charge than a copolymer containing fewer aminomethyl groups. Figure 3.3(c) summarizes the results of this study wherein the ζ-potential values of the seven copolymer coatings (CP1 through CP7) were plotted as a function of pH. The copolymer surfaces had isoelectric points (IEPs) ranging from 3-6, where the copolymer surfaces with IEPs close to 3 were mostly composed of the ester bromide whereas those closer to 6 were dominated by the aminomethyl containing repeating unit. We concluded that our copolymer charge could be tuned by controlling surface composition and that a progressively more positively charged surface could be obtained by increasing the concentration of aminomethyl groups relative to the ester bromide groups.

3.4.4 Adsorption rate of PS-COOH nanoparticles can be tuned by varying the surface composition

We studied three surfaces of varying AM/EB ratios and isoelectric points of 5.7, 4.8 and 3.6 respectively. The pH was maintained constant at 6.0 for all experiments. Though this pH value is higher than the isoelectric points of all three copolymers,

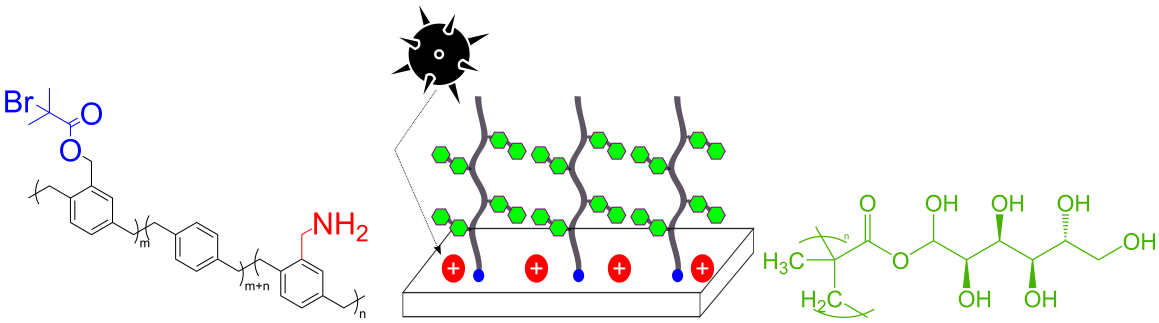

(a)

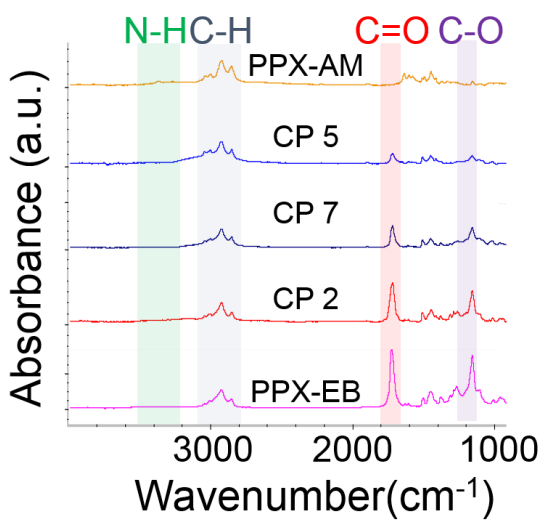

(b)

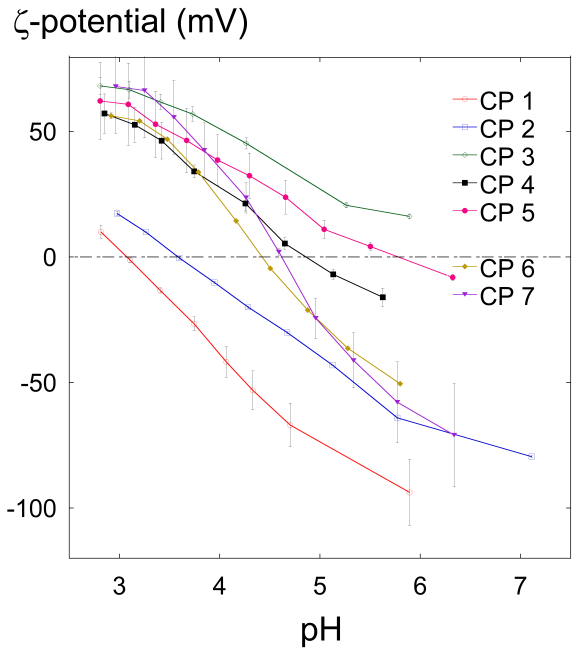

(c)

Figure 3.3: (a) Surface design used in our study. The base layer is composed of a copolymer synthesized using chemical vapor deposition, incorporating binding sites (aminomethyl groups or AM) and polymerization initiation sites (Ester bromide or EB). Negatively charged nanoparticles were expected to attach to the AM groups and we studied nanoparticle adsorption kinetics for different copolymer compositions. Sorbitol methacrylate brushes were grafted from the EB sites through SI-ATRP. (b) FTIR spectra showed that ratio of AM and EB is tunable. The decrease in peak heights of the carbonyl peak around 1730 cm^{-1} indicated that the ratio of EB relative to AM was reduced. (c) Surface charge of copolymer surfaces became more positive with increasing AM concentration. The isoelectric point was varied from 3-6 by changing the copolymer composition. Seven copolymer surfaces were studied (CP1 to CP7).

we anticipated that the proportion of ionized amine groups would be highest on the copolymer with the isoelectric point of 5.7.

We continuously measured changes in ζ-potential values with time before and after the addition of the nanoparticles. The addition of the PS-COOH nanoparticles to the electrolyte solution was accompanied by a steady decrease in the ζ-potential for all three samples (Figure 3.4). However, for copolymers with IEPs of 5.7 and 4.8, the decrease of ζ-potential was faster than it was for the sample with an IEP of 3.6. This is consistent with the predictions of models describing electrostatically driven adsorption[166], which demonstrate that a greater availability of binding sites increases the rate constant for the adsorption step. Also the magnitude of ζ-potential change (160 mV and 122 mV) was higher for the amine-rich surfaces than for the surfaces on which the EB groups were more abundant (51 mV). The relationship between adsorption rates and copolymer composition could be clearly discerned using real-time ζ-potential measurements. We concluded that nanoparticle adsorption rates could be tuned by modifying the surface concentration of aminomethyl groups.

Next, we studied the effect of incorporating glycopolymer brushes on the adsorption rate of nanoparticles. Poly(sorbitol methacrylate) brushes were grafted from the three sets of copolymers prepared. In all three cases, the adsorption rate was dramatically lower than what was observed without the polymer brushes. In two of the three experiments (Figure 3.4(c) and Figure 3.4(b)), the sorbitol brushes were successful in preventing adsorption of PS-COOH nanoparticles almost completely. However, in the case of the copolymer with the highest density of amine groups (Figure 3.4(a)), the sorbitol brushes were able to reduce the rate and extent of adsorption but could not prevent it completely.

We studied the variation of sorbitol brush thicknesses with copolymer composition through ellipsometry. The thickness was greatest for the sorbitol brushes

grafted from the copolymer with an IEP of 3.6 (8.7 nm) and lowest for the amine-rich copolymer with an IEP of 5.7 (3 nm). The copolymer with the intermediate IEP of 4.8 had 7.2 nm thick sorbitol brushes, which is the second largest brush thickness observed. This trend can be attributed to the lower density of ester bromide initiator groups in the more positively charged copolymer coatings, leading to a proportionally slower rate of brush growth and thinner brushes. Since initiator density and polymer brush growth rates have a linear relationship[167], if we maintain identical SI-ATRP conditions, the copolymer bearing more EB groups would have thicker brushes than the copolymer with fewer EB groups.

It is pertinent to note that even though all the brush thickness values are within the Debye screening length (9.62 nm) of the ionic environment, they still succeed in retarding nanoparticle adsorption. It is possible that thicker brushes improve the resistance to adsorption as they carry higher thermodynamic costs of brush compression[113], making it less likely for nanoparticles to adhere to the aminomethyl groups. However, this energy cost could be offset by promoting the electrostatic driving forces for adhesion in two ways-: a higher AM surface density or a more acidic environment that leads to a greater degree of amine protonation. Therefore, the critical polymer brush thickness required to span the aminomethyl binding sites and prevent binding is dependent on the relative densities of initiator and aminomethyl groups and on the pH value of the medium. Future work will focus on the interplay between the degree of amine ionization and the chain length distribution of the sorbitol brushes and their roles in shaping nanoparticle adsorption. Our results so far suggest that we can not only modulate binding rates of the particles by changing the copolymer composition, but also switch off binding by introducing sufficiently thick glycopolymer brushes.

To verify that sorbitol brushes function as barriers against nanoparticles and to validate the results from real-time electrokinetic measurements, we performed flu-

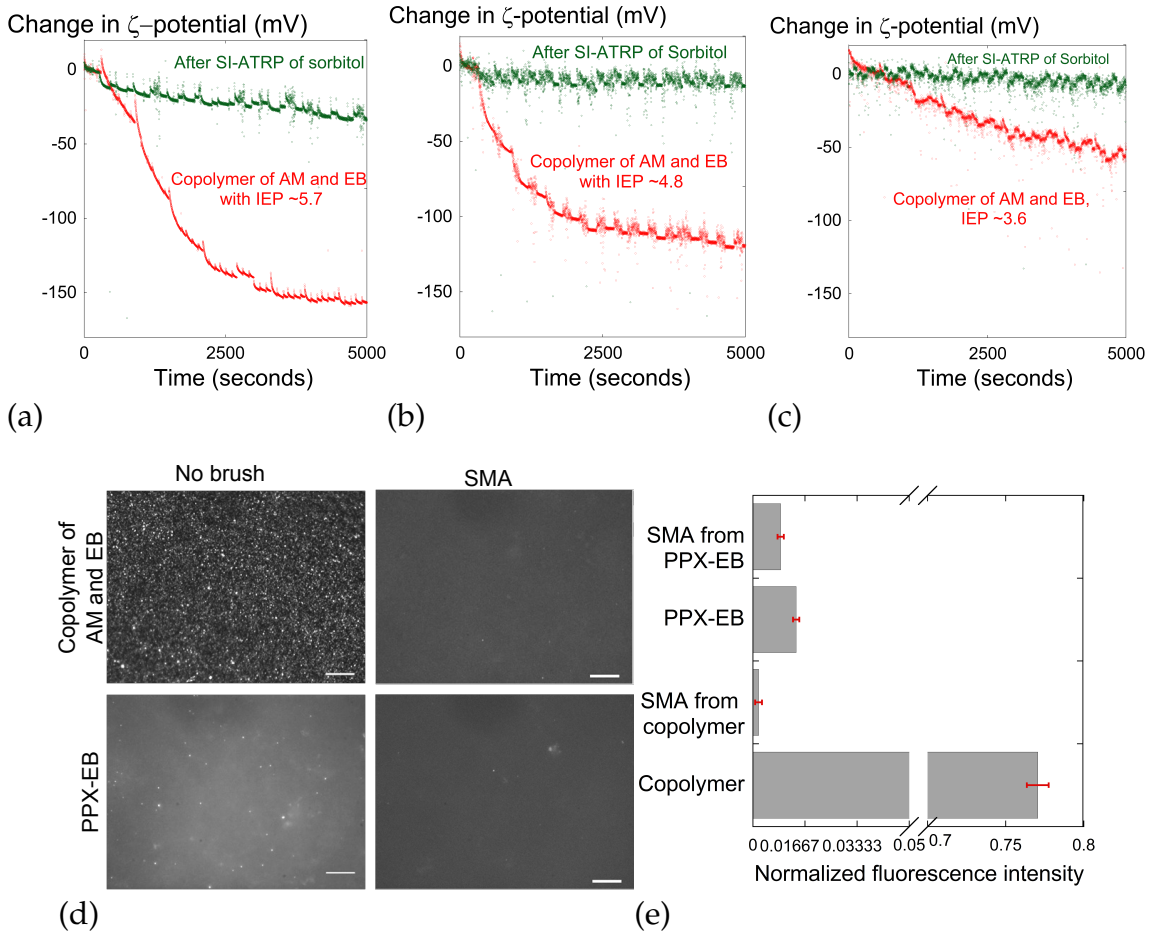

Figure 3.4: (a), (b), (c) Plots show how an increase in aminomethyl surface density (as measured by the isoelectric point) leads to a higher nanoparticle adsorption rate. The presence of the sorbitol brush is successful in retarding nanoparticle binding though in the case of (a), it is not entirely retarded. (d) Fluorescence study substantiates the results obtained from electrokinetic measurements. PS-COOH nanoparticles do not adhere to the sorbitol-grafted copolymer surfaces. Scale bar is 10μm (e) Comparison of surface density of fluorescent PS-COOH nanoparticles adsorbed on copolymer and PPX-EB before and after the SI-ATRP of sorbitol. High intensities were observed on the copolymer while low intensities were observed on PPX-EB (without amine groups) and also on sorbitol brushes grafted from PPX-EB and copolymer coatings. Error bars are in red.

orescence microscopy to compare equilibrium adsorption of fluorescent nanoparticles. Four sets of surfaces were compared: the copolymer containing AM and EB with an IEP of 4.8, PPX-EB without AM binding sites, as well as the respective surfaces after grafting sorbitol brushes. We observed very little PS-COOH binding to the PPX-EB surfaces (no AM groups), both before and after the introduction of the sorbitol brushes, indicating that the AM groups are required for for the nanoparticle to bind. Interestingly, fluorescence measurements showed a high particle density on the copolymer surfaces and almost no particles on the sorbitol brushes grafted from the copolymer (Figure 3.4(d) and Figure 3.4(e)). This observation is consistent with the decrease in ζ-potential observed during nanoparticle adsorption on the copolymers and little or no change in ζ-potential during the study of nanoparticle adsorption on the sorbitol brush. ζ-potential has been a valuable tool to develop a temporal map of virus-like particle adsorption events transpiring on polymer brush interfaces that are populated with electrostatic tethers. This is the first ζ-potential based study that has studied adsorption kinetics of a biologically relevant adsorbate on a complex biomimetic interface. We suggest that this electrokinetic characterization approach, so far limited to simple homogeneous surfaces such as glass, quartz and mica, can be readily extended to heterogeneous and nanotextured surfaces typical of biomaterials.

3.5 Conclusions

Using real-time ζ-potential measurements, we were not only able to detect the well-known binding of neutravidin to biotinylated surfaces, but also successfully quantify the neutravidin adsorption rate as a function of its concentration. By performing a parallel adsorption kinetics study using QCM, we could compare adsorption trends from ζ-potential with those obtained through QCM. Real-time ζ--potential measurements can be a powerful tool in understanding biomimetic sur-

faces possessing chemical heterogeneity, especially for applications sensitive to kinetic constraints as well as interfacial charge formation. We anticipate that this electrokinetic approach will be equally relevant to the study of affinity-based interactions of biological species with receptors as well as non-specific binding events that are electrostatically driven.

Employing a combination of chemical vapor deposition copolymerization and surface-initiated atom transfer radical polymerization, we successfully multifunctional polymer coatings where the ratio of glycopolymer brushes and positively charged binding sites could be tuned. Because CVD copolymerization affords exquisite control over the surface composition and ultimately the surface charge of these coatings, the isoelectric point of the base copolymer can be increased simply by increasing the density of aminomethy functional groups. Increasing the aminomethyl surface concentration resulted in a progressively more rapid adsorption trajectory of the virus-like nanoparticles on the copolymer surface. In addition to tailoring the adsorption rates of nanoparticles by varying the copolymer composition, we can also reduce the adsorption extent to near-zero levels by growing sorbitol brushes from the initiator sites present on the copolymer. Fluorescence microscopy was used to confirm findings from electrokinetic measurements of adsorption.

We conclude that the adsorption of virus-like nanoparticles is shaped by the interplay of aminomethyl concentration and sorbitol brush architecture. In future work, we will investigate the effect of glycopolymer brush composition by developing coatings based on glucose, galactose and mannose in their bioactive forms. We will also examine the adsorption of viruses such as adenoviruses and influenza on these surfaces as a function of amine density and glycopolymer brush architecture.

CHAPTER IV

A Study of Viral Adsorption on Electrostatically Heterogeneous Carbohydrate Brushes

The following chapter has been adapted from the following manuscript in preparation

Ramya Kumar, Domenic Kratzer, Kenneth Cheng, James Sugai, Julia Prisby and Joerg Lahann, "A Study of Viral Adsorption on Electrostatically Heterogeneous Carbohydrate Brushes"

4.1 Abstract

Nanoscale heterogeneity on material surfaces can transform its wettability, adhesion behaviour, and even colloidal interaction profiles. Chemical, topographical or electrostatic heterogeneity on biomaterial surfaces is profoundly consequential for bioadhesion, as it can aid or hinder biomaterial performance. To better understand the role of electrostatic heterogeneity in the adsorption of viruses on synthetic surfaces, we have developed a model surface. Our coating incorporates a tunable mixture of electrostatic tethers that serve as binding sites for negatively charged virus particles, and carbohydrate brushes, bearing pendant α-mannose, β-galactose or β-glucose side chains. Thermodynamic models predicted that a few

critical coating design parameters would determine the balance between attractive interactions offered by the binding sites and steric repulsion originating from the polymer brushes. Accordingly, we experimentally evaluated the impact of binding site density, brush composition and brush architecture, with the goal of identifying design specifications for coatings that would resist viral adsorption. Upon measuring the adsorption of adenoviruses, influenza and fibrinogen on a library of carbohydrate brushes co-immobilized with different ratios of positively charged binding sites, we concluded that the viral adhesion is shaped by the interplay between brush architecture and binding site density. When the fraction of binding sites is below 30%, resistance to viral adsorption can be preserved by engineering carbohydrate brushes with high thicknesses (3-5 nm). When brush thicknesses were lowered and binding site densities raised, we observed that the extent of viral adsorption was proportional to the surface concentration of binding sites. Ultimately, the brush architecture determines whether the binding sites are exposed to, or shielded from approaching viral particles. These insights will be of utility in guiding the design of polymer coatings in realistic settings where they will be populated with defects. By engineering sufficiently thick glycopolymer brushes, these surfaces can overcome the presence of electrostatically attractive defects and function successfully as barriers against viral attachment.

4.2 Introduction

Interactions between biomaterial surfaces and biomolecules, bacteria or viruses instantaneously transform its surface, resulting in beneficial or detrimental effects on its performance.[168] For instance, non-specific adsorption and denaturation of proteins on the surfaces of biomedical devices, such as insulin pumps, orthopedic devices and coronary stents, can adversely impact their function, causing implant failures, which often prove to be fatal. Spatiotemporal control of DNA adhe-

sion and transport in nanopore-based sequencing platforms still pose engineering challenges to which very solutions exist.[169] Beyond proteins and DNA, bacterial and viral adhesion pose even more complex challenges. Bacterial adsorption on catheters can trigger the formation of polymicrobial biofilm communities incorporating drug-resistant species.[170] Adsorption of viruses to crops, soils and water purification membranes are significant problems in agriculture and environmental engineering.[171] In recent years, viruses have gained attention as potential agents of biological warfare, especially the use of genetically modified influenza strains, Ebola and smallpox viruses, meriting investigations of virus-material interactions.[172]

Bioadhesion on synthetic materials has long been treated as a two-headed problem, encompassing both material design parameters and biological variables.[173] While biological variables such as environmental pH, ionic strength, the size, orientation and surface characteristics of the biological adsorbate involved, the presence of synergistic interactions in a mixture of biological adsorbates, can seldom be controlled, material properties can be modified to elicit the desired outcome. In order to elucidate the complex relationships between interfacial properties, such as surface charge, hydrophilicity, roughness, topographical and nanomechanical features or chemical heterogeneity on the interfacial behavior of protein, viruses or bacteria, model surfaces are required.[174] Model surfaces with tunable composition and structural features can be used to systematically test hypotheses and evaluate relationships between material features and adsorption outcomes, ultimately generating design guidelines or heuristics for engineering interfaces.

The use of self-assembled monolayers (SAMs) as model surfaces pioneered the pursuit of materials that can resist non-specific protein adsorption.[175] A combination of experimental effort and modeling studies involving SAMs has been used to understand the fundamental processes and mechanisms driving protein adsorp-

tion in molecular detail.[176] In seminal work by Whitesides et al., the protein resistance of large SAM libraries was evaluated, yielding several useful insights on molecular design: overall neutral charge, polar functional groups and the presence of hydrogen bond acceptors but not donors.[177] From this screening process, polyethylene glycol (PEG), carbohydrate and zwitterionic functionalities emerged as the most suitable choices for protein resistant SAMs.[174] Although SAM-based model surfaces have been useful in evaluating the molecular mechanisms of adhesion, their practical utility is limited by their instability, incompatibility with polymer-based materials, and requirement for pristine gold substrates.[178,179]

As model surfaces, polymer brushes enjoy distinct advantages over SAMs.[180] The advent of controlled radical polymerization techniques (CRP), such as surface-initiated nitroxide-mediated polymerization, (SI-NMP), surface-initiated reversible addition-fragmentation transfer, (SI-RAFT) polymerization and surface-initiated atom transfer radical polymerization (SI-ATRP), have enabled the creation of tailored zwitterionic and carbohydrate polymer brushes of diverse architectures.[17] Advances in SI-ATRP have helped to amplify zwitterionic and carbohydrate functionalities by presenting them with high spatial densities in the form of well-defined brushes.[181] These surfaces that can resist bacterial and cellular attachment, both in vitro and in vivo by interacting strongly with water molecules. The enthalpic cost of disrupting this hydration layer generates repulsive forces and ultimately renders adsorption thermodynamically unfavorable. Importantly, the substrate scope is almost unlimited, and the instability associated with SAMs can be circumvented.

While synthesizing polymer brushes on a large scale, impurities, contaminants and other processing limitations inevitably introduce defects on the surface, which are most often discounted in experimental and modeling studies. These defects sometimes take the form of positively charged regions, which compromise the ability of these brushes to resist bacterial and protein adsorption[182]. The electro-

static driving forces originating from these defects is particularly relevant especially since most bacteria and viruses and many protein molecules bear a negative surface charge at physiological pH.[122,183] Deliberately embedding what Santore et al. term as "engineered defects" at the base of the polymer brushes has been viewed as a promising approach to study the impact of chemical and electrostatic heterogeneity.[113] However, synthetic challenges have to be overcome in order to access model surfaces wherein electrostatic binding sites are randomly coimmobilized with polymer brushes.

The variation of brush density and architecture is accomplished by controlling the spatial organization of polymerization initiator groups that are deposited on the substrate. For CRP, a broad range of grafting densities can be accessed by using mixtures of initiator-functionalized and inert SAMs,[184] initiator backfilling,[185] tuning initiator solution concentrations and the reaction times in the initiator coupling step,[186] photo-decomposition of initiators,[187] or through the use of cleavable initiators.[188] In the case of "grafting to", the variation of grafting densities presents a greater challenge since high grafting densities can seldom be achieved, especially for polymer chains with large molecular weights. Common workarounds to this bottleneck include diblock or triblock copolymers incorporating an anchoring block that can irreversibly bind to the substrate through electrostatic[189] or hydrophobic interactions,[190] using progressively poorer solvent mixtures in the grafting step to facilitate dense chain packing,[191,192] cloud point grafting[193] in solutions of high salt concentrations, modifying the size and chemistry of the anchoring groups,[194] or simply by varying the molecular weight of the polymers.

Thanks to the above approaches, researchers have investigated the effect of brush architectural attributes on cell adhesion and migration,[195,196] bacterial adhesion[197] and most extensively, non-specific protein adsorption,[198] with the goal of identifying the optimal polymer brush design space. For instance the hemocom-

patibility of zwitterionic sulfobetaine[199] and phosphorylcholine brushes[200] was found to be strongly correlated with grafting density while sufficiently dense PEG layers were required to resist the adsorption of serum proteins.[191,193] Also, the relationships between bacterial adhesion and brush density,[201] composition,[181] thickness,[202] and architectures[203] have been systematically examined.

Despite methodological differences between these studies, they reached consensus on a few aspects: high brush densities are required to completely suppress protein, cellular and bacterial adhesion. Another finding is the critical role of polymer conformation; vast differences in bioadhesion between highly stretched polymer brushes and mushroom-like polymer coils have been repeatedly observed. As brush density is raised, they serve as increasingly effective steric and hydrophilic barriers against bacteria and viruses. Though there have been several efforts focused on brush architecture, the question of electrostatic interactions has remained under-investigated.[204] Though a few studies have examined the effect of surface charge on bacterial adhesion through coatings with tunable ζ-potential,[205,206] they were performed using polymer brushes of constant and spatially uniform grafting density. Though both "grafting to" and "grafting from" strategies enable precise control over the brush density and conformation, they cannot address electrostatic interactions. Whereas, LbL coatings and zwitterionic copolymer brushes allow us to systematically vary surface charge and examine its impact on biofouling, they are homogeneous and do not allow us to study the role of nanoscale electrostatic heterogeneity.[114,207]

To solve this, Santore et al. developed electrostatically heterogeneous PEG brushes with a tunable distribution of cationic poly(L-lysine) patches embedded at their base.[112] Using these "patchy" PEG surfaces, they demonstrated that design rules for surfaces that resist non-specific protein adsorption should not be applied in the design of brushes that will hinder bacterial adhesion.[114] By study-

ing the competing effects of steric repulsion and electrostatic attraction, they concluded that surface-bacteria interactions are governed by different mechanisms as opposed to surface-protein interactions.[113] Despite being ideal for studying nanoscale electrostatic heterogeneity and developing a mechanistic picture of bacterial adhesion, PLL-PEG coatings are limited by their "model" nature and cannot be applied on biomaterial surfaces in a stable and scalable manner.

Extensive use of model surfaces such as SAMs, peptidomimetic brushes[208] and patchy PEG-PLL brushes[113] has contributed to the development of heuristics for the design of surfaces with improved anti-fouling abilities and bacterial resistance. However, the majority of bioadhesion studies performed in the past have focused on protein adsorption, and to a limited extent bacterial adhesion, to the exclusion of adsorption processes involving viruses. This is further complicated by the fact that the interfacial behavior of proteins is not helpful in predicting the adsorption levels of the other adsorbates. For instance, it was widely believed that protein resistance was a prerequisite for the prevention non-specific bacterial adhesion. While some zwitterionic and glycopolymer brushes perform well against both bacteria and proteins, PEG brushes get colonized by bacteria despite repelling proteins. Recent studies have conclusively established that design rules for protein-resistant surfaces cannot be directly applied to prevent bacterial adhesion and vice versa.[134,209,210] Similar investigations probing the overlap in design criteria between virus-resistant surfaces and non-fouling surfaces are sorely lacking, largely because interactions between polymeric coatings and viruses are yet to be probed. Additionally, since viral attachment precedes the onset of infection, it is imperative to prevent this initial event. It has been shown that the first interactions of viruses with cells are often electrostatic and serve primarily to give a virus an initial catch-hold from which it can then recruit specific receptors that drive cellular entry.[211] Hence it would be critical to incorporate electrostatic interactions into

any model surface employed to probe viral attachment.

Recent years have witnessed increasing research activity in bacterial adhesion, but a significant gap in exists in our ability to control viral attachment to synthetic surfaces. So far interactions between viruses and material surfaces have not received much attention except in the development of biosensors.[212,213] No study so far has systematically examined the mechanism of viral adhesion and whether the forces driving protein adsorption are also implicated in viral attachment. As a result, there is a lot of uncertainty involved in designing surfaces that can resist viral attachment. To reduce this uncertainty, we propose a novel model surface using which we will derive design rules from simultaneously evaluated adsorption profiles of viruses and proteins on a rich multifaceted library of polymer coatings. In this contribution, we have developed a model surface wherein a tightly controlled distribution of electrostatic tethers for virus binding are incorporated at the base of well-defined carbohydrate brushes. We have jointly examined the effects of brush architecture and binding site density on viral adhesion and determined design criteria for virus-resistant surfaces.

In previous work, we developed robust, modular and multifunctional coatings using vapor-based polymerization of substituted [2,2]paracyclophanes. Chemical vapor deposition (CVD) polymerization is a versatile and simple process that offers several benefits: not only is it solvent-free, pinhole-free and substrate-independent, this process produces reactive coatings with exceptional stability.[214] We have a large paracyclophane library, containing a variety of functional groups, using which we can synthesize multifunctional copolymer coatings of desired composition.[214] Using our custom-designed two-source CVD system, we can achieve orthogonal presentation of the SI-ATRP initiators with either alkynes, amines, activated esters, ketones with fluorinated groups, or aldehydes.[92,95] Using CVD copolymerization, we have synthesized binary copolymers and demonstrated co-imm-

obilization of sugar molecules,[215] peptides and growth factors in order to regulate of cellular responses.[216] Additionally, we have investigated the adhesion of proteins[217] and DNA[218] on CVD-based copolymer coatings in several studies. CVD copolymerization is unique in its capacity to produce versatile surfaces that not only serve as model surfaces well-suited for basic research, but also speedily bridge the gap between fundamental insights and technological translation, owing to its scalability, substrate independence and reliability.[151] The results obtained from these surfaces will not only shed light on the mechanisms involved, but can also provide practically useful insights that can be readily implemented in engineering virus-resistant coatings.

Combining CVD copolymerization and SI-ATRP, we have developed model surfaces composed of positively charged binding sites and polymerization initiation sites for the growth of polymer brushes bearing carbohydrate residues (α-mannose, β-glucose and β-galactose). Binding sites were introduced in the form of ionizable aminomethyl groups whose positive charge can be exploited for viral and protein binding. The aminomethyl functionality was added to the surface in order to simulate coating defects that could compromise performance. We chose to investigate the virus-resistance capabilities of carbohydrate brushes since have glycopolymers have displayed promise as non-fouling surfaces against several bacteria species and most proteins. However, realizing that "perfect brushes" are unlikely to be produced at scale, we decided to investigate several questions conjointly. Do carbohydrate brushes possess the ability to retard viral adsorption? Is the ability to prevent non-specific protein adsorption predictive of virus-resistance? If defects exist on these carbohydrate brushes, in what circumstances will their presence lead to protein and viral adsorption? Our goal was to identify the design space in which defect-laden carbohydrate brushes could still function successfully as coatings that resist the attachment of viruses. Our modular synthetic

approach allows to control surface attributes independently, generating a library of electrostatically heterogeneous glycopolymer coatings to evaluate these unanswered questions.

We employed thermodynamic and statistical models to predict the degree of viral attachment as a function of surface attributes, and identified brush architecture and aminomethyl density as the key design variables. Thereafter, we synthesized and characterized a library of coatings with different ratios of aminomethyl groups and β-glucose brushes, thereby validating our ability to control surface composition orthogonally. We evaluated the adsorption of fibrinogen, adenoviruses and influenza H1N1 as a function of carbohydrate brush composition, brush architecture and aminomethyl concentration. Upon performing adsorption measurements, we observed two regimes of viral and protein adsorption. When the carbohydrate brushes were thin and sparse, adsorption was a function of the aminomethyl concentration. Whereas, with thicker denser brushes, viral and protein adsorption levels remained consistently low and were insensitive to the aminomethyl density, indicating that the viruses were prevented from interacting with the binding sites. We concluded that the interactions between the viruses and polymer coatings are shaped by the interplay between the electrostatic attraction, which is a product of the binding site density, and the resistance offered by the brush, which depends on brush architecture.

4.3 Experimental

4.3.1 Synthesis of initiator and copolymer coatings using chemical vapor deposition polymerization.

CVD copolymerization protocols developed by Kenneth Cheng.

The initiator coatings for SI-ATRP, poly[(*p*-xylylene-4-methyl-2-bromoisobutyrate)-*co*-(*p*-xylylene)] (PPX-EB)were prepared as described in Jiang et al.[95] Briefly, 32 mg of [2.2]paracyclophane-4-methyl 2-bromoisobutyrate (PCP-EB) was sublimed at 115-125 °C under reduced pressure (0.3 mbar) and then pyrolysed at 540 °C. The polymers were subsequently deposited on the substrates maintained at 14 °C.

Copolymer coatings comprised of [2.2]paracyclophane-4-methyl 2-bromoisobutyrate (PCP-EB) and 4-aminomethyl[2,2]paracyclophane (PCP-AM) were synthesized using a custom-built two-source CVD system.[151] In a typical experiment, 25 mg of PCP-AM and 32 mg of PCP-EB were loaded into the first and second tubes. Both source furnaces were heated to pyrolysis temperatures of 660 °C and 540 °C respectively using independently operated temperature controllers. In order to vary the ratio of the two functional groups deposited on the substrate, the separation distance between the precursor and the furnace was adjusted. For the PCP-EB precursor, this distance was maintained at 0.8 cm. For the copolymers CP44 through CP47, the separation between PCP-AM and the furnace was varied between 2.8 to 3.2 cm. For the copolymers CP40 through CP43, the separation between PCP-AM and the furnace was varied between 3-5 cm. Both precursors were sublimed between 80 °C and 110 °C at a pressure of 0.125 torr. The deposition chamber was cooled to 14 °C and the stage was rotated continuously to ensure uniform composition throughout the substrates. An argon flow rate of 10 standard cubic centimeters per minute was maintained in each tube and the sublimated dimers were transported into the pyrolysis zone by the argon carrier gas. Thereafter, they entered the deposition chamber to adsorb to the substrates and undergo copolymerization. Ultimately, coatings of poly[(*p*-xylylene-4-methyl-2-bromoisobutyrate)-*co*-(*p*-xylylene-4-aminomethyl)-*co*-(*p*-xylylene)] were formed on the substrates. Upon the complete sublimation of the PCP-EB precursor, depo-

sition was halted immediately.

4.3.2 Synthesis of 2′-acrylamidoethyl-α-d-mannopyranoside monomer

This synthetic method was developed by Dr. Domenic Kratzer.

In the first step, we synthesized 2′-acrylamidoethyl-2,3,4,6-tetra-O-acetyl-α-d-mannopyranoside

from α-d-mannose pentaacetate. In the final step, we deprotected the latter to synthesize 2′-acrylamidoethyl-α-d-mannopyranoside.

Briefly, 5 g (0.012moles) of α-d-mannose pentaacetate (Sigma Aldrich) was added to a clean and dry round-bottomed flask under argon. The solid was degassed using three cycles of vacuum-argon purging to remove adventitious moisture. Then, 50 mL of anhydrous dichloromethane was added under argon through a degassed needle and syringe. This mixture was stirred to dissolution under argon atmosphere and then cooled to 0-5 °C. Then, 2 mL (1.5 equivalents, 0.0188 moles) of hydroxy ethyl acrylamide (Sigma Aldrich) was injected into the reaction mass under argon. Finally 3.5 mL boron trifluoride diethyl etherate (1.2 equivalents, 0.015 moles) was added slowly over 15-30 minutes to the cooled reaction mass under argon. The flask was maintained at 0-5 °C for 30 minutes and then the reaction was allowed to proceed overnight at 22 °C. The next morning, the reaction mass was washed thoroughly with a saturated solution of sodium bicarbonate, then with deionized water and finally with a saturated solution of sodium chloride. The dichloromethane was removed at 37 °C in a rotavap until a yellow and oily crude was obtained. The crude was purified using column chromatography using a 7:3 mixture of ethyl acetate and n-hexane. The product was obtained by distilling off the ethyl acetate-hexane mixture under vacuum at 39 °C and 1.2 g of a white solid was obtained. After thorough drying on a schlenk line, this solid was analyzed using NMR to confirm the formation of 2′-acrylamidoethyl-2,3,4,6-tetra-O-acetyl-

α-d-mannopyranoside.

In the second step, 40 mL of anhydrous methanol was added to 1 g (0.033 moles) of the above material and stirred to dissolution under argon. Then 2.3 mL of 25 % sodium methoxide in methanol (3 equivalents, 0.01 moles) was added slowly over 15 minutes under argon. The reaction mass was stirred for 1.5 hours under argon at 22 °C. Then a small quantity of the ion-exchange resin Dowex 500, which was pre-washed with methanol, was added to the reaction mass and stirred for 10 minutes. Then the Dowex was filtered off and the methanol filtrate was distilled at 37 °C in a rotavap to obtain a white foamy solid. After thorough drying on a schlenk line, this solid was analyzed using NMR to confirm the formation of 2'-acrylamidoethyl-α-d-mannopyranoside. Similar procedures were adopted to synthesize 2'-acrylamidoethyl-β-d-galactopyranoside and 2'-acrylamidoethyl-β-d-glucopyranoside from their respective pentaacetate forms.

4.3.3 Surface-initiated atom transfer polymerization

Substrates bearing bromoisobutyryl groups (EB), either the homopolymer PPX-EB or the copolymer with PCP-AM, were prepared according to the CVD processes described above. The initial and final values of the coating thickness were ascertained using nulling ellipsometry before and after SI-ATRP. In a typical SI-ATRP run, copper (I) chloride, copper (II) chloride and Me_6Tren were purchased from Sigma Aldrich and used without further purification. Substrates were placed in a glove bag and degassed using 3 cycles of vacuum-argon purge and left at room temperature under argon. The respective carbohydrate-functionalized acrylamide monomer (2'-acrylamidoethyl-β-d-galactopyranoside or 2'-acrylamidoethyl-β-d-glucopyranoside or 2'-acrylamidoethyl-α-d-mannopyranoside) was synthesized as described previously. Typically, about 1 g of the monomer contained within a 50 mL flask was degassed using 3 cycles of vacuum-argon purges. In parallel, 25 mL

of milli-Q water, 500 mg NaCl and 200 μL of Me_6Tren were added to a 50 mL schlenk flask and three cycles of freeze-pump thaw were performed. After completion of the third freeze operation, 29 mg CuCl and 3 mg $CuCl_2$ were added to the catalyst flask under argon. Pump and thaw operations were continued subsequent to catalyst addition. Upon dissolution, the blue-colored catalyst mixture was transferred to the degassed monomer flask and mixed thoroughly at room temperature under argon atmosphere. This mixture was transferred to the glove bag and distributed such that each substrate was submerged completely in the reaction solution. The SI-ATRP reaction was allowed to proceed for either 1 hour or 24 hours under argon atmosphere. Finally, substrates were rinsed repeatedly with 0.05 M EDTA solution and deionized water and dried.

4.3.4 Ellipsometry

Ellipsometry was performed on silicon wafers (Silicon Valley Microelectronics, CA) with a native silicon dioxide layer of 2.5 nm thickness. Coating thickness was measured before and after SI-ATRP with a nulling ellipsometer (EP3 Nanofilm, Accurion GmbH, Germany). Ellipsometric delta and psi values were collected at a wavelength of 531.9 nm. Fixed values were used for the real (n=1.58) and imaginary (k=0) components of the refractive index of the polymer coatings. Using spectroscopic measurements, we verified that the refractive index of the initiator coating was very close to that of the carbohydrate brushes. After SI-ATRP, the thickness of the carbohydrate coatings formed was calculated by subtracting the initial thickness of the initiator layer from the post-ATRP thickness. Two substrates were used per experimental run.

4.3.5 Fourier transformed infrared spectroscopy

To verify whether the desired functional groups were present on the surface of the polymer coatings, Fourier-transformed infrared (FTIR) spectroscopy was performed using Nicolet 6700 spectrophotometer in the grazing angle configuration against a gold background. Polymers were deposited on gold wafers and 128 scans were collected with a resolution of 4 cm^{-1}. The absorbance intensities were normalized using the OMINIC software.

4.3.6 X-ray photoelectron spectroscopy

XPS was performed on an Axis Ultra X-ray photoelectron spectrometer (Kratos Analyticals, UK) equipped with a monochromatized Al-Kα X-ray source. All peaks were calibrated with respect to the non-functionalized aliphatic carbon with a binding energy of 285.0 eV. The area under each high resolution spectra was quantified and elemental compositions calculated using relative sensitivity factors of 1, 2.93, 2.84 and 1.8 for C_{1s}, O_{1s}, Br_{3d} and N_{1s} respectively. Peak fitting and analysis was performed using Casa XPS software.

4.3.7 Modeling

The model plots were developed jointly with Julia Prisby (undergraduate researcher)
For the statistical models, the Poisson cumulative distribution functions were calculated as a function of actual amine density on the copolymer surface and the critical amine density required for viral capture. The latter is dependent on the dissociation constant (K_{eq}) of aminomethyl, which is assumed to be of 10^5 and the pH value. The area of the electrostatic zone of influence was determined as per the Derjaguin approximation ($2 \times \sqrt{ParticleRadius \times DebyeLength}$).

The interaction energy was calculated as the sum of the three terms, U_{VDW}, U_{EDL} and U_{brush}. For the Van Der Waals contribution to the interaction energy,

we assumed a Hamaker constant of 10^{-20} J and a particle radius of 20 nm. U_{EDL}, stemming from electrostatic interactions, was quantified by assuming a virus surface charge of -43.5 mV and a Debye Length of 1 nm. For surfaces from which brushes were grafted, U_{brush}, the interaction energy was first calculated assuming a Kuhn length of 0.2 nm, excluded volume of 0.5 nm^3 and a grafting density of 0.4 chains/nm^2. Both elastic energy and excluded volume contributions were considered in calculating U_{brush}.

4.3.8 Quartz crystal microbalance measurements

The QCM-200 instrument (Stanford Research Systems, CA) was used for these studies. AT-cut quartz crystals coated with chrome/gold (O100RX1, Stanford Research Systems, CA) were functionalized with polymer coatings prepared using CVD and SI-ATRP as described in earlier sections.

For fibrinogen adsorption measurements, the following procedure was employed. Prior to measurement, the polymer-coated crystal surfaces were allowed to equilibrate overnight in a solution of 10 mM phosphate buffered saline (PBS). After the crystal was mounted on a flow cell, a syringe pump was employed to circulate the PBS through the flow cell at a rate of 0.1 mL/hour. Once a stable baseline was established, the pump inlet was switched from PBS to a reservoir containing the fibrinogen solution in PBS (concentration of 10 μg/mL). This solution was injected into the flow cell for over 5000 seconds and the adsorption response recorded at intervals of 1 second. The adsorbed fibrinogen mass was computed from the frequency decrease through the Sauerbrey equation.

For influenza H1N1 adsorption measurements, a similar procedure was employed. Influenza A/PR/8/34 H1N1 strain was obtained from Charles River avian vaccine services (catalog # 10100782). Again, the polymer-coated crystal surfaces were allowed to equilibrate overnight in a solution of 10 mM PBS. Then, the crystal

was mounted on a flow cell and the PBS buffer was pumped through the flow cell at a flow rate of 0.1 mL/hour using a syringe pump. Once a stable baseline was observed, the pump inlet was switched over to a reservoir of the influenza suspension in PBS (diluted to achieve a final concentration of 500 HA units/mL). This suspension was injected into the flow cell for over 5000 seconds and the adsorption response recorded at intervals of 1 second. The adsorbed mass of the virus was computed from the frequency decrease through the Sauerbrey equation.

4.3.9 Adenovirus adsorption measurements

Viral incubation performed by James Sugai, Giannobile Lab. SEM analysis was performed by Kenneth Cheng

Si wafers of size 0.5 cm $\times$ 0.5 cm were functionalized with the polymer coatings of interest as described earlier. These were placed in a 24-well plate and sterilized with 70% ethanol for 30 minutes. Thereafter, they were washed 5 $\times$ 5 minutes with sterile PBS. Then, 1 mL of a solution of Ad-pLpA (obtained from the University of Michigan's Vector Core) was added to each of the wells and incubated for 3-4 hours at 4 °C while being shaken gently. The viral concentration was maintained at 1×10^{11} particles/mL. The virus solution was subsequently aspirated and the wafers washed 5 $\times$ 5 minutes with sterile PBS. Finally the viruses adsorbed to the polymer coatings were fixed using 2.5 % paraformaldehyde (Electron Microscopy Services) in PBS. The samples were then dehydrated in ethanol and dried in a dessicator overnight. Viral adsorption was compared across different surfaces using scanning electron microscopy. Samples were mounted on a copper-taped SEM mount and sputter-coated with gold for 120 seconds. All images were acquired at 10,000 $\times$ magnification using the FEI Helios 650 nanolab instrument. For each sample group, viral particles were counted manually twice from four images for each sample group. Bright particles of the size range 50-100 nm were included in

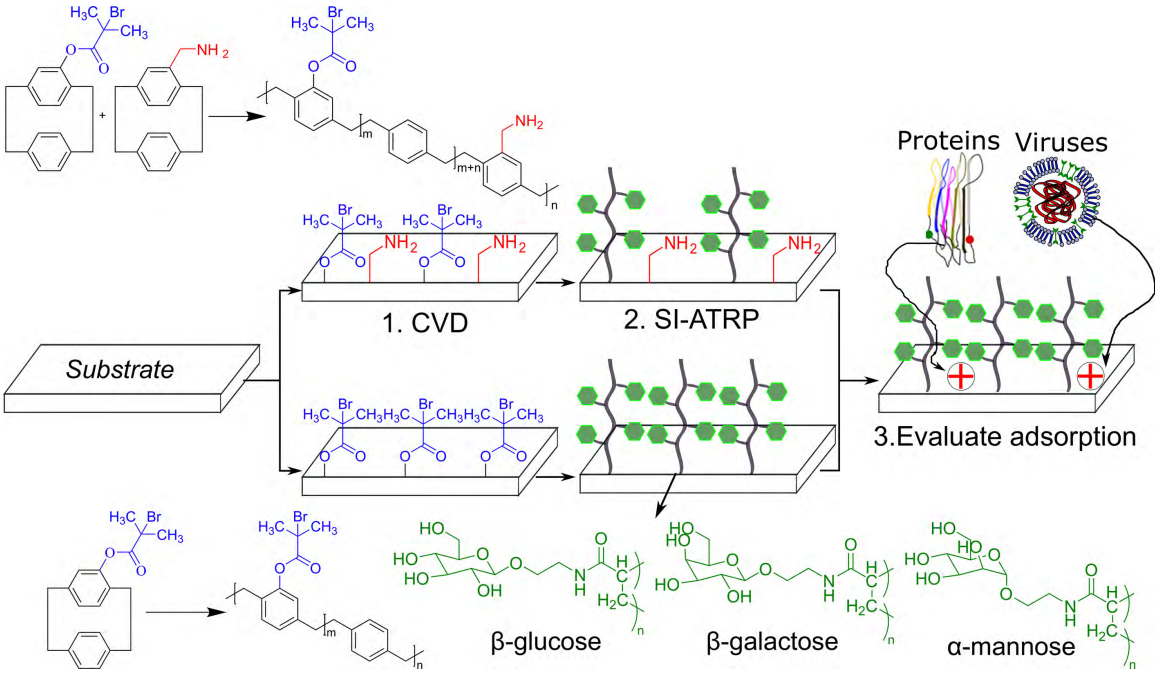

Figure 4.1: Synthetic strategy for model surfaces: In the first step we employed chemical vapor deposition (CVD) copolymerization to functionalize substrates with polymerization initiators (bromoisobutyryl groups, abbreviated as EB) and aminomethyl moieties (CH_2NH_2 groups, abbreviated as AM). The positively charged AM groups serve as binding sites for electrostatically driven adsorption of viral species and protein molecules. The ratio between AM and EB functional groups can be controlled by varying CVD operating parameters. In the second step, polymer brushes with pendant carbohydrate residues (α-glucose or β-galactose or α-mannose.) were grafted from the EB groups using surface-initiated atom transfer radical polymerization (SI-ATRP). Surfaces devoid of AM groups were used as controls. Our two-step synthetic strategy affords precise control over brush density, thickness, composition and binding site density. Finally, the effects of each of these variables on protein and viral adsorption was examined.

the count.

4.4 Results and discussion

Our model surface (Figure 4.1) consists of two components. The base layer is a binary copolymer synthesized via CVD copolymerization of functional paracyclophanes -: 1) The aminomethyl group (AM), with a pKa value of 10, acquires a positive charge upon protonation.[219] 2) The ester bromide (EB) functionality,

which initiates surface-initated atom transfer radical polymerization of glycopolymer brushes.

The ratio of AM to EB on the surface of the copolymer can be tuned by modulating the CVD operating conditions and compositional control has already been demonstrated in our previous work[220]. In Kumar et al.[220], we had studied the adsorption kinetics of virus-like nanoparticles on model surfaces where the commercially available glycomonomer sorbitol methacrylate had been used. In this contribution, we have extended the scope of our investigation to surfaces with greater chemical complexity by incorporating carbohydrate moieties in their bioactive pyranose forms. Our library of glycopolymers consists of polymer brushes with poly(acrylamide) backbones bearing pendant side chains composed of either α-glucose or β-galactose or α-mannose.

In another step forward from the previous work, we have replaced particulate models of viruses (carboxylated polystyrene nanoparticles) with two viral strains, adenoviruses and influenza H1N1. By using these two viral strains, we anticipated that we would acquire a realistic and practically useful picture of polymer-virus interactions.

4.4.1 Predictive models of virus-polymer interactions: Identifying key surface design variables

Before evaluating viral and protein adhesion on our library of coatings, we constructed simplified models to identify the surface design variables that would exert the most influence.

First, we employed a statistical treatment developed by Duffadar et al.[207] to calculate the capture efficiency of viral particles by brush-free copolymer surfaces composed of AM and EB moieties. This approach has been successfully employed in the past to probe the attachment behavior of micron-sized particles on hetero-

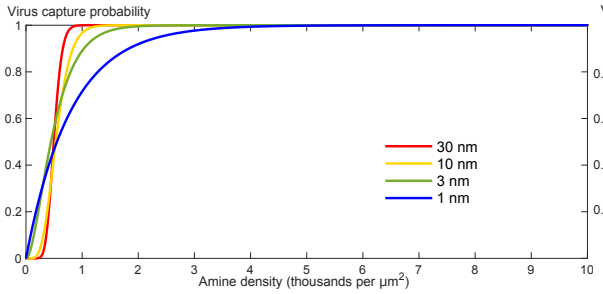

(a) pH=4, Viral Radius 100 nm

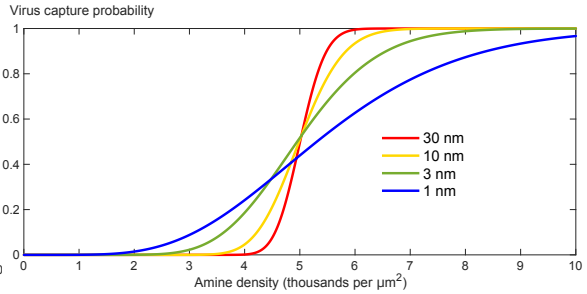

(b) pH=5, Viral Radius 100 nm

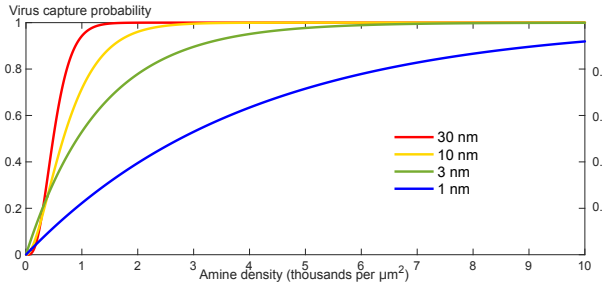

(c) pH=4, Viral Radius 20 nm

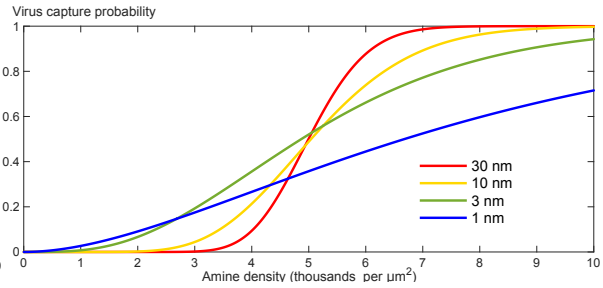

(d) pH=5, Viral Radius 20 nm

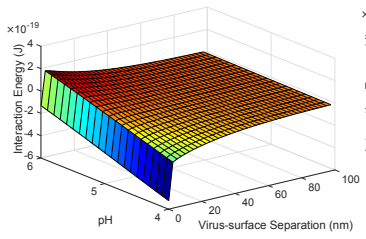

(e) No brushes

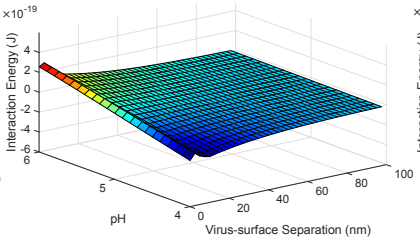

(f) 10 nm thick brushes

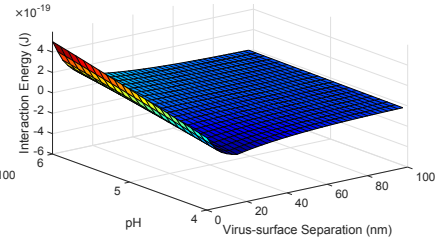

(g) 15 nm thick brushes

Figure 4.2: (a)-(d) Statistical models describe the probability of capturing viruses on copolymer surfaces (IEP of 4.9) when polymer brushes are absent. The probability is calculated as a function of copolymer compositions (amine density), pH values (4 or 5), Debye Lengths (red: 30 nm, yellow: 10 nm, green: 3 nm, blue: 1 nm) and viral radii (20 nm or 100 nm). (e) At pH values above the copolymer isoelectric point (4.9), repulsive interaction energy was calculated whereas attractive interactions were observed below the IEP. (f) When a 10 nm thick layer of polymer brushes is introduced, repulsive interactions gradually begin to dominate over a larger range of pH values. (g) When the brush thickness is increased further to 15 nm, repulsive interactions prevail over the entire pH range.

geneous surfaces. In this calculation, we assume that the AM groups are randomly distributed in patch-wise fashion on the copolymer surface according to the Poisson distribution. Despite the existence of an overall or global negative zeta potential on the copolymer coatings, the AM groups provide "hotspots" of local positive charge to which viral particles can bind through point-wise interactions. However, these interactions cannot be predicted if we consider the averaged out surface charge of the copolymer coatings. Though DLVO theory predicts repulsive interactions between negatively charged particles and surfaces with a net negative ζ-potential, viral adsorption can still occur if the number of attractive elements present on the surface exceeds the threshold value.[221] A statistical treatment is capable of identifying this threshold, which is dependent on several variables- ionic strength, contact area between the virus and the surface and the pH-dependent degree of ionization of the AM groups.

The contact area over which electrostatic interactions are exerted is calculated in accordance with the Derjaguin approximation for the sphere plate geometry as shown previously.[113] At a pH value of 4, (Figure 4.2(a)), the probability of capturing a viral particle with a radius of 20 nm increases monotonically as we add more amine groups to the surface, before hitting a plateau at an amine concentration where viral adsorption is certain. Additionally, as the environment becomes less acidic, upon increasing the pH to 5, the capture probabilities are greatly reduced while keeping the copolymer composition constant (Figure 4.2(b)). This is because a lower proportion of AM groups are likely to be protonated at a pH of 5, rendering viral capture less probable. Viral radius was singled out as another pertinent factor, with a particle radius of 20 nm resulting in lowered capture efficiencies (Figures 4.2(c) and 4.2(d)). This is due to the reduction in the area of the electrostatic zone of influence. Finally the dependence on capture efficiency on the density of electrostatic tethers can range from sigmoid at low ionic strength (Debye length of

30 nm) to linear at higher ionic strength (1 nm) (Figure 4.2(d)).

From our statistical model, we learned that when polymer brushes are absent, viral adhesion is largely shaped by "external factors" such as ionic environment and the viral geometry and is dependent to a lesser extent, on controllable factors such as the surface composition. Since the magnitude and length scale of electrostatic repulsion exerted by the AM-containing copolymer surface are dependent on pH and Debye length respectively, the surface cannot be shielded from viruses merely by minimizing the AM density. Reduction of local electrostatic driving forces by controlling the AM density is therefore not a reliable strategy to control viral adhesion. This analysis underscores the necessity of a design element that functions as a barrier against adsorbing viral particles, namely polymer brushes with the optimal architecture and composition.

To investigate the effect of polymer brush thickness and density on the thermodynamics of virus-surface interactions, we neglected the mosaic-like nature of our model surfaces. To minimize computational effort, we performed DLVO calculations by employing a mean-field approximation. Assuming that the copolymer surface had an isoelectric point of 4.9 and that the viral radius was 20 nm, we quantified the energy of the virus-surface interaction as a function of pH and distance separating the virus from the copolymer surface. The electrostatic repulsion (or attraction) arising from the electrical double layer forces was added to the Van Der Waals attraction (copolymer and brush VdW forces were described by a single Hamaker constant). In Figure 4.2(e), we can see that when the pH is above the IEP of the copolymer, the virus is repelled from the surface whereas attractive interactions result at pH values lower than the IEP (4.9). However, when a 10 nm thick polymer brush is introduced (Figure 4.2(f)), the interaction energy assumes positive values, indicating that it becomes thermodynamically unfavorable for the virus to adhere to the surface across a broad range of pH values. When

the brush thickness is increased further to 15 nm (Figure 4.2(g)), the height of the energy barrier forbidding viral adhesion only grows further. When a virus adsorbs to the surface, it either penetrates the polymer brushes in regions where its brush character is compromised by the interspersed AM groups, or it compresses the brush, resulting in a decrease in its equilibrium height. In the latter case, the brush compression imposes an entropic penalty and carries high thermodynamic costs, whereas in the former case, excluded volume interactions prohibit viral penetration of the brush. Irrespective of the mechanism involved, we expect polymer brushes to prevent viral adsorption, possibly through phenomena that resemble those involved in protein resistance. In our model, we have only included the effects of entropic loss and steric repulsion. In reality, the water structure associated with the exceptionally hydrophilic glycopolymer brushes will also be disrupted by the adsorbed virus, giving rise to hydration repulsion caused by displacement of water molecules. However, hydration repulsion has not been accounted for in our model. Notwithstanding this approximation, our modeling study predicts that the thermodynamic landscape of virus-polymer interactions is transformed by the incorporation of the polymer brushes.

4.4.2 Synthesis and characterization of copolymer coatings and carbohydrate brushes

From the models described above, we anticipated that viral adhesion would be promoted by AM groups and inhibited by the carbohydrate brushes. We wanted to verify this hypothesis through experimental measurements that help us understand how viral and protein adsorption would be affected by the incorporation of AM binding sites and carbohydrate brushes. To this end, we synthesized four groups of surfaces:

- Initiator coatings solely composed of EB.

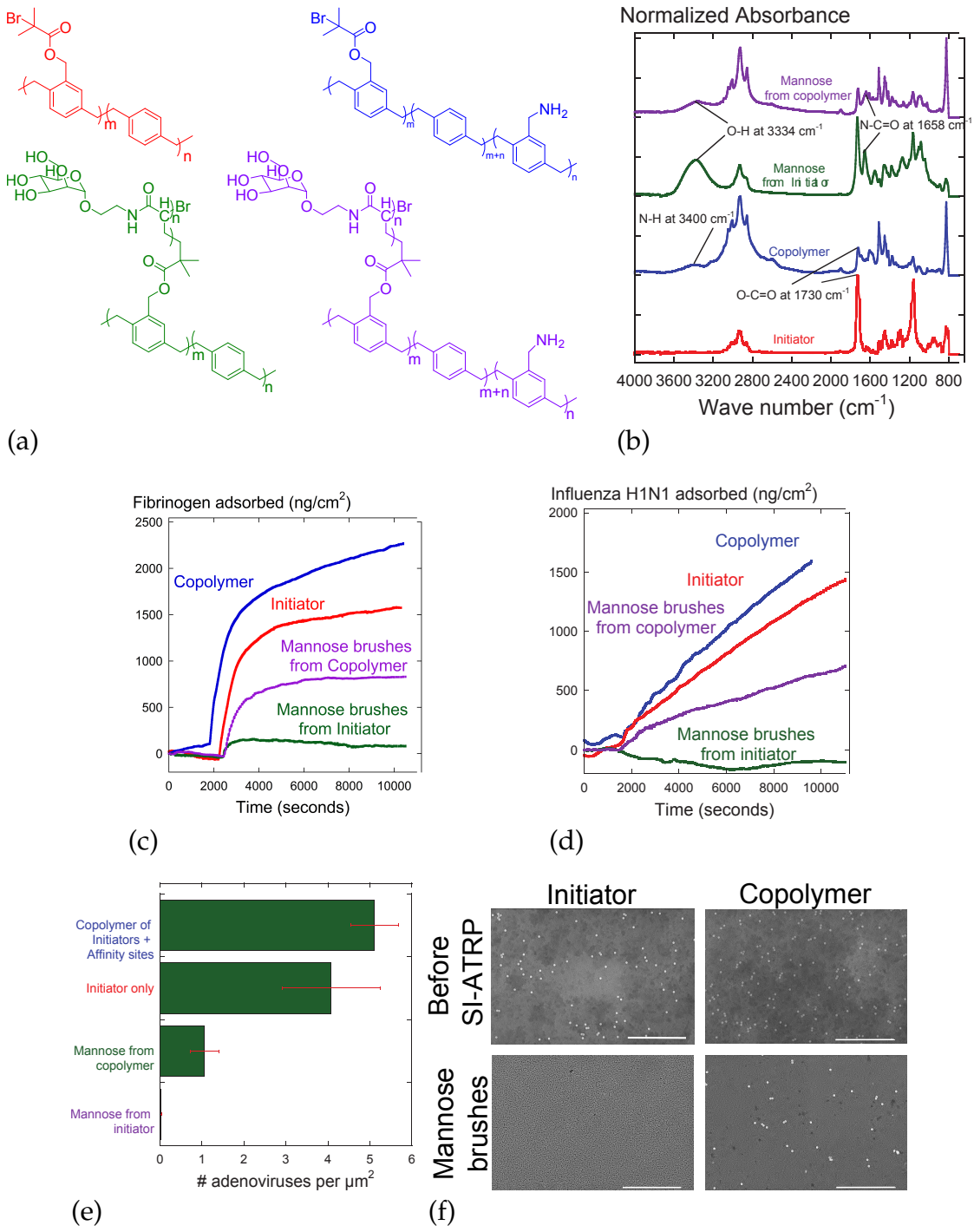

Figure 4.3: (a) Chemical structures of the four surfaces studied. (b) FTIR confirms the chemical structures of these coatings. Effect of surface composition on the adsorption kinetics of (c) fibrinogen and (d) influenza H1N1 particles on the four surfaces. In both (c) and (d), aminomethyl-containing surfaces promoted adsorption while the mannose brushes reduced adsorption levels. (e) Quantification of adenovirus attachment on surfaces. (f) Representative SEM images. Scale bar: 5 μm. Adsorption trends were similar to the ones observed in fibrinogen and influenza.

- Copolymer surfaces composed of both EB and AM.
- α-mannose brushes grafted from the initiator coatings.
- α-mannose brushes grafted from the copolymer coatings.

The chemical structures of the above surfaces are shown in Figure 4.3(a). The initiator and copolymer surfaces were both synthesized using CVD (co)polymerization. Both sets of surfaces were subsequently used as substrates in the same SI-ATRP run to synthesize α-mannose brushes from each, giving rise to four groups of coatings. Fourier-transformed infrared (FTIR) spectroscopy was used to verify the presence of functional groups associated with each coating. The initiator coatings were characterized by the presence of bands in the 1730 cm^{-1} and 1100 cm^{-1} regions, that are signature peaks belonging to the C=O and C−O bonds from the ester bromide. In addition to these two bands, the copolymer coatings also gave rise to a broad N−H peak in the 3400 cm^{-1} area, signifying that AM groups were present. Moreover, the bands belonging to the C−H stretches were much stronger in the copolymer coating than in the initiator coating owing to the preponderance of methylene groups from the CH_2NH_2. After SI-ATRP, mannose brushes grafted from the copolymer and the initiator were analyzed using ellipsometry, FTIR spectroscopy (Figure 4.3(b)) as well as X-ray photoelectron spectroscopy (Figure 4.4) .

We observed the appearance of two new signals in the FTIR spectra upon grafting mannose polymers from the surface. The 3300cm^{-1} band that is typical of the hydroxyl group and the N−C=O amide stretch at 1658 cm^{-1}, both of which confirm the formation of the mannose polymer brush.

XPS analysis of the mannosylated sample revealed that the elemental composition was in close agreement with the theoretical values derived from the molecular structure. High resolution scans of the C_{1s} region were performed in order to

quantify signals from the aliphatic C-C bonds, the C-C-O bonds from the pyranose ring, the N-C bonds and the C=O from the acrylamide. The distribution of areas under each of the fitted peaks matches the theoretical contribution from each component, which provides additional validation that the α-mannose brushes were synthesized successfully. Since XPS has a penetration depth of 5-10 nm, only the α-mannose polymer brushes were sampled when they were grafted from the initiator as their thickness (18 nm) exceeds this limit. On the other hand, when they were grafted from the copolymer, they were thinner (3 nm) and hence presented a mixture of signals from both the brush and the copolymer, rendering analysis a challenge.

Overall, from our characterization studies, we were able to confirm that all four surfaces were successfully synthesized and that the chemical structure of α-mannose side chains remained intact after SI-ATRP.

4.4.3 Evaluation of virus and protein adhesion on mannose brushes

Next we proceeded to examine the effect of surface composition on the ability of these surfaces to retard non-specific adsorption of fibrinogen, influenza H1N1 and adenoviruses. Specifically, we wanted to evaluate the impact of introducing AM groups and α-mannose brushes on viral and protein interfacial behaviour. Accordingly we challenged the four surfaces characterized above (initiator coatings, copolymer coatings, α-mannose brushes grafted from each of them) with a solution of fibrinogen and measured the adsorption response using QCM. Since undesired fibrinogen adsorption to biomedical implants is known to trigger thrombosis, it is frequently used as a model protein molecule to evaluate non-fouling abilities of polymeric surfaces.

As seen in Figure 4.3(c), the quantities of fibrinogen deposited on the the copolymer and initiator surfaces were quite high (2000 and 1500 ng/cm^2 respectively).

B.E	C 1s	N 1s	O 1s
eV	285	399	532
Exp. (atom %)	66.6	5.0	28.3
Theo. (atom %)	57.8	5.2	36.8

(a)

B.E.	C-C	C-C-O	N-C	C=O
eV	285	286	287.6	288.8
Exp. (%)	25.4	55.7	17.3	1.7
Theo. (%)	38.9	44.4	11.1	5.6

(b)

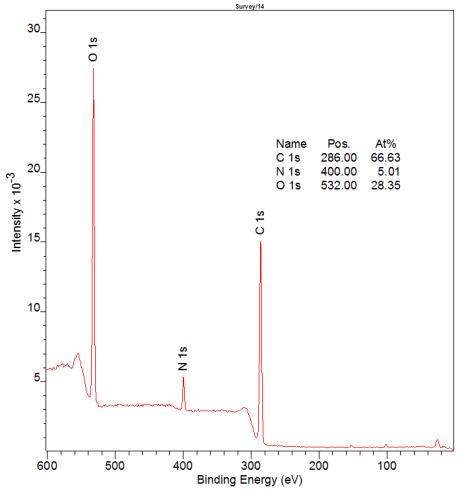

(c)

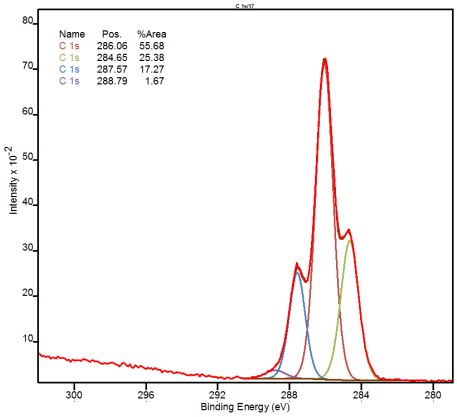

(d)

Figure 4.4: XPS characterization of poly(2′-acrylamidoethyl-α-d-mannopyranoside) brushes grafted from ATRP initiator coatings. (a) Elemental composition of α-mannose brushes as measured using high resolution XPS scans. (b) & (d) High resolution XPS spectra of C_{1s} further confirms the chemical composition of the α-mannose brushes. (c) XPS Survey spectra of the surface bearing α-mannose brushes.

Streaming potential measurements have previously shown[220] that the isoelectric point of the copolymer coatings is higher than that of the initiator coatings. We concluded that the difference in surface charge between the copolymer and initiator enhanced the deposition of fibrinogen (IEP of 5.8), whose adsorption behaviour is known to be sensitive to pH and electrostatic double layer thickness.

In contrast to the unmodified copolymer and initiator surfaces, the fibrinogen adsorption was greatly reduced when mannose brushes were grafted (750 and 50 ng/cm^2 respectively). This represents a 63% reduction in protein adsorption for the copolymer surfaces and a 97% reduction for the initiator surfaces. However protein adsorption was 15 times higher on the mannose brushes which were co-immobilized with AM on the copolymer than on surfaces composed of mannose brushes alone. Overall these results suggest that the while the mannose brushes are capable of preventing fibrinogen deposition, the incorporation of AM groups promotes fibrinogen adsorption.

In the case of influenza H1N1 adsorption, we observed similar trends (Figure 4.3(d)). The mass of virus particles adhering to the copolymer and the initiator were quite high and unlike fibrinogen, the difference in the extent of adsorption between these two coatings was negligible. At a pH of 7.4 and in a 10 mM PBS solution, conditions identical to those in which QCM was performed, the ζ-potential of influenza was recorded as -29 mV. From this, we realized that the the interactions between the influenza and the polymer coatings are not as sensitive to electrostatic attraction as compared to fibrinogen.

The adsorption traces of influenza differed from those of fibrinogen in another aspect. While the adsorbed fibrinogen mass increased exponentially with time before hitting a plateau, representing a typical first-order adsorption profile, the adsorption profile of influenza followed a linear trend. It appears that fibrinogen's adsorption kinetics fit the monoexponential model in which the protein unfolds at

the surface, forms a monolayer and ceases to adsorb to the surface upon reaching saturation coverage. On the other hand, influenza's adsorption kinetics suggest an accumulation process resulting in the formation of a multilayer.

However, the introduction of α-mannose to the interface has the effect of suppressing viral adsorption on both the copolymer and the initiator surfaces. While a plateau value of around 500 ng/cm^2 was reached for the mannose brushes grafted from the copolymer, the frequency did not change much on the mannose brushes grafted from the initiator, indicating near-zero levels of adsorbed influenza. These observations closely mirror the results from the fibrinogen study.

Influenza H1N1 apart, we also tested these four surfaces against adenoviruses. After incubation, the surfaces were washed, fixed, and imaged using scanning electron microscopy and the density of viruses on the surfaces evaluated (Figure 4.3(e)). The copolymer had the highest number of adenoviruses adsorbed per μm^2, followed by the initiator coating and the mannose brushes grafted from the copolymer. The α-mannose brushes free of AM groups had nearly no adenoviruses on its surface, implying that the α-mannose brushes are successful in preventing the adsorption of not just the influenza viral particles but also adenoviruses. However, the virus-resistance displayed by the α-mannose brushes grown from the copolymer was not as effective, indicating that the AM functions as a binding site for the adenoviruses.

The results from the fibrinogen, influenza and adenovirus studies follow a consistent trend and prove that the α-mannose brushes serve as a barrier against viral adhesion. They also verify the predictions of the models which suggested that the electrostatic attraction offered by the AM groups could be counteracted by the presence of the carbohydrate brushes. This study was repeated for β-glucose and β-galactose polymer brushes, with similar results. We concluded that viral and protein adsorption trends were largely independent of the composition or stereo-

chemistry of the carbohydrate brushes, possibly because neither viral strain bears lectins possessing specific affinities for the glycans we employed.[222]

In the first phase of our study, we established that our tunable coating comprising carbohdyrate brushes and electrostatic tethers, is an effective model surface to probe the competing effects of Coulombic forces and steric repulsion. In the second phase of our study, we synthesized surfaces with varying ratios of brushes and electrostatic tethers and simultaneously evaluated the impact of polymer conformation and binding site density on viral and protein adhesion outcomes.

4.4.4 Thin carbohydrate coatings with high AM densities

We proceeded to evaluate the effect of AM surface concentration and brush architecture on the adsorption kinetics of influenza H1N1 and fibrinogen. Two sets of surfaces were synthesized. In the first set, we sought to create thin and sparse glucose brushes from four copolymer surfaces with varying amine concentrations.

The relative concentrations of aminomethyl and ester bromide repeat units were varied in copolymers CP44 through CP47. As seen in Figure 4.5(a), the carbonyl bands at 1730 cm^{-1} are prominent in CP47, but not as intense in CP44 and CP45, indicating that CP47 has the highest EB density. Conversely, the C−H and N−H bands associated with the aminomethyl are most intense in CP44 and their intensities decline steadily from CP45 to CP47, implying that the CP44 has the highest proportion of AM repeat units. These observations from FTIR studies were further verified using XPS scans (Figure 4.5(b)). From XPS, it was revealed that the nitrogen content is highest in CP44 and lowest in CP47. Overall, the FTIR and XPS results verified that copolymer coatings with a broad compositional range were prepared successfully.

Upon synthesizing and characterizing copolymer surfaces using CVD, glucose brushes were grafted from CP44 through CP47. We ensured that all the copoly-

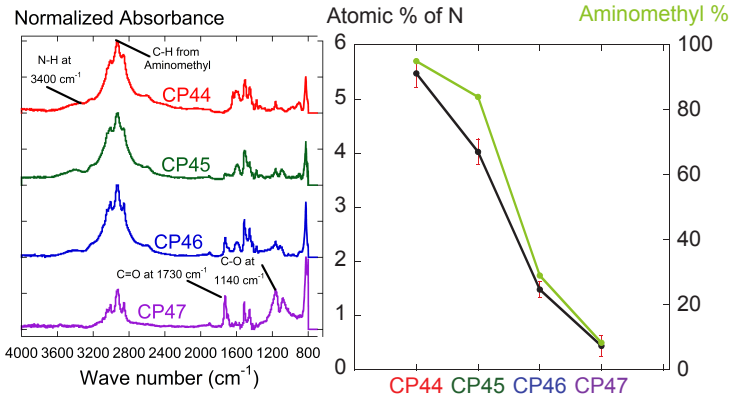

(a) (b)

Copolymer	Nitrogen atom %	Mean AM %	Glucose layer thickness (nm)
CP44	5.5	95	0.1 ± 0
CP45	4.0	84	0.2 ± 0
CP46	1.5	29	1.7 ± 0.2
CP47	0.4	8.3	4.7 ± 0.4

(c)

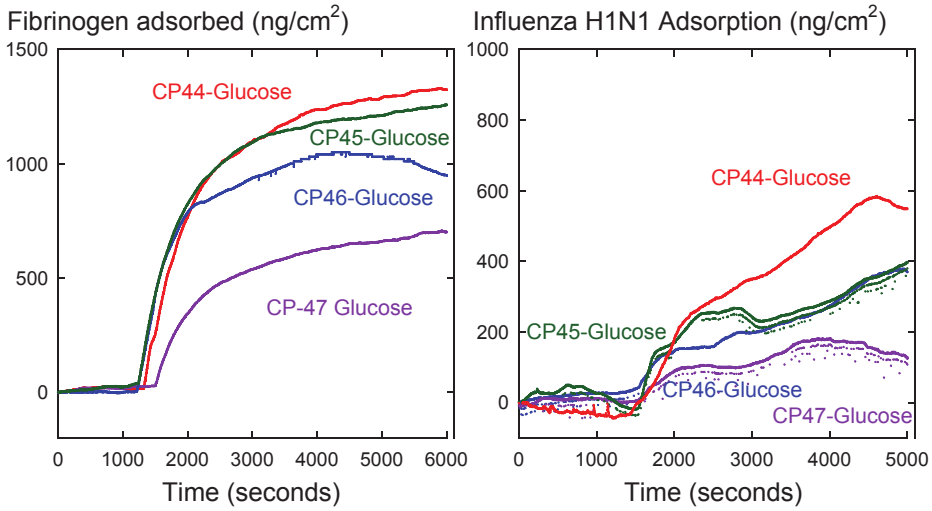

(d) (e)

Figure 4.5: Four sets of copolymers (CP44-red, CP45-green, CP46-blue, CP47-purple) with different concentrations of aminomethyl (AM) and ester bromide (EB) groups were prepared. (a) FTIR and (b) XPS measurements together verified that the AM concentration decreased progressively from CP 44 to CP47. Conversely ,the EB content increased as shown by the growing intensity of the carbonyl band. (c) Ellipsometric thicknesses of glucose polymers grafted from the copolymer coatings. QCM traces of (d) fibrinogen and (e) influenza indicate that the adsorption levels of both the protein and the virus particles are correlated with the AM density.

mer surfaces underwent SI-ATRP in the same experimental run to ensure that they were exposed to identical polymerization conditions. During the synthesis of glucose brushes, the SI-ATRP reaction time was restricted to one hour with the intent of obtaining short polymer chain lengths. Even though all the copolymers were treated to the same SI-ATRP conditions, we anticipated that the grafting density of the glucose brushes would vary due to differences in AM/EB ratios. Ellipsometric characterization (Table 4.5(c)) of the resulting glucose coatings indicated that the thickness was highest in CP47 and lowest in CP44, suggesting that differences in polymer conformation caused these variations. Despite the fact that these glucose chains are expected to be around the same molecular weight by virtue of being synthesized under identical reaction conditions, the thicknesses ranged from under 1 nm for AM-rich copolymers CP44 and CP45 to nearly 5 nm for CP47, which had the least AM density and consequently the highest grafting density. These results agree with previous studies which concluded that high grafting densities promote the formation of thicker brush-like polymers while lower densities result in thin and sparse mushroom-like polymers.[204]

Finally, we performed QCM measurements of influenza and fibrinogen adsorption on these four glucose surfaces to ascertain the impact of AM density and polymer conformation on adhesion kinetics. For fibrinogen, we observed that glucose brushes grafted from CP44 had the highest adsorbed mass of protein at around 1200 ng/cm^2 while those grafted from CP47 displayed the least fibrinogen adsorption among the four surfaces compared. We observed similar trends for influenza adsorption, though the difference in adsorbed viral masses between CP44-glucose and CP47-glucose was lower. It is pertinent to note that the glucose chain density is highest for CP47-glucose and lowest for CP44-glucose. It appears that the fibrinogen and influenza adsorption can be promoted or retarded merely by varying the proportion of AM and EB functionalities.

4.4.5 Thick carbohydrate coatings with lower AM content

In the second set of surfaces studied, we desired to graft glucose brushes from the copolymer surfaces such that they had higher thicknesses and grafting densities than in the first of surfaces. Accordingly, we synthesized copolymer coatings where the AM surface density would be lower than those in the first set, thereby ensuring sufficiently numerous ATRP initiators (EB) exist on the coating.

As seen in Figure 4.6(a), though the FTIR bands representing the aminomethyl functionality are quite prominent in CP40, the remaining surfaces in this set, CP41, CP42 and CP43 are mostly composed of the EB repeat unit. This finding is apparent in XPS measurements (Figure 4.6(b)), where we can see that with the exception of CP40, whose composition reflects 75%-25% split between the AM and EB components respectively, the nitrogen content is consistently low in the remaining surfaces. In CP41, CP42 and CP43, the AM proportion varies between 25% to 30%, thereby ensuring adequate initiator coverage.

Later, glucose brushes were synthesized from these four surfaces in the same SI-ATRP experiment in order to ensure that they were all subjected to identical reaction conditions. In this ATRP run, we allowed the reaction to proceed for 24 hours so that the maximum possible degree of polymerization could be attained for these surface-grafted polymer chains. Thicknesses of these glucose-functional layers were determined using ellipsometry and tabulated in Table 4.6(c). We observed that though the glucose layer thickness is quite thin in the CP40 surfaces, the glucose coatings were significantly higher in the remaining samples (CP41, CP42 and CP43), ranging from 3-5 nm. This striking contrast in brush thickness between CP40 and the other copolymers can be attributed to the higher AM content in CP40 and denser distribution of ATRP-initiating EB moieties in CP41 through CP43. Additionally, the increase in reaction time compared to the first set of surfaces (24 hours as opposed to 1 hour) likely allowed us to attain higher degree of

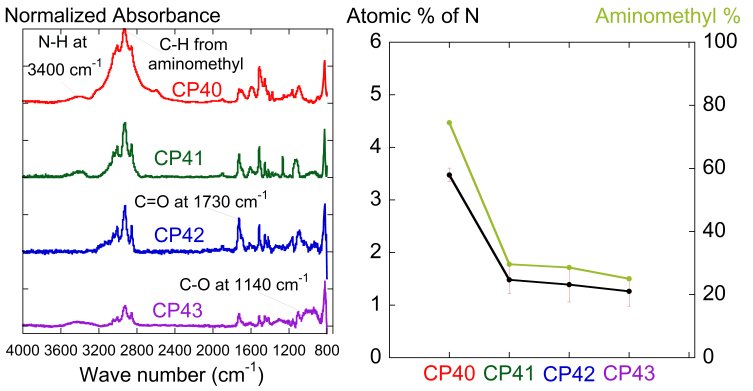

(a) (b)

Copolymer	Nitrogen atom %	Mean AM %	Glucose layer thickness (nm)
CP40	3.5	74.5	0.2 ± 0
CP41	1.5	29.6	4.6 ± 0.3
CP42	1.4	28.6	3.7 ± 0.5
CP43	1.3	25	4.5 ± 0.5

(c)

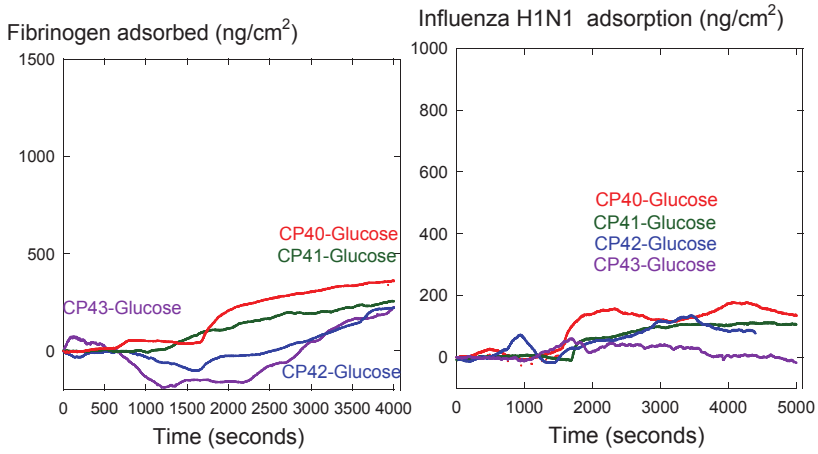

(d) (e)

Figure 4.6: Four sets of copolymer coatings (CP40-red, CP41-green, CP42-blue, CP43-purple) with different ratios of aminomethyl (AM) and ester bromide (EB) groups were synthesized and differences in adsorption evaluated. (a) FTIR spectra and (b) X-ray photoelectron spectroscopy (XPS) were jointly employed to assess variations in AM content. Subsequently, glucose polymer chains (ellipsometric thicknesses tabulated in (c)) were grafted from these surfaces using SI-ATRP. The adsorption kinetics of (d) fibrinogen and (e) influenza H1N1 on glucose chains grown from copolymers were studied using QCM. For both fibrinogen and influenza, adsorbed masses were near baseline levels, indicating that the glucose layers prevented non-specific protein and viral adsorption.

polymerization and consequently thicker coatings.

Subsequently, we evaluated the interactions between these glucose-functional surfaces and fibrinogen using QCM measurements. In the CP40-glucose surface, we detected a small decrease in the measured frequency upon the introduction of fibrinogen (around 1800 seconds), indicating that only a low quantity of protein had been adsorbed. As for the rest of the surfaces, the deviation of frequency measurements from baseline levels was even smaller, and in two cases (CP42-glucose and CP43-glucose) could not be distinguished from the noise in the baseline reading. Similar results were obtained when we assessed influenza H1N1 adsorption on these surfaces, with barely discernible decreases in frequency being recorded upon the injection of the influenza suspension. Overall, we concluded that both non-specific protein and viral adsorption levels were minimal (100-200 ng/cm^2) in the second set of surfaces (CP40 to CP43).

We note the dissimilarities in the adsorption trends observed between the first set of surfaces and the second set of surfaces (Figure 4.5 and Figure 4.6). In the former, the extent of viral and protein adsorption was dependent on the copolymer composition, with a strong correlation between the adsorption response and the AM concentration. In contrast, the latter case presents a scenario wherein the adsorption remained low on all samples irrespective of whether the AM levels were at their highest (as in the case of CP40) or lowest (CP43). The fact that the adsorption profiles were independent of binding site density in Figure 4.6 but varied with AM density in Figure 4.5 suggests that AM density alone cannot influence adsorption outcomes. From these two studies, it is apparent that adsorption behavior is shaped by the complex interplay between binding site density and polymer conformation.

In the first case, the polymer chains were short, thin and dilute and did not flop over to form a bridge across adjacent the AM binding sites. As a result, the

AM groups were able to interact with the approaching virus particle or protein molecule, leading to AM concentration-dependent adsorption trends. In the second case, due to a combination of higher reaction time as well as initiator density, the polymer chains were long enough and numerous enough to shield the AM binding sites, thereby preventing adsorption altogether and screening the electrostatic attraction offered by the AM binding sites. While the electrostatic screening provided by the addition of electrolytes has limited utility in the prevention of Coulombically driven viral adsorption, our carbohydrate polymer brushes function as hydrophilic and steric screens that can ward off viruses in a manner independent of Debye length and pH.

4.5 Conclusions

In identifying design guidelines for virus-resistant coatings, model surfaces can prove to be useful in bridging the gap between theoretical predictions and technological applications. In this study, we developed a model surface incorporating carbohydrate brushes of tailored composition and architecture as well as AM groups, which served as binding sites promoting viral adhesion. Employing a combination of chemical vapor deposition copolymerization and surface-initiated atom transfer radical polymerization, we successfully synthesized multifunctional polymer coatings where the carbohydrate brushes and positively charged binding sites could be co-immobilized in the desired ratio. We observed two effects on copolymer surfaces enriched with AM groups have 1) reduced initiator densities leading to a thinner diluted brush, thereby compromising its ability to screen viral adsorption 2) enhancement of electrostatically driven adsorption of fibrinogen and influenza H1N1. Further, we examined the adsorption of fibrinogen and influenza on a diverse set of coatings and concluded that the adsorption of virus-like nanoparticles is a complex function of AM concentration and carbohydrate brush architecture.

By allowing the carbohydrate brushes to grow to their maximum extent and attain brush thicknesses in the order of 3-5 nm, low levels of protein and viral adsorption could be achieved, even when the AM proportion was as high as 25-30%. When carbohydrate polymer chains were sufficiently long and numerous, the resulting steric and hydration repulsions could effectively block the virus from interacting with the positively charged affinity sites. Among coatings where AM was the dominant repeat unit the viral and protein adsorption varied in accordance with the aminomethyl concentration, especially since short and sparse polymer chains did not form a viable barrier. We posit that viral resistance can remain uncompromised despite the existence of positively charged aminomethyl-like "defects" on the coatings if our design guidelines (maintaining defect density below 30%, maximizing the degree of polymerization of grafted brushes) are implemented. We conclude that virus-resistant coatings will retain their ability to repel proteins and viruses if the surrounding carbohydrate chains are carefully engineered to mask the attractive interactions offered by the defects.

CHAPTER V

A Predictive Model for the Design of Zwitterionic Polymer Brushes: A Statistical Design of Experiments Approach

The material in this chapter has been adapted with minor modifications from the following published articles

- Xu Qian, Luis G. Villa-Diaz, Ramya Kumar, Joerg Lahann, Paul H. Krebsbach,"Enhancement of the propagation of human embryonic stem cells by modifications in the gel architecture of PMEDSAH polymer coatings", *Biomaterials*, 2014, 35, (36), 9581-9590

- Ramya Kumar and Joerg Lahann, "Predictive Model for the Design of Zwitterionic Polymer Brushes: A Statistical Design of Experiments Approach", *ACS Applied Materials & Interfaces*, 2016, 8, (26), 16595-16603

Nanoindentation studies herein performed jointly with Salwan Butrus, undergraduate researcher.

5.1 Abstract

The performance of polymer interfaces in biology is governed by a wide spectrum of interfacial properties. With the ultimate goal of identifying design parameters for stem cell culture coatings, we developed a statistical model that describes the dependence of brush properties on surface-initiated polymerization (SIP) parameters. Employing a design of experiments (DOE) approach, we identified operating boundaries within which four gel architecture regimes can be realized, including a new regime of associated brushes in thin films. Our statistical model can accurately predict the brush thickness and the degree of intermolecular association of poly[{2-(methacryloyloxy) ethyl} dimethyl-(3-sulfopropyl) ammonium hydroxide] (PMEDSAH), a previously reported synthetic substrate for feeder-free and xeno-free culture of human embryonic stem cells. DOE-based multifunctional predictions offer a powerful quantitative framework for designing polymer interfaces. For example, model predictions can be used to decrease the critical thickness at which the wettability transition occurs by simply increasing the catalyst quantity from 1 mol% to 3 mol%.

5.2 Introduction

The performance of responsive polymer brushes[223–228], anti-fouling coatings[103], anti-microbial coatings[229,230], biosensor coatings[231], or substrates for regenerative medicine is defined by the subtle interplay of interfacial properties such as thickness, wettability, swelling ratio, friction coefficient, roughness or charge[11,227,232]. In the case of polymer brushes, these properties are readily modified by varying the brush composition, i.e., by choosing a suitable monomer, as well as by varying the brush architecture. Recent advances in controlled radical polymerization techniques (CRP), such as surface-initiated nitroxide-mediated polymeriza-

tion[65] (SI-NMP), surface-initiated reversible addition-fragmentation transfer[233,234] (SI-RAFT) polymerization and surface-initiated atom transfer radical polymerization[43] (SI-ATRP), have enabled the creation of tailored polymer brushes of desired architectures. CRP, when used to grow polymer brushes from substrate-bound initiators, has far-ranging possibilities, with a vast and steadily expanding library of monomers, initiator systems, substrate choices and polymer architectures[17,19,235]. Compared to other CRP techniques, SI-ATRP is compatible with a wider range of functional monomers, more tolerant of impurities and easier to access experimentally.

The selection of optimal SI-ATRP conditions is a critical element in polymer brush design, because the resultant brush properties are influenced by several experimental parameters and sometimes even combinations of SI-ATRP parameters[236,237]. The traditional iterative approach that relies on one-factor-at-a-time[238] optimization of polymerization recipe is inefficient and time-consuming. High-throughput combinatorial approaches[239] and computer-aided methods[240] for screening and optimizing solution ATRP conditions have been proposed, but it is unclear whether these will be effective when translated to SI-ATRP. A recent study tried to address this issue by developing a photonic microring resonator for real time monitoring[241] of brush growth, but data interpretation remains difficult.

Properties of polymer brushes prepared by surface-initiated polymerization (SIP) have been predicted using a combination of experimental investigations and mathematical models[242]. Kinetic modeling and simulations have been employed successfully to predict polymer film thickness as a function of time[243,244]. In predicting the kinetic trajectory for certain polymerization conditions, these studies have also provided mechanistic insights on the nature of initiation, chain transfer, propagation and termination[245] in SI-ATRP. However, the development of these mathematical models requires prior knowledge of the rate constants as well as ex-

perimental determination of the chain length distribution (CLD) of tethered polymer chains. Obtaining this information is usually not straightforward. Releasing tethered polymer chains from the substrate can introduce impurities and the severed polymers are not always obtained in a quantity that is sufficient for molecular weight determination using size exclusion chromatography (SEC)[246]. Precise experimental determination of rate constants neccessitates use of special methods, such as pulsed laser polymerization and electron paramagnetic resonance (EPR)[247,248], which can be difficult to implement. Sometimes, if the experimental estimates of rate constants are unavailable, they are iteratively determined so as to bring the model predictions in line with experimental results[242].

Non-idealities inherent to the SI-ATRP process further complicate the development of *ab initio* models. These include confinement effects caused by a high grafting density, gradients in monomer and catalyst concentration and mass transfer limitations[249]. In some cases, the catalysts and the monomer are not equally accessible to all growing chains, resulting a broader CLD for the surface-initiated process as compared to the highly monodisperse molecular weight distribution than is routinely obtained in a solution ATRP process[250,251]. Techniques such as Monte Carlo[252] and Gillespie Stochastic Simulation Algorithm (GSSA)[253,254] simulations that can account for these non-idealities require computationally expensive approaches. Finally, the predictive scope of these models is restricted to CLD alone and does not include other interfacial properties, such as surface charge or wettability.

Due to these limitations, developing a quantitative understanding of the dependence of polymer coating properties on SI-ATRP parameter design through stochastic methods and molecular modeling can be challenging. In contrast, we decided to develop an alternative modeling approach using statistical design of experiments (DOE).

Poly[{2-(methacryloyloxy) ethyl} dimethyl-(3-sulfopropyl) ammonium hydroxide] (PMEDSAH), a zwitterionic polymer brush, undergoes a hydrophilic to hydrophobic transition that is governed by brush-specific parameters (e.g., thickness and monodispersity) as well as kinetic features of the polymerization step (e.g., propagation rate during ATRP[255]).To create tailored polymer architectures and tunable CLD for PMEDSAH, surface-initiated atom transfer radical polymerization (SI-ATRP[256]) has been used[257]. For PMEDSAH brushes produced by SI-ATRP, Cheng et al.[255] found that thin brushes are usually unassociated and hydrophilic, whereas thick brushes may or may not produce self-associated hydrophobic brushes depending on the propagation rate. If the critical thickness for the hydrophilic-to-hydrophobic transition can be lowered, typically achieved by bringing about low propagation rates in SI-ATRP, unusually thin associated gel architectures can be realized[255].

PMEDSAH brushes have been identified as promising synthetic substrates for culturing human embryonic stem cells (hESCs) under feeder-free and xeno-free conditions[258]. PMEDSAH coatings can maintain hESC pluripotency in fully defined culture conditions during long-term expansion, thereby circumventing the drawbacks of animal-derived products[259]. Earlier, we reported that hESC proliferation rates are highly sensitive to differences in the gel architecture of PMEDSAH, with a coating possessing a moderate degree of self association favoring rapid stem cell self-renewal[260]. In Qian et al.[260], we concluded that the rate of stem cell self-renewal can be increased or decreased by modifying the gel architecture of PMEDSAH. Therefore, the architecture of PMEDSAH brushes is a key design parameter that exerts a substantial influence over the proliferation rate of hESCs cultured for tissue engineering applications. Our work was motivated by the need for a property prediction tool that could guide SI-ATRP parameter selection and enable access to PMEDSAH brushes possessing any desired architecture.

We anticipate that accurate prediction of SI-ATRP outcomes will aid the synthesis of PMEDSAH brushes with the optimal properties for facilitating rapid expansion of hESC populations.

In this paper, we report the development of a statistical model that successfully guided the SI-ATRP of PMEDSAH brushes of diverse architectures and functions, including a previously inaccessible polymer brush regime. This predictive model will be more effective in informing experimentalists about reaction conditions for obtaining polymer brushes with desired interfacial properties, compared to conventional trial-and-error approaches.

5.3 Experimental

5.3.1 Chemical vapor deposition polymerization of ATRP initiator

Using a previously described chemical vapor deposition (CVD) polymerization approach,[95] the initiator coatings were deposited on the substrates in the form of a thin film bearing bromoisobutyryl ester groups for subsequent ATRP initiation. Using Fourier-transformed infrared (FTIR) spectroscopy, two characteristic bands – the first at 1730 cm^{-1}, indicative of the C=O bond of the ester groups and the second band at 1160 cm^{-1}, which is characteristic of the C-O-C stretches, were used to confirm the chemical structure of the initiator.[95]

5.3.2 Experimental design for SI-ATRP

To conduct a systematic exploration of the experimental space of SI-ATRP, we used a general factorial design with the three design variables set at the levels summarized in Table 5.1. The design variables form the inputs to our statistical model and the responses (thickness and contact angle) are its outputs. It is important to note that these 45 combinations merely represent a systematic sampling of the

Table 5.1: Experimental space constructed for statistical model development. This general factorial design gave rise to 45 combinations (3*3*5). This statistical model, developed from a finite number of experimental runs, can predict the results of a larger superset of possible experiments within the range of SI-ATRP parameters studied.

Factor	Coding	Number of Levels	Units	Factor Levels Studied				
Cat. Qty [CuCl]:[Monomer]	A	3	Mol%	1%	2%	3%		
Cat. Ratio [CuCl]:[$CuCl_2$]	B	3	–	2.5	5	10		
Reaction time	C	5	hours	1	4	8	12	24

infinite combinations possible within the SI-ATRP parameter space. Each of the 45 experimental runs was performed twice. Once a satisfactory statistical model was obtained, it was not necessary to conduct further replicates (the supporting information section includes a description of the procedure used for model discrimination and selection of the best statistical model). By analyzing results from this small sample space, we can make predictions about any point in the entire experimental space, including those points about which we have no prior knowledge. The order of experimental runs was randomized to ensure independence of the data points. Experimental results from the systematic sampling were used to construct the statistical model. Other experimental variables, i.e., monomer concentration, solvent composition, ratio of ligand (2,2-bipyridyl) to total copper and reaction temperature were maintained constant throughout the study.

5.3.3 Procedure for SI-ATRP of MEDSAH

Unless otherwise specified, all the chemicals described in this section were purchased from Sigma Aldrich and used without further purification. The surface-initiated ATRP of [2-{(methacryloyloxy)ethyl}] dimethyl-(3-sulfopropyl) ammonium hydroxide (MEDSAH) (Monomer Polymer Dajac Labs, Trevose, PA) was conducted using the procedure detailed by Qian et al.[260] In brief, the ATRP reaction was allowed to proceed for the desired duration (1, 4, 8, 12, 24 hours) under argon atmo-

sphere at 22 °C. Upon completion, substrates were rinsed with 1% sodium chloride solution and deionized water and dried with a jet of nitrogen. The solvent ratio (methanol: water) and the concentration of monomer (0.4 g/ml) was maintained constant for all experiments whereas the molar ratio of copper (I) chloride to monomer and the molar ratio of copper (I) chloride and copper (II) chloride was varied across experiments according to the values specified in the experimental design (Table 5.1). The number of moles of 2,2 bipyridyl charged was maintained constant at twice the total number of moles of copper (I) chloride and copper (II) chloride.

5.3.4 Thickness measurements using ellipsometry

Ellipsometry was performed on silicon wafers (Silicon Valley Microelectronics, CA) with a native silicon dioxide layer of 2.5 nm thickness. Coating thickness was measured before and after ATRP with a nulling ellipsometer (EP3 Nanofilm, Accurion GmbH, Germany). Ellipsometric Δ and Ψ values were collected at a wavelength of 531.9 nm. Fixed values were used for the real (n=1.58) and imaginary (k=0) components of the refractive index of the polymer coatings. It should be noted that the refractive index of the initiator coating was very close to that of PMEDSAH. After ATRP was completed, the thickness of the PMEDSAH coating formed was calculated by subtracting the initial thickness of the initiator layer from the post-ATRP thickness. Three readings were collected for each substrate and two substrates were used for each experimental run.

5.3.5 Contact angle measurements

Static contact angles of deionized water were measured using a contact angle goniometer (Ramé-Hart 200-F1 goniometer). Measurements were taken at three different locations and averaged for each substrate. Two substrates were used per

experimental run.

5.3.6 Data analysis using analysis ofvariance

Analysis of variance (ANOVA) is a statistical inference tool that identifies significant causes of variation – main effects and interactions between experimental factors. ANOVA was performed for thickness and contact angle on Minitab (Minitab Inc, State College, PA) with a 5% level of significance. Model reduction was performed by selecting the significant factor effects identified from the regression ANOVA (Partial sum of squares - Type III) and discarding insignificant model terms. Regression analysis was performed using response surface reduced quadratic model on Design Expert 9 software (Stat-ease Inc, Minneapolis, MN).

5.3.7 Validation experiments

For every regime of gel architecture, the statistical model was verified by performing validation experiments and comparing their results to predictions. We selected validation points such that they did not overlap with the points used for statistical model construction. Four points were chosen in the design space so that each point would yield coatings belonging to each of the four regimes. All validation runs was replicated to be consistent with the experimental design (n=2). In total, eight validation experiments were performed to see whether the statistical model equations were successful in predicting thickness and contact angle in the four regimes identified. The point prediction tool of Design Expert 9 (Stat-ease Inc, Minneapolis, MN) was used to generate predictions.

5.4 Results and discussion

5.4.1 Effect of PMEDSAH gel architecture on physicochemical characteristics : Comparison of ζ-potential, roughness and nanomechanical properties

With the goal of identifying the causes and mechanisms behind the stark differences in hESC propagation rates between PMEDSAH brushes of varying gel architectures, we compared physicochemical properties. Briefly, we evaluated the ζ-potential, roughness, reduced Young's modulus and hardness of PMEDSAH brushes possessing different thicknesses and wettabilities. In Qian et al.[260], PMEDSAH polymer coatings were fabricated using two different surface-initiated polymerization procedures: UVO-initiated free radical polymerization (UVO-grafting) and surface-initiated atom transfer radical polymerization (SI-ATRP). With the latter, we could vary SI-ATRP parameters in order to independently control thicknesses and the strength of inter-chain associations. Because neither grafting density nor molecular weight distribution can be precisely controlled[256] in UVO-grafted films, the resulting polymer brush is likely to be thin, polydisperse and unassociated. In the unassociated state, ionic attractions between the sulphonate and the ammonium groups in the side chains are not dominant, allowing the polymer to be fully hydrated, resulting in a low contact angle. In contrast, ATRP coatings have a controllable and high grafting density that results in greater proximity of polymer chains and increased opportunities for short-range ionic interactions.

Previous studies suggest that maximal cell adhesion to metallic biomaterial surfaces are promoted by tuning the surface charge to fall within an optimal range[261]. This finding prompted us to examine the ζ-potential of the different PMEDSAH surfaces used in our hESC study[260], to verify whether differences in hESC behaviour could be explained by variations in ζ-potential .As seen in Figure 5.1(a), the ζ-potential of UVO-grafted PMEDSAH was less negative than ATRP coatings.

In addition, the 25 nm and 176 nm thick PMEDSAH coatings exhibited more negative charge than the 105 nm thick coating in the neutral range of pH values. However, we concluded that the surface charge differences did not explain the trends observed in hESC culture. Based on the surface charge, the UVO-initiated surface should offer the least electrostatic repulsion to the hESCs and possess the most favorable interfacial environment for hESC culture. However, this was not observed and the propagation rates observed on the UVO-initiated PMEDSAH brushes was much lower than the brushes prepared using SI-ATRP[260].

In several studies, engineering roughness into soft cell culture substrates in the form of nano-grooves and pillars has been shown to play a role in mediating cell adhesion[262]. Thus, the roughness of the four coatings possessing different thicknesses and hydrophilicities, was quantified with a topographical examination using atomic force microscopy (AFM). It has been shown that surfaces with a roughness of R_a around 1 nm, which are categorized as smooth, support hESCs growth better than nano-rough surfaces with a R_a of 75-150 nm[263]. Our AFM analyses of substrate roughness on all four surfaces (Figure 5.1(b)) showed a R_a lower than 1.5 nm and had no statistical differences among them, which suggested that all these surfaces could be considered smooth. We concluded that differences in hESC propagation and adhesion on PMEDSAH brushes could not be attributed to roughness effects. However, the roughness data confirms that the differences in wettability were caused by zwitterionic self-association alone and not induced by roughness differences.

Finally, we conducted nanoindentation studies using four groups of polymer brushes: thick and thin brushes with hydrophobic or hydrophilic properties. Prior work has indicated that surface rigidity and elasticity are influential parameters that can affect cell attachment, spreading, proliferation and differentiation[262]. The properties evaluated from our experiments were reduced Young's modulus (E_r),

which is a measure of deformability, and hardness (H), which is a measure of the relative resistance that the brush surface imposes against the penetration of a harder body. The data (shown in Figure 5.1(c) and Figure 5.1(d)) indicate that E_r and H were significantly higher for coatings with lower wettabilities. The thin hydrophobic brushes displayed higher E_r and H than the thick hydrophobic ones. We speculate that the contributions arising from the underlying stiff PPX-EB initiator coating (E_r=0.94 GPa, H=1.22) is much higher for the former (where the brush thickness is insufficient to insulate the PPX-EB contributions) than the latter (where thickness cushions the PPX-EB's influence).

Performing ANOVA for E_r and H (Figure 5.1(e)) , we concluded that thickness is the strongest contributing term for E, with higher thicknesses reducing the observed magnitudes of E_r and H. In contrast, higher contact angles led to increases in E_r and H values. We suspect that highly associated brushes are stiffer than less associated ones. The thickness-wettability interaction term also exhibiting a significant influence, suggesting that the nanomechanical behaviour is shaped by a complex interplay between thickness and wettability .We could draw three conclusions from the nanomechanical studies-: 1) A higher degree of electrostatically promoted inter-chain association between PMEDSAH brushes renders the surface stiffer and harder. 2) Synthesizing thicker brushes is an effective way to attain "softer" surfaces. 3) The ultimate values of E_r and H are shaped by both these competing effects of thickness and self-association as indicated by the interaction term.

We suggest that differences in E_r and H across polymer brushes can explain the cell behavior in Qian et al.[260]. Cells did not propagate as rapidly on the most hydrophobic brushes due its high level of zwitterionic self-association which in turn resulted in higher levels of stiffness and hardness. The cells also did not propagate as rapidly on the thin hydrophilic coating, because the environment

provided by the thin brush was likely too hard to maintain self-renewal, despite its hydrophilicity. Thus, cells preferred the moderately thick and moderately hydrophobic coatings as they likely had the optimal nanomechanical properties for rapid hESC propagation.

These results emphasized the importance of gel architecture of PMEDSAH brushes and motivated us to pursue a modeling based approach to achieving independent and simultaneous control over the wettability and thickness, thus enabling us to tune gel architecture precisely.

We hypothesized that a response surface methodology (RSM)[264,265] will enable determination of the SI-ATRP reaction parameters required to achieve a desired gel architecture. Although RSM is used widely in organic synthesis[266,267] to predict reaction outcomes, this study is, to the best of our knowledge, the first report of an RSM-based study of surface-initiated polymerization. The initial goal was to identify a quantitative relationship between the property space of PMEDSAH coatings and the vast experimental space accessible by SI-ATRP. We implemented a factorial design of experiments (Table 5.1) to sample the experimental space systematically and analyzed the roles of statistically significant main effects and interactions in determining thickness and wettability. The result was a predictive model that described thickness and contact angle as a function of (i) catalyst quantity, (ii) ratio of activator Cu^{I} to deactivator Cu^{II} species and (iii) reaction time. After a validation phase, the statistical model was employed to guide the synthesis of thin associated brushes, a gel architecture that was discovered to be limited to a narrow experimental region.

5.4.2 Comparing the impact of design variables on thickness and contact angle

After completing 90 experimental runs (Table 5.1), the next step was to perform a statistical analysis of the results in order to identify the most significant sources

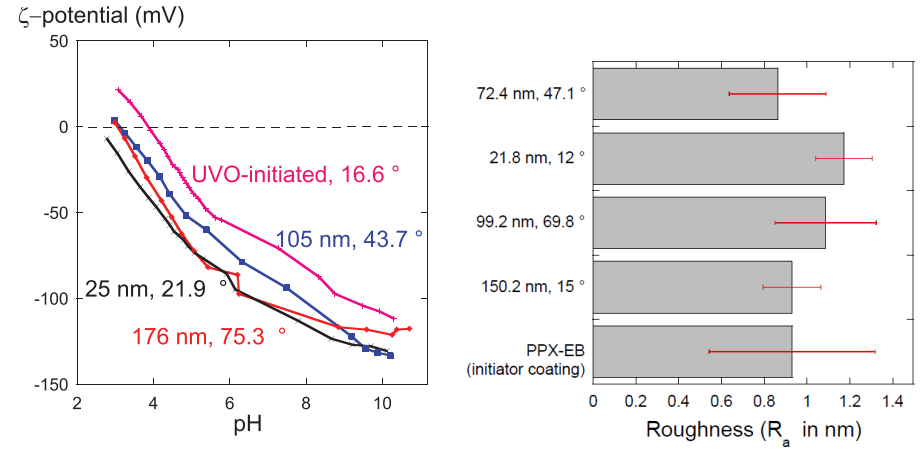

(a) (b)

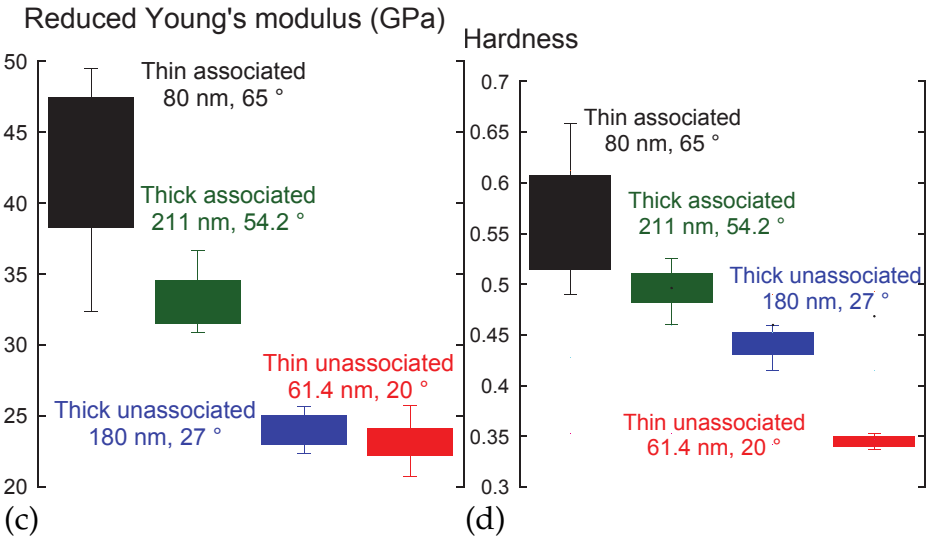

(c) (d)

Source of Variation	Sum of Squares	Degrees of Freedom	Mean Square	F_0	P-value
Thickness	582, 0.036	1	582, 0.036	163.32, 67.8	<0.0001
Contact Angle	329.5, 0.011	1	329.5, 0.011	92.5, 20.9	<0.0001
Interaction	338.3, 0.069	1	338.3, 0.069	94.9, 128.2	<0.0001
Error	85.53, 0.0128	24	3.6, 0.0054		
Total	2107, 0.217	27			

(e)

Figure 5.1: (a) ζ-potential variations as a function of brush thickness and wettability. (b) Roughness is about the same on all surfaces irrespective of thickness and water contact angle. (c) & (d) Nanomechanical properties (data collection: Salwan Butrus), E_r (reduced Young's Modulus) and H (hardness) depend on degree of association as well as thickness. (e) ANOVA for E_r and H respectively where F-values are separated by commas. For E_r, thickness has the most impact, followed by the interaction term and contact angle. For H, the interaction termis most significant, followed by the thickness and contact angle

of variation and thereby understand the roles of the three experimental variables on thickness and contact angle. We thus completed two sets of ANOVA analysis for thickness and contact angle. ANOVA yields F-ratios, which forms the basis for rank-ordering main effects and understanding their relative importance. Apart from quantifying the impact of the three main effects on each response, ANOVA is well-suited to identifying statistically significant two-factor and three-factor interactions. In Table 5.2, polymer brush thickness is found to be significantly influenced by all parameters studied (all p-values are below 10^{-3}). The ANOVA analy-

Table 5.2: Summary of ANOVA results for thickness. The tabulated values of the F-test statistic help identifying the principal sources of variation in thickness, with higher F-ratios implying a greater contribution.Here, catalyst ratio and reaction time are the two most significant factors.

Source of Variation	Sum of Squares	Degrees of Freedom	Mean Square	F_0	P-value
Cat. Qty (A)	1536.0	2	768.0	15.6	$<10^{-3}$
Cat. Ratio (B)	19489.2	2	9744.6	198.1	$<10^{-3}$
Time (C)	57124.6	4	14281.2	290.4	$<10^{-3}$
AB	4260.8	4	1065.2	21.6	$<10^{-3}$
AC	1946.8	8	243.4	4.9	$<10^{-3}$
BC	3432.7	8	429.0	8.7	$<10^{-3}$
ABC	6623.0	16	413.9	8.4	$<10^{-3}$
Error	2212.9	45	49.2		
Total	96626.1	89	1085.7		

sis identifies reaction time, followed by catalyst ratio, as the lead parameters with the highest impact. In the range of catalyst quantity studied (1-3 mol%), thickness does not appear to be particularly sensitive to catalyst quantity. However, catalyst quantity has a strong interaction (AB) with catalyst ratio. In contrast, the ANOVA analysis for contact angle (Table 5.3) presents a completely different picture, with catalyst quantity identified as the clearly dominant factor. The higher the quantity of catalyst, the more hydrophobic are the resulting coatings. Interestingly, catalyst quantity was even more relevant than reaction time, which also favored higher contact angles. Catalyst ratio, however, only marginally influences contact angle, a

finding that contrasts with the strong effect of catalyst ratio on thickness. Among the interaction terms, the interaction between reaction time and catalyst quantity is most significant (AC).

Table 5.3: Summary of ANOVA analysis for contact angles. Unlike in the film thickness model, the catalyst quantity dominates the statistical model for contact angles. Reaction time is prominent both, as a stand-alone effect and because of its interaction with catalyst quantity.

Source of Variation	Sum of Squares	Degrees of Freedom	Mean Square	F_0	P-value
Cat. Qty (A)	7195.9	2	3598.0	90.9	$<10^{-3}$
Cat. Ratio (B)	1511.0	2	755.5	19.1	$<10^{-3}$
Time (C)	10826.4	4	2706.6	68.4	$<10^{-3}$
AB	939.3	4	234.8	5.9	0.001
AC	5092.2	8	636.5	16.1	$<10^{-3}$
BC	1289.3	8	161.2	4.1	0.001
ABC	1151.7	16	72.0	1.8	0.059
Error	1781.8	45	39.6		
Total	29787.6	89	3598.0		

Predictive models for thickness and contact angle were constructed using regression analysis, as described in sections 4 and 5 of the supporting information section. Two equations, each describing thickness and contact angle as functions of significant model terms, were obtained. These include main effects and interaction terms. The statistical model equations are depicted graphically in the form of response surface plots as shown in Figure 5.2. These 3D surface plots are complete representations of the effects of all three experimental variables and their interactions.

5.4.3 Prediction of four regimes of gel architecture

The contact angle and thickness results obtained from the 90 experimental runs were plotted in the form of a scatter plot (Figure 5.3(a)) and then segmented into four quadrants (Figure 5.3(b)), as described below. The thickness ranged from 2.5 nm to 140.5 nm. Coatings thicker than 70 nm (median value) were classified

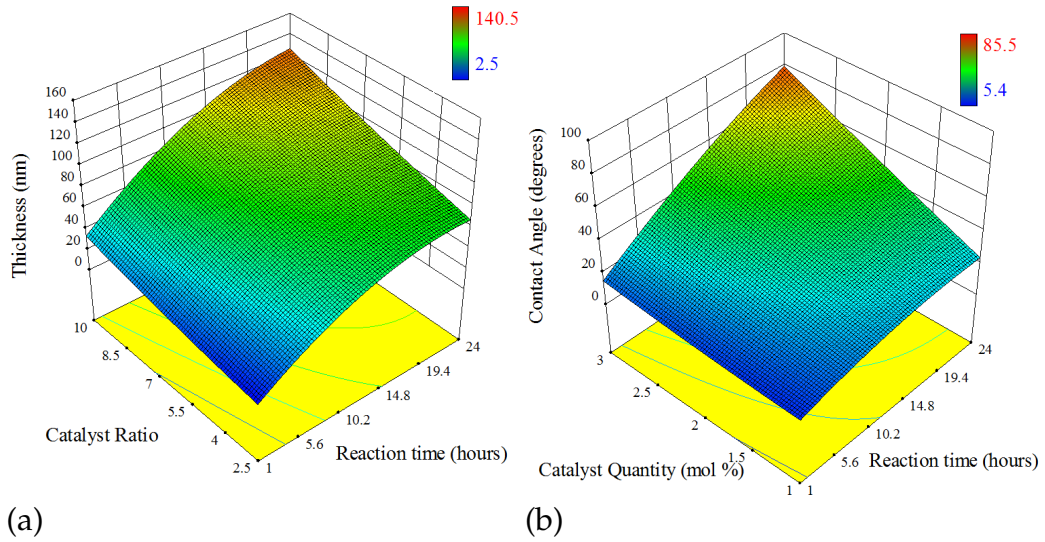

Figure 5.2: (a)Three-dimensional surface plot predicting film thickness as a function of catalyst ratio and reaction time at 1.5 mol% catalyst quantity. The statistical model that this plot represents, can predict thickness across all possible experiments that can be performed within the studied range. (b) Three-dimensional surface plot predicting film contact angle as a function of catalyst quantity and reaction time at a catalyst ratio of 9.

as thick and those below 70 nm were denoted thin. For segmenting contact angle data, we have to consider zwitterionic self-association[255,268–270] of PMEDSAH, which causes an increase in contact angle in proportion to the degree of self-association. Consistent with previous studies[255,269], contact angles less than 30° were considered to belong to the hydrophilic and unassociated regime, those greater than 30° fall within the self-associated regime[255,269]. Therefore, the data can be grouped into four regimes: thick associated, thick unassociated, thin unassociated and thin associated.

From the scatter plot in Figure 5.3(a), we deduced that there exists a weak overall correlation (R^2 = 0.514) between contact angle and thickness. In the thick associated regime and the thin unassociated regime alone, where the thickness-dependent behavior of contact angle is evident, the correlation between the hydrophobicity of the coatings and its thickness is very strong. However, if we consider the data points in the thick unassociated regime and the thin associated

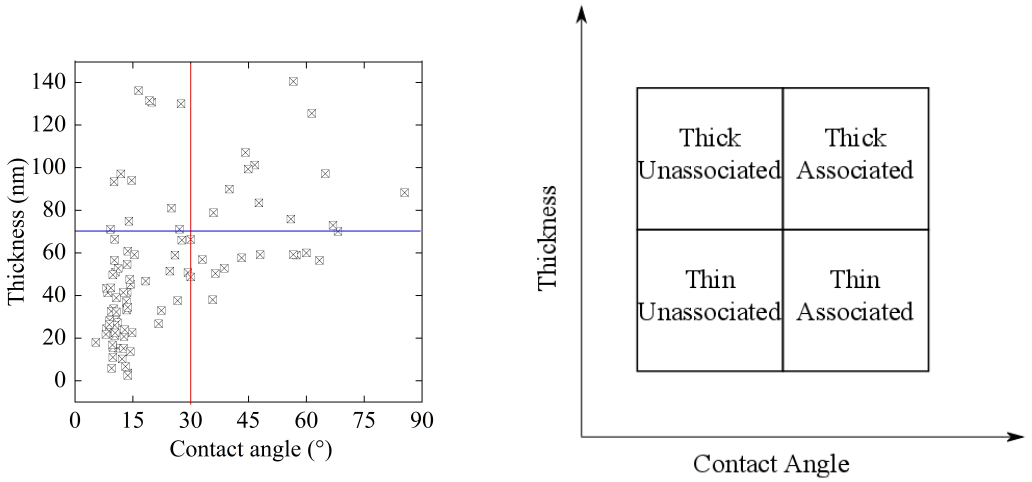

(a) (b)

Figure 5.3: (a) Scatter plot of thickness versus contact angle. The data were classified into four regimes by setting boundaries of 70 nm (horizontal blue line) for thickness and 30°(vertical red line) for contact angle. (b) Quadrants representing four regimes of gel architecture, as identified from the scatter plot.

regime alone, this correlation does not hold and thickness and contact angle are independent of each other. Based on this analysis, it appears that the relationship between PMEDSAH's thickness and its degree of self-association is regime-dependent and complex.

5.4.4 Assessment and validation of the predictive character of the statistical model

By simultaneously solving model equations for thickness and contact angle, it should be possible to experimentally access arbitrary combinations of contact angle and thickness, thereby realizing the desired gel architecture. As an example, if we wish to synthesize a thin associated brush architecture with a target thickness of 70 nm and a target contact angle of 45°, we would have to employ the following ATRP conditions: catalyst quantity of 3 mol%, catalyst ratio of 9 and a reaction time of 10 hours, as suggested by the simultaneous solution of thickness and contact

angle model equations. In Figure 5.4, experimental values were plotted against predicted values for each regime. We found that the experimental results correlate well with statistical model predictions in all four regimes.

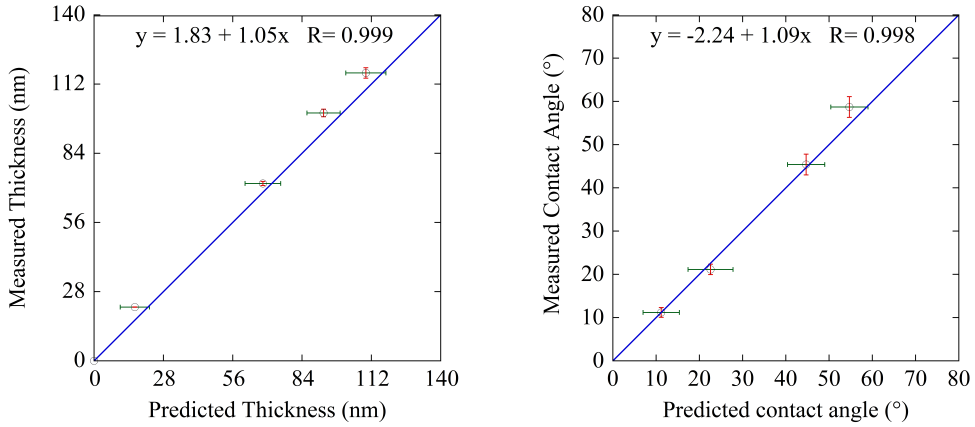

(a) (b)

Figure 5.4: Comparison of experimental and predicted values (hollow circles) for (a) thickness and (b) contact angle. Horizontal error bars in green indicate 95% confidence interval of the statistical model prediction while vertical error bars in red represent standard deviation of experimental measurement. The blue line is a reference representing an ideal agreement between predicted and measured values (y=x).

5.4.5 Identifying a design space for the thin associated regime

In Figure 5.3(a), we observed prominent differences of the population density in the four regimes, with the thin unassociated regime being the most densely populated and the thick unassociated and the thin associated regimes the most sparsely populated. This suggests that the thin unassociated regime is the easiest brush architecture to obtain experimentally, whereas it is feasible to obtain the thick unassociated and the thin associated regimes only within narrow regions. This observation raises the following question: Can our statistical model identify experimental boundaries, within which a given gel architecture can be obtained

reliably? If so, does this hold even for atypical brushes such as thin and associated brushes? In Figure 5.5, regions of experimental viability predicted for thin associated brushes have been represented graphically. Model equations for contact angle and thickness were solved simultaneously to yield a design space where thickness will be 70 nm or less and contact angle 30° or greater. At a catalyst concentration of 1.5 mol% and below, no solution exists, indicating that it is unfeasible to produce thin associated brushes at low catalyst concentrations. As we increase the catalyst quantity to 2 mol% and higher, the solution space widens, attaining a maximum area at 3 mol% catalyst quantity.

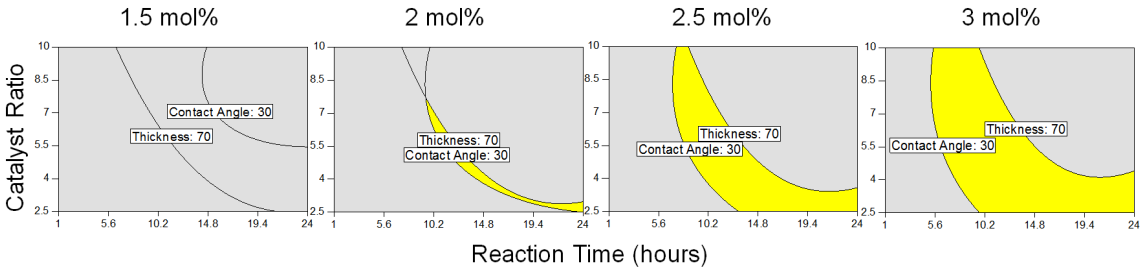

Figure 5.5: Design space for thin associated brushes across different catalyst quantities (in mol%). The yellow regions represent the experimental boundaries within which it is possible to obtain coatings belonging to this regime of gel architecture. The design space was obtained by simultaneous solution of statistical model equations to yield operating conditions which will lead to thickness less than 70 nm and contact angle greater than 30°. These plots show how the experimentally accessible space becomes larger with increasing catalyst quantity.

5.4.6 Reaction time and catalyst ratio dominate film thickness

From the ANOVA analysis, we established that all three main effects (reaction time, catalyst quantity and catalyst ratio) were significant in determining thickness. The individual impact of each effect can be pictured as protagonistic or antagonistic depending on whether the slope of the plot in Figure 5.6 is positive or negative. Reaction time had the highest slope, with thickness growing linearly with increasing reaction time. With time, more monomer is added to the grow-

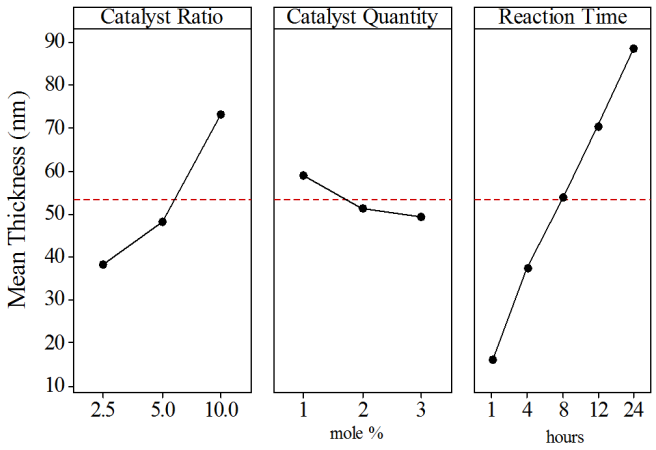

Figure 5.6: Main effects on thickness. From left to right, the effects of catalyst ratio, catalyst quantity and reaction time on thickness are plotted. The red dotted line refers to the location of the overall mean thickness (53.4 nm) of all 90 data points. By comparing slopes, we can see that reaction time and catalyst ratio have the strongest effects on thickness. The effect of catalyst quantity is less pronounced.

ing PMEDSAH chain, resulting in a linear increase of thickness with time. The rate of increase of thickness with time is controlled by the catalyst ratio. Increasing the initial quantity of the activating Cu^{I} relative to the deactivating Cu^{II} will affect the equilibrium position of the activation-deactivation step[271]. Thus for the same reaction time, thicker coatings are obtained for a higher ratio of Cu^{I} to Cu^{II}. The effect of catalyst quantity on thickness, though statistically significant (Table 5.2), was less pronounced and had the lowest F-ratio among the three main effects. Unlike the other two effects, it was observed to have an antagonistic effect on thickness, with a slight decrease in thickness observed upon increasing catalyst quantity (Figure 5.6). According to SI-ATRP kinetic models, the time-evolution of chain length distribution is expected to depend only on the catalyst ratio and not on the catalyst quantity. The migration-termination hypothesis[245] has explained the departure of these experimental trends from SI-ATRP kinetic models. Among two-factor interaction terms, the interaction AB between catalyst quantity and catalyst ratio was the most relevant (Table 5.2, AB interaction, p-value less than 0.001). Figure 5.7 indicates that the sensitivity of thickness to catalyst ratio is lowered, when a high

catalyst quantity is employed, whereas thickness is highly correlated with catalyst ratio at low levels of catalyst quantity. Interestingly, the interdependence of catalyst quantity and catalyst ratio suggests that they operate in tandem rather than independently.

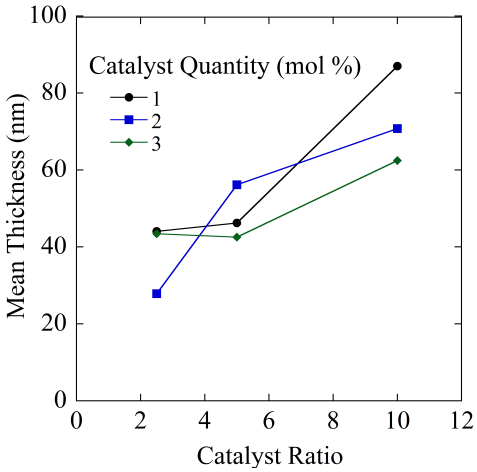

Figure 5.7: Interaction plot for thickness. The increase of thickness with catalyst ratio is dependent on the catalyst quantity.

5.4.7 Hydrophilic-to-hydrophobic transition is controlled by catalyst quantity

The four regimes of gel architecture differ clearly in the degree of correlation between thickness and contact angle, with high correlation in the thick associated and thin unassociated regimes and none in the thick unassociated and thin associated regimes. In spite of possessing a lower mean brush thickness than the thick associated regime, the polymer brushes in the thin associated regime still exhibit a high degree of association, with contact angles comparable to those of the thick associated regime. Secondly, although thick unassociated brushes are much thicker than thin unassociated brushes, they remain unassociated and are as hydrophilic as those in the thin unassociated regime. This anomalous behavior of brushes belonging to the thick unassociated and thin associated regimes indicates that a high thickness is not a necessary condition for forming association in zwitterionic poly-

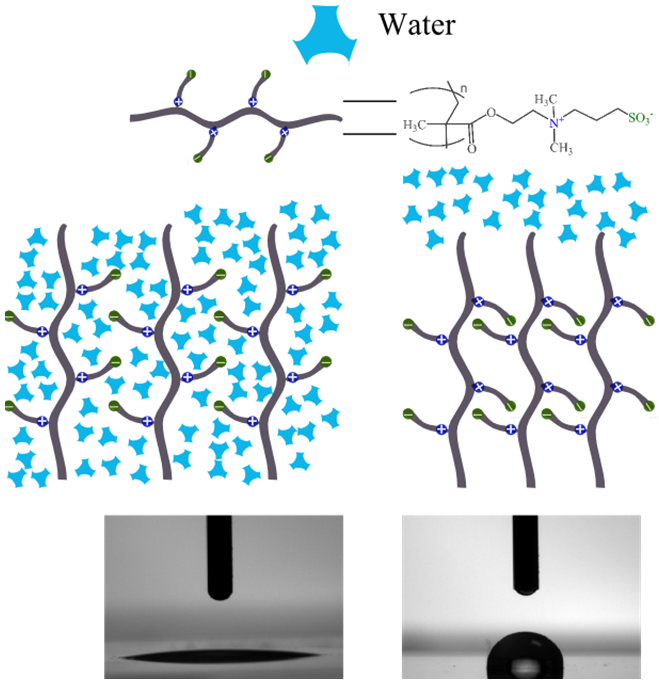

Figure 5.8: Wettability transition of PMEDSAH from hydrophilic to hydrophobic. The schematic represents the architecture of a PMEDSAH brush and its interaction with water when it is unassociated and when it undergoes hydrophobic collapse due to zwitterionic self-association. Images of representative water droplets illustrate the wettability differences.

mer brushes. It is well established that PMEDSAH undergoes a transition from its original hydrophilic state to a hydrophobic brush as a consequence of zwitterionic self-association[269,270,272]. Water is excluded from the brush due to the formation of inter-chain and intra-chain association between the quaternary ammonium cation and sulfonate anion of adjacent side chains[255] (Figure 5.8). Thicker brushes are likely to have increased chain association and thus exclude more water from the brush, explaining the increase of contact angle with reaction time. What is surprising is that the catalyst quantity variable, which had only a slightly negative effect on thickness, is the most powerful factor in the contact angle model. Considering the slopes of the main effects plots for contact angle (Figure 5.9) and thickness (Figure 5.6), catalyst quantity has a positive slope in Figure 5.9, whereas it has a negative slope in Figure 5.6. Moreover, catalyst quantity is highly influential not

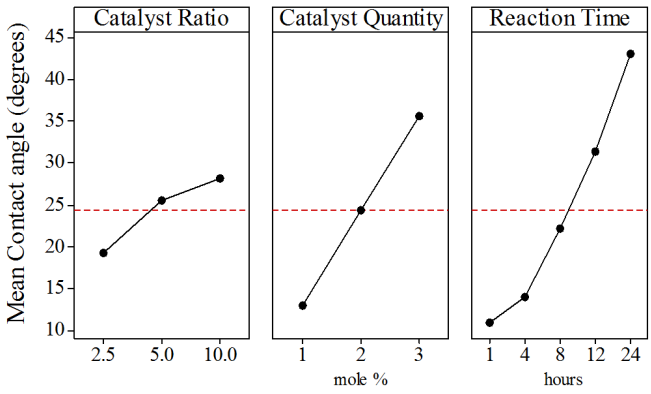

Figure 5.9: Main effects on contact angle. From left to right, the effects of catalyst ratio, catalyst quantity and reaction time on contact angle are plotted. The red dotted line refers to the overall average contact angle (24°) of all 90 data points. From the slopes, we can conclude that catalyst quantity and reaction time exert the most prominent effect on contact angle.

only as a standalone effect, but also in its interaction with reaction time, which has the highest F-ratio among all interaction terms in the contact angle model. The interaction plot for contact angle is shown in Figure 5.10, where the contact angle increases rapidly with reaction time at high catalyst quantity, whereas it remains unaffected by reaction time at low catalyst quantity. Therefore the sensitivity of contact angle to reaction time is governed by the level of catalyst quantity employed. In order to understand these findings, it is helpful to refer to the study performed by Cheng et al.[255] The authors noted that the self-association of PMEDSAH is driven by two factors: the thickness of the brush as well as the monodispersity of the CLD. In a monodisperse brush, the critical thickness required to trigger self-association is lower than it would be for a polydisperse brush. Exploring only 6 combinations of catalyst quantity and catalyst ratio, Cheng et al.[255] reported that that decreasing the ratio of activator to deactivator (Cu^{I}:Cu^{II}) would reduce the critical thickness by improving monodispersity. However, this study not explored the effects of catalyst quantity as exhaustively and systematically. From our statistical models, we established that catalyst ratio, albeit an important determinant of thickness, has only a marginal role in determining contact angle. Hence we pro-

pose that the critical thickness at which zwitterionic association causes wettability changes is controlled by catalyst quantity and not by catalyst ratio.

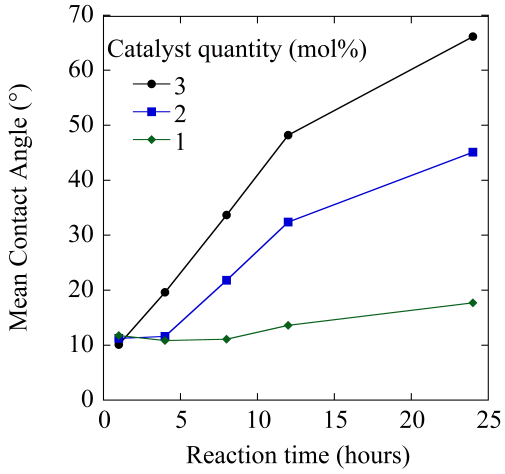

Figure 5.10: Interaction plot for contact angle. The level of catalyst quantity employed determines the dependence of contact angle on reaction time. At a higher catalyst quantity, the contact angle becomes more dependent on reaction time.

5.4.8 Physical validity of the statistical model and potential uses for hESC culture.

In all four validation tests, the experimental results for thickness and contact angle were within the predicted range. Therefore, this statistical model can be considered a valid mathematical representation of the SI-ATRP process and employed as a predictive tool to obtain PMEDSAH coatings of the desired gel architecture. In Qian et al. [260], we reported that PMEDSAH's capacity for facilitating hESC self-renewal could be tuned by modifying the gel architecture. We had studied three coatings: two belonging to the thick associated regime and one to the thin unassociated regime. Even though they all had similar surface charge and roughness, the thick associated coating with a moderate degree of association was found to have higher hESC propagation rates. Using the predictive tool established in this paper, we can now access coatings from the yet unevaluated thick unassociated

and thin associated regimes, perform hESC culture studies using these coatings, and discover whether higher or lower rates of hESC expansion result.

5.5 Conclusions

We quantified the dependence of brush thickness and wettability on key SI-ATRP parameters by constructing and validating a statistical model that simultaneously predicted the thickness-time trajectory as well as the degree of zwitterionic self-association. Our model indicates that we can reduce the critical thickness at which self-association triggers wettability changes by increasing the catalyst quantity. This provides reliable polymerization conditions to synthesize coatings with unusual gel architectures, such as thin associated brushes. Since our model is constructed from empirical results of systematically designed experiments, we did not require any simplifying assumptions. Moreover, as a property prediction tool, DOE, unlike *ab initio* modeling, can be used to model a range of coating properties. We further developed a quantitative relationship between the properties of PMEDSAH brushes and SI-ATRP parameters. This predictive tool provides on-demand access to PMEDSAH brushes for four regimes of gel architecture. Since our modeling approach can predict the outcomes of SIP accurately, it can be extended to other SIP systems to discover, design and identify unusual combinations of polymer brush attributes.

CHAPTER VI

α-mannose Functional Polymer Brushes Promote Selective Adhesion of Pro-Regenerative M2 Macrophages

The following chapter has been adapted from the following manuscript in preparation.

Ramya Kumar, Nahal Habibi, Amber de Groot, Domenic Kratzer, Irina Kopyeva, Kenneth Pienta, and Joerg Lahann,"α-Mannose Functional Polymer Brushes Promote Selective Adhesion of Pro-Regenerative M2 Macrophages"

6.1 Abstract

Dysregulated macrophage polarization has been implicated in many disorders such as diabetes, resulting in severe consequences such as chronic non-healing wounds. In order to accelerate healing and achieve wound closure, the population imbalance between pro-inflammatory M1 macrophages, and pro-repair M2 macrophages needs to be remedied. In this contribution, we describe a coating which promotes the selective adhesion of M2 macrophages while resisting the attachment of M1 macrophages. We synthesized polymer coatings decorated with mannose molecules, either in the form of monolayers or as polymer brushes with

pendant glycan side chains. Initially the interactions of these surfaces with a model lectin was probed in order to assess its bioactivity. We discovered that the architecture of the glycans was as important as its stereochemistry, since poor lectin binding was observed on the mannose monolayers. This agreed with the predictions of thermodynamic models, which were developed to understand multivalency effects. Thereafter, we examined the adhesion of macrophages in two parallel studies. In one study, we employed primary macrophages derived from blood donors, and in the other we derived M1 and M2 macrophages from a monocyte cell line. In both cases, we observed selective binding of M2 macrophages on the mannose surfaces, which was promoted by the upregulation of mannose-binding CD206 receptors on the M2 cells compared to the M1 cells. We concluded that cell-based wound-healing constructs coated with mannose could be a promising therapeutic strategy to administer M2 macrophages.

6.2 Introduction

Type-2 diabetes is a chronic disease that has assumed epidemic proportions, affecting one in eleven people in the world.[273] Among all the causes of diabetes-related morbidity and mortality, chronic non-healing wounds are particularly pernicious. Often taking the form of foot ulcers, these wounds carry high risks of sepsis and consequent lower limb amputation, resulting in costs upwards of $116 billion in the US alone.[273] It is believed that the normal progression of wound healing is compromised in diabetes patients due to dysfunctional macrophage activation, leading to the persistence of a chronic inflammatory state and delays in healing.[274] Though cell-based therapeutics hold the promise of mitigating inflammation by delivering pro-regenerative macrophages to the wound, they need to be supported by the development of biomaterials that ensure efficacious wound closure.[275] In this contribution we present a coating composed of α-mannose-functionalized poly-

mer brushes that can selectively adhere to macrophages possessing a pro-regenerative phenotype, while resisting the adhesion of pro-inflammatory macrophages. Due to its ability to capture pro-regenerative macrophages with high phenotypic selectivity, these polymer brushes can be easily grafted from wound healing mats and dressings to accelerate healing in diabetic individuals.

In the early phase of wound healing, classically activated macrophages (M1 Mps) infiltrate the wound site and trigger host defense mechanisms by initiating inflammatory responses and removing damaged tissue debris through phagocytosis.[276] In contrast, during the later stages of healing, M1 Mps make way for alternatively activated (M2 Mps) macrophages, which resolve inflammation and remodel tissue, eventually promoting wound repair.[277] Unlike in healthy individuals, the regulation of macrophage polarization states and the maintenance of the optimal population balance between pro-inflammatory M1 Mps and the pro-healing M2 Mps (M1/M2 ratio) is severely impaired in diabetics.[278] Though inflammation is necessary in the early stages of wound healing, a failure to resolve this initial inflammatory burst stalls the healing process.[279] Delays and defects in the phenotypic transition from M1 to M2 results in a high M1/M2 ratio and prolonged inflammatory responses, ultimately delaying tissue regeneration in diabetic wounds.[280]

To control macrophage behaviour *in vivo*, specifically to address this M1/M2 imbalance, three classes of therapeutic strategies have been proposed : a) Sequential injection of chemoattractant proteins and cytokines to recruit and polarize endogenous macrophages towards the required phenotype.[281,282] b) Micro and nanoparticles decorated with macrophage-targeting ligands, that undergo phagocytosis and subsequently induce the desired macrophage response.[283] c) Administration of *in vitro* polarized M2 Mps at the wound site.[284]

The first strategy relies on identifying the modulators of macrophage polariza-

tion and then releasing these molecules in a timed manner in order to reprogram the wound environment and mitigate inflammation. In theory, if we engineer a therapeutic that switches macrophage polarization on demand, it is possible to either promote inflammation or tissue repair responses. In reality, the extracellular milieu of wounds is a complex and dynamic soup of signaling cues, where several stimuli act simultaneously upon unpolarized macrophages, across different time intervals and spatial locations.[285] Analyzing the relative contributions of these disparate stimuli on polarization fate is challenging. Hence the underlying cellular pathways dictating macrophage activation and phenotypic switching are yet to be understood completely.[286] Therefore, a cytokine-based strategy is not viable until a sufficiently advanced understanding of macrophage responses to these signals is obtained.

Though the use of micro and nanoparticles holds great therapeutic potential in targeting macrophages, particle uptake by macrophages is highly sensitive to surface charge, particle size, particle geometry, hydrophobicity and surface chemistry.[287,288] In order to be approved for clinical use, this multi-dimensional particle design space has to be thoroughly investigated in order to achieve consistently reproducible levels of safety and therapeutic efficacy. However, this a highly complex and time-consuming endeavor, rendered more challenging by the polydispersity in the micro and nanoparticle design space.[289]

Another promising approach is the direct administration of M2 Mps that have been polarized *in vitro*, at the site of the chronic wound. Typically, M2 Mp based cell therapy has employed direct injection of the M2 Mps at the wound site, with contradictory results on healing time.[284] These conflicting results may be explained by the timing of M2 administration, which appears to be a critical variable determining the success of M2 administration.[284] If the M2 Mps are introduced too early in the inflammatory phase of the healing cycle, wound healing is compromised as

the M2 Mps interfere with the initial acute inflammatory response that is essential to ward off infections. On the other hand, if the M2 Mps are applied too late, then the inflammatory response becomes so persistent that healing becomes compromised. Therefore, there is a dire need for research that focuses on optimizing both the timing and the mode of cell delivery during M2 macrophage administration.

From a biomaterials standpoint, it would be highly desirable to develop therapeutic alternatives to the practice of directly Mp injection. When M2 Mps were injected exogenously, without using a scaffold or a hydrogel, poor localization was observed at the wound bed after 3-4 days.[284] Engineering scaffolds, whose surfaces have been functionalized to support a high density of phenotypically well-characterized M2 macrophages, may resolve this issue. We hypothesize that the surface modification of wound healing constructs using polymer brushes will create a bioactive wound-material interface that promotes the persistence of M2 Mps at the wound site and ultimately tissue remodeling and re-epithelialization.

In this paper, we propose a surface modification strategy based on polymer brushes bearing pendant α-mannose groups to promote phenotype-specific adhesion of Mps on wound dressing materials. We rely on differences in the expression of the macrophage mannose receptor (MMR or the CD206 receptor) between the M1 and M2 populations[290] in order to selectively capture M2 Mps. Since the CD206/MMR receptor is upregulated in M2 Mps, many drug and siRNA delivery platforms have targeted this receptor to bring about CD206/MMR-mediated macrophage uptake of nanoparticles for varied applications. These include targeting tumor associated macrophages in prostate cancer, gene silencing, overcoming multi-drug resistance, management and diagnosis of infectious diseases.[291] We suggest that the overexpression of the CD206/MMR on M2 Mps compared to M1 Mps makes it a very attractive target, not just for drug-loaded and siRNA-loaded nanoparticles, but also for modifying biomaterial surfaces to promote wound heal-

ing.

In the case of polymeric drug carriers such as nanoparticles, this is typically accomplished by covalently conjugating the α-mannose ligand via a variety of click chemistry strategies, resulting in a monolayer of α-mannose molecules tethered rigidly to the surface.[292–294]. In other reports, polymers were modified with mannose through post-polymerization processes and then these block copolymers underwent self-assembly into glyconanoparticles of diverse architectures. Recent studies[295 295] verified that the spatial presentation of the mannose ligand plays a decisive role in determining how strongly the ligand-decorated substrate binds to the CD206 receptor. Structural investigations of the CD206-mannose interaction reveal that not only is the stereochemistry and conformation of the ligand critical, but also the density of mannose molecules presented.[296] CD206 is a transmembrane receptor that possesses eight mannose recognition domains on its surface, allowing each receptor to interact simultaneously with eight copies of the mannose ligand, thereby strengthening the interaction through the "glycocluster" or "multivalency" effects. Though the interaction between mannose and CD206 possesses high specificity, the affinity between the receptor and the monovalent carbohydrate ligand is low (around 10^{-7} M^{-1}).[297] We posit that a multivalent presentation of mannose ligands is required to achieve binding avidity strong enough to create a densely adherent layer of M2 Mps on our coating. It is unclear whether the inflexible monolayer topology is optimal for enhancing the avidity of the CD206-mannose interaction. On the other hand, densely grafted and flexible glycopolymer brushes wherein all the glycopolymer chains are maintained in an extended conformation would be the ideal polymer architecture for designing coatings to maximize surface-macrophage interactions and ultimately the adhesion of M2 Mps. Therefore, instead of organizing the mannose ligands in the form of a monolayer, we decided to exploit the glycocluster effect by developing polymer brush coatings

bearing pendant α-mannose side chains.

Research involving polymer brushes functionalized with carbohydrate residues has hitherto focused on their application as glycocalyx-mimetic interfaces that can achieve near-zero levels of non-specific protein adsorption.[298] Their exceptional performance as non fouling surfaces has led to their extensive use as hemocompatible coatings on catheters and other biomedical implants.[299] Surprisingly, the specific interactions of these brushes with carbohydrate-binding proteins present on cell surfaces has received sparse attention in comparison. A few studies have exploited these affinity-based interactions to develop label-free biosensors that can selectively capture several sub-types of influenza viruses and bacterial strains such as *E.Coli*, *S.Aureus* and *P.Aeruginosa*, that express carbohydrate-binding receptors. Other applications of carbohydrate brushes include glycan-based microarrays that serve as high-throughput screening platforms and in protein purification, particularly in affinity chromatography and membrane separation processes.[300,301] We could only find one report where polymer brushes were employed to selectively capture a specific cell type- hepatocellular carcinoma cancer cells (HepG2) were grown on galactose-functional polymer brushes by engineering specific interactions between galactose and the hepatic asialoglycoprotein receptors (ASGPR).[302]

In this study we engineer a surface modification strategy for the selective isolation of M2 Mps, thereby paving the way for bioactive wound healing constructs. Specifically, we evaluate the effect of carbohydrate stereochemistry as well as architecture on the ability of carbohydrate-functionalized surfaces to bind to M2 Mps. We synthesized and characterized four sets of surfaces– α-mannose and β-glucose in the form of polymer brushes and monolayers. We employed surface-initiated atom transfer radical polymerization (SI-ATRP) to graft the carbohydrate-functional monomers from a parylene-based SI-ATRP initiator coating. This vapor-deposited SI-ATRP initiator coating, apart from being biocompatible, is also sub-

strate independent and can be applied to virtually any surface including wound dressing materials.

Initial studies performed with *Concanavalin A* or Con A, a mannose-binding lectin, revealed that Con A binding was dependent on both the stereochemistry as well as the architecture of the carbohydrate-functional surfaces. In contrast, the M2 Mps, despite preferring α-mannose to β-glucose surfaces, was insensitive to the spatial presentation of the carbohydrate residues. We were able to explain these results using thermodynamic calculations of the free energy of carbohydrate-protein associations in both binding configurations, monolayers and brushes.

Our study demonstrates the potential of coating wound dressing surfaces with α-mannose polymer brushes to support the selective adhesion of M2 Mps. We suggest that this strategy is a promising alternative to the manipulation and modulation of of macrophage behaviour *in vivo* by use of cytokines and cytokine-loaded particles. Overall, our coating lends itself very well to both fundamental biological studies of macrophage function as well as clinical investigations of macrophage-based wound healing therapeutics. Future work will employ α-mannose coated wound healing mats and meshes in *in vivo* studies, where the timing of M2 Mps delivery and the macrophage density will be investigated.

6.3 Experimental

All chemicals were purchased from Sigma Aldrich unless otherwise mentioned.

6.3.1 Chemical vapor deposition polymerization

Following the procedure outlined in Nandivada et al.[92], ethynyl[2,2]paracyclophane was sublimed at 100 °C and then pyrolysed at 660 °C under a pressure of 0.3 bar. The radical species entered the deposition chamber from the pyrolysis

chamber and then adsorbed to the cooled substrates (15 °C). Coatings composed of poly(4-ethynyl-*p*-xylylene-*co*-*p*-xylylene) (PPX-alkyne) were obtained upon polymerization. For preparing poly[(*p*-xylylene-4-methyl-2-bromoisobutyrate)-*co*-(*p*-xylylene)] (PPX-EB), we followed the CVD procedure described in Jiang et al.[95] In brief, 32 mg of [2.2]paracyclophane-4-methyl 2-bromoisobutyrate (PCP-EB) was sublimed at 115-125 °C under reduced pressure (0.3 mbar) and then pyrolysed at 540 °C. Deposition of the polymer onto the substrate occurred on a sample holder maintained at 14 °C.

6.3.2 Copper catalyzed alkyne azide cycloaddition reaction for preparing surfaces 3 and 4

To conjugate β-D-glucopyranosyl azide (LC Scientific, Ontario, Canada) to substrates coated with PPX-alkyne, the following protocol was adopted. An aqueous solution containing 10 mg/mL of the azidosaccharide, 1 mM $CuSO_4$ and 8 mM sodium ascorbate was prepared. After thorough dissolution, this solution was poured on top of PPX-alkyne substrates and gently shaken (90 RPM) on an orbital rotator overnight. Finally, substrates were removed from the solution, washed with deionized water and dried under a stream of nitrogen. An identical procedure was employed to obtain mannose monolayers from α-D-mannopyranosyl azide

6.3.3 Surface-initiated atom transfer radical polymerization for preparing surfaces 1 and 2

Standard air-free techniques involving a vacuum-argon manifold and the usual precautions against oxygen entry were employed. In a typical SI-ATRP run, 25 mL of milli-q water, 400 mg sodium chloride and 150 μL Me_6Tren were taken in a schlenk flask and degassed using three cycles of freeze pump thaw. Simultaneously, 800 mg of 2'-acrylamidoethyl-α-D-mannopyranoside in a round bottom

flask was degassed using 3 cycles of vacuum and argon. In parallel, glass chamber slides, cover slips silicon and gold substrates coated with PPX-EB were placed in a glove bag and degassed using 3 cycles of vacuum and argon. After the completion of the third freeze operation, 20 mg CuCl and 5 mg $CuCl_2$ were added to the schlenk flask under argon. After the final pump and thaw operations, the catalyst mixture was stirred to dissolution under continuous argon flow. Then the solution was transferred to the monomer flask using a degassed luer lock syringe and luer lock needle and the monomer was stirred to dissolution under an argon environment. Subsequently, the flask with the combined solution was taken into the glove bag. After evacuating and inflating the bag 3 times to eliminate air, the flask was opened and the solution was distributed among all the substrates. At the end of the reaction time, substrates were removed from the bag, washed thoroughly with 0.05 M EDTA and deionized water and dried under a stream of nitrogen. Coatings comprised of poly(2'-acrylamidoethyl-α-d-mannopyranoside) were thus obtained. A similar procedure was used to prepare poly(2'-acrylamidoethyl-β-D-glucopyranoside)

6.3.4 Quartz crystal microbalance measurements of *Concanavalin A* binding

The QCM-200 instrument from Stanford research systems, CA was used along with a flow cell (catalog # O100FC). AT-cut quartz crystals coated with gold (catalog # O100RX1) were coated with **1**, **2**, **3**, and **4** surfaces respectively. The functionalized QCM substrates were subsequently used to collect time-resolved measurements of Con A binding. The lectin conjugation buffer was composed of 10 mM HEPES, 0.15 M NaCl, 1 mM $MnCl_2$ and 1 mM $CaCl_2$. First the QCM substrates were blocked with a solution of 1 mg/mL Bovine Serum Albumin (BSA) dissolved in 10 MM PBS with 0.01% v/v Tween-20. this was done to prevent non-specific Con A adsorption. Then, the blocked QCM substrates were placed in the crystal

holder and allowed to equilibrate in the buffer overnight. The next day, the flow cell was mounted on the crystal holder and connected through tubings to a syringe pump and a 50 mL reservoir of the lectin conjugation buffer. The buffer was pumped through the flow cell at 0.1 mL/hour until a stable baseline was observed (fluctuation of less than 5 Hz in 60 minutes). Then the Con A was injected into the flow circuit at a concentration of 50 μg/mL. The decrease in frequency with time was measured continuously at intervals of 1 second. The mass of Con A adsorbed was computed from the ΔF values using the Sauerbrey equation.

6.3.5 Fluorescence microscopy for *Concanavalin A* imaging

For comparing Con A binding across surfaces, **1**, **2**, **3**, and **4**, glass cover slips were coated with each of these four polymers. Thereafter, the surfaces were incubated with a solution of 1 mg/mL bovine serum albumin (BSA) dissolved in 10 MM PBS with 0.01% v/v Tween-20 for 30 minutes and washed throughly with 10 mM PBS. Then, a solution Con A tagged with Alexa Fluor 547 (Thermo Fisher) was dissolved in the lectin conjugation buffer (10 mM HEPES, 0.15 M NaCl, 1 mM $MnCl_2$ and 1 mM $CaCl_2$) to attain a concentration of 50 μg/mL. The substrates were immersed in the solution and shaken gently for 2 hours in the dark. Then, they were washed with the lectin conjugation buffer, 10 mM PBS, deionized water and dried thoroughly. The binding of Con A was observed using a fluorescence scanner (Fluorochem M, Protein Simple Inc) with an exposure time of 400 ms. The fluorescence intensity was quantified using ImageJ and an average was obtained from three substrates for each sample group. For the patterned mannose brushes, a similar procedure was performed for Con A conjugation. Imaging was done using a Nikon E-800 fluorescence microscope using a 20$\times$ objective.

6.3.6 X-ray photoelectron spectroscopy

XPS was performed on an Axis Ultra X-ray photoelectron spectrometer (Kratos Analyticals, UK) equipped with a monochromatized Al-Kα X-ray source. All peaks were calibrated with respect to the non-functionalized aliphatic carbon with a binding energy of 285.0 eV. The area under each high resolution spectra was quantified and elemental compositions calculated using relative sensitivity factors of 1, 2.93 and 1.8 for carbon, oxygen and nitrogen respectively. Peak fitting and analysis was performed using Casa XPS software.

6.3.7 FTIR spectroscopy

To verify whether the desired functional groups were present on the surface of the four groups of polymer coatings, Fourier-transformed infrared (FTIR) spectroscopy was performed. We used a Nicolet 6700 spectrophotometer in the grazing angle configuration against a gold background. Gold wafers were coated with the desired polymers and 128 scans were collected with a resolution of 4 cm^{-1}.The instrument was continuously purged with nitrogen gas for an hour prior to spectrum acquisition.

6.3.8 Ellipsometry

Ellipsometry was performed on silicon wafers (Silicon Valley Microelectronics, CA) with a native silicon dioxide layer of 2.5 nm thickness. Coating thickness was measured before and after ATRP with a nulling ellipsometer (EP3 Nanofilm, Accurion GmbH, Germany). Ellipsometric delta and psi values were collected at a range of wavelengths between 458 nm to 712 nm in order to allow for simultaneous determination of the optical constants as well as coating thickness using the Cauchy model. After SI-ATRP was completed, the thickness of the carbohydrate brushes formed was calculated by subtracting the initial thickness of the PPX-EB

initiator layer from the post-ATRP thickness. One reading was collected for each substrate and two substrates were used for each data point. It is advised to wash the PPX-EB susbtrates with acetone prior to ellipsometry and SI-ATRP. For surfaces **3** and **4**, ellipsometry was not performed as the thickness increment caused by the monolayer fomation (<0.5 nm) falls within the range of measurement error of the instrument.

6.3.9 Development of a thermodynamic model

Model calculations performed jointly with Irina Kopyeva, undergraduate researcher

We employed the thermodynamic model proposed by Kitov and Bundle that addresses the effects of tailored multivalency. The free energy of binding was estimated by adding inter-molecular, intra-molecular and entropic contributions

$$\Delta G^{\circ}_{\text{avidity}} = \Delta G^{\circ}_{\text{inter}} + \Delta G^{\circ}_{\text{intra}} \sum_{i=1}^{i_{\max}} w_i(i-1) + RT \sum_{i=1}^{i_{\max}} w_i \ln(w_i/\Omega_i) \tag{6.1}$$

The degeneracy term Ω was computed for the brush and the monolayer using combinatoric arguments.

$$\Omega_i(\text{monolayer}) = (n-i+1)(m-i+1) \tag{6.2}$$

$$\Omega_i(\text{brush}) = \frac{n!m!}{(n-i)!(m-i)!} \tag{6.3}$$

The free energy for each binding state i was estimated using a similar argument.

$$\Delta G^{\circ}_i = \Delta G^{\circ}_{\text{inter}} + (i-1)\Delta G^{\circ}_{\text{intra}} - RT \ln \Omega_i \tag{6.4}$$

The partition function w_i was defined according to:

$$w_i = \frac{e^{-\Delta G^{\circ}_i / RT}}{\sum_{i=1}^{i_{\max}} e^{-\Delta G^{\circ}_i / RT}} \tag{6.5}$$

6.3.10 Polarization of THP-1 monocytes

Flow cytometry, sorting, cell culture, polarization and microscopy of THP-1 monocytes performed by Nahal Habibi (Lahann Lab)

THP-1 (ATCC) monocytes were terminally differentiated into M0 macrophages by

treatment with 150 nM phorbol 12-myristate 13-acetate (PMA) over three days. M0 cells were polarized to M2 Mps by incubating them with 20 ng/mL of IL-4 and IL-13 for 3 days. For M1 polarization, cells were incubated with 20 ng/mL IFN-γ and 2400 ng/mL LPS for 2 days. Both M1 and M2 polarized macrophages were seeded on media-conditioned and UV-sterilized **1**, **2**, **3**, **4**, and glass surfaces at a density of 50,000 cells/mL and imaged after 24 hours of incubation.

6.3.11 Polarization of monocytes from peripheral blood

Flow cytometry, sorting, cell culture, polarization and microscopy performed by Jelani Zarif and Amber de Groot (Pienta Lab, Johns Hopkins University)

Monocytes were harvested from blood samples donated by human volunteers by magnetic sorting. A negative selection procedure was used to remove non-monocytic white blood cells (WBCs), red blood cells (RBCs), platelets and plasma by exploiting differences in the upregulation of CD14 receptors on monocytes. Non-monocytes, which do not possess CD14 were gradually depleted till a pure population of monocytes was obtained. These were differentiated into M0 cells and then polarized into M1 and M2 Mps using procedures similar to the ones described in the previous section.

6.4 Results and discussion

6.4.1 Synthesis and characterization of α-mannose and β-glucose functionalized surfaces

Our objective was to simultaneously examine the effects of glycan stereochemistry and glycan architecture on their ability to recognize and selectively bind to M2 macrophages. To this end, we prepared surfaces functionalized with both α-mannose and β-glucose, either in the form of polymer brushes through SI-ATRP

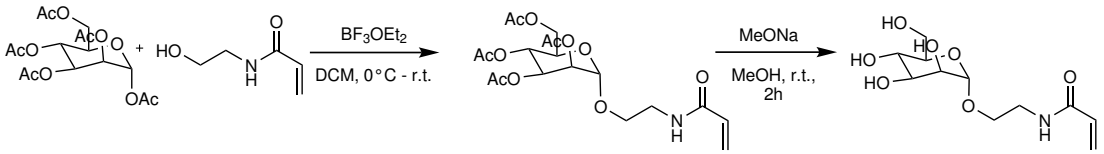

(a)

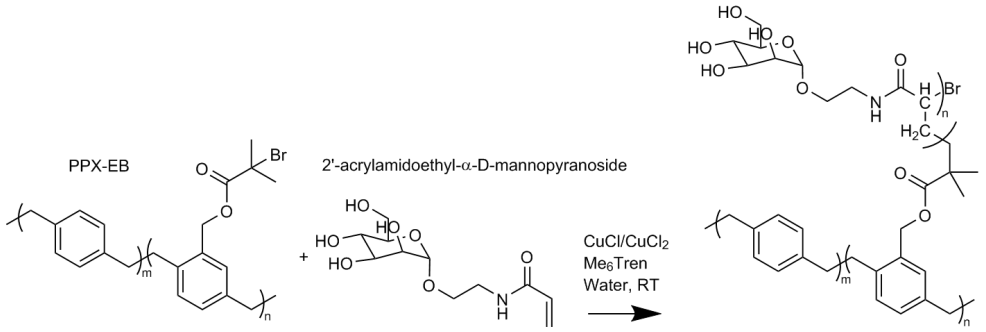

(b)

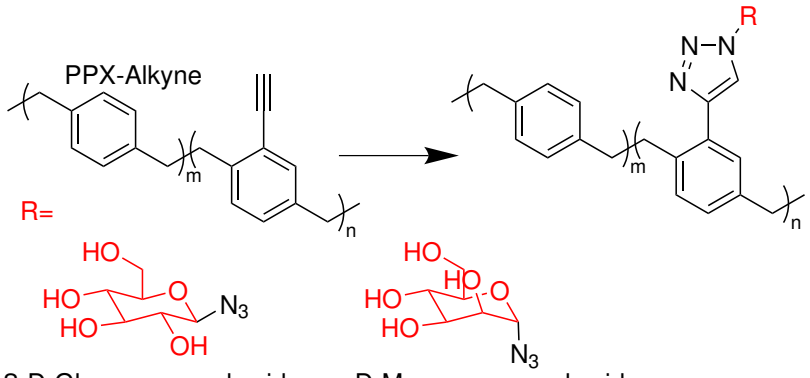

(c)

Polymers studied	
1	poly(2′-acrylamidoethyl-α-D-mannopyranoside)
2	poly(2′-acrylamidoethyl-β-D-glucopyranoside)
3	α-D-mannopyranosyl azide clicked to PPX-alkyne
4	β-D-glucopyranosyl azide clicked to PPX-alkyne

(d)

Figure 6.1: Synthetic schemes for the polymer coatings under study (a) Synthesis of 2′-acrylamidoethyl-2,3,4,6-tetra-O-acetyl-α-D-mannopyranoside from α-mannose pentaacetate and the subsequent deprotection to synthesize 2′-acrylamidoethyl-α-D-mannopyranoside. (b) Surface-initiated atom transfer radical polymerization from the initiator coating PPX-EB to form poly(2′-acrylamidoethyl-α-D-mannopyranoside) brushes. (c) Synthesis of monolayers bearing α-mannose and β-glucose molecules by copper catalyzed Huisgen 1,3-dipolar cycloaddition of PPX-alkyne with the azidosaccharides. (d) Tabular list of polymer coatings and their abbreviations used in this paper.

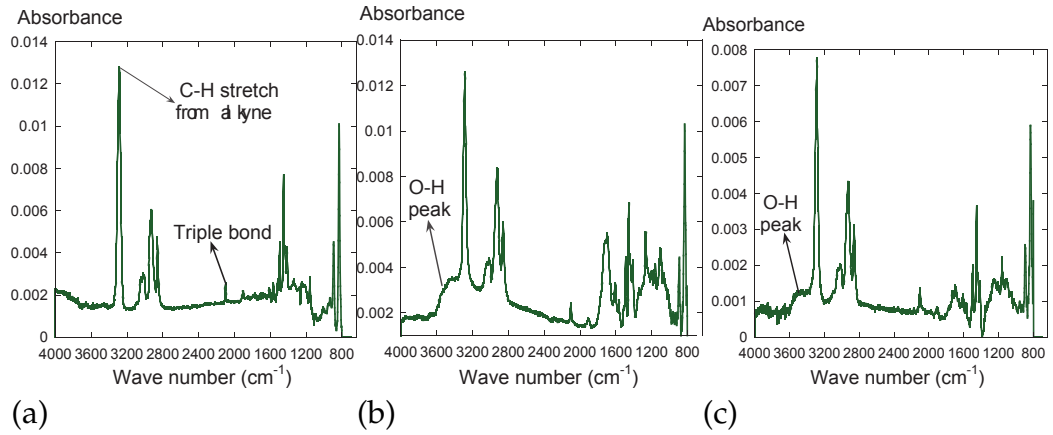

Figure 6.2: IRRAS spectrum of (a) poly(4-ethynyl-*p*-xylylene-*co*-*p*-xylylene) (PPX-alkyne) coating indicates the presence of reactive alkyne groups. (b) β-D-glucopyranosyl azide clicked to PPX-alkyne surfaces to yield **4**. (c) α-D-mannopyranosyl azide clicked to PPX-alkyne to yield **3**. The click reaction resulted in the appearance of the hydroxyl peaks adjacent to the alkynyl C-H stretch. Since only a monolayer is formed, most of the subsurface alkyne groups remain unreacted.

or as monolayers through a click reaction. In total, we studied four sets of surfaces (Figure 6.1(d)). The β-glucose coatings were selected as negative controls since both M1 and M2 polarized macrophages lack glucose receptors.

In order to prepare monolayers of α-mannose and β-glucose (**3** and **4**) , we employed the Cu(I)-catalyzed Huisgen 1,3-dipolar cycloaddition (Figure 6.1(c)) to conjugate the azidosaccharides to poly(4-ethynyl-p-xylylene-co-p-xylylene) (PPX-alkyne), which displays highly reactive alkyne functional groups[92]. We used α-D-mannopyranosyl azide and β-D-glucopyranosyl azide to ensure that the stereochemistry and orientation of the mannose and glucose molecules were identical on both the monolayers and brushes. α-mannose monolayer was included in the study in order to ascertain whether the glycan architecture played a significant role in shaping interactions with macrophages. Though these are chemically identical to the α-mannose brushes, the spatial distribution and topology of the α-mannose molecules change significantly when they are presented as monolayers instead of brushes. Similarly, the β-glucose monolayer was added to the study as an addi-

tional negative control.

The successful formation of the glycan monolayers was assessed via Fourier-transformed infrared spectroscopy (FTIR) where the characteristic peaks associated with the hydroxyl groups appeared completion of the click reaction appeared (Figure 6.2). Contact angle goniometry also confirmed the completion of the click reaction as indicated by a decrease in water contact angles (70 ± 8.5 °) compared to the unfunctionalized PPX-alkyne (93.5 ± 3 °). We adopted a two-step synthetic route to prepare 2'-acrylamidoethyl-α-D-mannopyranoside as seen in Figure 6.1(a). This synthetic strategy allows us to conjugate carbohydrates in their pyranose form to a polymerizable moiety, 2-hydroxy ethyl acrylamide, while still maintaining the glycan bioactivity. We opted for deprotection of the pyranose ring prior to polymerization instead of post-polymerization deprotection since the latter is seldom quantitative. As reported earlier,[298], both approaches yield well-defined α-mannosebrushes however, poor control over polymerization rates and broad polydispersity was observed for post-polymerization deprotection.

After the monomer was synthesized successfully, (Figure 6.1(a)), we proceeded to graft polymer brushes through SI-ATRP. First, substrates were functionalized with the initiator bearing the ATRP initiator groups via chemical vapor deposition polymerization.[95] Subsequently, poly(2'-acrylamidoethyl-α-D-mannopyranoside) brushes (**1**) were grafted from the initiator coatings (Figure 6.1(b)). Similar procedures for monomer synthesis and polymer brush growth were employed for preparing poly(2'-acrylamidoethyl-β-D-glucopyranoside) brushes (**2**).

For the brushes, we performed a more detailed characterization using X-ray photoelectron spectroscopy (XPS), FTIR and ellipsometry. The XPS survey scan of poly(2'-acrylamidoethyl-α-D-mannopyranoside) brushes is shown in Figure 6.3(c). Since, we observed signals from C_{1s}, N_{1s} and O_{1s} in the survey spectra, we proceeded to collect high resolution spectra from these three regions. This allowed

B.E.	C 1s	N 1s	O 1s
eV	285	399	532
Exp. (atom %)	63.7	4.1	32
Theo. (atom %)	57.8	5.2	36.8

(a)

B.E.	C-C	C-C-O	N-C	C=O
eV	285.6	287	288.6	289.7
Exp. (%)	35.2	48.3	14.4	2.05
Theo. (%)	38.9	44.4	11.1	5.6

(b)

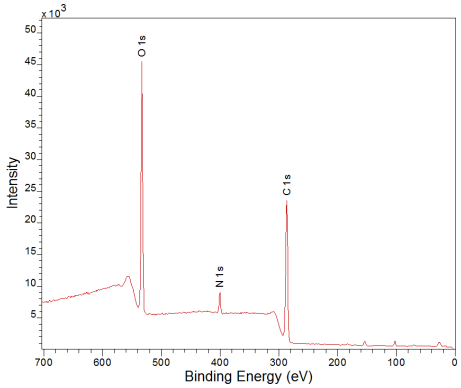

(c)

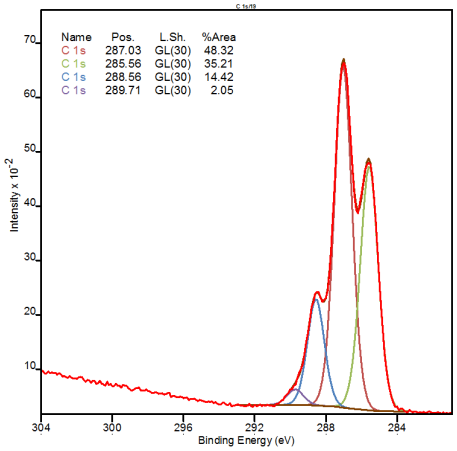

(d)

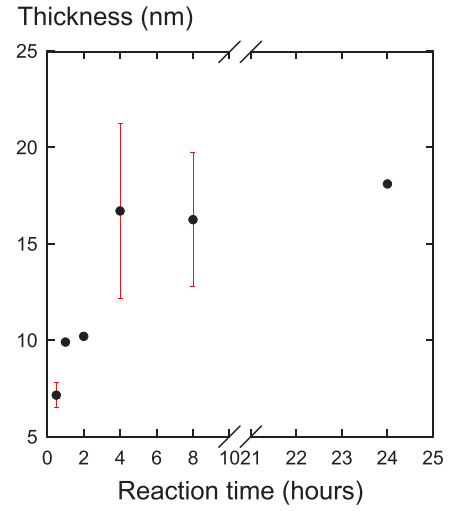

(e)

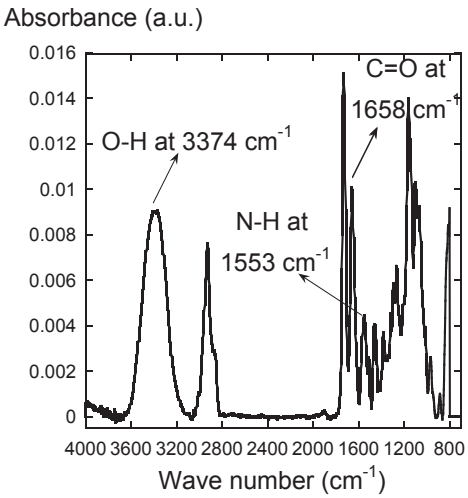

(f)

Figure 6.3: Surface characterization of poly(2′-acrylamidoethyl-α-D-mannopyranoside) brushes. (a) Elemental composition of α-mannose brushes as measured using high resolution XPS scans is in close agreement with theoretical values. (b) & (d) High resolution XPS spectra of carbon (Figure 6.3(d) and Table 4.4(b)) further confirms the chemical composition of the α-mannose brushes. (c) XPS Survey spectra of the surface bearing α-mannose brushes. (e) Thickness of the brushes increases in a non-linear and rapid fashion, reaching a plateau within 8 hours, with very little increase in thickness occuring between 8-24 hours. (f) IRRAS spectrum of α-mannose brushes recorded after SI-ATRP reaction. The presence of N-H and carbonyl peaks from the amide, as well as the hydroxyl groups were verified.

us to quantify the elemental composition of the α-mannose brushes (Figure 6.3(a) which compared well with the theoretical values of the brushes. Using the high resolution spectra of C_{1s}, we were able to further characterize the chemical structure of the brushes (Figure 6.3(d)). The C_{1s} spectrum shows signals for aliphatic C-C bonds, the C-C-O bonds from the pyranose ring, the N-C bonds and the C=O from the acrylamide. The contribution from each component is in close agreement with theoretical values as shown in Table 6.3(b).

Structural confirmation of the α-mannose brushes was also completed using FTIR spectroscopy in the grazing angle mode. Characteristic functional groups of the α-mannose brushes can be associated with absorption bands at 3374 cm^{-1} due to the hydroxyl groups, a strong, sharp peak at 1658 cm^{-1} indicative of the N$-$C=O bond of the amide group, and a peak at 1553 cm^{-1}, which is due to C$-$N stretches of the amide (Figure 6.3(f)).

The kinetics of α-mannose brush growth was studied using ellipsometric measurements. We studied film thickness as a function of polymerization time and concluded that the polymerization was not well-controlled. In the first eight hours, the reaction proceeded with an almost exponential increase of brush thickness with time before reaching a plateau around 18 nm. Since the ATRP was conducted in an aqueous medium, we expected the reaction to be dominated by irreversible chain termination reactions and loss of catalyst activity through disproportionation. Despite the addition of sodium chloride to suppress Cu^{I} disproportionation[303], we still observed significant formation of metallic copper over the course of the ATRP. Nevertheless, we can control the thickness within a 5-20 nm range merely by varying the reaction time. Finally, we observed that the advancing water contact angle decreased from 86$\pm$6 $^{\circ}$observed for the initiator coatings to 26$\pm$8 $^{\circ}$and 20$\pm$10 $^{\circ}$for the mannose and glucose brushes respectively.

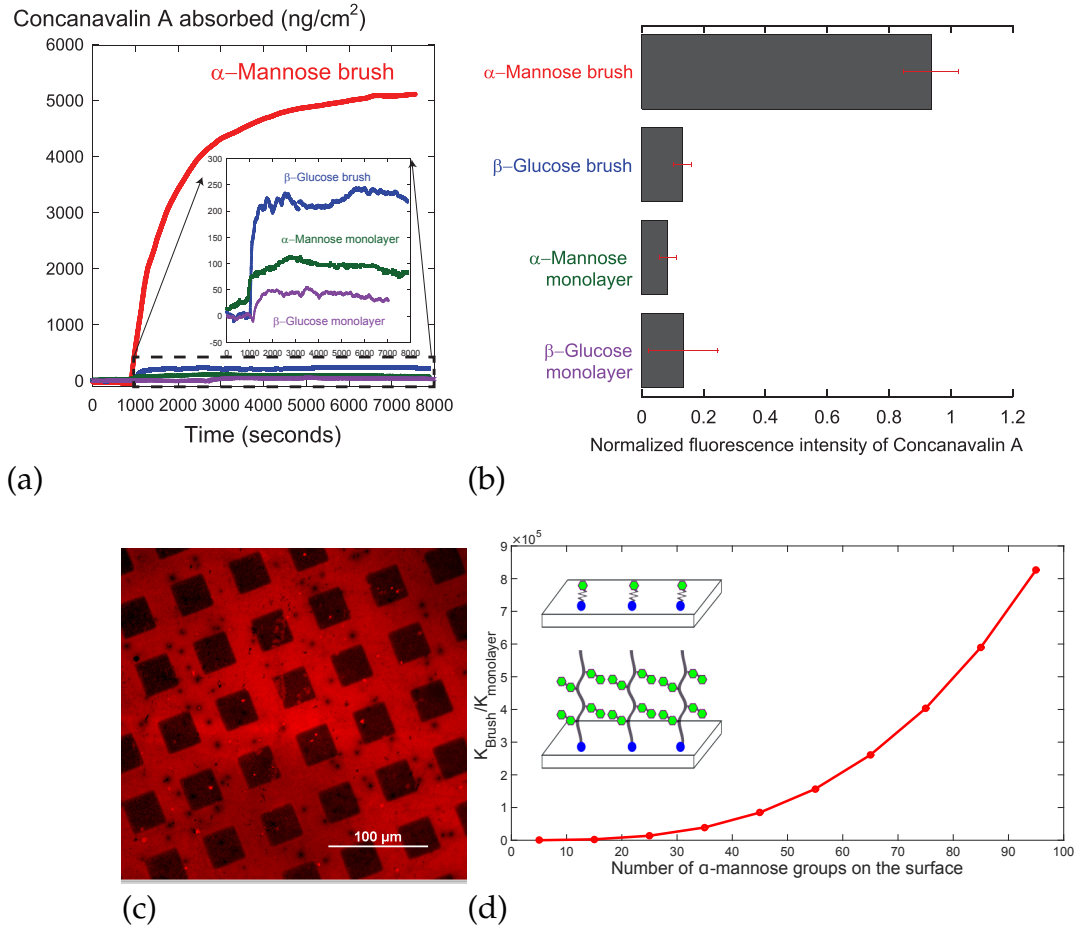

Figure 6.4: Assessing bioactivity of α-mannose brushes by measuring *Concanavalin A* binding. (a) QCM studies were undertaken to evaluate *Con A* binding kinetics to four sets of surfaces. While the α-mannose brushes exhibited strong lectin uptake, very little lectin binding was observed on the α-mannose monolayer, indicating that the brush architecture promotes multivalent protein-carbohydrate binding. The β-glucose monolayer and brushes were not expected to bind to the α-mannose-specific lectin. (b) The binding extent of Alex Fluor tagged *Con A* was compared on four surfaces using fluorescence measurements. Adsorption trends were similar to those from QCM measurements. (c) *Con A* patterns were obtained by synthesizing microstructured α-mannose brushes (on the gridlines) and subsequent incubation with the lectin. *Con A* adsorption occurred only on regions where the α-mannose brushes were present and not on the underlying SI-ATRP initiator coating. Scale bar is 100 μm. (d) Our thermodynamic model predicts that for the same number of α-mannose molecules on the surface, the brush architecture results in a far higher equilibrium constant of Con A binding compared to the monolayer architecture. Our model explains the contrasts in Con A binding between the α-mannose brushes and the monolayers.

6.4.2 Avidity of the α-mannose surfaces for Con A is architecture-dependent

Before we proceeded to examine differences in M1 and M2 macrophage binding on these four surfaces, we compared the binding kinetics of *Concanavalin* A, a carbohydrate-binding protein or lectin, that associates with α-mannose molecules through specific carbohydrate-protein affinity based interactions. The objective was to verify whether the surfaces (both the brush and the monolayer) composed of α-mannose were bioactive. Con A-mannose binding is a classic example of multivalent interactions found in nature, wherein a protein and a carbohydrate are unable to form a strongly bound complex due to weak univalent protein-glycan interactions. Instead, they bind multivalently by utilizing several copies of glycan molecules. Con A, a tetrameric protein isolated from the plant, *Canavalia ensiformis*, was one of the earliest lectins to be discovered and its mannose-binding behaviour has been widely studied. With four binding sites that interact strongly and highly specifically with α-mannose, this protein has served as a useful model molecule in examining the effects of multivalent glycan presentation on protein-carbohydrate interactions.[304] In the monovalent binding mode, the binding constant or the K_a value is around $7.5e^{-3}M^{-1}$, which indicates that the weak affinity between the protein and the carbohydrate renders the binding event reversible.[305] To exploit the glycocluster effect, a variety of glycopolymer architectures that can span multiple lectin binding sites have been developed. By controlling the properties of the glycopolymers binding to Con A, such as changing the framework from linear to dendrimeric architectures, or tuning the number and physical characteristics of the terminal functional groups, high avidity can be achieved despite low affinity.[306]Previously, binding avidities of dendrimers with upwards of 172 mannose groups were compared against that of the monovalent methyl mannose.[305] It was found that glycopolymers long enough to bind bivalently exhibited vastly stronger avidity, whereas shorter polymers could not wrap around the protein, binding

monovalently and resulting in a weaker avidity.[305] We expected to observe similar trends when we compared the lectin adsorption on mannose monolayers and brushes.

Though Con A also has a weak interaction with β-glucose, previous studies report that in their monovalent forms, α-mannose shows approximately twenty times higher affinity to Con A compared with β-glucose.[307] We hypothesized that the enhanced affinity for α-mannose over β-glucose would be amplified when we use multivalent topologies such as monolayers and brushes due to the glycocluster effect. Hence the extent of Con A binding to both the β-glucose brushes and monolayers were also examined. We wished to understand the effects of both stereochemistry and glycan architecture on the rate and extent of Con A binding and in ascertaining which architecture best promoted multivalent lectin binding, the brush or the monolayer architecture.

We employed a combination of fluorescence imaging and QCM to compare Con A binding on surfaces **1**, **2**, **3**, and **4**. The adsorption traces obtained from QCM allow us to map the decrease in resonant frequency as a function of time. This adsorption response was converted into the mass of Con A adsorbed on the active area of the flow cell using the Saueberey equation. The results, as seen in Figure 6.4(a), indicate that the Con A adsorption observed on **1** is at least 30 times higher than those observed on the other three surfaces. Surprisingly, the **3** coating displayed extremely low levels of Con A binding, even lower than the **2** surface and only slightly higher than **4**.

We assessed the binding of fluorescently tagged Con A on these four surfaces to further confirm the QCM results. The fluorescence intensity observed on **1** was far higher than the remaining groups. Again, **2** exhibited the second-highest Con A binding, followed by **3** and **4**, a trend consistent with our QCM observations. Finally, as an additional experiment to confirm these results, we created patterned

mannose brushes against a background composed of the deactivated initiator coating. Using imaging ellipsometry (data not shown), we detected thickness differences between the mannosylated regions and the initiator, confirming that mannose is present in the borders not in the square islands. The fluorescently tagged Con A bound exclusively to the mannose domains while avoiding non-specific binding to the initiator coating, which is shown in Figure 6.4(c).

To understand our Con A results better, we developed a thermodynamic model using the framework proposed by Kitov and Bundle[308]. Our model includes a degeneracy term that accounts for all the possible configurations of ligation between Con A and mannose. Unlike the rigid monolayer, the brushes are more flexible and can span all four binding sites on the Con A, thereby maximizing degeneracy. Assuming an identical number of α-mannose molecules presented per unit area, the brushes have a lower free energy of binding compared to the monolayer. As the α-mannose density increases on both topologies, the free energy gap between the two architectures widens, leading to a much higher equilibrium constant for the binding of Con A with the multivalent mannose brushes as compared to the multivalent mannose monolayer (Figure 6.4(d)). Our results suggest that lectin binding is a function of not only whether the glycan possesses the right stereochemistry but also on whether the glycan presentation is optimized to maximize multivalent interactions between the lectin and the glycan.

6.4.3 Examining differences in M1 and M2 Mp adhesion

We wished to examine whether the high uptake of Con A by α-mannose brushes would directly translate into an ability to capture pro-repair M2 polarized macrophages, which bear mannose-binding CD206 receptors. We hypothesized that the presence of mannose receptors on the M2 cell surface is expected to result in their selective adhesion to α-mannose surfaces. In contrast, we anticipated that the pro-

inflammatory M1 polarized macrophages will not bind to the α-mannose surfaces, since M1 macrophages do not display mannose receptors. We also wished to verify whether the spatial presentation of mannose molecules (brush vs. monolayer) will have a significant effect on the selectivity as well as avidity of M2 macrophage isolation. In addition to the **1**,**2**, **3** and **4** functionalized chamber slides, we employed unfunctionalized glass chamber slides as additional controls.

We conducted two sets of studies, one using macrophages derived from a monocyte cell line (THP-1) and the other study employing macrophages differentiated from primary monocytes. THP-1 is an immortalized human leukemia monocyte cell line that is frequently used by immunologists as an *in vitro* model of monocyte and macrophage behavior. THP-1 has been routinely used in the Lahann Lab as it offers several advantages over primary cells. They are convenient to procure, freeze and store for long durations. With a doubling time of 35-50 hours, they can proliferate quite easily, compared to primary cells. However, due to their cancerous origin, PMA-differentiated THP-1 macrophages may exhibit unnatural *in vitro* behavior in response to polarization stimuli and display much lower levels of expression of M1 and M2 markers. Macrophages derived from primary cells, on the other hand, are expected to be more plastic and result in greater upregulation of M1 and M2 markers upon polarization. Our collaborators at Johns Hopkins University have well-established procedures for isolating monocytes from blood samples and then differentiating them into M0 cells, which are finally polarized into M1 and M2 Mps. The rationale behind using both primary cells and cell lines is to evaluate whether mannose coatings could be of utility, not just in clinically relevant settings employing macrophages derived from the patient's blood stream, but also in basic research on wound healing that employs cell lines for reasons of cost and convenience.

Next, we evaluated the adhesion of macrophages derived from primary human

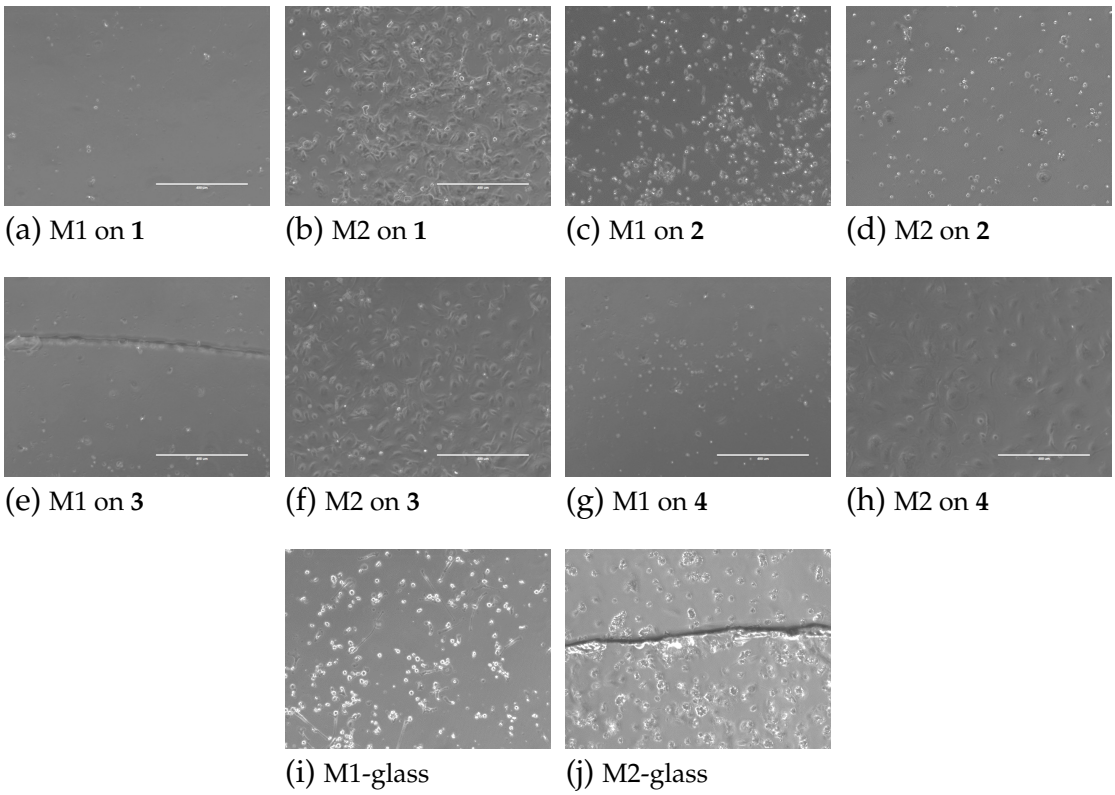

(a) M1 on **1** (b) M2 on **1** (c) M1 on **2** (d) M2 on **2**

(e) M1 on **3** (f) M2 on **3** (g) M1 on **4** (h) M2 on **4**

(i) M1-glass (j) M2-glass

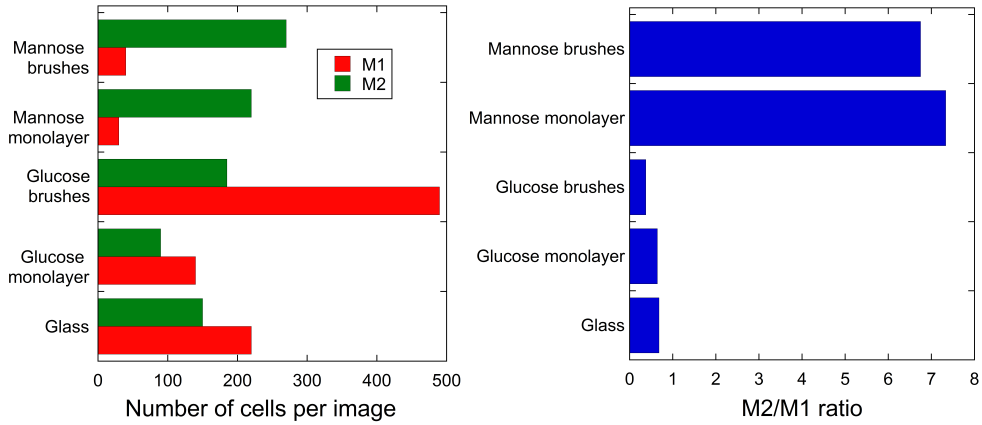

(k) (l)

Figure 6.5: Results from studies performed with Mps derived from peripehral blood (a) - (d) Representative images of M1 and M2 Mps adhered to mannose and glucose brushes (**1** and **2**). (e) - (h) Representative images of M1 and M2 Mps adhered to monolayers of mannose and glucose (**3** and **4**). (i)-(j) Representative images of M1 and M2 Mps adhered to unfunctionalized glass. (k) Cell numbers of M1 and M2 Mps adhering to the surfaces evaluated. (l) Selectivity ratio of the surfaces under study.

bone marrow mononuclear cells on glass, mannosylated (**1** and **3**) and glucosylated (**2** and **4**) surfaces. The mannose brushes (**1**) possessed a thickness of 15.5 $\pm$ 3.5 nm while the glucose brushes (**2**) were measured to be 19 $\pm$ 3 nm. We ensured that both sets of brushes had comparable thicknesses to eliminate confounding factors arising from brush architecture and the possible differences in steric repulsions caused by brush thickness.

On glass surfaces (Figures 6.5(i) and 6.5(j)), both M1 and M2 Mps adhered well but the cell numbers were not vastly different, indicating that cell adhesion was mediated by non-specific factors such as electrostatic and hydrophobic attractions.[309,310] Upon changing the surface chemistry from glass to glucose monolayer (**4**) coatings, we found that the numbers of adhered M1 and M2 Mps were similar to those recorded on glass (Figures 6.5(g) and 6.5(h)). We also observed distinct morphological differences between M1 and M2 Mps, with the former adopting compact rounded shapes that minimized cell-surface contact areas and the latter forming elongated spindles that maximized spreading and the area of adhesion. Next, we modified the spatial presentation of glucose molecules on the surface by switching to a brush architecture from the monolayer, while preserving the chemical composition and glycan stereochemistry (Figures 6.5(c) and 6.5(d)). We observed a modest increase (2$\times$) in the number of M2 cells but a much more pronounced increase (3.5$\times$) in the M1 Mps adhering to the glucose brushes compared to the glucose monolayers.(Figure 6.5(k)) Interestingly, the M2 cells adopted a rounded morphology on the glucose brushes compared to the elongated shapes on the glucose monolayers. This could be attributed to the non-fouling cell-resistant properties of the glucose brushes, which inhibit cell adhesion and spreading.

Finally, in Figures 6.5(e), 6.5(f), 6.5(a), and 6.5(a), we observed that we could hardly find any M1 Mps on the mannose surfaces while the M2 Mps adhered in high densities. It appears that only cells possessing mannose-binding CD206 re-

ceptors were able to adhere to mannosylated surfaces, indicating that non-specific cell adhesion of M1 Mps was inhibited. However the preference for M2 over M1 Mps was high for both the mannose brushes as well as the monolayers, indicating that the M2 Mps were insensitive to the architecture of the mannose-functional surfaces (Figure 6.5(l)).

For THP-1 derived macrophages, the upregulation in the expression of CD206 (for M2a) and CCR7 (for M1) was studied using flow cytometry and sorting was performed to remove unpolarized M0 cells. As seen in Figure 6.6(a), M1 macrophage markers were not detected in M2 polarized macrophages and vice versa. After sorting, M1 and M2 cells were seeded on five sets of surfaces and incubated for 24 hours. Finally, surfaces were washed gently with D-PBS, imaged using a light microscope and adherent cells were enumerated using manual counting. In Figure 6.6(b), the results of this cell count have been plotted and we can see the differences in adhesion behavior between M0, M1 and M2 Mps on glass, surfaces **1**, **2**, **3**, and **4**. We noticed stark differences in the ability of surfaces to preferentially adhere to M2 Mps (Figure 6.6(c)). While glass, **2**and **4** surfaces did not distinguish between M1 and M2 cells, the **1** and **3** surfaces had much higher densities of adherent M2 cells compared to M1s. Surface **3** not only displayed the highest number of M2 cells, but were the only group where significant differences were observed between M2 and M1 and between M2 and M0 cells. Overall, the cell adhesion results obtained from THP-1 derived Mps displayed several similarities with the data obtained from primary cells. The glucose and glass surfaces were unable to "select for" M2 Mps while the mannose brushes (**1**) displayed a high selectivity for M2 Mps. In the case of primary cells, the selectivity of mannose monolayers (**3**) was comparable to those of the mannose brushes. However, the mannose monolayers did display the same level of selectivity with the THP-1 macrophages. One reason for this could be that the density of CD206 receptors is lower on M2 Mps derived from THP-1 cells

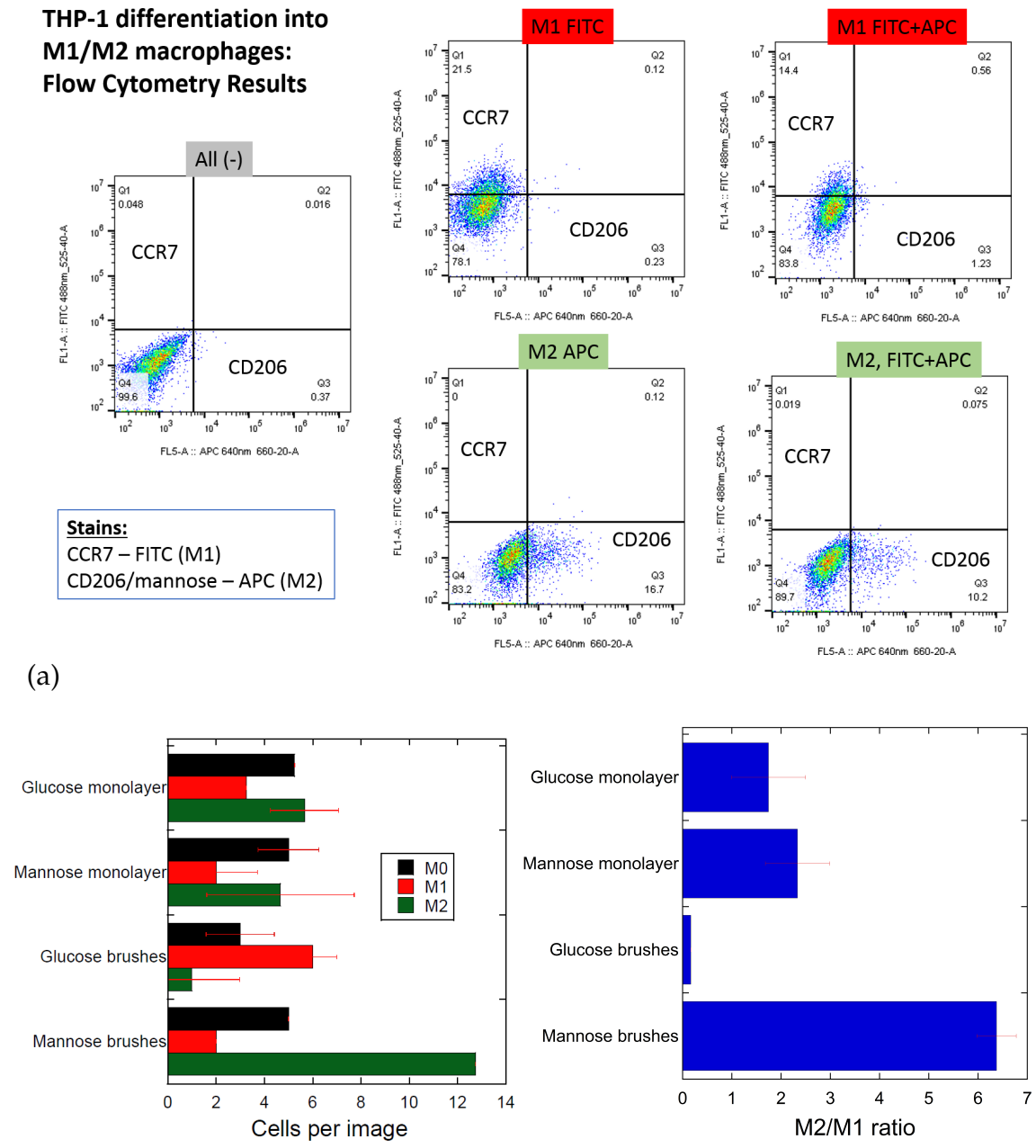

Figure 6.6: Results from studies performed with Mps derived from THP-1 monocytes. (a) Flow cytometry was performed to measure the expression of CD206 in M2 Mps and CCR7 in M1 Mps. Our results indicated that the polarization protocol was successful in transforming M0 Mps into M1 and M2 phenotypes. Subsequently, polarized cells were sorted from unpolarized M0 Mps using magnetic sorting. (b) Cell count of M1, M2 and Mo Mps on various surfaces. Error bars indicate two standard deviations. (c) Ratio of M2 to M1 cell numbers for each coating.

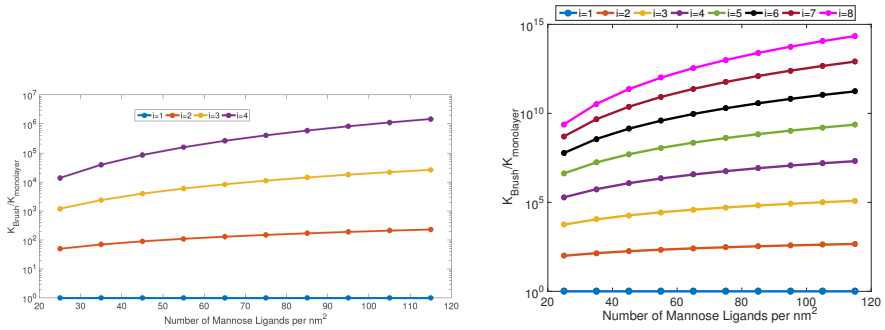

(a) (b)

Figure 6.7: The ratio of equilibrium constants between brushes and monolayers is plotted as a function of binding state i for (a) Mannose-Con A interactions with a K_a of $7.5e^{-3}M^{-1}$ (b) Mannose-CD206 interactions which have a K_a of $2e^{-7}M^{-1}$

compared to M2 Mps derived from primary monocytes. As a result, multivalent CD206-mannose binding may require a higher number and denser distribution of mannose molecules on the surface, which is provided by surface **1** but not **3**.

For binding processes involving Con A and mannose, the brushes displayed a much higher avidity than the monolayers did whereas in the case of the primary macrophages, this difference was not observed. In order to understand the reasons for this disparity, we compared the roles of binding affinity, K_a and binding state i for both the binding pairs, Con A-mannose and CD206-mannose (Figure 6.7). At values of i close to 1, monovalent binding is predominant and therefore both brushes and monolayers are expected to have equal avidities for Con A and CD206. As i approaches the maximal binding state (4 for Con A and 8 for CD206) the equilibrium constant for binding is brushes is 10^5 to 10^{15} times higher than with the monolayers as multivalent modes of binding are accessed. This effect is further amplified when the density of mannose molecules on the surface is increased. Also, since the CD206 has a weaker affinity for mannose compared to Con A, as indicated by the difference in K_a estimates, we expected degeneracy and entropic effects to assume greater significance for the former. Accordingly, we can see that the differences between brush and monolayers and much starker for the

CD206 (Figure 6.7(a)) than the Con A association (Figure 6.7(b)). In this light, the results obtained for primary M2 Mps seem even more puzzling and unexpected. There are two probable causes for the deviation between experimental results and model predictions. One explanation is that the binding processes between CD206 and mannose surfaces are monovalent, rendering the binding strength indifferent to both glycan architecture and mannose density, but this seems unlikely given the weak binding strength between a single CD206 receptor and monovalent mannose (K_a of $2e^{-7}M^{-1}$). Another explanation is that the smaller size of the Con A molecule (4 nm diameter) enables them to access and bind to mannose molecules present along the entire length of the extended polymer brushes through insertion into the brushes or ternary adsorption. In contrast, ternary adsorption is not possible for macrophages, which are more likely to maximize interactions with mannose molecules through cell spreading and elongation rather than brush insertion. Due to this limitation, the M2 Mps "perceive" both the brushes and the monolayers as monolayers, ensuring comparable avidities and adhesion trends.

Though our initial results testing adhesion differences between M1 and M2 macrophages seem promising, further work needs to be done to ensure that our coatings perform in the intended manner *in vivo*. Immunofluorescence studies and viability assays are being planned in order to verify that the M2 phenoptype is maintained and to ensure that the M2 Mps remain competent to induce healing outcomes. Since other cell types such as keratinocytes and dermal fibroblasts also over-express CD206, co-culture experiments need to be performed to evaluate whether the competition for mannose ligands between M2 Mps and other cell types results in the displacement of M2 Mps from the coatings.

6.5 Conclusions

In this chapter, we engineered bioactive carbohydrate-based coatings that could potentially be applied in cell-based therapeutics targeting dysregulated macrophage polarization, such as wound healing constructs for diabetic wounds. We hypothesized that the upregulation of mannose-binding receptors on alternatively activated M2 macrophages confers mannose-decorated surfaces with the ability to bind to them selectively. We demonstrated the ability of polymer brushes bearing pendant α-mannose brushes to resist the adhesion of pro-inflammatory M1 macrophages while displaying a high avidity for pro-repair M2 macrophages. These surfaces have been characterized extensively and the effects of glycan stereochemistry and architecture were examined using both thermodynamic models as well as experimental model systems employing a mannose binding lectin, Con A. With further work, these coatings will be a promising strategy to deliver pro-healing macrophages to the wound site to resolve inflammation and to accelerate wound closure.

CHAPTER VII

Conclusions & Future Directions

7.1 Conclusions

In this dissertation, zwitterionic and carbohydrate polymer brushes were extensively used to tailor the interactions of biomaterial surfaces with cells, biomolecules and viruses. By borrowing these powerful chemical motifs from nature, and amplifying them in the form of polymer brushes, we established a modular multifunctional materials platform wherein composition, architecture and spatial presentation can be independently controlled. Synergies with thermodynamic and statistical modeling as well as with chemical vapor deposition (CVD) polymerization were identified and exploited to discover optimal polymer brush design parameters for several biomedical applications.

In Chapter II, CVD-based surface initiated-atom transfer radical polymerization (SI-ATRP) initiator coatings were spatioselectively deactivated through UV treatment in order to isolate the growth of polymer brushes to selected masked areas, where the polymerization initiators remained functional. These micropatterned polymer brushes could be used to organize the deposition of proteins in two ways: patterned phosphorylcholine brushes could structure non-specific protein adsorption while biotinylated polymer brushes could promote the recognition of streptavidin-tagged biomolecules along the desired regions. The substrate-

independence of this technique was demonstrated on a range of polymer surfaces and on steel.

In Chapter III, a novel electrokinetic approach was developed to visualize the adsorption of proteins and nanoparticles on biomedically relevant surfaces. By monitoring temporal changes in ζ-potential, we could map the binding of neutravidin molecules on biotinylated surfaces and validated this technique by comparing the kinetic profiles of neutravidin-biotin binding with those acquired from quartz crystal microbalance measurements. Additionally, we synthesized electrostatically tunable coatings incorporating poly(sorbitol methacrylate) brushes and studied the adsorption kinetics of virus-like nanoparticles as a function of surface composition using real-time ζ-potential measurements. We demonstrated that this label-free and inexpensive technique can be a useful tool in characterizing biointerfacial events that are sensitive to electrostatic forces.

In Chapter IV, we developed a model surface comprising β-glucose, β-galactose and α-mannose based polymer brushes coimmobilized with positively charged viral binding sites, with the goal of enhancing our understanding of virus-material interactions. CVD copolymerization enabled us to vary the ratio between SI-ATRP initiator sites and aminomethyl functional groups, allowing for a systematic study of the role of nanoscale electrostatic heterogeneity on viral and protein adsorption profiles. The aminomethyl groups, which model coating defects, promoted the binding of influenza and adenoviruses while the carbohydrate brushes prevented viral adsorption. Using our modular coating, we explored the effects of brush composition, architecture and binding site density and concluded that viral adsorption is a complex function of brush thickness and aminomethyl surface concentration. Our model surfaces generated guidelines for the design of virus-resistant coatings, considering realistic scenarios where coating defects can influence performance.

In Chapter V, a design of experiments (DOE) approach was employed to de-

scribe brush properties as mathematical functions of SI-ATRP parameters. Specifically, we investigated the SI-ATRP of a model zwitterionic hydrogel, poly[2-{methacryloyloxy} ethyl dimethyl-{3-sulfopropyl} ammonium hydroxide] (PMEDSAH). PMEDSAH is of special interest to the stem cell engineering community as it can sustain feeder-free and xeno-free stem cell proliferation. Our previous work indicated that the rate of stem cell propagation is sensitive to modifications of the gel architecture of PMEDSAH. We developed and validated a predictive model that simultaneously captures both phenomena that determine the gel architecture of PMEDSAH- the SI-ATRP reaction kinetics and the degree of zwitterionic self-association. We concluded that DOE is a promising data-driven modeling framework for the design and synthesis of polymer brushes. This approach allowed us to access hitherto unrealized gel architectures merely by increasing the catalyst concentration.

In Chapter VI, the ability of α-mannose brushes to capture M2 polarized macrophages in a phenotypically selective manner was investigated. The effect of glycan stereochemistry and architecture was evaluated simultaneously since our thermodynamic models and lectin binding experiments indicated that the spatial presentation of α-mannose molecules would play a key role in determining the avidity of M2 macrophages for α-mannose surfaces. While M1 macrophages, which lack mannose-binding receptors did not discriminate between β-glucose and α-mannose surfaces, M2 macrophages adhered exclusively to α-mannose surfaces. In contrast to the lectin experiments, no significant differences in macrophage adhesion between monolayers and brushes were observed.

In summary, the polymer coatings, modeling frameworks and applications developed in this dissertation can serve as a foundation for engineering interfaces that solve diverse problems at the intersection of materials and biomedical research. In the following sections, selected extensions of dissertation research and

ideas for additional projects will be discussed briefly.

7.2 Future directions: Stem cell engineering on synthetic substrates

7.2.1 Elucidating the mechanisms by which PMEDSAH facilitates stem cell self-renewal

Although PMEDSAH is well-characterized and is ideally positioned for adoption in regenerative medicine, a critical aspect has remained under-investigated. What is the mechanism by which PMEDSAH facilitates stem cell self renewal? Since synthetic polymers do not have inherent bioactivity, they are sometimes conjugated with certain peptide sequences in order to interact specifically with stem cell receptors, thus sending pluripotency-supportive signals[311]. PMEDSAH, however, is employed as a purely synthetic polymer and does not carry these peptide modifications. An alternative mode of interaction is biomimicry, wherein a structural resemblance of the polymer to a key functional component of the extracellular matrix is exploited. Adding to this picture is the interesting observation that PMEDSAH is a non-fouling material[312] and cannot have physisorption-based non-specific interactions with the proteins present in the cell culture environment. Hence identifying the exact molecular mechanism of PMEDSAH's bioactivity presents an intriguing prospect.

Basic fibroblast growth factor (bFGF-2) is a key component of the human pluripotent stem cell (hPSC) culture environment as it plays a critical role in promoting self-renewal.[313] bFGF is a heparin binding growth factor and is believed to be stabilized by heparin sulfate, a proteoglycan present in the extracellular matrix.[314] The chemical structure of PMEDSAH suggests that it bears some resemblance to heparin sulfate on account of the terminal sulfonate group present in the zwitterionic side chain.[315] We hypothesized that PMEDSAH is unique among zwitterionic

polymer brushes because it stabilizes bFGF through biomimicry of heparin sulfate. In order to test this hypothesis, we performed bFGF adsorption studies using enzyme linked immunoadsorbent assay (ELISA). The ELISA studies were performed by our collaborator, Tugba Topal (Krebsbach Lab).

Initially, we were interested in quantifying the concentration of unbound and bioactive bFGF that exist as free molecules in solution. In this experiment, we did not consider surface-bound bFGF. Four sets of surfaces- heparin (positive control), untreated polystyrene(negative control), tissue culture-treated polystyrene (TCPS, negative control) and PMEDSAH, were compared. Two time points (initial and 2 hours) and three bFGF loadings (0, 320 and 640 pg/mL) were studied. We did not observe significant differences in solution bFGF concentration between the four surfaces (Figure 7.1(a)). We also noted that bFGF concentration did not decrease after 2 hours of incubation at 37°C. The solution concentration only seemed to depend on the initial loading of bFGF.

Next, we increased the time horizon for our observations from 2 to 24 hours and then estimated the concentration of bioactive bFGF remaining in solution after 24 hours of incubation on either PMEDSAH or TCPS surfaces (Figure 7.1(b)). We discovered that while PMEDSAH coatings managed to retain between 5-10% of the loaded bFGF with its native structure intact, the concentrations of bioactive bFGF on TCPS surfaces were close to zero levels. We attribute these differences between PMEDSAH and TCPS surfaces to the hydrophilic non-fouling nature of the former and the hydrophobic surface characteristics of the latter, which promote protein denaturation and unfolding. We concluded that while short-term differences in bFGF solution stability between TCPS and PMEDSAH were minimal, the long-term consequences of hydrophobic interactions and prolonged exposure to TCPS caused a steep drop in the availability of bioactive bFGF molecules in the solution.

Finally we estimated the adsorption of bFGF on TCPS and PMEDSAH by mea-

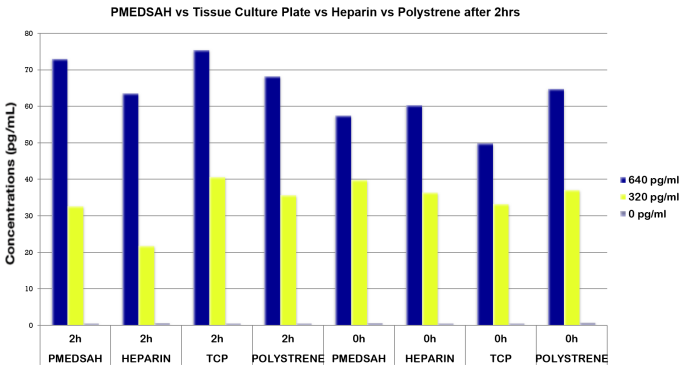

(a) Solution bFGF 2 hours

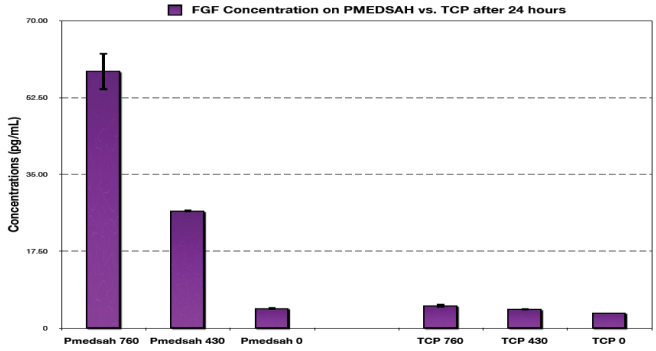

(b) Solution bFGF 24 hours

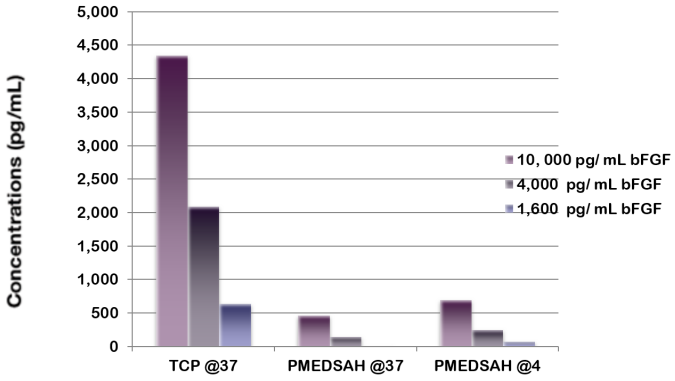

(c) Adsorbed bFGF

Figure 7.1: ELISA data collected by Tugba Topal. (a) Comparison of solution concentrations of bFGF across TCPS, polystyrene, heparin and PMEDSAH at 0 and 2 hour time points. Only negligible differences were observed (b) ELISA measurements of bFGF concentration after 24 hours incubation on TCPS and PMEDSAH as a function of bFGF loading. PMEDSAH seems to shield bFGF from denaturation even after 24 hours while TCPS surfaces did not. (c) Adsorbed quantities of bFFGF were quite low on PMEDSAH compared to TCPS. Lowering the temperature did not increase the adsorption of bFGF on PMEDSAH

suring its surface-bound concentration. In this experiment, high bFGF loadings (1600, 4000 and 10000 pg/mL) were employed to make it easier for us to detect surface binding. While the TCPS surfaces retained some of this bFGF, PMEDSAH resisted bFGF adsorption and displayed near-baseline levels of bFGF surface concentration at both 4°C and 37°C . From the results in Figures 7.1(b) and 7.1(c), we can see that surface and solution bFGF concentration profiles follow very different trends. PMEDSAH surfaces do not interact with bFGF but stabilize it in solution, suggesting that like most typical zwitterionic brushes, it is non-fouling. On the other hand, though the TCPS surfaces bind to bFGF at high loadings, they lower its availability in solution by destabilizing its native structure. We anticipate that the non-fouling PMEDSAH surfaces are better at stabilizing the native structure of bFGF in vitro and perhaps extend the protein's half-life, thereby bringing about long-term self-renewal. To prove this conclusively, sum-frequency generation (SFG) spectroscopy would be the ideal approach for elucidating the differences in hydration structure and bFGF stability between PMEDSAH, TCPS and heparin.

A second line of investigation that can provide molecular insights, is a comparative study of adsorption of relevant proteins on a family of zwitterionic polymers, including PMEDSAH. This will help us derive a general chemical basis for the design of polymer coatings for stem cell culture. By identifying both the critical proteins which mediate polymer-cell interactions as well as the relevant molecular motif(s) of the zwitterionic entity, we can expand the library of materials which can support stem cell self renewal, beyond PMEDSAH.

Our unpublished experiments reveal that two other zwitterionic polymer coatings have been successful in self-renewal of hPSCs- poly[2-methacryloyloxyethyl phosphorylcholine] (PMPC), in which the sulfonate (SO_3^-) anion of PMEDSAH is replaced by a phosphonate (PO_4^-) group and poly[({3-methacryloylamino}pro-

pyl)dimethyl {3-sulfopropyl} ammonium hydroxide inner salt] (PMPDSAH) which is the amide analogue of PMEDSAH.[316,317] It is quite possible that these three non-fouling polymers share a molecular motif, perhaps the structure and molecular conformation of the zwitterionic side chains, which may bring about stem cell self-renewal. It has been previously shown that even slight modifications in charge density, ionic separation and chemical functionality can lead to drastic consequences on the self-association, hydration and protein interactions for zwitterionic materials.[318] Hence a systematic investigation of the zwitterionic molecular design parameters on their affinity for ECM proteins would be highly promising.

To investigate polymer-protein interactions further, it would be best to employ surface plasmon resonance (SPR), a sensitive optical technique that can provides a real time view of molecular interactions on a surface.[319,320] Observations can be collected to measure the adsorbed masses of bFGF, collagen, laminin, fibronectin and vitronectin on five surfaces- PMEDSAH, PMPC, PMAPDSAH, the non-zwitterionic PEGMA, and heparin. The first four surfaces are non-fouling and should not retain any protein unless a specific interaction exists, an interaction whose kinetics SPR can capture accurately. Twenty five pairs of adsorption studies will be conducted, real time data collected and adsorption levels quantified. This will enable identification of both critical ECM proteins mediating stem cell-surface signaling as well as shed some light on the effect of chemical structure on specific protein interactions. SPR results can be supplemented by deriving a detailed molecular level understanding from ToF-SIMS (Time-of-flight - secondary ion mass spectrometry) studies of the protein-bound surfaces.

A final recommendation to future investigators is to probe the role of zwitterionic charge distance on the water structure and ability to stabilize bFGF or any of the other molecules in their bioactive conformations. Kratzer et al.[321] have developed synthetic approaches for varying the number of methylene groups be-

tween the sulfonate and the quatenary ammonium charge centers. The variation of charge distance is capable of transforming not only molecular behavior such as its hydration shell,[322] water residence time distributions[323] and the strength of counter-ion associations,[323] but also macroscopically observable behaviour such as UCST transitions.[324] SFG spectroscopic studies on the family of sulfobetaine brushes reported by Kratzer et al.[321] would be an interesting approach to discover whether variations in charge distance can promote or hinder the stabilization of bFGF and other biomolecules critical for self-renewal.

7.2.2 Resetting somatic cells into naïve induced pluripotent stem cells on synthetic substrates

The shortage of organs for transplantation, such as kidneys for patients suffering polycystic kidney disease, or lungs for those afflicted with cystic fibrosis, is aggravated by the difficulty of finding matches from the small pool of brain-dead donors.[325] Immune-matched autologous organs derived from patient cells represent an attractive solution but several engineering barriers exist. Many researchers are currently engineering organs *in vitro* from patient-derived iPSCs using scaffolds composed of decellularized organs, 3D printed constructs or other materials technology for generating "organoids". However, a common criticism of this approach is that this is a reductionist style of thinking that fails to account for the complexity of the cellular niche.[326] Since the exquisite spatiotemporal signaling profiles achieved in our bodies are challenging to replicate *in vitro*, partly due to our imperfect understanding,[325] and partly due to the inaccessibility of complex vascularized organ architectures through bioprinting,[327] it has been suggested that we turn instead to *in vivo* organogenesis via inter-species chimeras.[328]

By integrating patient-derived pluripotent stem cells into suitable host animal embryos, we can allow nature to guide the formation of human pancreases, livers

or kidneys within sheep, pigs or cows.[295] Unfortunately, when hPSCs were introduced into pig embryos, the efficiency of chimera formation was very low and the contribution of the engrafted human stem cells to the organ niche was found to be poor.[329] However rodent PSCs were competent in forming chimeras, triggering investigations into the differences in pluripotent potential between human stem cells and mouse stem cells. These investigations transformed the commonly held understanding of what pluripotency really means and led researchers to question the pluripotent identity of conventional human PSCs.[330] Pluripotent stem cells occupy a continuum of states ranging from "naïve pluripotency", where cells are in a more developmentally immature state and remain unbiased towards differentiation outcomes, to "primed pluripotency" where cells are on the verge of lineage-specific differentiation.[331] From a molecular biology standpoint, naïve stem cells differ from their primed counterparts in their gene expression profiles and in the signaling mechanisms facilitating their self-renewal.[332] Moreover, naïve cells are distinct from conventional primed hPSCS such as hESCs and hiPSCs in two aspects relevant to regenerative medicine. Firstly, they have broader and more robust differentiation potential and can overcome the differentiation biases associated with conventional primed hPSCs.[331] Secondly, naïve hPSCs can competently engraft into chimeras and facilitate organogenesis whereas with primed cells, chimera formation is inefficient and plagued by defects.[331]

The discovery of naïve pluripotency has redrawn the research landscape of stem cell biology but material scientists working in the realm of stem cell engineering are yet to adapt to this new paradigm. Both somatic cells such as fibroblasts as well as embryonic stem cells can be "reset" or reprogrammed into naïve stem cells using specific cell culture conditions, since the maintenance of ground state naïve pluripotency requires use of several cytokines and small molecule inhibitors.[333] Though this resetting has been performed on feeder layers comprising

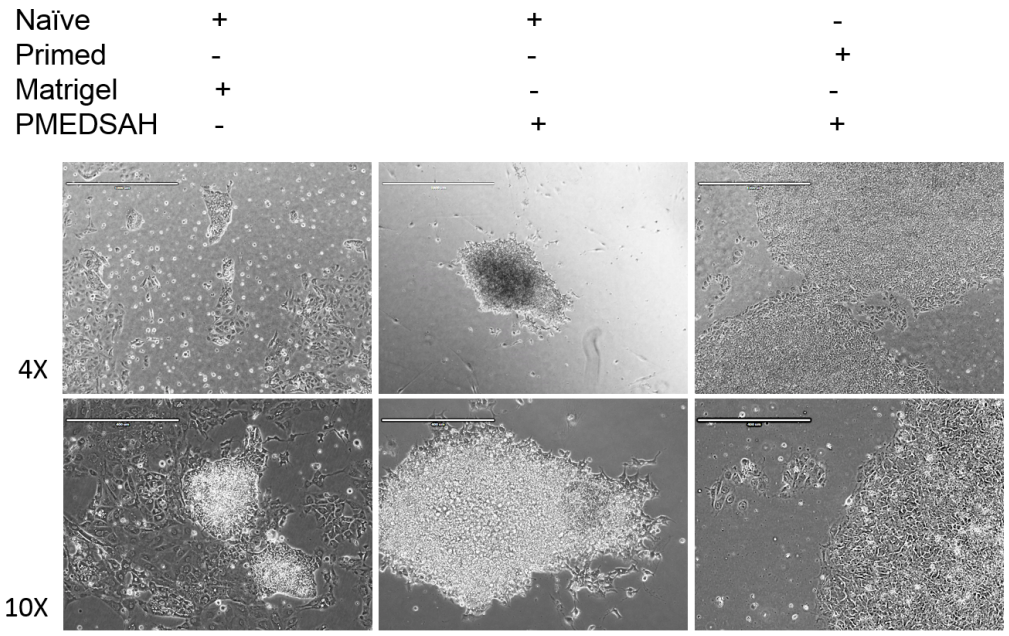

Figure 7.2: Cell culture and reprogramming performed by Prof. Villa-Diaz's lab at Oakland University. Optical micrographs display morphological differences between naïve hIPSCs on matrigel (left) and PMEDSAH (center) and primed cells on PMEDSAH (right). Scale bars are 1000 μm for 4$\times$ and 400 μm for 10$\times$ respectively.

mitotically inactivated mouse embryonic fibroblasts (MEFs), it is anticipated that the development of a fully defined and feeder-free system will minimize the variability associated with the resetting process.

There are two factors motivating the use of PMEDSAH surfaces for resetting and culturing naïve hPSCs. From an industrial research standpoint, it is desirable to ensure reproducibility, stability, ease of use and to reduce batch-to-batch variations by replacing biologically derived substrates with PMEDSAH during this resetting process.[334] From a basic research standpoint, PMEDSAH would be useful in examining the biological effects of stem cell culture substrates on the expression of naïve pluripotency.[335] This aspect is yet to be understood, especially since most studies involving naïve hPSCs were performed on either feeder cells or on Matrigel, both of which are poorly defined.[336] There is a strong consensus among stem cell researchers that integrin expression pathways and the roles played by

various ECM proteins in self-renewal differ substantially between stem cells in the naïve and primed states of pluripotency. Unfortunately it is difficult to probe these differences systematically on ill-defined substrates like Matrigel, whose composition fluctuates randomly from batch to batch.[338] The non-fouling PMEDSAH surfaces, on the other hand, do not participate in integrin signaling processes and are hence ideally positioned to identify the mechanisms and ECMps that facilitate naïve pluripotency.

Our collaborators at Oakland University reported success in reprogramming human fibroblasts into naïve iPSCs on UVO-initiated PMEDSAH surfaces. In Figure 7.2, we can see images from three experiments-: primed iPSCs cultured on PMEDSAH, naïve iPSCs on Matrigel and naïve iPSCS on PMEDSAH. We observed characteristic compact, dome-shaped colonies of naïve iPSCs on PMEDSAH as well as on the Matrigel control surface. In contrast, the primed iPSCs on PMEDSAH exhibited several morphological differences: they were flattened, less densely packed than the naive cells were and lacked the well-defined borders typical of naïve cells. While the naïve iPSCs on PMEDSAH could be more easily dislodged from the surface and were less prone to spontaneous differentiation, their Matrigel-cultured counterparts, despite proliferating faster, differentiated frequently. Embryoid bodies could be generated from the naïve cells, indicating that they maintained their pluripotency on PMEDSAH. These reprogramming studies are currently being replicated for the third time and a detailed evaluation of genetic expression, cell surface markers (preliminary immunostaining results in Figure 7.3) and pluripotency potential are being planned.

Our preliminary results suggest that PMEDSAH is a promising synthetic substrate for resetting fibroblasts into naive stem cells. Future experiments could focus on extending these results to PMEDSAH surfaces prepared using SI-ATRP as opposed to UVO-initiated polymerization. Specifically, by varying the SI-ATRP con-

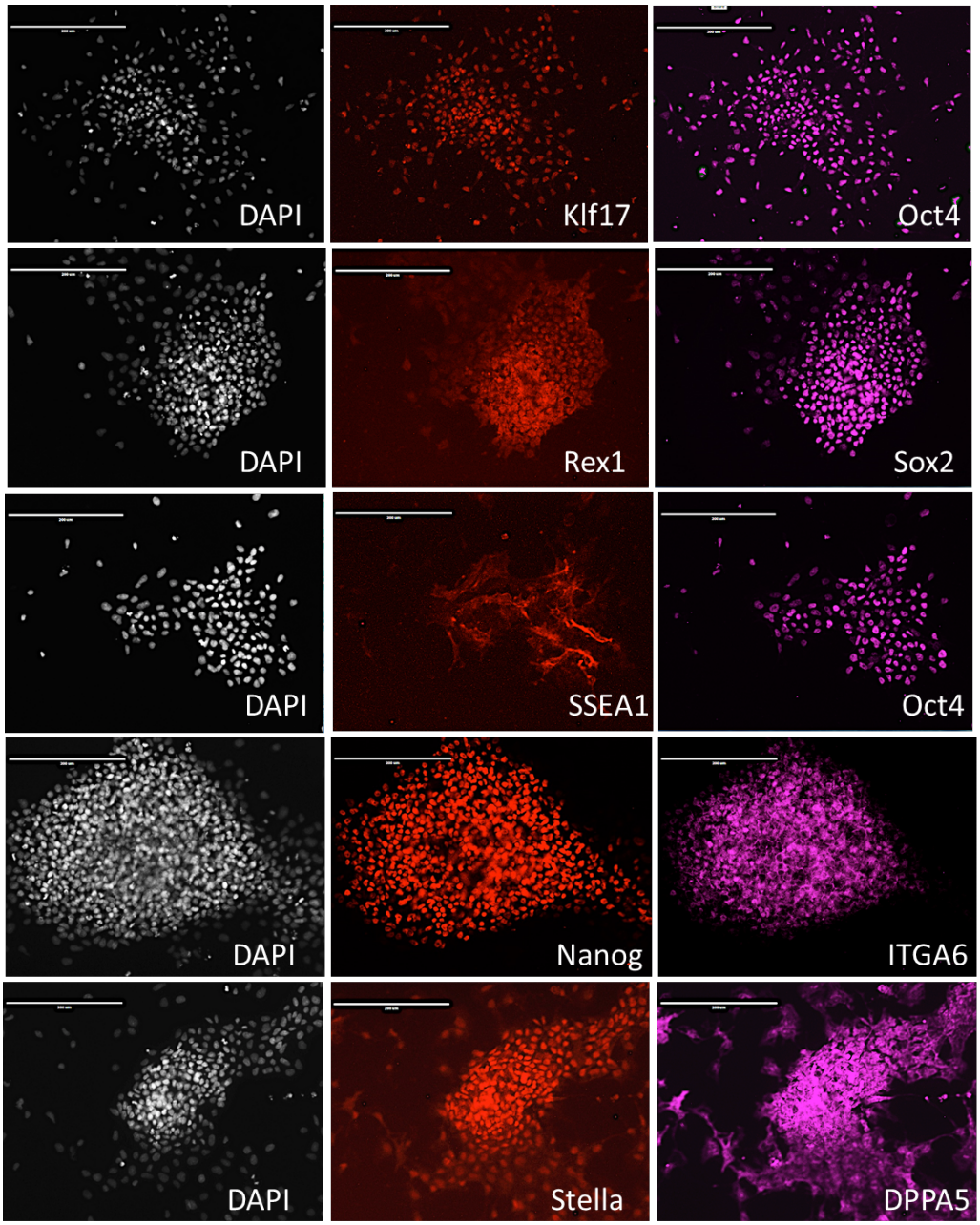

Figure 7.3: Cell culture and reprogramming performed by Prof. Villa-Diaz's lab at Oakland University. Immunostaining reveals the presence of the characteristic cellular markers for naïve hiPSCS

ditions, different polymer brush attributes can be achieved as described in Chapter V. Exploring the impact of PMEDSAH's physiochemical properties on the growth milieu experienced by naïve hiPSCs would be a logical next step for research, especially if we discover a correlation between the coating properties and the development potential of the naïve hiPSCs. If this is true, it would offer a way to enhance the development potential of hiPSCs through simple modifications of the cell culture substrate.

7.3 Future directions: Carbohydrate-functional polymer brushes

7.3.1 Biosensors for influenza

In Chapter IV, we demonstrated the potential of carbohydrate brushes bearing α-mannose, β-glucose and β-galactose side chains as virus-resistant polymer coatings. One of the main sources of their resistance to influenza and adenoviral adhesion is that none of them possess specific interactions with carbohydrate-recognition proteins present on the viral surface. On the other hand, engineering specific affinity-based interactions with viral proteins paves the way for coatings with biosensing capabilities. Preliminary investigations have been concluded with surfaces functionalized with α2,3-linked and α2,6-linked sialyl lactose, which are specific receptors for the binding of avian and human influenza strains respectively[339]. By presenting virus-specific sialyl lactose molecules in the form of polymer brushes, a sensitive, rapid, specific biosensor with the ability to identify different strains of influenza viruses can be synthesized. Prior work on influenza sensors has employed molecular monolayers of α2,3-linked and α2,6-linked sialyllactose, which are receptors for avian and human influenza respectively.[339] Though these glycan-based biosensors have proven to be more sensitive than antibody-based influenza sensors, they do not possess the optimal spatial presentation of

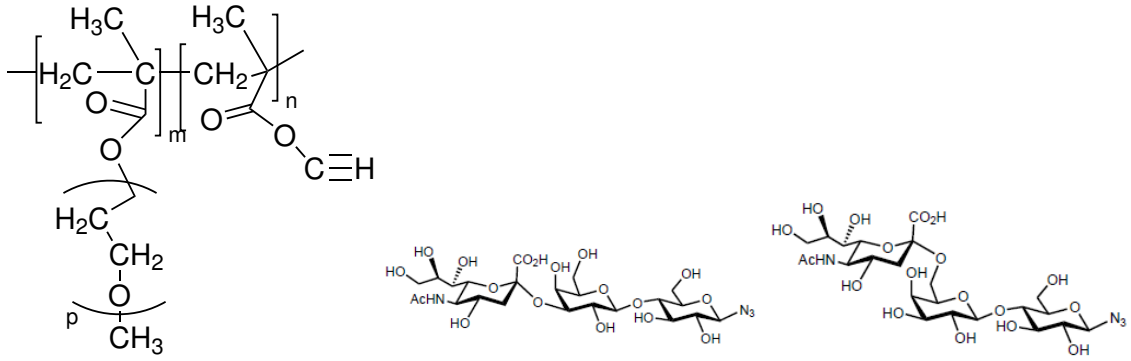

(a) (b) (c)

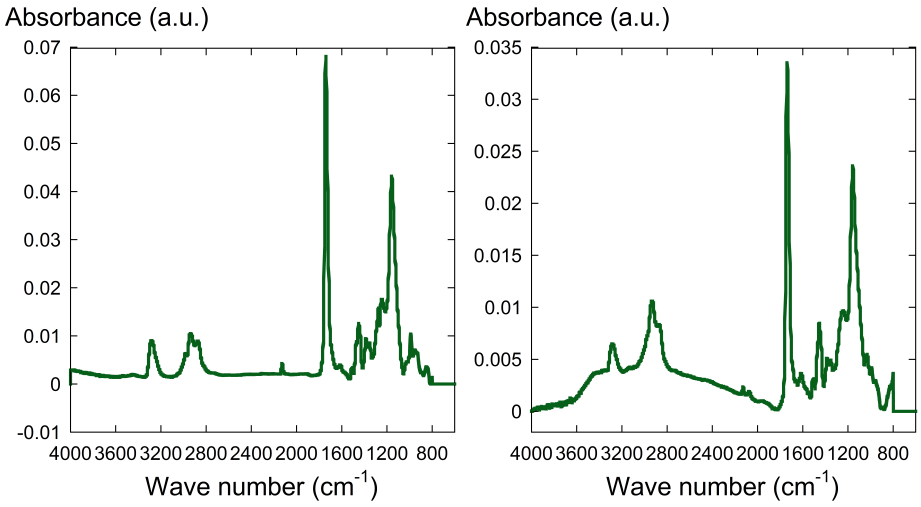

(d) Before Sialyllactose conjugation (e) After Sialyllactose conjugation

Figure 7.4: Chemical structures of (a) poly(propargyl methacrylate-co-{poly(ethylene glycol) methacrylate}) (b) 3′-Sialyllactose azide and (c) 6′-Sialyllactose azide. Using the propargyl-based copolymer brushes as scaffolds, we could obtain surfaces with pendant sialyllactose groups. FTIR spectroscopy confirmed the presence of reactive alkyne groups in (d) at 3325 and 2125 cm^{-1}. The formation of sialyllactose-functional polymer brushes is evident from the appearance of the hydroxyl bands in the 3300 cm^{-1} region as seen in (e).

glycan ligands to maximize virus-glycan avidity. From model predictions of multivalent binding generated in Chapter VI, it appears that influenza-sialyllactose interactions will be more thermodynamically favorable if a brush architecture is employed rather than the monolayers used in recent reports.[48,340] I hypothesize that presenting sialyllactose groups on polymer brushes will result in an orders-of-magnitude improvement in sensor sensitivity over sialyllactose monolayers.

In order to synthesize sialyl lactose brushes, post-polymerization modification of polymer brushes would be preferable since sialyllactose-functional acrylate or acrylamide monomers can be challenging to synthesize.[341,342] To this end, we have employed polymer brushes composed of poly(propargyl methacrylate-co-{poly(ethylene glycol) methacrylate}), which bear pendant alkyne groups, as discussed in in Chapter II. To these propargyl repeat units we can conjugate 3'-sialyllactose azide or 6'-sialyllactose azide, which were synthesized using schemes described elsewhere.[343] Using FTIR, we were able to verify the formation of polymer brushes modified with α2,6-linked sialyllactose (Figure 7.4). Similar conjugation procedures can be used to obtain polymer brushes with pendant α2,3-linked sialyllactose groups. The impact of sialyllactose stereochemistry and architecture on the strain-selectivity and detection limit for two influenza subtypes (H1N1 and H3N2) is yet to be investigated and could be an interesting research avenue for future investigators.

7.3.2 Mannose-functionalized electrospun or 3D-printed mats for wound healing

In Chapter VI, a surface modification strategy for achieving phenotypically selective adhesion of M2 macrophages was outlined. This coating can be translated three-dimensional (3D) wound healing constructs that are biodegradable, where mechanical and geometric features can be finely tuned. While bulk properties such as the mechanical compliance, the degree of fiber alignment and rate of degrada-

tion can be controlled by choosing the appropriate polymer (PLGA or PCL for instance) and the appropriate electrospinning or 3D-printing operating parameters, the wound-material interface can be functionalized with mannose molecules in order to promote the infiltration of M2-polarized macrophages. This gives us a way to independently control the chemical and physical characteristics of the scaffold. *In vivo* studies can be conducted to compare wound healing outcomes from direct injection of M2 macrophages and macrophage-colonized scaffolds of varying geometries and mechanical characteristics.

7.4 Automated high throughput platforms for polymer brush synthesis and data-driven discovery

In this dissertation, multifunctional polymer brushes have been used to develop a platform that is capable of producing large and complex datasets. Future researchers should direct their efforts towards developing tools that can harness the power of data to design improved biomaterial surfaces. Though our synthetic platform gives rise to a rich multidimensional design space, it is nearly impossible to fully explore and exploit this design space using an exclusively experimental approach. In an ideal scenario, we could formulate first-principles based models that maps polymer brush design to physicochemical properties and ultimate biointerfacial behavior, but this is a difficult undertaking. First-principles knowledge is not completely established even for simplistic and well-studied materials systems such as SAMs and is near-impossible to obtain for polymer brushes of novel compositions and architectures. Additionally, knowledge-driven models do not account for material defects and non-idealities. Unbiased data-driven models constructed from decision-oriented design of experiments in combination with statistically guided experimental efforts can result in overarching predictive models

that will prove useful in diverse applications.

There are several challenges to be overcome in order to fully leverage data-driven modeling techniques. In Chapter V, multifactorial statistical models were used to simultaneously evaluate the effects of numerous design variables on material performance on the basis of an economical number of experiments. By systematically sampling a thin slice of the entire design space through an orthogonal experimental matrix where several design variables are varied simultaneously, we can construct response surface models. These regression-based models provide a powerful quantitative framework for not only predicting the material performance in the entire design space, but also provide guidelines for improving performance. A major weakness of this DOE approach is that response surface models require factorially designed experiments, with variable combinations that are defined well in advance, and are executed with a good understanding of the confounding noise factors. Currently, the results obtained from SI-ATRP are sensitive even to seemingly trivial factors such as the rigor of the air-free technique used by the chemist,[344] whether the fume hood lights are on,[345] the inhibitor removal procedures, the presence of contaminants on the substrate etc. For instance, kinetic studies of polymer brush growth conducted by one lab can seldom be replicated exactly in another lab, due to variations in technique and reaction set ups. This scenario is not ideal for the development of data-driven models since they will fail to distinguish between experimental noise and actual effects caused by changes in process variables if we employ a heterogeneous dataset collected from multiple sources. To facilitate data-driven discovery of interesting material properties and the processing condtions that they require, we need dedicated efforts for developing low-cost automated polymer brush synthesis systems.[346]

Modeling efforts will only yield benefits if we can access large datasets, which necessitates automation of the experimental procedures and protocols used. In the

fields of synthetic organic chemistry and to some extent in tissue engineering, this has already happened. Automated (bio)reactors and high throughput platforms are routinely used for screening, optimization and DOE studies, but this technology is yet to be adapted to polymer brush synthesis. Automated high throughput polymer brush synthesis and *in situ* surface characterization will lead to the universal adoption of standardized techniques and protocols, reducing human intervention and operator error to the minimum possible extent. In addition, parallel experimentation is expected to generate much higher volumes of data with the same expenditure of raw material and time. The last consideration is particularly important as sometimes biofunctional monomers such as the carbohydrate-functional acrylamides used in this dissertation, are quite difficult to synthesize and are usually produced in low quantities.[347,348]

A second weakness of DOE-based models is that they are not suitable for retrospective analysis of historical data, say of data found in the literature from irregularly designed and poorly controlled experiments. For instance, SI-ATRP literature is rife with examples of "one factor at a time" (OFAT) experimentation, where one variable is fixed while the other is varied from the lowest level to the highest levels in 3 to 4 increments. OFAT datasets prevent the derivation of reliable statistical models through response surface methodologies as OFAT experimentation ignores the existence of interaction terms and produces high errors in model fitting. However, with the advent of powerful machine learning techniques based on random decision forests, artificial neural networks,[349] robust predictive models can be built retrospectively even from "happenstance data" that is generated from non-factorial and unsystematic experiments. While multivariate regression is of limited utility when confronted with faulty experimental design, other algorithms employed in machine learning are capable of handling these imperfect datasets. However, machine learning will also require large volumes of data,[350] suggesting

that the development of automated high throughput platforms for polymer brush synthesis is an inevitable necessity, irrespective of the algorithms used.

References

[1] Kocak, G.; Tuncer, C.; Butun, V. *Polym. Chem.* **2017**, *8*, 144–176.

[2] Tanaka, M. *Current Opinion in Colloid Interface Science* **2013**, *18*, 432 – 439.

[3] Israelachvili, J. N. In *Intermolecular and Surface Forces (Third Edition)*, third edition ed.; Israelachvili, J. N., Ed.; Academic Press: San Diego, 2011; pp 577 – 616.

[4] Andrews, R. N.; Co, C. C.; Ho, C.-C. *Current Opinion in Chemical Engineering* **2016**, *11*, 28–33.

[5] Israelachvili, J. N. In *Intermolecular and Surface Forces (Third Edition)*, third edition ed.; Israelachvili, J. N., Ed.; Academic Press: San Diego, 2011; pp 617 – 633.

[6] Dunlop, J. W.; Weinkamer, R.; Fratzl, P. *Materials Today* **2011**, *14*, 70 – 78.

[7] Williams, D. F. *Biomaterials* **2014**, *35*, 10009 – 10014.

[8] Ratner, B. D.; Hoffman, A. S.; Schoen, F. J.; Lemons, J. E. In *Biomaterials Science (Third Edition)*, third edition ed.; Ratner, B. D., Hoffman, A. S., Schoen, F. J., Lemons, J. E., Eds.; Academic Press, 2013; pp xxv – xxxix.

[9] Chen, H.; Yuan, L.; Song, W.; Wu, Z.; Li, D. *Progress in Polymer Science* **2008**, *33*, 1059 – 1087.

[10] Kingshott, P.; Andersson, G.; McArthur, S. L.; Griesser, H. J. *Current Opinion in Chemical Biology* **2011**, *15*, 667 – 676, Molecular Machines/Analytical Techniques.

[11] Azzaroni, O. *Journal of Polymer Science Part A: Polymer Chemistry* **2012**, *50*, 3225–3258.

[12] Edmondson, S.; Osborne, V. L.; Huck, W. T. S. *Chemical Society reviews* **2004**, *33*, 14–22.

[13] Zhao, B.; Brittain, W. *Progress in Polymer Science* **2000**, *25*, 677 – 710.

[14] Minko, S. In *Polymer Surfaces and Interfaces: Characterization, Modification and Applications*; Stamm, M., Ed.; Springer Berlin Heidelberg: Berlin, Heidelberg, 2008; pp 215–234.

[15] Brittain, W. J.; Minko, S. *Journal of Polymer Science Part A: Polymer Chemistry* **2007**, *45*, 3505–3512.

[16] Husseman, M.; Malmstrom, E. E.; McNamara, M.; Mate, M.; Mecerreyes, D.; Benoit, D. G.; Hedrick, J. L.; Mansky, P.; Huang, E.; Russell, T. P.; Hawker, C. J. *Macromolecules* **1999**, *32*, 1424–1431.

[17] Barbey, R.; Lavanant, L.; Paripovic, D.; Schüwer, N.; Sugnaux, C.; Tugulu, S.; Klok, H.-A. *Chemical Reviews* **2009**, *109*, 5437–5527.

[18] Chen, W.-L.; Cordero, R.; Tran, H.; Ober, C. K. *Macromolecules* **2017**, *50*, 4089–4113.

[19] Krishnamoorthy, M.; Hakobyan, S.; Ramstedt, M.; Gautrot, J. E. *Chemical Reviews* **2014**, *114*, 10976–11026.

[20] He, W.; Jiang, H.; Zhang, L.; Cheng, Z.; Zhu, X. *Polym. Chem.* **2013**, *4*, 2919–2938.

[21] von Werne, T.; Patten, T. E. *Journal of the American Chemical Society* **1999**, *121*, 7409–7410.

[22] Guo, K.; Freguia, S.; Dennis, P. G.; Chen, X.; Donose, B. C.; Keller, J.; Gooding, J. J.; Rabaey, K. *Environmental Science & Technology* **2013**, *47*, 7563–7570.

[23] Ameringer, T.; Ercole, F.; Tsang, K. M.; Coad, B. R.; Hou, X.; Rodda, A.; Nisbet, D. R.; Thissen, H.; Evans, R. A.; Meagher, L.; Forsythe, J. S. *Biointerphases* **2013**, *8*, 16.

[24] Sanchez, L. D.; Brack, N.; Postma, A.; Pigram, P. J.; Meagher, L. *Biomaterials* **2016**, *106*, 24 – 45.

[25] Yuan, W.; Feng, Y.; Wang, H.; Yang, D.; An, B.; Zhang, W.; Khan, M.; Guo, J. *Materials Science and Engineering: C* **2013**, *33*, 3644 – 3651.

[26] Kim, J. Y.; Lee, B. S.; Choi, J.; Kim, B. J.; Choi, J. Y.; Kang, S. M.; Yang, S. H.; Choi, I. S. *Angewandte Chemie International Edition* **2016**, *55*, 15306–15309.

[27] Zoppe, J. O.; Ataman, N. C.; Mocny, P.; Wang, J.; Moraes, J.; Klok, H. A. *Chemical Reviews* **2017**, *117*, 1105–1318.

[28] Matyjaszewski, K.; Tsarevsky, N. V. *Nature Chemistry* **2009**, *1*, 276 EP –, Review Article.

[29] Peng, B.; Johannsmann, D.; Ruhe, J. *Macromolecules* **1999**, *32*, 6759–6766.

[30] Hamelinck, P. J.; Huck, W. T. S. *J. Mater. Chem.* **2005**, *15*, 381–385.

[31] Hou, L.; Zhou, M.; Dong, X.; Wang, L.; Xie, Z.; Dong, D.; Zhang, N. *Chemistry - A European Journal* **2017**, *23*, 13337–13341.

[32] Whiting, G. L.; Snaith, H. J.; Khodabakhsh, S.; Andreasen, J. W.; Breiby, D. W.; Nielsen, M. M.; Greenham, N. C.; Friend, R. H.; Huck, W. T. S. *Nano Letters* **2006**, *6*, 573–578, PMID: 16522065.

[33] Alexander, S., *J. Phys. France* **1977**, *38*, 983–987.

[34] de Gennes, P. G. *Macromolecules* **1980**, *13*, 1069–1075.

[35] Milner, S. T. *Science* **1991**, *251*, 905–914.

[36] Lai, P.; Zhulina, E. *Journal de physique II* **1992**, *2*, 547–560.

[37] Dan, N.; Tirrell, M. *Macromolecules* **1992**, *25*, 2890–2895.

[38] Carignano, M.; Szleifer, I. *journal of chemical physics* **1993**, *98*, 5006–5018.

[39] Halperin, A. *Langmuir* **1999**, *15*, 2525–2533.

[40] Chakrabarti, A. *Journal of Chemical Physics* **1994**, *100*, 631–635.

[41] Sofia, S.; Premnath, V.; Merrill, E. *Macromolecules* **1998**, *31*, 5059–5070.

[42] Matyjaszewski, K.; Miller, P. J.; Shukla, N.; Immaraporn, B.; Gelman, A.; Luokala, B. B.; Siclovan, T. M.; Kickelbick, G.; Vallant, T.; Hoffmann, H.; Pakula, T. *Macromolecules* **1999**, *32*, 8716–8724.

[43] Pyun, J.; Kowalewski, T.; Matyjaszewski, K. *Macromolecular Rapid Communications* **2003**, *24*, 1043–1059.

[44] Lee, K.-B.; Park, S.-J.; Mirkin, C. A.; Smith, J. C.; Mrksich, M. *Science* **2002**, *295*, 1702–1705.

[45] Falconnet, D.; Csucs, G.; Grandin, H. M.; Textor, M. *Biomaterials* **2006**, *27*, 3044 – 3063.

[46] Tseng, P.; Di Carlo, D. *Advanced Materials* **2014**, *26*, 1242–1247.

[47] Oyelaran, O.; Gildersleeve, J. C. *Current Opinion in Chemical Biology* **2009**, *13*, 406 – 413, Analytical Techniques/Mechanisms.

[48] Hushegyi, A.; Pihikova, D.; Bertok, T.; Adam, V.; Kizek, R.; Tkac, J. *Biosensors and Bioelectronics* **2016**, *79*, 644 – 649.

[49] Offenhausser, A.; Bocker-Meffert, S.; Decker, T.; Helpenstein, R.; Gasteier, P.; Groll, J.; Moller, M.; Reska, A.; Schafer, S.; Schulte, P.; Vogt-Eisele, A. *Soft Matter* **2007**, *3*, 290–298.

[50] Tan, K. Y.; Lin, H.; Ramstedt, M.; Watt, F. M.; Huck, W. T. S.; Gautrot, J. E. *Integr. Biol.* **2013**, *5*, 899–910.

[51] Chen, S.; Li, L.; Zhao, C.; Zheng, J. *Polymer* **2010**, *51*, 5283 – 5293.

[52] Delaney, J. T.; Smith, P. J.; Schubert, U. S. *Soft Matter* **2009**, *5*, 4866–4877.

[53] Hoff, J. D.; Cheng, L. J.; Meyhöfer, E.; Guo, L. J.; Hunt, A. J. *Nano Letters* **2004**, *4*, 853–857.

[54] Xie, Z.; Chen, C.; Zhou, X.; Gao, T.; Liu, D.; Miao, Q.; Zheng, Z. *ACS Applied Materials and Interfaces* **2014**, *6*, 11955–11964.

[55] Wood, M. *Journal of The Royal Society Interface* **2007**, *4*, 1–17.

[56] Bat, E.; Lee, J.; Lau, U. Y.; Maynard, H. D. *Nature Communications* **2015**, *6*, 6654.

[57] Javaherian, S.; O'Donnell, K. A.; McGuigan, A. P. *PLOS ONE* **2011**, *6*, 1–8.

[58] Suh, K.; Langer, R.; Lahann, J. *Advanced Materials* **2004**, *16*, 1401–1405.

[59] Voskuhl, J.; Brinkmann, J.; Jonkheijm, P. *Current Opinion in Chemical Biology* **2014**, *18*, 1–7.

[60] Filipponi, L.; Livingston, P.; Kašpar, O.; Tokárová, V.; Nicolau, D. V. *Biomedical Microdevices* **2016**, *18*, 1–7.

[61] Chen, W.; Villa-Diaz, L. G.; Sun, Y.; Weng, S.; Kim, J. K.; Lam, R. H. W.; Han, L.; Fan, R.; Krebsbach, P. H.; Fu, J. *ACS Nano* **2012**, *6*, 4094–4103, PMID: 22486594.

[62] Bernards, M. T.; Cheng, G.; Zhang, Z.; Chen, S. *Macromolecules* **2008**, *41*, 4216–4219.

[63] Waichman, S.; Bhagawati, M.; Podoplelova, Y.; Reichel, A.; Brunk, A.; Paterok, D.; Piehler, J. *Analytical Chemistry* **2010**, *82*, 1478–1485.

[64] Gautrot, J. E.; Huck, W. T. S.; Welch, M.; Ramstedt, M. *ACS Applied Materials and Interfaces* **2010**, *2*, 193–202.

[65] Hawker, C. J.; Bosman, A. W.; Harth, E. *Chemical Reviews* **2001**, *101*, 3661–3688.

[66] Shanmugam, S.; Xu, J.; Boyer, C. *Macromolecules* **2016**, *49*, 9345–9357.

[67] Yang, Q.; Lalevée, J.; Poly, J. *Macromolecules* **2016**, *49*, 7653–7666.

[68] Discekici, E. H.; Pester, C. W.; Treat, N. J.; Lawrence, J.; Mattson, K. M.; Narupai, B.; Toumayan, E. P.; Luo, Y.; McGrath, A. J.; Clark, P. G.; Read de Alaniz, J.; Hawker, C. J. *ACS Macro Letters* **2016**, *5*, 258–262.

[69] Page, Z. A.; Narupai, B.; Pester, C. W.; Bou Zerdan, R.; Sokolov, A.; Laitar, D. S.; Mukhopadhyay, S.; Sprague, S.; McGrath, A. J.; Kramer, J. W.; Trefonas, P.; Hawker, C. J. *ACS Central Science* **2017**, *3*, 654–661.

[70] Johnson, A.; Madsen, J.; Chapman, P.; Alswieleh, A.; Al Jaf, O.; Bao, P.; Hurley, C.; Cartron, M. L.; Evans, S.; Hobbs, J.; Hunter, N.; Armes, S. P.; Leggett, G. J. *Chem. Sci.* **2017**, *8*, 4517–4526.

[71] Zhou, X.; Wang, X.; Shen, Y.; Xie, Z.; Zheng, Z. *Angewandte Chemie - International Edition* **2011**, *50*, 6506–6510.

[72] Zhou, X.; Liu, X.; Xie, Z.; Zheng, Z. *Nanoscale* **2011**, *3*, 4929.

[73] Chen, C.; Zhou, X.; Xie, Z.; Gao, T.; Zheng, Z. *Small* **2015**, *11*, 613–621.

[74] Li, Y.; Zhang, J.; Fang, L.; Jiang, L.; Liu, W.; Wang, T.; Cui, L.; Sun, H.; Yang, B. *Journal of Materials Chemistry* **2012**, *22*, 25116.

[75] Li, Y.; Zhang, J.; Liu, W.; Li, D.; Fang, L.; Sun, H.; Yang, B. *ACS Applied Materials and Interfaces* **2013**, *5*, 2126–2132.

[76] Kettling, F.; Vonhören, B.; Krings, J. A.; Saito, S.; Ravoo, B. J. *Chem. Commun.* **2015**, *51*, 1027–1030.

[77] Fan, X.; Lin, L.; Dalsin, J. L.; Messersmith, P. B. *Journal of the American Chemical Society* **2005**, *127*, 15843–15847.

[78] Wei, Q.; Yu, B.; Wang, X.; Zhou, F. *Macromolecular Rapid Communications* **2014**, *35*, 1046–1054.

[79] Rodriguez-Emmenegger, C.; Preuss, C. M.; Yameen, B.; Pop-Georgievski, O.; Bachmann, M.; Mueller, J. O.; Bruns, M.; Goldmann, A. S.; Bastmeyer, M.; Barner-Kowollik, C. *Advanced Materials* **2013**, *25*, 6123–6127.

[80] Paik, M. Y.; Xu, Y.; Rastogi, A.; Tanaka, M.; Yi, Y.; Ober, C. K. *Nano Letters* **2010**, *10*, 3873–3879.

[81] Rastogi, A.; Paik, M. Y.; Tanaka, M.; Ober, C. K. *ACS Nano* **2010**, *4*, 771–780.

[82] Arumugam, S.; Orski, S. V.; Locklin, J.; Popik, V. V. *Journal of the American Chemical Society* **2012**, *134*, 179–182.

[83] Iwata, R.; Suk-In, P.; Hoven, V. P.; Takahara, A.; Akiyoshi, K.; Iwasaki, Y. *Biomacromolecules* **2004**, *5*, 2308–2314.

[84] Panzarasa, G.; Soliveri, G.; Sparnacci, K.; Ardizzone, S. *Chem. Commun.* **2015**, *51*, 7313–7316.

[85] Ahn, S. J.; Kaholek, M.; Lee, W.-K.; LaMattina, B.; LaBean, T. H.; Zauscher, S. *Advanced Materials* **2004**, *16*, 2141–2145.

[86] Okazaki, S. *Microelectronic Engineering* **2015**, *133*, 23 – 35.

[87] Hu, Z.; Shao, Q.; Moloney, M. G.; Xu, X.; Zhang, D.; Li, J.; Zhang, C.; Huang, Y. *Macromolecules* **2017**, *50*, 1422–1429.

[88] Rajender, N.; Suresh, K. I. *Macromolecular Materials and Engineering* **2016**, *301*, 81–92.

[89] Wang, X.; Zhou, M.; Zhu, Y.; Miao, J.; Mao, C.; Shen, J. *J. Mater. Chem. B* **2013**, *1*, 2132–2138.

[90] Nandivada, H.; Chen, H. Y.; Lahann, J. *Macromolecular Rapid Communications* **2005**, *26*, 1794–1799.

[91] Koenig, M.; Lahann, J. *Beilstein Journal of Nanotechnology* **2017**, *8*, 1250–1256.

[92] Nandivada, H.; Chen, H.-y.; Bondarenko, L.; Lahann, J. *Angewandte Chemie (International ed. in English)* **2006**, *45*, 3360–3363.

[93] Deng, X.; Friedmann, C.; Lahann, J. *Angewandte Chemie International Edition* **2011**, *50*, 6522–6526.

[94] Chen, H.-Y.; Rouillard, J.-M.; Gulari, E.; Lahann, J. *Proceedings of the National Academy of Sciences* **2007**, *104*, 11173–11178.

[95] Jiang, X.; Chen, H.-Y.; Galvan, G.; Yoshida, M.; Lahann, J. *Advanced Functional Materials* **2008**, *18*, 27–35.

[96] Chen, H. Y.; Lahann, J. *Advanced Materials* **2007**, *19*, 3801–3808.

[97] Chen, H. Y.; Lahann, J. *Langmuir* **2011**, *27*, 34–48.

[98] Crespo-Quesada, M.; Andanson, J. M.; Yarulin, A.; Lim, B.; Xia, Y.; Kiwi-Minsker, L. *Langmuir* **2011**, *27*, 7909–7916.

[99] Aliaga, C.; Park, J. Y.; Yamada, Y.; Lee, H. S.; Tsung, C.-k.; Yang, P.; Somorjai, G. A. *Journal of Physical Chemistry C* **2009**, *113*, 6150–6155.

[100] Sheridan, R. J.; Orski, S. V.; Muramoto, S.; Stafford, C. M.; Beers, K. L. *Langmuir* **2016**, *32*, 8071–8076, PMID: 27442615.

[101] Goda, T.; Ishihara, K.; Miyahara, Y. *Journal of Applied Polymer Science* **2015**, *132*.

[102] Wiarachai, O.; Vilaivan, T.; Iwasaki, Y.; Hoven, V. P. *Langmuir* **2016**, *32*, 1184–1194, PMID: 26695478.

[103] Zhang, Z.; Chen, S.; Chang, Y.; ; Jiang, S. *The Journal of Physical Chemistry B* **2006**, *110*, 10799–10804.

[104] Werner, C. In *Polymer Surfaces and Interfaces: Characterization, Modification and Applications*; Stamm, M., Ed.; Springer Berlin Heidelberg: Berlin, Heidelberg, 2008; pp 299–318.

[105] Ratner, B. D. *Journal of Biomedical Materials Research* **1993**, *27*, 837–850.

[106] Hoffman, A. S. *Biomaterials: Interfacial Phenomena and Applications*; American Chemical Society, 1982; Chapter 2, pp 3–8.

[107] Shen, L.; Zhu, J. *Advances in Colloid and Interface Science* **2016**, *228*, 40 – 54.

[108] Bedair, T. M.; Cho, Y.; Joung, Y. K.; Han, D. K. *Colloids and Surfaces B: Biointerfaces* **2014**, *122*, 808 – 817.

[109] Higaki, Y.; Kobayashi, M.; Murakami, D.; Takahara, A. *Polymer Journal* **2016**, *48*, 325–331.

[110] Hadjesfandiari, N.; Yu, K.; Mei, Y.; Kizhakkedathu, J. N. *J. Mater. Chem. B* **2014**, *2*, 4968–4978.

[111] Gon, S.; Bendersky, M.; Ross, J. L.; Santore, M. M. *Langmuir* **2010**, *26*, 12147–12154, PMID: 20557060.

[112] Gon, S.; Santore, M. M. *Langmuir* **2011**, *27*, 1487–1493, PMID: 21207949.

[113] Gon, S.; Kumar, K.-N.; NÃijsslein, K.; Santore, M. M. *Macromolecules* **2012**, *45*, 8373–8381, PMID: 23148127.

[114] Kalasin, S.; Dabkowski, J.; Nüsslein, K.; Santore, M. M. *Colloids and Surfaces B: Biointerfaces* **2010**, *76*, 489–495.

[115] Duffadar, R. D.; Davis, J. M. *Journal of Colloid and Interface Science* **2008**, *326*, 18–27.

[116] Qin, G.; Cai, C. *Chem. Commun.* **2009**, 5112–5114.

[117] Luk, Y.-Y.; Kato, M.; Mrksich, M. *Langmuir* **2000**, *16*, 9604–9608.

[118] Reitsma, S.; Slaaf, D. W.; Vink, H.; van Zandvoort, M. A. M. J.; oude Egbrink, M. G. A. *Pflügers Archiv - European Journal of Physiology* **2007**, *454*, 345–359.

[119] Ham, H. O.; Park, S. H.; Kurutz, J. W.; Szleifer, I. G.; Messersmith, P. B. *Journal of the American Chemical Society* **2013**, *135*, 13015–13022, PMID: 23919653.

[120] Hower, J. C.; He, Y.; Bernards, M. T.; Jiang, S. *The Journal of Chemical Physics* **2006**, *125*, 214704.

[121] Hower, J. C.; He, Y.; Jiang, S. *The Journal of Chemical Physics* **2008**, *129*, 215101.

[122] Michen, B.; Graule, T. *Journal of Applied Microbiology* **2010**, *109*, 388–397.

[123] Young, A. G.; McQuillan, A. J. *Langmuir* **2009**, *25*, 3538–3548.

[124] Cuba-Chiem, L. T.; Huynh, L.; Ralston, J.; Beattie, D. A. *Langmuir* **2008**, *24*, 8036–8044.

[125] Seitz, R.; Brings, R.; Geiger, R. *Applied Surface Science* **2005**, *252*, 154–157.

[126] Vörös, J.; Ramsden, J. J.; Csúcs, G.; Szendro, I.; Paul, S. M. D.; Textor, M.; Spencer, N. D. *Biomaterials* **2002**, *23*, 3699–3710.

[127] Höök, F.; Vörös, J.; Rodahl, M.; Kurrat, R.; Böni, P.; Ramsden, J. J.; Textor, M.; Spencer, N. D.; Tengvall, P.; Gold, J.; Kasemo, B. *Colloids and Surfaces B: Biointerfaces* **2002**, *24*, 155–170.

[128] Wertz, C. F.; and Maria M. Santore, *Langmuir* **2002**, *18*, 1190–1199.

[129] Toscano, A.; and Maria M. Santore, *Langmuir* **2006**, *22*, 2588–2597.

[130] Schönherr, H.; Johnson, J. M.; Lenz, P.; Frank, C. W.; and Steven G. Boxer, *Langmuir* **2004**, *20*, 11600–11606.

[131] Cheng, C. I.; Chang, Y.-P.; Chu, Y.-H. *Chem. Soc. Rev.* **2012**, *41*, 1947–1971.

[132] Dixon, M. C. **2008**, 151–158.

[133] Mao, Y.; Bao, Y.; Wang, W.; Li, Z.; Li, F.; Niu, L. *American journal of analytical chemsitry* **2011**, *22011*, 589–604.

[134] Wang, W.; Wolff, M. W.; Reichl, U.; Sundmacher, K. *Journal of Chromatography A* **2014**, *1326*, 125–129.

[135] Scherr, S. M.; Daaboul, G. G.; Trueb, J.; Sevenler, D.; Fawcett, H.; Goldberg, B.; Connor, J. H.; Selim, M. U. *ACS nano* **2016**,

[136] Tandon, V.; Bhagavatula, S. K.; Nelson, W. C.; Kirby, B. J. *Electrophoresis* **2008**, *29*, 1092–1101.

[137] Patolsky, F.; Zheng, G.; Hayden, O.; Lakadamyali, M.; Zhuang, X.; Lieber, C. M. *Proceedings of the National Academy of Sciences of the United States of America* **2004**, *101*, 14017–14022.

[138] Froeter, P.; Huang, Y.; Cangellaris, O. V.; Huang, W.; Dent, E. W.; Gillette, M. U.; Williams, J. C.; Li, X. *ACS Nano* **2014**, *8*, 11108–11117.

[139] Tofail, S. A. M.; Bauer, J. *Advanced Materials* **2016**, *28*, 5470–5484.

[140] Hunt, J. A.; Flanagan, B. F.; McLaughlin, P. J.; Strickland, I.; Williams, D. F. *Journal of Biomedical Materials Research* **1996**, *31*, 139–144.

[141] Norde, W.; Fraaye, J. G. Î. M.; Lyklema, J. Protein Adsorption at Solid-Liquid Interfaces : A Colloid-Chemical Approach. 1987.

[142] Norde, W.; Rouwendal, E. *Journal of Colloid and Interface Science* **1990**, *139*, 169–176.

[143] Etheve, J.; Dejardin, P. *Langmuir* **2002**, *18*, 1777–1785.

[144] Rezwan, K.; Meier, L. P.; Rezwan, M.; Vo, J.; Textor, M.; Gauckler, L. J. *Langmuir* **2004**, *20*, 10055–10061.

[145] Wasilewska, M.; Adamczyk, Z. *Langmuir* **2011**, *27*, 686–696.

[146] Armanious, A.; Aeppli, M.; Jacak, R.; Refardt, D.; Sigstam, T.; Kohn, T.; Sander, M. *Environmental Science & Technology* **2016**, *50*, 732–743.

[147] Gutierrez, L.; Mylon, S. E.; Nash, B.; Nguyen, T. H. *Environmental Science & Technology* **2010**, *44*, 4552–4557.

[148] Adamczyk, Z.; Zaucha, M.; Zembala, M. *Langmuir* **2010**, *26*, 9368–9377.

[149] Savaji, K. V.; Niitsoo, O.; Couzis, A. *Journal of Colloid And Interface Science* **2014**, *431*, 165–175.

[150] Dev, A.; Horak, J.; Kaiser, A.; Yuan, X.; Perols, A.; Björk, P.; Karlström, A. E.; Kleimann, P.; Linnros, J. *Biosensors and Bioelectronics* **2016**, *82*, 55–63.

[151] Elkasabi, Y.; Chen, H.-Y.; Lahann, J. *Advanced Materials* **2006**, *18*, 1521–1526.

[152] Sharon L. Walker,; Bhattacharjee, S.; Eric M. V. Hoek,; and Menachem Elimelech, *Langmuir* **2002**, *18*, 2193–2198.

[153] Werner, C.; Zimmermann, R.; Kratzmüller, T. *Colloids and Surfaces A: Physicochemical and Engineering Aspects* **2001**, *192*, 205–213.

[154] Werner, C.; Körber, H.; Zimmermann, R.; Dukhin, S.; Jacobasch, H.-J. *Journal of Colloid and Interface Science* **1998**, *208*, 329–346.

[155] Lyklema, J.; Overbeek, J. *Journal of Colloid Science* **1961**, *16*, 501–512.

[156] Sauerbrey, G. *Zeitschrift für Physik* **1959**, *155*, 206–222.

[157] Jain, A.; Cheng, K. *Journal of Controlled Release* **2017**, *245*, 27 – 40.

[158] Srisa-Art, M.; Dyson, E. C.; deMello, A. J.; Edel, J. B. *Analytical Chemistry* **2008**, *80*, 7063–7067, PMID: 18712935.

[159] Livnah, O.; Bayer, E. A.; Wilchek, M.; Sussman, J. L. *Proceedings of the National Academy of Sciences* **1993**, *90*, 5076–5080.

[160] Su, X.; Wu, Y.-j.; Knoll, W. *Biosensors and Bioelectronics* **2005**, *21*, 719–726.

[161] Seto, H.; Yamashita, C.; Kamba, S.; Kondo, T.; Hasegawa, M.; Matsuno, M.; Ogawa, Y.; Hoshino, Y.; Miura, Y. *Langmuir* **2013**, *29*, 9457–9463.

[162] Nguyen, T. T.; Sly, K. L.; Conboy, J. C. *Analytical Chemistry* **2012**, *84*, 201–208, PMID: 22122646.

[163] Edwards, P.; Gill, A.; Pollardknight, D.; Hoare, M.; Buckle, P.; Lowe, P.; Leatherbarrow, R. *Analytical Biochemistry* **1995**, *231*, 210–217.

[164] Zhang, L.; Huo, W.; Gao, Y.; Shi, S.; Gao, Y. *IEEE Transactions on Magnetics* **2015**, *51*, 1–4.

[165] Weinbaum, S.; Zhang, X.; Han, Y.; Vink, H.; Cowin, S. C. *Proceedings of the National Academy of Sciences* **2003**, *100*, 7988–7995.

[166] Koopal, L. K.; Avena, M. *Colloids and Surfaces A: Physicochemical and Engineering Aspects* **2001**, *192*, 93–107.

[167] Jones, D. M.; Brown, A. A.; Huck, W. T. S. *Langmuir* **2002**, *18*, 1265–1269.

[168] Palacio, M. L. B.; Bhushan, B. *Philosophical Transactions of the Royal Society A: Mathematical, Physical and Engineering Sciences* **2012**, *370*, 2321–2347.

[169] Wang, D.; Harrer, S.; Luan, B.; Stolovitzky, G.; Peng, H.; Afzali-Ardakani, A. *Scientific Reports* **2015**, *4*, 3985.

[170] Campoccia, D.; Montanaro, L.; Arciola, C. R. *Biomaterials* **2006**, *27*, 2331–2339.

[171] Seidel, M.; Jurzik, L.; Brettar, I.; H??fle, M. G.; Griebler, C. *Environmental Earth Sciences* **2016**, *75*.

[172] Shoham, D. *Critical reviews in microbiology* **2013**, *39*, 123–138.

[173] Katsikogianni, M.; Missirlis, Y. F. *European Cells and Materials* **2004**, *8*, 37–57.

[174] Kevin L . Prime and George M . Whitesides, *Science (New York, N.Y.)* **2009**, *252*, 1164–1167.

[175] Ostuni, E.; Chapman, R. G.; Liang, M. N.; Meluleni, G.; Pier, G.; Ingber, D. E.; Whitesides, G. M. *Langmuir* **2001**, *17*, 6336–6343.

[176] Mrksich, M.; Whitesides, G. M. *Annual Review of Biophysics and Biomolecular Structure* **1996**, *25*, 55–78.

[177] Mrksich, M.; Sigal, G. B.; Whitesides, G. M. *Langmuir : the ACS journal of surfaces and colloids* **1995**, *11*, 4383–4385.

[178] Srisombat, L.; Jamison, A. C.; Lee, T. R. *Colloids and Surfaces A: Physicochemical and Engineering Aspects* **2011**, *390*, 1–19.

[179] Flynn, N. T.; Tran, T. N. T.; Cima, M. J.; Langer, R. *Langmuir* **2003**, *19*, 10909–10915.

[180] Hucknall, A.; Rangarajan, S.; Chilkoti, A. *Advanced Materials* **2009**, *21*, 2441–2446.

[181] Yu, K.; Lo, J. C.; Mei, Y.; Haney, E. F.; Siren, E.; Kalathottukaren, M. T.; Hancock, R. E.; Lange, D.; Kizhakkedathu, J. N. *ACS Applied Materials and Interfaces* **2015**, *7*, 28591–28605.

[182] Hori, K.; Matsumoto, S. *Biochemical Engineering Journal* **2010**, *48*, 424–434.

[183] Norde, W.; Lyklema, J. *Colloids and Surfaces* **1989**, *38*, 1–13.

[184] Suzuki, H.; Muhammad Nurul, H.; Seki, T.; Kawamoto, T.; Haga, H.; Kawabata, K.; Takeoka, Y. *Macromolecules* **2010**, *43*, 9945–9956.

[185] Wu, T.; Efimenko, K.; Genzer, J. *Journal of the American Chemical Society* **2002**, *124*, 9394–9395.

[186] Lego, B.; François, M.; Skene, W. G.; Giasson, S. *Langmuir* **2009**, *25*, 5313–5321.

[187] Yamamoto, S.; Ejaz, M.; Tsujii, Y.; Fukuda, T. *Macromolecules* **2000**, *33*, 5608–5612.

[188] Wolski, K.; Gruszkiewicz, A.; Wytrwal-Sarna, M.; Bernasik, A.; Zapotoczny, S. *Polym. Chem.* **2017**, *8*, 6250–6262.

[189] Kalasin, S.; Letteri, R. A.; Emrick, T.; Santore, M. M. *Langmuir* **2017**, *33*, 13708–13717.

[190] Schneck, E.; Schollier, A.; Halperin, A.; Moulin, M.; Haertlein, M.; Sferrazza, M.; Fragneto, G. *Langmuir* **2013**, *29*, 14178–14187.

[191] Faulón Marruecos, D.; Kastantin, M.; Schwartz, D. K.; Kaar, J. L. *Biomacromolecules* **2016**, *17*, 1017–1025.

[192] Al-Ani, A.; Pingle, H.; P Reynolds, N.; Wang, P.-Y.; Kingshott, P. *Polymers* **2017**, *9*, 343.

[193] Emilsson, G.; Schoch, R. L.; Feuz, L.; Höök, F.; Lim, R. Y.; Dahlin, A. B. *ACS Applied Materials and Interfaces* **2015**, *7*, 7505–7515.

[194] Heinen, S.; Weinhart, M. *Langmuir* **2017**, *33*, 2076–2086.

[195] Singh, N.; Cui, X.; Boland, T.; Husson, S. M. *Biomaterials* **2007**, *28*, 763–771.

[196] Wu, J.; Mao, Z.; Gao, C. *Biomaterials* **2012**, *33*, 810–820.

[197] Cringus-Fundeanu, I.; Luijten, J.; Van Der Mei, H. C.; Busscher, H. J.; Schouten, A. J. *Langmuir* **2007**, *23*, 5120–5126.

[198] Choi, S.; Choi, B. C.; Xue, C.; Leckband, D. *Biomacromolecules* **2013**, *14*, 92–100.

[199] Chang, Y.; Chang, Y.; Higuchi, A.; Shih, Y. J.; Li, P. T.; Chen, W. Y.; Tsai, E. M.; Hsiue, G. H. *Langmuir* **2012**, *28*, 4309–4317.

[200] Lu, C. Y.; Zhou, N. L.; Xiao, Y. H.; Tang, Y. D.; Jin, S. X.; Wu, Y.; Zhang, J.; Shen, J. *Applied Surface Science* **2012**, *258*, 3920–3926.

[201] Ibanescu, S. A.; Nowakowska, J.; Khanna, N.; Landmann, R.; Klok, H. A. *Macromolecular Bioscience* **2016**, *16*, 676–685.

[202] Yadav, V.; Jaimes-Lizcano, Y. A.; Dewangan, N. K.; Park, N.; Li, T.-H.; Robertson, M. L.; Conrad, J. C. *ACS Applied Materials & Interfaces* **2017**, acsami.7b14416.

[203] Pidhatika, B.; Möller, J.; Benetti, E. M.; Konradi, R.; Rakhmatullina, E.; Mühlebach, A.; Zimmermann, R.; Werner, C.; Vogel, V.; Textor, M. *Biomaterials* **2010**, *31*, 9462–9472.

[204] Zou, Y.; Rossi, N. A.; Kizhakkedathu, J. N.; Brooks, D. E. *Macromolecules* **2009**, *42*, 4817–4828.

[205] Zhu, X.; Guo, S.; He, T.; Jiang, S.; Jańczewski, D.; Vancso, G. J. *Langmuir* **2016**, *32*, 1338–1346.

[206] Guo, S.; Jańczewski, D.; Zhu, X.; Quintana, R.; He, T.; Neoh, K. G. *Journal of Colloid and Interface Science* **2015**, *452*, 43–53.

[207] Duffadar, R.; Kalasin, S.; Davis, J. M.; Santore, M. M. *Journal of Colloid and Interface Science* **2009**, *337*, 396–407.

[208] Lau, K. H. A.; Sileika, T. S.; Park, S. H.; Sousa, A. M. L.; Burch, P.; Szleifer, I.; Messersmith, P. B. *Advanced Materials Interfaces* **2015**, *2*, 1–10.

[209] Cheng, G.; Zhang, Z.; Chen, S.; Bryers, J. D.; Jiang, S. *Biomaterials* **2007**, *28*, 4192–4199.

[210] Wei, J.; Ravn, D. B.; Gram, L.; Kingshott, P. *Colloids and Surfaces B: Biointerfaces* **2003**, *32*, 275–291.

[211] Grove, J.; Marsh, M. *The Journal of Cell Biology* **2011**, *195*, 1071–1082.

[212] Ramstedt, M. **2000**,

[213] Riedel, T.; Rodriguez-Emmenegger, C.; de los Santos Pereira, A.; Bdajnkov, A.; Jinoch, P.; Boltovets, P. M.; Brynda, E. *Biosensors and Bioelectronics* **2014**, *55*, 278–284.

[214] Deng, X.; Lahann, J. *Journal of Applied Polymer Science* **2014**, *131*.

[215] Bally, F.; Cheng, K.; Nandivada, H.; Deng, X.; Ross, A. M.; Panades, A.; Lahann, J. *ACS applied materials & interfaces* **2013**, *5*, 9262–8.

[216] Deng, X.; Lahann, J. *Macromolecular rapid communications* **2012**, *33*, 1459–65.

[217] Katira, P.; Agarwal, A.; Fischer, T.; Chen, H. Y.; Jiang, X.; Lahann, J.; Hess, H. *Advanced Materials* **2007**, *19*, 3171–3176.

[218] Deng, X.; He, S.; Xie, F.; Friedmann, C.; Hess, H.; Lahann, J. *Advanced Materials* **2016**, *28*, 2367–2373.

[219] Kohn, T.; Sander, M. *Environmental science and technology* **2016**, *50*, 732–743.

[220] Kumar, R.; Kopyeva, I.; Cheng, K.; Liu, K.; Lahann, J. *Langmuir* **2017**, *33*, 6322–6332, PMID: 28574709.

[221] Bendersky, M.; Santore, M. M.; Davis, J. M. *Journal of Colloid and Interface Science* **2015**, *449*, 443–451.

[222] Van Breedam, W.; PÃűhlmann, S.; Favoreel, H. W.; de Groot, R. J.; Nauwynck, H. J. *FEMS Microbiology Reviews* **2014**, *38*, 598–632.

[223] Stuart, M. A. C.; Huck, W. T. S.; Genzer, J.; Muller, M.; Ober, C.; Stamm, M.; Sukhorukov, G. B.; Szleifer, I.; Tsukruk, V. V.; Urban, M.; Winnik, F.; Zauscher, S.; Luzinov, I.; Minko, S. *Nat Mater* **2010**, *9*, 101–113.

[224] Zhou, F.; Hu, H.; Yu, B.; Osborne, V. L.; Huck, W. T. S.; Liu, W. *Analytical Chemistry* **2007**, *79*, 176–182.

[225] Zhou, F.; Biesheuvel, P. M.; Choi, E.-Y.; Shu, W.; Poetes, R.; Steiner, U.; Huck, W. T. S. *Nano Letters* **2008**, *8*, 725–730.

[226] Comrie, J. E.; Huck, W. T. S. *Macromolecular Rapid Communications* **2008**, *29*, 539–546.

[227] Zhou, F.; Shu, W.; Welland, M. E.; Huck, W. T. S. *Journal of the American Chemical Society* **2006**, *128*, 5326–5327.

[228] Azzaroni, O.; Brown, A. A.; Huck, W. T. S. *Advanced Materials* **2007**, *19*, 151–154.

[229] Cheng, G.; Li, G.; Xue, H.; Chen, S.; Bryers, J. D.; Jiang, S. *Biomaterials* **2009**, *30*, 5234–5240.

[230] Yuan, S. J.; Pehkonen, S. O.; Ting, Y. P.; Neoh, K. G.; Kang, E. T. *Langmuir* **2010**, *26*, 6728–6736.

[231] Welch, M.; Rastogi, A.; Ober, C. *Soft Matter* **2011**, *7*, 297–302.

[232] Uhlmann, P.; Merlitz, H.; Sommer, J.-U.; Stamm, M. *Macromolecular Rapid Communications* **2009**, *30*, 732–740.

[233] Barner-Kowollik, C.; Davis, T. P.; Heuts, J. P. A.; Stenzel, M. H.; Vana, P.; Whittaker, M. *Journal of Polymer Science Part A: Polymer Chemistry* **2003**, *41*, 365–375.

[234] Baum, M.; ; Brittain, W. J. *Macromolecules* **2002**, *35*, 610–615.

[235] Mansfeld, U.; Pietsch, C.; Hoogenboom, R.; Becer, C. R.; Schubert, U. S. *Polym. Chem.* **2010**, *1*, 1560–1598.

[236] Jeyaprakash, J. D.; Samuel, S.; Dhamodharan, R.; Rühe, J. *Macromolecular Rapid Communications* **2002**, *23*, 277–281.

[237] Rodda, A. E.; Ercole, F.; Nisbet, D. R.; Forsythe, J. S.; Meagher, L. *Macromolecular Bioscience* **2015**, *15*, 799–811.

[238] Czitrom, V. *The American Statistician* **1999**, *53*, 126–131.

[239] Siegwart, D. J.; Leiendecker, M.; Langer, R.; Anderson, D. G. *Macromolecules* **2012**, *45*, 1254–1261.

[240] Toloza Porras, C.; D'hooge, D. R.; Reyniers, M.-F.; Marin, G. B. *Macromolecular Theory and Simulations* **2013**, *22*, 136–149.

[241] Limpoco, F. T.; Bailey, R. C. *J. Am. Chem. Soc.* **2011**, *133*, 14864–14867.

[242] Bain, E. D.; Turgman-Cohen, S.; Genzer, J. *Macromolecular Theory and Simulations* **2013**, *22*, 8–30.

[243] Gao, X.; Feng, W.; Zhu, S.; Sheardown, H.; Brash, J. L. *Macromolecular Reaction Engineering* **2010**, *4*, 235–250.

[244] Xiao, D.; and Mary J. Wirth, *Macromolecules* **2002**, *35*, 2919–2925.

[245] Zhou, D.; Gao, X.; Wang, W. J.; Zhu, S. *Macromolecules* **2012**, *45*, 1198–1208.

[246] Kang, C.; Crockett, R. M.; Spencer, N. D. *Macromolecules* **2014**, *47*, 269–275.

[247] Barner-Kowollik, C.; Buback, M.; Egorov, M.; Fukuda, T.; Goto, A.; Olaj, O. F.; Russell, G. T.; Vana, P.; Yamada, B.; Zetterlund, P. B. *Progress in Polymer Science* **2005**, *30*, 605–643.

[248] Barner-Kowollik, C.; Beuermann, S.; Buback, M.; Castignolles, P.; Charleux, B.; Coote, M. L.; Hutchinson, R. A.; Junkers, T.; Lacik, I.; Russell, G. T.; Stach, M.; van Herk, A. M. *Polym. Chem.* **2014**, *5*, 204–212.

[249] Kim, J.-B.; Huang, W.; Miller, M. D.; Baker, G. L.; Bruening, M. L. *Journal of Polymer Science Part A: Polymer Chemistry* **2003**, *41*, 386–394.

[250] Prucker, O.; and J. Rühe, *Macromolecules* **1998**, *31*, 602–613.

[251] Martinez, A. P.; Carrillo, J.-M. Y.; Dobrynin, A. V.; Adamson, D. H. *Macromolecules* **2016**, DOI:10.1021/acs.macromol.5b02261.

[252] Milchev, A.; Wittmer, J. P.; Landau, D. P. *The Journal of Chemical Physics* **2000**, *112*, 1606–1615.

[253] Gillespie, D. T. *Journal of Computational Physics* **1976**, *22*, 403–434.

[254] Gillespie, D. T. *The Journal of Physical Chemistry* **1977**, *81*, 2340–2361.

[255] Cheng, N.; Brown, A. A.; Azzaroni, O.; Huck, W. T. S. *Macromolecules* **2008**, *41*, 6317–6321.

[256] Huang, X.; Wirth, M. J. *Macromolecules* **1999**, *32*, 1694–1696.

[257] Liu, P.; Domingue, E.; Ayers, D. C.; Song, J. *ACS Applied Materials & Interfaces* **2014**, *6*, 7141–7152.

[258] Villa-Diaz, L. G.; Nandivada, H.; Ding, J.; Nogueira-de Souza, N. C.; Krebsbach, P. H.; O'Shea, K. S.; Lahann, J.; Smith, G. D. *Nat Biotech* **2010**, *28*, 581–583.

[259] Villa-Diaz, L.; Ross, A.; Lahann, J.; Krebsbach, P. *Stem Cells* **2013**, *31*, 1–7.

[260] Qian, X.; Villa-Diaz, L. G.; Kumar, R.; Lahann, J.; Krebsbach, P. H. *Biomaterials* **2014**, *35*, 9581–9590.

[261] Hallab, N.; Bundy, K.; O'Connor, K.; Clark, R.; Moses, R. *Journal of Long-Term Effects of Medical Implants* **1995**, *5*, 209–231, cited By 102.

[262] Ross, A. M.; Jiang, Z.; Bastmeyer, M.; Lahann, J. *Small* **2012**, *8*, 336–355.

[263] Chen, W.; Villa-Diaz, L. G.; Sun, Y.; Weng, S.; Kim, J. K.; Lam, R. H. W.; Han, L.; Fan, R.; Krebsbach, P. H.; Fu, J. *ACS Nano* **2012**, *6*, 4094–4103.

[264] Ferdosian, F.; Yuan, Z.; Anderson, M.; Xu, C. C. *RSC Adv.* **2014**, *4*, 31745–31753.

[265] Kaith, B. S.; Sharma, R.; Kalia, S.; Bhatti, M. S. *RSC Adv.* **2014**, *4*, 40339–40344.

[266] Deming, S. N.; Morgan, S. L. *Experimental Design: A Chemometric Approach*; Elsevier, Amsterdam, 1987.

[267] Bess, E. N.; Bischoff, A. J.; Sigman, M. S. *Proceedings of the National Academy of Sciences* **2014**, *111*, 14698–14703.

[268] Soto, V. M. M.; Galin, J. C. *Polymer* **1984**, *25*, 254–262.

[269] Azzaroni, O.; Brown, A. A.; Huck, W. T. S. *Angewandte Chemie (International ed. in English)* **2006**, *45*, 1770–1774.

[270] Rubinstein, M.; Dobrynin, A. V. *Current Opinion in Colloid & Interface Science* **1999**, *4*, 83–87.

[271] Shipp, D. A.; Matyjaszewski, K. *Macromolecules* **2000**, *33*, 1553–1559.

[272] Schulz, D. N.; Peiffer, D. G.; Agarwal, P. K.; Larabee, J.; Kaladas, J. J.; Soni, L.; Handwerker, B.; Garner, R. T. *Polymer* **1986**, *27*, 1734–1742.

[273] World Health Organization, *Global Report on Diabetes*; 2016; Vol. 978; p 88.

[274] Chavez-Gaan, L.; Olleros, M. L.; Vesin, D.; Garcia, I. *Frontiers in Immunology* **2015**, *6*, 1–15.

[275] Pop, M. A.; Almquist, B. D. *Experimental Dermatology* **2017**, *26*, 760–763.

[276] Minutti, C. M.; Knipper, J. A.; Allen, J. E.; Zaiss, D. M. *Seminars in Cell and Developmental Biology* **2017**, *61*, 3–11.

[277] Rodero, M. P.; Khosrotehrani, K. *International Journal of Clinical and Experimental Pathology* **2010**, *3*, 643–653.

[278] Khanna, S.; Biswas, S.; Shang, Y.; Collard, E.; Azad, A.; Kauh, C.; Bhasker, V.; Gordillo, G. M.; Sen, C. K.; Roy, S. *PLoS ONE* **2010**, *5*.

[279] Garash, R.; Bajpai, A.; Marcinkiewicz, B. M.; Spiller, K. L. *Experimental Biology and Medicine* **2016**, *241*, 1054–1063.

[280] Kraakman, M. J.; Murphy, A. J.; Jandeleit-Dahm, K.; Kammoun, H. L. *Frontiers in Immunology* **2014**, *5*, 1–6.

[281] Tang, Y.; Zhang, M. J.; Hellmann, J.; Kosuri, M.; Bhatnagar, A.; Spite, M. *Diabetes* **2013**, *62*, 618–627.

[282] Leal, E. C.; Carvalho, E.; Tellechea, A.; Kafanas, A.; Tecilazich, F.; Kearney, C.; Kuchibhotla, S.; Auster, M. E.; Kokkotou, E.; Mooney, D. J.; Logerfo, F. W.; Pradhan-Nabzdyk, L.; Veves, A. *American Journal of Pathology* **2015**, *185*, 1638–1648.

[283] Qie, Y.; Yuan, H.; von Roemeling, C. A.; Chen, Y.; Liu, X.; Shih, K. D.; Knight, J. A.; Tun, H. W.; Wharen, R. E.; Jiang, W.; Kim, B. Y. S. *Scientific reports* **2016**, *6*, 26269.

[284] Jetten, N.; Roumans, N.; Gijbels, M. J.; Romano, A.; Post, M. J.; De Winther, M. P. J.; Van Der Hulst, R. R. W. J.; Xanthoulea, S. *PLoS ONE* **2014**, *9*, 1–9.

[285] Kasiewicz, L. N.; Whitehead, K. A. *Biomater. Sci.* **2017**, *5*, 1962–1975.

[286] Ferrante, C. J.; Leibovich, S. J. *Advances in wound care* **2012**, *1*, 10–16.

[287] McWhorter, F. Y.; Davis, C. T.; Liu, W. F. *Cellular and Molecular Life Sciences* **2015**, *72*, 1303–1316.

[288] Ogle, M. E.; Segar, C. E.; Sridhar, S.; Botchwey, E. A. *Experimental Biology and Medicine* **2016**, *241*, 1084–1097.

[289] Jones, D. E.; Ghandehari, H.; Facelli, J. C. *Computer Methods and Programs in Biomedicine* **2016**, *132*, 93 – 103.

[290] Pan, Z.; Kang, X.; Zeng, Y.; Zhang, W.; Peng, H.; Wang, J.; Huang, W.; Wang, H.; Shen, Y.; Huang, Y. *Polym. Chem.* **2017**,

[291] Azad, A. K.; Rajaram, M. V. S.; Schlesinger, L. S. *Journal of Cytol Mol Biol* **2007**, *137*, 2696–2700.

[292] Yu, S. S.; Lau, C. M.; Barham, W. J.; Onishko, H. M.; Nelson, C. E.; Li, H.; Smith, C. A.; Yull, F. E.; Duvall, C. L.; Giorgio, T. D. *Molecular pharmaceutics* **2013**, *10*, 975–87.

[293] Ortega, R. a.; Barham, W. J.; Kumar, B.; Tikhomirov, O.; McFadden, I. D.; Yull, F. E.; Giorgio, T. D. *Nanoscale* **2015**, *7*, 500–510.

[294] Zhao, P.; Yin, W.; Wu, A.; Tang, Y.; Wang, J.; Pan, Z.; Lin, T.; Zhang, M.; Chen, B.; Duan, Y.; Huang, Y. *Advanced Functional Materials* **2017**, *1700403*, 1700403.

[295] Wu, J. et al. *Cell* **2017**, *168*, 473–486.e15.

[296] Boskovic, J.; Arnold, J. N.; Stilion, R.; Gordon, S.; Sim, R. B.; Rivera-Calzada, A.; Wienke, D.; Isacke, C. M.; Martinez-Pomares, L.; Llorca, O. *Journal of Biological Chemistry* **2006**, *281*, 8780–8787.

[297] Azad, A. K.; Rajaram, M. V. S.; Metz, W. L.; Cope, F. O.; Blue, M. S.; Vera, D. R.; Schlesinger, L. S. *The Journal of Immunology* **2015**, *195*, 2019–2029.

[298] Yu, K.; Kizhakkedathu, J. N. *Biomacromolecules* **2010**, *11*, 3073–3085, PMID: 20954736.

[299] Vaisocherová, H.; Brynda, E.; Homola, J. *Analytical and Bioanalytical Chemistry* **2015**, *407*, 3927–3953.

[300] Von Der Ehe, C.; Bu??, T.; Weber, C.; Stumpf, S.; Bellstedt, P.; Hartlieb, M.; Schubert, U. S.; Gottschaldt, M. *ACS Macro Letters* **2016**, *5*, 326–331.

[301] Von Der Ehe, C.; Weber, C.; Gottschaldt, M.; Schubert, U. S. *Progress in Polymer Science* **2016**, *57*, 64–102.

[302] Chernyy, S.; Jensen, B. E. B.; Shimizu, K.; Ceccato, M.; Pedersen, S. U.; Zelikin, A. N.; Daasbjerg, K.; Iruthayaraj, J. *Journal of Colloid and Interface Science* **2013**, *404*, 207–214.

[303] Fantin, M.; Isse, A. A.; Gennaro, A.; Matyjaszewski, K. *Macromolecules* **2015**, *48*, 6862–6875.

[304] Hollas, M. A.; Webb, S. J.; Flitsch, S. L.; Fielding, A. J. *Angewandte Chemie International Edition* **2017**, *56*, 9449–9453.

[305] Mangold, S. L.; Cloninger, M. J. *Organic & Biomolecular Chemistry* **2006**, *4*, 2458.

[306] MacK, E. T.; Snyder, P. W.; Perez-Castillejos, R.; Bilgiçer, B.; Moustakas, D. T.; Butte, M. J.; Whitesides, G. M. *Journal of the American Chemical Society* **2012**, *134*, 333–345.

[307] Mandal, D. K.; Kishore, N.; Brewer, C. F. *Biochemistry* **1994**, *33*, 1149–1156, PMID: 8110746.

[308] Kitov, P. I.; Bundle, D. R. *Journal of the American Chemical Society* **2003**, *125*, 16271–16284.

[309] Faust, J. J.; Christenson, W.; Doudrick, K.; Ros, R.; Ugarova, T. P. *Biomaterials* **2017**, *128*, 160 – 171.

[310] Tsai, I. Y.; Kuo, C.-C.; Tomczyk, N.; Stachelek, S. J.; Composto, R. J.; Eckmann, D. M. *Soft Matter* **2011**, *7*, 3599–3606.

[311] Lambshead, J. W.; Meagher, L.; O'Brien, C.; Laslett, A. L. *Cell regeneration (London, England)* **2013**, *2*, 7.

[312] Zhang, L.; Cao, Z.; Bai, T.; Carr, L.; Ella-Menye, J.-R.; Irvin, C.; Ratner, B. D.; Jiang, S. *Nature biotechnology* **2013**, *31*, 553–6.

[313] Levenstein, M. E.; Ludwig, T. E.; Xu, R.-H.; Llanas, R. a.; VanDenHeuvel-Kramer, K.; Manning, D.; Thomson, J. a. *Stem cells (Dayton, Ohio)* **2006**, *24*, 568–74.

[314] Levenstein, M. E.; Berggren, W. T.; Lee, J. E.; Conard, K. R.; Llanas, R. a.; Wagner, R. J.; Smith, L. M.; Thomson, J. a. *Stem cells (Dayton, Ohio)* **2008**, *26*, 3099–107.

[315] Nguyen, T. H.; Kim, S.-H.; Decker, C. G.; Wong, D. Y.; Loo, J. a.; Maynard, H. D. *Nature chemistry* **2013**, *5*, 221–7.

[316] Nandivada, H. Development of biomimetic interfaces and their applications. Ph.D. thesis, Univeristy of Michigan, Ann Arbor, 2009.

[317] Topal, T.; Villa-Diaz, L.; Kumar, R.; Lahann, J.; Krebsbach, P. H. *Unpublished*

[318] Shao, Q.; Jiang, S. *Advanced Materials* **2015**, *27*, 15–26.

[319] Hook, A. L.; Thissen, H.; Voelcker, N. H. *Langmuir : the ACS journal of surfaces and colloids* **2009**, *25*, 9173–81.

[320] Green, R. J.; Davies, J.; Roberts, C. J.; Tendler, S. J. B. *Biomaterials* **1997**, *18*, 4015–413.

[321] Kratzer, D.; Barner, L.; Friedmann, C.; Brase, S.; Lahann, J. *European Journal of Organic Chemistry* **2014**, *2014*, 8064–8071.

[322] Higaki, Y.; Inutsuka, Y.; Sakamaki, T.; Terayama, Y.; Takenaka, A.; Higaki, K.; Yamada, N. L.; Moriwaki, T.; Ikemoto, Y.; Takahara, A. *Langmuir* **2017**, *33*, 8404–8412, PMID: 28737401.

[323] Shao, Q.; Mi, L.; Han, X.; Bai, T.; Liu, S.; Li, Y.; Jiang, S. *The Journal of Physical Chemistry B* **2014**, *118*, 6956–6962, PMID: 24885910.

[324] Hildebrand, V.; Laschewsky, A.; Pach, M.; Muller-Buschbaum, P.; Papadakis, C. M. *Polym. Chem.* **2017**, *8*, 310–322.

[325] Suchy, F.; Yamaguchi, T.; Nakauchi, H. *Cell Stem Cell* **2018**, *22*, 21–24.

[326] De Vos, J.; Assou, S. *Clinics and Research in Hepatology and Gastroenterology* **2017**, *41*, 249–253.

[327] Kolesky, D. B.; Homan, K. A.; Skylar-Scott, M. A.; Lewis, J. A. *Proceedings of the National Academy of Sciences* **2016**, *113*, 3179–3184.

[328] Graham, D. M. *Lab Animal* **2017**, *46*, 77–77.

[329] Gafni, O. et al. *Nature* **2013**, *504*, 282–286.

[330] Hanna, J.; Cheng, A. W.; Saha, K.; Kim, J.; Lengner, C. J.; Soldner, F.; Cassady, J. P.; Muffat, J.; Carey, B. W.; Jaenisch, R. *Proceedings of the National Academy of Sciences* **2010**, *107*, 9222–9227.

[331] Weinberger, L.; Ayyash, M.; Novershtern, N.; Hanna, J. H. *Nature Reviews Molecular Cell Biology* **2016**, *17*, 155–169.

[332] Guo, G.; Von Meyenn, F.; Santos, F.; Chen, Y.; Reik, W.; Bertone, P.; Smith, A.; Nichols, J. *Stem Cell Reports* **2016**, *6*, 437–446.

[333] Fang, R.; Liu, K.; Zhao, Y.; Li, H.; Zhu, D.; Du, Y.; Xiang, C.; Li, X.; Liu, H.; Miao, Z.; Zhang, X.; Shi, Y.; Yang, W.; Xu, J.; Deng, H. *Cell Stem Cell* **2014**, *15*, 488–496.

[334] Chen, K. G.; Mallon, B. S.; McKay, R. D.; Robey, P. G. *Cell Stem Cell* **2014**, *14*, 13–26.

[335] Hayashi, Y.; Furue, M. K. *Stem Cells International* **2016**, *2016*.

[336] Theunissen, T. W. et al. *Cell Stem Cell* **2014**, *15*, 471–487.

[337] Villa-Diaz, L. G.; Kim, J. K.; Laperle, A.; Palecek, S. P.; Krebsbach, P. H. *Stem Cells* **2016**, *34*, 1753–1764.

[338] Theunissen, T. W. et al. *Cell Stem Cell* **2016**, *19*, 502–515.

[339] Stencel-Baerenwald, J. E.; Reiss, K.; Reiter, D. M.; Stehle, T.; Dermody, T. S. *Nature Reviews Microbiology* **2014**, *12*, 739.

[340] Hushegyi, A.; Bertok, T.; Damborsky, P.; Katrlik, J.; Tkac, J. *Chem. Commun.* **2015**, *51*, 7474–7477.

[341] Lees, W. J.; Spaltenstein, A.; Kingery-Wood, J. E.; Whitesides, G. M. *Journal of Medicinal Chemistry* **1994**, *37*, 3419–3433, PMID: 7932570.

[342] Mammen, M.; Dahmann, G.; Whitesides, G. M. *Journal of Medicinal Chemistry* **1995**, *38*, 4179–4190, PMID: 7473545.

[343] Tang, S.; Puryear, W. B.; Seifried, B. M.; Dong, X.; Runstadler, J. A.; Ribbeck, K.; Olsen, B. D. *ACS Macro Letters* **2016**, *5*, 413–418.

[344] Guerrero-Sanchez, C.; Keddie, D. J.; Saubern, S.; Chiefari, J. *ACS Combinatorial Science* **2012**, *14*, 389–394.

[345] Zhang, T.; Gieseler, D.; Jordan, R. *Polym. Chem.* **2016**, *7*, 775–779.

[346] Cosson, S.; Danial, M.; Saint-Amans, J. R.; Cooper-White, J. J. *Macromolecular Rapid Communications* **2017**, *38*, 1–6.

[347] Chapman, R.; Gormley, A. J.; Stenzel, M. H.; Stevens, M. M. *Angewandte Chemie - International Edition* **2016**, *55*, 4500–4503.

[348] Enciso, A. E.; Fu, L.; Russell, A. J.; Matyjaszewski, K. *Angewandte Chemie - International Edition* **2018**, 933–936.

[349] Lu, W.; Xiao, R.; Yang, J.; Li, H.; Zhang, W. *Journal of Materiomics* **2017**, *3*, 191–201.

[350] Liu, Y.; Zhao, T.; Ju, W.; Shi, S.; Shi, S.; Shi, S. *Journal of Materiomics* **2017**, *3*, 159–177.